A Measurement of the Inclusive Semileptonic Branching Fractions of b Hadrons

by
Christopher Robert Jones
of
Magdalene College

A dissertation submitted to the University of Cambridge
for the degree of Doctor of Philosophy
August 1999

A Measurement of the Inclusive Semileptonic Branching Fractions of b Hadrons

Christopher Robert Jones

Abstract

The OPAL detector at the LEP collider at CERN recorded 3.35 million hadronic Z^0 decays between 1992 and 1995. Measurements of the inclusive semileptonic branching fractions of b hadrons derived from this data sample, are presented in this thesis.

An enriched sample of $Z^0 \to b\overline{b}$ decays is obtained using a method which exploits the relatively long lifetime and high mass of the b quark. A method for measuring the b purity of this sample from the data is described. Electron and muon candidates are selected from this b enriched sample and an improved algorithm for identifying electrons is presented. A new method for determining the fraction of leptons from semileptonic decays is developed, which compares the distribution of several kinematic variables using artificial neural networks. A fit for the fraction of semileptonic decays in the lepton samples is performed, which also yields $\langle x_E \rangle_{\mathrm{b}}$, the average fraction of the beam energy carried by the weakly decaying b hadron, giving

$$
\begin{aligned}
\mathcal{B}(\mathrm{b} \to \mathrm{X}\ell\nu_\ell) &= (10.83 \pm 0.10\ (\mathrm{stat.}) \pm 0.20\ (\mathrm{syst.})\ {}^{+\,0.20}_{-\,0.13}\ (\mathrm{model}))\,\%, \\
\mathcal{B}(\mathrm{b} \to \mathrm{c} \to \mathrm{X}\ell\nu_\ell) &= (8.40 \pm 0.16\ (\mathrm{stat.}) \pm 0.21\ (\mathrm{syst.})\ {}^{+\,0.33}_{-\,0.29}\ (\mathrm{model}))\,\%, \\
\langle x_E \rangle_{\mathrm{b}} &= 0.709 \pm 0.003\ (\mathrm{stat.}) \pm 0.003\ (\mathrm{syst.}) \pm 0.013\ (\mathrm{model}),
\end{aligned}
$$

where b denotes all weakly decaying b hadrons and ℓ represents either e or μ. The first errors are statistical and the second include all experimental systematic uncertainties. The modelling errors are due to theoretical uncertainties in the semileptonic b decay lepton momentum spectra and the b quark fragmentation spectra.

The OPAL detector and the LEP accelerator are briefly summarised. A theoretical overview of semileptonic decays is presented and the predictions are compared with these and other experimental results.

Declaration

This dissertation is the result of my own work, except where explicit reference is made to the work of others, and has not been submitted for another qualification to this or any other university.

Christopher R. Jones

Preface

I joined the Cavendish research group as a Ph.D. research student after applying for a studentship during my final year of the undergraduate Natural Sciences Tripos at Magdalene College, Cambridge. During that year, the lectures given by Richard Batley, Andy Parker and David Ward helped me to decide to continue my studies as a particle physics research student. In September 1995 I joined the Cambridge OPAL group under the supervision of Richard Batley. I would like to acknowledge PPARC (Particle Physics and Astronomy Research Council) for funding my studentship and visits to CERN, and Magdalene College for my Leslie Wilson Scholarship.

I would like to thank Richard for his help throughout my studies. From the start, when he helped me understand the mysteries of the OPAL data format, to the final stages with the proof reading of the many drafts of this thesis, Richard's support has been instrumental in bringing the thesis to its finished state. I would also like to thank the other members of the Cambridge particle physics group, particularly Janet Carter, Val Gibson, Bruce Hay, Chris Hawkes, John Hill, David Ward, Pat Ward and Jan White for their much appreciated assistance.

Whilst a member of the Cambridge group, I have been lucky enough to spend two summers resident in Geneva, Switzerland, whilst working at the CERN Laboratory. During this time I had the fortune to work with many people from other institutes within the OPAL heavy flavour working group and also whilst helping with the daily running of the silicon microvertex detector. In particular I would like to thank Ties Behnke, Oliver Cooke, Richard Hawkings, Sijbrand de Jong, Rocio Pérez-Ochoa and Pippa Wells. Special thanks should go to Pauline Gagnon with whom I have worked closely to bring this analysis to its final state and ultimately to publication as an OPAL paper.

Life as a research student would have been a lot duller without the company of my fellow students and contemporaries. In particular, I thank my Magdalene undergraduate colleagues who also stayed on after graduating to undertake postgraduate studies; Chris, Colin, Mike, Nic and Robin, and those who decided to pursue a career in the city; Ali, Amarjit and Toby.

At the Cavendish laboratory and at CERN, my thanks goes to my fellow high energy physics students; Andrea, Chris, David, Helen, Kate, Kyle, Matt, Niklas, Paul, Scott, Simon and many many others, all of whom helped make the daily work more enjoyable.

Finally, I would like to thank my family, who still do not understand what I have been doing, but without whom it would not have been possible.

Contents

List of Figures

List of Tables

Chapter 1

Introduction

This thesis presents measurements of the inclusive semileptonic branching fractions of b hadrons $\mathcal{B}(\mathrm{b} \to \mathrm{X}\ell\nu_\ell)$ and $\mathcal{B}(\mathrm{b} \to \mathrm{c} \to \mathrm{X}\ell\nu_\ell)$. The data used in this analysis consists of 3.35 million hadronic Z^0 decays collected with the OPAL detector at the LEP accelerator between 1992 and 1995.

The inclusive semileptonic branching fraction $\mathcal{B}(\mathrm{b} \to \mathrm{X}\ell\nu_\ell)$ is defined as the fraction of ground state b hadrons (hadrons containing a b quark)[a] that decay weakly to a final state containing a lepton and lepton neutrino pair, where the lepton is either an electron or muon. The branching fraction $\mathcal{B}(\mathrm{b} \to \mathrm{c} \to \mathrm{X}\ell\nu_\ell)$ refers to the fraction of b hadrons that decay weakly to a state containing a charm hadron, which then proceeds to decay semileptonically. The ground state b mesons are the B^0, B^+, $\mathrm{B_s}$ and $\mathrm{B_c}$ mesons, whilst the weakly decaying ground state b baryons are generically referred to as Λ_b, and consist of the Λ_b^0, Ξ_b, Σ_b and Ω_b baryons.

Studies of the weak decays of heavy hadrons play an important role in testing the Standard Model of particle physics and in the determination of some of the parameters not predicted by the theory. Measurements of the branching fraction $\mathcal{B}(\mathrm{b} \to \mathrm{X}\ell\nu_\ell)$ provide information on the heavy quark masses and Cabibbo-Kobayashi-Maskawa (CKM)

[a] Throughout this thesis charge conjugation is implied unless otherwise stated.

matrix elements, which determine quark mixing. In addition, the weak decays of hadrons provide a probe into the parts of the strong interaction that are least well understood; the perturbative and non–perturbative forces which bind quarks and gluons inside hadrons. Experimentally, the high momentum leptons from semileptonic $\mathrm{b} \to \ell$ decays provide a relatively clean and distinctive signature for b decays. 'Cascade' decays, $\mathrm{b} \to \mathrm{c} \to \ell$, also produce high momentum leptons and form an important background to 'direct' $\mathrm{b} \to \ell$ decays. Theoretically, cascade decays are less interesting than direct decays since the heavy quark $\mathrm{c} \to \ell$ decay is convoluted with the $\mathrm{b} \to \mathrm{c}$ decay kinematics. The $\mathcal{B}(\mathrm{b} \to \mathrm{c} \to \mathrm{X}\ell\nu_\ell)$ branching fraction is of interest experimentally however and is commonly determined simultaneously with $\mathcal{B}(\mathrm{b} \to \mathrm{X}\ell\nu_\ell)$ to minimise systematic uncertainties.

In Chapter 2 an introduction to the Standard Model is presented. The theory behind the production and weak decay of b hadrons is discussed, together with an overview of the current status of experimental measurements and theoretical predictions for $\mathcal{B}(\mathrm{b} \to \mathrm{X}\ell\nu_\ell)$. The various phenomenological models used to describe the semileptonic decay lepton momentum spectra are also described.

Chapter 3 gives a description of the LEP accelerator and the OPAL detector and explains how the data used in this analysis were collected. In this thesis, the semileptonic branching fractions are measured by calculating the ratio of the number of leptons that originate from semileptonic $\mathrm{b} \to \ell$ and $\mathrm{b} \to \mathrm{c} \to \ell$ decays, to the total number of weak b decays in a data set enhanced in $\mathrm{Z}^0 \to \mathrm{b}\overline{\mathrm{b}}$ events. Chapter 4 describes the raw data sets used in this analysis, and the techniques used to select from these data a sample enhanced in b hadron decays. A method for measuring the b purity of the b hadron enhanced sample from the data itself is described, allowing the true number of b decays in the data to be determined.

In Chapter 5 the techniques used to identify electron and muon candidate tracks in the Z^0 events are described together with the use of simulated Monte Carlo data to determine the efficiencies of these selections. The development of an improved algorithm for identifying electron candidates is discussed in detail. The methods used to determine the fraction of the selected lepton samples that originate from $\mathrm{b} \to \ell$ and $\mathrm{b} \to \mathrm{c} \to \ell$

decays are described in Chapter 6, and in Chapter 7 the final results for the semileptonic branching fractions are presented together with a discussion of the systematic and modelling uncertainties. Finally, Chapter 8 discusses the implications of the results and gives an outlook on the future developments in b physics.

Chapter 2

Review of Weak b Hadron Decays

In this chapter an overview of the current theories of particle physics which comprise the Standard Model is presented. The chapter starts with a brief summary of the particles and forces in nature and their theoretical description within the Standard Model. An overview of b hadron production is then given and the models used to describe these processes are discussed. Following this, the theoretical description of the weak decays of b hadrons is presented with a summary of the current theoretical and experimental status of semileptonic weak decays. Finally, the chapter ends with a discussion of the phenomenological models used to describe the lepton momentum spectra from weak b hadron decays.

2.1 Introduction

There are currently thought to be four fundamental forces in nature. The Standard Model encompasses gauge theories describing three of these forces: the electromagnetic, weak and strong forces. The fourth force, gravitation, has not as yet been successfully incorporated into the Standard Model. It is however, very weak when compared to the other forces at currently available experimental energies and hence its omission is expected to have negligible impact on the theoretical predictions.

The Standard Model contains two different species of elementary particles, the bosons and fermions. The bosons are the gauge particles which mediate the forces and have integer spin[a]. The fermions are further divided into quarks and leptons, both having spin $\frac{1}{2}$.

In the following sections a brief description of the Standard Model is given, focusing on those areas relevant to this thesis. A more detailed discussion can be found in the literature, for example [1, 2].

2.1.1 Gauge Bosons and Forces

Gauge bosons are the mediating particles for the fundamental forces (Table 2.1).

Interaction		Boson		Spin	Mass / GeV/c^2
Electroweak	Electromagnetic	Photon	γ	1	massless
	Charged current	W boson	$W^{\pm}$	1	80.41 ± 0.10
	Neutral current	Z boson	Z^0	1	91.188 ± 0.007
QCD		8 Gluons	g	1	massless
Gravitation		Graviton	G	2	massless

Table 2.1: *The gauge bosons of the four fundamental forces. Mass values taken from [3].*

The electromagnetic force acts on all electric charge carriers and is mediated by the photon, a massless spin 1 boson with zero electric charge. Since the photon is electrically neutral it cannot interact directly with other photons, and since it is massless the electromagnetic force has infinite range. The electromagnetic interactions are described to a high level of accuracy by the theory of Quantum Electrodynamics (QED).

[a]Spin measured in units of $\hbar$.

The strong force couples particles which carry colour charge and is mediated by the massless gluon. The gluon itself carries colour charge and therefore self–interactions between gluons can occur. These interactions limit the effective range of the strong force. The theory describing the strong interactions is Quantum Chromodynamics (QCD).

The weak force couples to all particles and is mediated by the massive $W^{\pm}$ and Z^0 gauge bosons. The large masses of the $W^{\pm}$ and Z^0 gauge bosons means the force has a finite range[b]. At an energy scales sufficient to directly create these bosons, the weak force is as strong as the electromagnetic force, allowing these forces to be successfully united in the theory of electroweak interactions.

Gravity is thought to be mediated by the graviton, a massless particle with spin 2, which has not yet been observed. Gravity is very weak at current experimental energies.

2.1.2 Quarks and Leptons

The fermions are divided into two classes, the quarks and the leptons. The quarks are distinguished from the leptons in that they feel the strong force. There are six flavours of quark; the up, charm and top quarks have electric charge[c] $+\frac{2}{3}e$ whilst the down, strange and bottom quarks have charge $-\frac{1}{3}e$. There are also six types of lepton; the electron, muon and tau which have electric charge $-e$, and their associated neutral leptons, the neutrinos. The fermions are grouped together forming three 'generations' where each generation contains a quark and lepton doublet as shown in Table 2.2. The particles in each generation have similar properties, differing only in their respective mass scales.

The first generation consists of the lightest quark (up and down) and lepton (e and ν_e) pairs which together form the building blocks of ordinary matter. The remaining heavier quarks form particles which quickly decay to lighter particles containing the u and d quarks.

[b]From the uncertainty principle $\Delta E \cdot \Delta t \geq \hbar$, a particle with finite mass can only be created from the vacuum for a finite time period.

[c]e is the magnitude of the charge of the electron.

	Generations			Electric charge	Colour charge
	I	II	III		
Quarks	**u** 1.5–5 MeV/c^2 **d** 3–9 MeV/c^2	**c** 1.1–1.4 GeV/c^2 **s** 60–170 MeV/c^2	**t** 174±5 GeV/c^2 **b** 4.1–4.4 GeV/c^2	$+\frac{2}{3}e$ $-\frac{1}{3}e$	r,g,b
Leptons	$\boldsymbol{\nu}_{\mathbf{e}}$ <15 eV/c^2 **e** 0.511 MeV/c^2	$\boldsymbol{\nu}_{\boldsymbol{\mu}}$ <0.17 MeV/c^2 $\boldsymbol{\mu}$ 105.7 MeV/c^2	$\boldsymbol{\nu}_{\boldsymbol{\tau}}$ <18.2 MeV/c^2 $\boldsymbol{\tau}$ $1.78^{+0.29}_{-0.26}$ GeV/c^2	0 $-e$	0

Table 2.2: *The spin $\frac{1}{2}$ fermions in the Standard Model and their measured masses [3].*

In addition, there are the partner anti–matter particles to those listed in Table 2.2. Anti–matter particles are identical in many respects to their partners, differing only in their internal quantum numbers, such as electric and colour charge, which are reversed (for example the electron anti–matter partner, the positron, has electric charge $+e$). Antiquarks are donated by a bar above their name (for example, the antitop quark is $\overline{\mathrm{t}}$).

2.1.3 Hadrons

Due to the nature of the strong interaction, quarks and antiquarks can only exist in bound states, termed hadrons. Hadrons are divided into two categories, baryons and mesons. Baryons are clusters of three quarks. The proton and neutron are common examples of baryons, where the proton contains two up quarks and one down quark (uud), whilst the neutron contains one up quark and two down quarks (ddu). Mesons consist of a quark and an antiquark pair; for example, combining an up quark with an antidown quark ($\mathrm{u}\overline{\mathrm{d}}$) gives the positive pion, π^+, whilst combining an antiup quark with a down quark ($\overline{\mathrm{u}}\mathrm{d}$) gives the π^+ antiparticle partner, the π^-.

2.2 Gauge Field Theories

Any system of interacting particles can be represented theoretically using the Lagrangian description of the system. Classically, the Lagrangian L is defined as the difference between the kinetic energy, T, and the potential energy, V, of the system, $L = T - V$.

Quantum mechanically, field theories are used which describe particles as quantised perturbations of physical fields. The propagation and interaction of these fields can also be described in terms of the Lagrangian description. The Lagrangian is constructed with the requirement that it is invariant under a set of symmetry transformations which reflect conservation laws in nature.

In quantum field theory, complex fields are used in the Lagrangian to describe the fermions, with the corresponding quantum mechanical complex phases being unobservable. Changes in these phases, known as *gauge transformations*, should therefore leave the Lagrangian unaltered. Global gauge invariance, where the Lagrangian is required to be invariant under a constant phase change for all space–time coordinates, predicts the conservation of charge. Local gauge invariance requires that the Lagrangian remains unaltered under phase transformations that are themselves functions of the space–time coordinates $\boldsymbol{x}$,

$$\Psi(\boldsymbol{x}) \to e^{i\alpha(\boldsymbol{x})}\Psi(\boldsymbol{x}) \tag{2.1}$$

where $\Psi(\boldsymbol{x})$ represents the gauge field. Preservation of the invariance of the fermion Lagrangian under such transformations requires the introduction of additional fields to the Lagrangian. These fields turn out to correspond to the gauge bosons of the theory.

Thus, by demanding invariance under a local gauge transformation, terms are introduced into the Lagrangian that correspond to the dynamics of the fermion interactions. The choice of the symmetry groups for a particular transformation depend upon the interaction to be described and are discussed in the following sections. First however, the process of *renormalisation* is described which allows calculable results to be obtained from the gauge theories.

2.2.1 Renormalisation

Theoretical predictions from the quantum field theories are obtained using perturbative expansions in the fields. A convenient technique for this is to use *Feynman diagrams* which are graphical representations of each term in the perturbative expansions. For a given physical process the total amplitude is the sum of all possible Feynman diagrams that have incoming and outgoing lines representing the interacting particles.

Figure 2.1a shows the zeroth order vertex in the simple QED process for e^+e^- annihilation. The amplitude for this process can be calculated through well behaved convergent expressions. Figures 2.1b-d show first order corrections to this process. Figure 2.1b shows a loop correction that involves the creation and subsequent annihilation of a fermion pair by the photon. Figure 2.1c shows a correction where a photon is exchanged between the incoming electron and positron, whilst Figure 2.1d shows the emission and re–absorption of a photon by one incoming fermion. In these higher order corrections, the momenta of the internal lines in the loops are free and give rise to integrals over infinite momentum ranges in the subsequent calculations. Such integrals are divergent.

The technique of *renormalisation* deals with these divergences. The loop corrections are split into infinite and finite parts, and for field theories with local gauge invariance, such as those in the Standard Model, the infinite parts of the corrections are found to cancel to all orders in the perturbative expansions. Renormalisation involves absorbing the divergent diagrams into the definition of the model parameters. In the case of Figure 2.1b, the infinities are absorbed into the definition of the charge of the electron. The bare charge is infinite with the observed finite charge renormalised to the physical measurement. Conceptually, this shielding of the bare electric charge can be viewed as resulting from a cloud of virtual pairs of particles surrounding the electron. The charge of the electron polarises these surrounding virtual pairs with the positive particles attracted and negative particles repelled. In a similar manner, Figures 2.1c and 2.1d are absorbed through renormalisation of the electron magnetic moment and mass respectively.

One consequence of this is that the higher the energy of the probe used to investigate

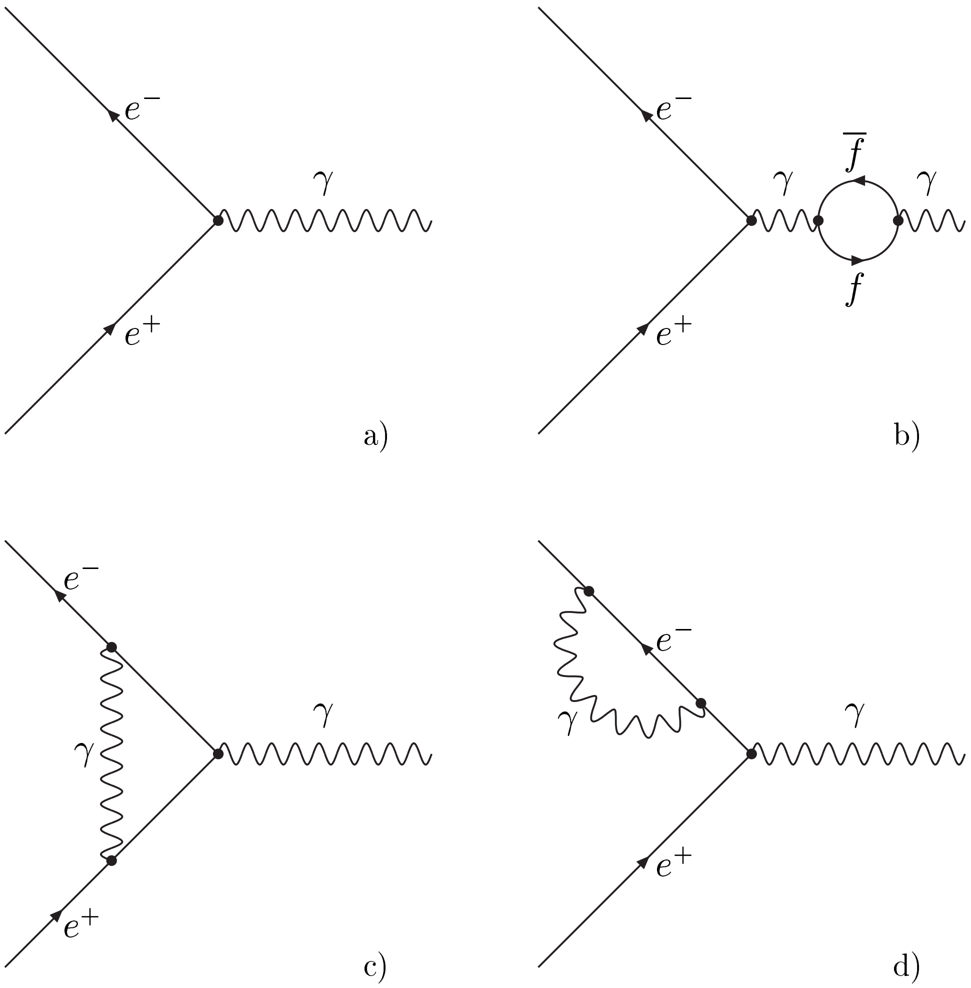

Figure 2.1: *Feynman diagrams for the QED e^+e^- annihilation vertex. Figure a) shows the zeroth order diagram, Figure b) shows a loop correction with internal fermion pair production, Figure c) shows a first order correction with photon exchange between the incoming e^+ and e^- whilst Figure d) shows the emission and re-absorption of a photon by the incoming e^-.*

the structure of the electron, the deeper into the virtual shielding sea is studied and hence the higher the observed electron charge. This is accounted for in the theory by a running electromagnetic coupling constant, α_{em}, which increases with increasing energy. A similar phenomenon is observed with the strong force but due to gluon self–interactions the effect is reversed, the strong coupling constant decreases with increasing energy scale. This effect is known as *asymptotic freedom*.

After renormalisation, the calculations are based on experimentally measured parameters, taken at some reference energy scale μ. The physical predictions of the theory do not depend on this renormalisation scale, but only if all the remaining finite components of each diagram in the perturbative expansion are summed. This is not always possible and the perturbative expansion must be evaluated to fixed order, which can lead to theoretical uncertainties in the predictions depending on the renormalisation scale μ and the particular scheme used to renormalise the divergences.

2.3 Quantum Chromodynamics

Quantum chromodynamics (QCD) is the gauge theory describing the strong interactions based on the $SU(3)_c$ 'colour' group structure proposed by Fritzsch, Leutwyler and Gell–Mann in 1973 [4]. QCD describes the strong interactions that bind quarks into mesons ($q\overline{q}$) and baryons (qqq), and are mediated by the gluon gauge boson.

Gluons couple to the 'colour' charge carried by quarks and gluons. Colour charge differs from the analogous electric charge in QED in that three types of colour charge are postulated: red, green and blue (with the corresponding anticolours $\overline{\text{red}}$, $\overline{\text{green}}$ and $\overline{\text{blue}}$). Eight physical gluons are needed to maintain local gauge invariance under the $SU(3)_c$ transformation, each of which carries a colour–anticolour combination. Quarks carry a single colour charge. Similarly, the antiquarks carry a single anticolour charge.

The strength of the strong force, mediated by the strong coupling constant α_s, increases with increasing separation and decreasing energy scale. This results in the phenomenon known as 'colour confinement' where only colourless particles can be observed since coloured quarks cannot exist alone. Isolated quarks or composite quark states of non–zero colour have as yet not been observed.

Precise predictions can be made in QED using perturbation theory since the electromagnetic coupling constant is relatively small. For a given process the coupling constant enters into probability amplitude calculations to the power of the number of boson–

fermion interaction vertices. Higher order diagrams therefore involve higher powers of the coupling constant. In QCD however, the strong coupling constant is relatively large; for example at the energy scale of the Z^0 resonance, $\alpha_s(90\,\mathrm{GeV}) \sim 0.12$ compared to the electromagnetic coupling constant, $\alpha_{em}(90\,\mathrm{GeV}) \sim 0.008$. Perturbative calculations in QCD are therefore only viable for applications involving small distances or large energy scales, greater than $\mathcal{O}(\text{a few GeV})$, where α_s is small and the quarks can be considered essentially as free particles.

2.4 Electroweak Theory

Electroweak theory describes the unified electromagnetic and weak forces. The electromagnetic and weak interactions were first unified in 1961 by Glashow [5] and later reformulated in terms of a renormalisable gauge theory by Weinberg [6] and Salam [7].

The weak interaction is parity violating so the left and right handed[d] fermions have to be treated differently. Left handed fermions in each generation are considered as two states of a system with weak isospin $\mathrm{I}_W = \frac{1}{2}$, differing in their third component of the isospin, $\mathrm{I}_W^{(3)}$, which is $\pm\frac{1}{2}$. The right handed fermions enter the theory as singlet states with $\mathrm{I}_W = 0$. Local gauge invariance is demanded under rotation in weak isospin space, which transforms a particle into its doublet partner. These transformations belong to the $\mathrm{SU(2)_L}$ rotation group, the L subscript denoting that only left handed particles are involved. In order to keep the weak Lagrangian gauge invariant under this transformation three additional gauge fields are introduced ($\mathrm{W}_i;\ i = 1, 2, 3$). The physical fields associated with the charged current interactions are then linear combinations of the W_1 and W_2 fields,

$$\mathrm{W}^{\pm} = \mathrm{W}_1 \pm i\mathrm{W}_2. \tag{2.2}$$

Neutral current interactions cannot be fully described by the $\mathrm{SU(2)_L}$ transformation

[d] Right handed states have their spin aligned parallel to their direction of motion, left handed states aligned anti–parallel.

alone. In order to explain the weak neutral current interaction an additional $\mathrm{U}(1)_{\mathrm{Y}}$ gauge transformation is introduced and invariance under the combined transformation $\mathrm{SU}(2)_{\mathrm{L}} \times \mathrm{U}(1)_{\mathrm{Y}}$ is required. The $\mathrm{U}(1)_{\mathrm{Y}}$ transformation gives rise to the neutral field B, that couples to weak hypercharge Y, defined as $\mathrm{Y} = 2(Q - \mathrm{I}_W^{(3)})$ where Q is the electromagnetic charge.

The physical fields, corresponding to the Z^0 and A (photon) bosons are given by linear combinations of the neutral weak isospin field W_3 and the weak hypercharge field B,

$$\mathrm{Z}^0 = \mathrm{W}_3 \cos\theta_W - \mathrm{B} \sin\theta_W \tag{2.3}$$

$$\mathrm{A} = \mathrm{W}_3 \sin\theta_W + \mathrm{B} \cos\theta_W \tag{2.4}$$

where the weak mixing angle (θ_W) defines the relative strengths of the weak and electromagnetic interactions. The weak mixing angle is not predicted by the Standard Model and must therefore be determined experimentally.

Examples of electroweak interaction vertices are shown in Figure 2.2. The photon and Z^0 boson carry the neutral current and couple to fermion pairs. The $\mathrm{W}^{\pm}$ bosons carry the charged current which results in the change of quark flavours, or the interchange of a charged lepton with its associated neutrino.

The charged current for leptons can be expressed as

$$J_\mu^{(\mathrm{lept})} = \begin{pmatrix} \overline{\nu}_{\mathrm{e}} & \overline{\nu}_\mu & \overline{\nu}_\tau \end{pmatrix} \gamma_\mu \, (1 - \gamma_5) \begin{pmatrix} e \\ \mu \\ \tau \end{pmatrix} \tag{2.5}$$

where the $\{\gamma_\mu;\ \mu = 0, 1, 2, 3\}$ represent the Dirac spin matrices and $\gamma_5 = i\gamma_0\gamma_1\gamma_2\gamma_3$.

The charged current couples leptons together within the same generation only. Quarks however, can couple to quarks from other generations. The charged current for quarks

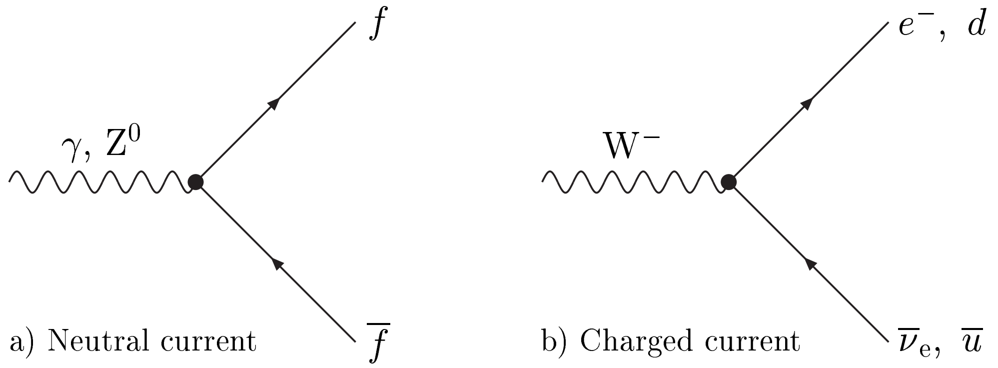

Figure 2.2: *The Feynman diagrams for the neutral and charged current electroweak interaction vertices. a) The neutral current decay of the Z^0 or photon to a fermion–antifermion pair. b) Examples of the charged current interactions of the W^- boson decay.*

is similar to Equation 2.5 except for an additional V_{CKM} factor,

$$J_\mu^{(\mathrm{quark})} = \begin{pmatrix} \overline{\mathrm{u}} & \overline{\mathrm{c}} & \overline{\mathrm{t}} \end{pmatrix} \gamma_\mu \, (1-\gamma_5) \, V_{\mathrm{CKM}} \begin{pmatrix} \mathrm{d} \\ \mathrm{s} \\ \mathrm{b} \end{pmatrix} \tag{2.6}$$

where V_{CKM} is the Cabibbo–Kobayashi–Maskawa (CKM) matrix [8, 9]. This unitary matrix describes quark mixing and can be approximately represented by the commonly used parameterisation suggested by Wolfenstein [10]

$$\begin{pmatrix} V_{ud} & V_{us} & V_{ub} \\ V_{cd} & V_{cs} & V_{cb} \\ V_{td} & V_{ts} & V_{tb} \end{pmatrix} = \begin{pmatrix} 1-\lambda^2/2 & \lambda & A\lambda^3(\rho - i\eta) \\ \lambda & 1-\lambda^2/2 & A\lambda^2 \\ A\lambda^3(1-\rho-i\eta) & -A\lambda^2 & 1 \end{pmatrix} + \mathcal{O}(\lambda^4) \tag{2.7}$$

where $\lambda = \sin(\theta_{\mathrm{Cabibbo}})$, the sine of the Cabibbo mixing angle and A, ρ and η are real parameters.

The elements of the CKM matrix are not predicted by the Standard Model but can be determined experimentally from weak decays or deep inelastic neutrino scattering experiments. The current experimental situation gives;

$$\begin{pmatrix} V_{ud} & V_{us} & V_{ub} \\ V_{cd} & V_{cs} & V_{cb} \\ V_{td} & V_{ts} & V_{tb} \end{pmatrix} = \begin{pmatrix} 0.9745-0.9760 & 0.217-0.224 & 0.0018-0.0045 \\ 0.217-0.224 & 0.9737-0.9753 & 0.036-0.042 \\ 0.004-0.013 & 0.035-0.042 & 0.9991-0.9994 \end{pmatrix}$$

where the quoted ranges correspond to the 90 % confidence levels [3].

The existence of the CKM matrix is a direct consequence of the fact that the weak interaction eigenstates differ from the mass eigenstates. Mixing of the quarks occurs via these inter–generation couplings. The CKM matrix is essential for electroweak theory since it allows CP violation, i.e. the violation of the invariance under the combined charge and parity transformation, through non–zero complex phases in the CKM matrix [11,12].

2.5 Higgs Mechanism

Electroweak theory described thus far is inconsistent with nature in that it can only describe the weak gauge bosons as massless particles, whereas in fact they are massive. Including explicit mass terms in the electroweak Lagrangian destroys its gauge invariance and the predictive power of the theory is lost. This situation is resolved by introducing an additional complex scalar Higgs field into the theory with a non–zero vacuum expectation value [13]. This field destroys the symmetry of the gauge theory when the vacuum chooses one of the infinite number of expectation values for the vacuum state, but preserves the underlying symmetry of the Lagrangian allowing the theory to be renormalised.

In the Standard Model, four real Higgs fields are introduced in the form of a weak isospin doublet of complex scalar fields with couplings such that the vacuum has weak isospin and hypercharge to which the particles can couple, generating mass terms. Three of the Higgs fields combine with the weak gauge boson fields giving mass to the Z^0 and $W^{\pm}$ bosons. The remaining field manifests itself as the neutral Higgs boson. The theory does not predict the masses of the Z^0 or $W^{\pm}$ bosons but allows these masses to be calculated from the measured electromagnetic and weak coupling constants. The Higgs mechanism also gives mass to fermions, the values of which have to be measured experimentally.

As yet the Higgs boson has not been observed. Searches by the LEP experiments however give the lower limit on the Higgs boson mass, $m_H > 77.5\,\mathrm{GeV/c^2}$ at the 95 % confidence level [3] whilst global fits to measured Standard Model parameters yield the upper limit $m_H \lesssim 1\,\mathrm{TeV/c^2}$.

2.6 b Physics

In e^+e^- collisions at the Z^0 resonance, $q\overline{q}$ pair production occurs dominantly through the process $e^+e^- \rightarrow Z^0 \rightarrow q\overline{q}$. QCD confinement ensures that the primary quark and antiquark are not observed as isolated particles. Additional quarks and antiquarks are produced from the vacuum in order to form colourless hadrons in a process called *fragmentation*. Such events produce a large number of final state hadrons and are termed 'multi–hadronic' events. Around 21 % [14] of multi–hadronic decays contain a primary $b\overline{b}$ pair, the heaviest quark–antiquark pairs that can be produced from the decay of the Z^0 resonance. Due to their high mass, the resulting b hadrons are unstable and decay to lower mass hadrons.

The decays of b hadrons are experimentally very distinctive; the high mass of b hadrons means that the decay products, for example leptons from semileptonic decays $b \rightarrow c\ell^-\overline{\nu}_\ell$, have high momenta and are therefore relatively easy to identify amongst the other particles in the event. Another feature of b hadrons is their relatively long lifetimes ($\sim 1.5\,\mathrm{ps}$) compared to lighter hadrons, allowing them to be tagged via the reconstruction of secondary decay vertices displaced from the primary interaction point.

The study of b physics is theoretically interesting since the high b quark mass means that reliable calculations can be carried out using Heavy Quark Effective Theory (HQET). Using HQET, the theoretical uncertainties are significantly reduced by exploiting the symmetries of the heavy–light quark system in heavy hadrons. The following sections give a brief discussion of the areas of b physics relevant to the analysis presented in this thesis.

2.6.1 b Hadron Production

Figure 2.3 shows the annihilation of an e^+e^- pair into a Z^0 or excited photon which subsequently decays into a primary $q\overline{q}$ pair. This process can be modelled to a high degree of accuracy using perturbative electroweak calculations. The primary quark and antiquark subsequently separate from the primary interaction point producing more partons[e] during the fragmentation process. The strong force potential between the quark and antiquark increases with increasing separation to the point where it is energetically more favourable to produce a light quark–antiquark pair from the vacuum than it is for the primary $q\overline{q}$ pair to separate further. In addition, the quarks can radiate gluons which in turn form quark–antiquark pairs.

This process can be effectively modelled using perturbative QCD until the average parton energy is too low to allow reliable perturbative calculations due to the increasing strength of the strong coupling constant. At this point empirical hadronisation models are used to produce the final colourless hadronic particle states from the parton shower, during a process know as *hadronisation*.

The distribution of the variable z, defined as the ratio of the b hadron energy (or momentum) to that of the primary quark, is known as the *fragmentation function*. Due to the high mass of a primary b quark, it is not significantly decelerated when combined

[e] Generic name for a quark, antiquark or gluon.

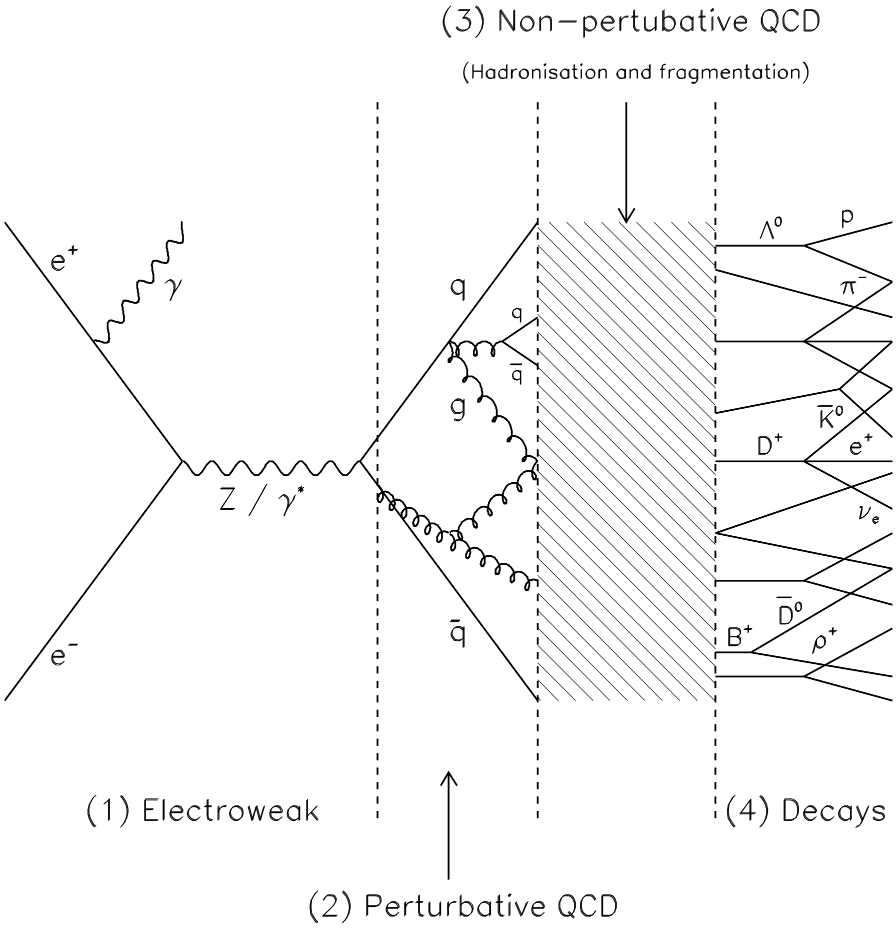

Figure 2.3: *A schematic representation of the production and hadronic decay of a Z^0 or excited photon in e^+e^- collisions.*

with a light quark or quarks to form a b hadron. The fragmentation function for heavy quarks is therefore peaked towards $z = 1$.

In the absence of reliable QCD calculations various empirical fragmentation models have been proposed to describe the z distribution;

- The model of Peterson *et al.* [15] is the most popular and widely used for heavy quark fragmentation. In non–relativistic quantum mechanics, first order perturbation theory predicts that the amplitude for the transition from a heavy quark state Q with momentum p, to a system containing a heavy hadron state H with momentum zp and a light quark q with momentum $(1-z)p$, via the perturbing Hamiltonian H' is given by $\langle \mathrm{H}_q|H'|Q\rangle/\Delta E$, where[f] $\Delta E = E_Q - E_H - E_q$. The fragmentation function is then proportional to the square of this amplitude, giving

$$f(z) \propto \frac{1}{z(\Delta E)^2} \tag{2.8}$$

where the $1/z$ factor arises from longitudinal phase space. If the masses are assumed small compared to p and $m_H \simeq m_Q$ then

$$\begin{aligned} E_Q &= \sqrt{p^2+m_Q^2} &&\simeq p + \frac{m_Q^2}{2p} && (2.9)\\ E_H &= \sqrt{z^2p^2+m_H^2} &&\simeq zp + \frac{m_Q^2}{2zp} && (2.10)\\ E_q &= \sqrt{(1-z)^2p^2+m_q^2} &&\simeq (1-z)p + \frac{m_q^2}{2(1-z)p} && (2.11)\end{aligned}$$

giving the fragmentation function

$$f(z) \propto \frac{1}{z\left(1-\frac{1}{z}-\frac{\epsilon_Q}{1-z}\right)^2} \tag{2.12}$$

where $\epsilon_Q = m_q^2/m_Q^2$.

Although the Peterson function is widely used, several alternatives have also been proposed;

- The model of Collins and Spiller [16] gives

$$f(z) \propto \left(\frac{(1-z)}{z}+\frac{(2-z)\tilde{\epsilon}}{(1-z)}\right)\left(1+z^2\right)\left(1-\frac{1}{z}-\frac{\tilde{\epsilon}}{(1-z)}\right)^{-2} \tag{2.13}$$

with $\tilde{\epsilon}$ as an adjustable model parameter.

[f] The heavy quark Q, heavy hadron H and light quark q have energies E_Q, E_H and E_q, and masses m_Q, m_H amd m_q respectively.

- Kartvelishvili *et al.* [17] give the functional form

$$f(z) \propto z^{\alpha}(1-z) \tag{2.14}$$

with α as a free model parameter.

- The Lund symmetric model [18] gives

$$f(z) \propto \frac{1}{z}(1-z)^{a} \exp\left(-\frac{bM_T^2}{z}\right). \tag{2.15}$$

This is mainly used for light flavour fragmentation, with a and b as free parameters and M_T^2 the square of the transverse mass of the heavy–light quark system[g].

Experimentally, the z parameter is not directly accessible since initial–state photon and gluon radiation means that the energy of the primary quark, E_{quark}, is not necessarily the same as the beam energy, $E_{cm}/2$, where E_{cm} is the centre of mass energy. The accessible variable is then the scaled energy of the hadron, $x_E = 2E_{hadron}/E_{cm}$.

Figure 2.4a shows the four different fragmentation functions with their model parameters as determined from OPAL data [19]. The analysis uses the full reconstruction of the charm meson in $\overline{\mathrm{B}} \to \mathrm{D}\ell\mathrm{X}$ and $\overline{\mathrm{B}} \to \mathrm{D}^*\ell\mathrm{X}$ decays to determine the $\overline{\mathrm{B}}$ energy from the kinematics of the $\mathrm{D}^{(*)}\ell$ combination. The various models are then fitted to the data to extract the model parameters. Since most b quarks result directly from the Z^0 decay and not the subsequent hadronisation process, almost all b hadrons contain a primary b quark and therefore the z and x_E distributions show similar characteristics peaking towards one, as can be seen in Figure 2.4b. The statistical precision of the data is currently unable to distinguish between the various models.

[g] Experimentally, the product bM_T^2 is taken as a free parameter.

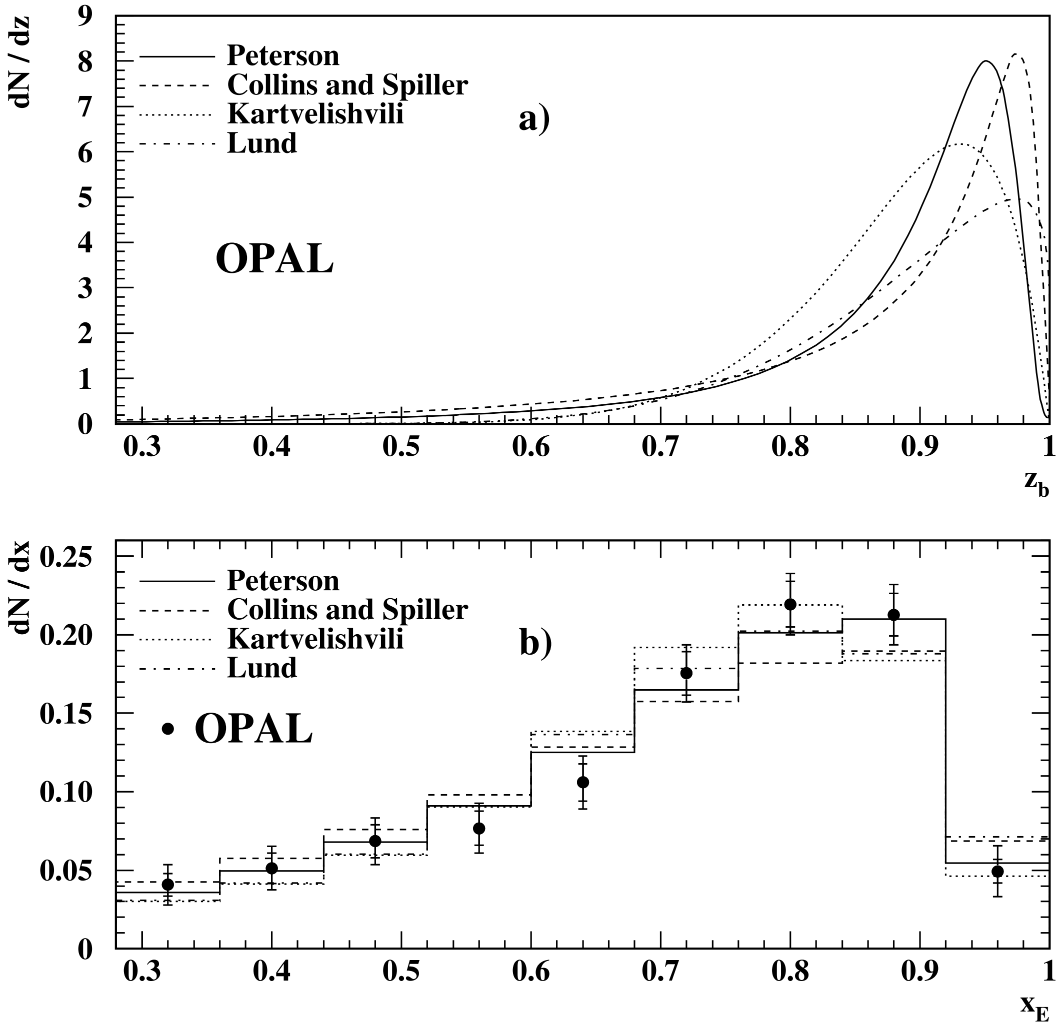

Figure 2.4: *OPAL data [19] for a) normalised b fragmentation functions with their respective model parameters as determined from fits to the data, and b) the corresponding distributions for x_E obtained using the different fragmentation models, fitted to the OPAL data.*

2.6.2 b Hadron Decays

At the energies available at the Z^0 resonance, the full range of weakly decaying ground state b hadrons are kinematically accessible, with the relative production fractions as shown in Table 2.3.

b hadron	Quark Composition	Production Fraction / %
B^+	$\overline{b}u$	$39.7\,^{+1.8}_{-2.2}$
B^0	$\overline{b}d$	$39.7\,^{+1.8}_{-2.2}$
B^0_s	$\overline{b}s$	$10.5\,^{+1.8}_{-1.7}$
Λ_b	$\overline{b}\overline{q}\overline{q'}$	$10.1\,^{+3.9}_{-3.1}$
B^+_c	$\overline{b}c$	negligible

Table 2.3: *Summary of the b hadrons produced at LEP (charge conjugates assumed) [3]. Λ_b represents a generic b baryon.*

B mesons dominate b hadron production at LEP, where the b or $\overline{b}$ quark combines with a single quark from the vacuum about 90 % of the time. b baryon (generically referred to as Λ_b) production is suppressed since it requires the b quark to combine with a pair of quarks during hadronisation. The formation of s and c quarks during fragmentation is suppressed relative to lighter quarks due to their high masses and accordingly, B^0_s mesons only account for approximately 10 % of the b sample, with negligible B^+_c production.

Approximately 30 % of all B mesons are produced in an orbitally excited (L=1) state, denoted B^{**}, and decay via the strong interaction to ground state B mesons. The ground state B mesons are the pseudoscalar and vector mesons denoted B (25 %) and B^* (75 %) respectively. The B^* mesons can only decay electromagnetically to the B meson with the emission of a photon, since the $B^* - B$ mass difference is only $\sim 46\,\mathrm{MeV}/c^2$ [3]. Λ_b baryons are either produced as, or expected to decay strongly to, the weakly decaying ground state Λ^0_b, Ξ_b, Σ_b and Ω_b baryons.

The ground state b hadrons can only decay to lighter hadrons through the charged

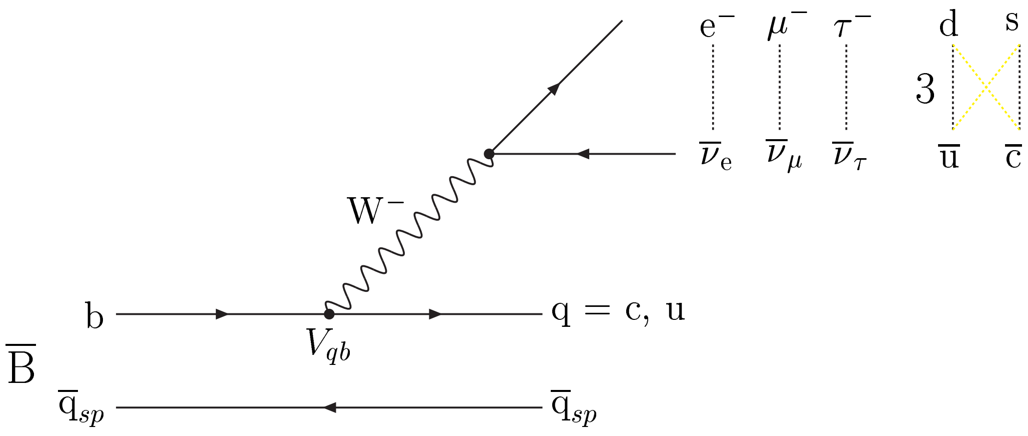

Figure 2.5: *Feynman diagram for spectator decays of B mesons.*

current weak decays. Figure 2.5 shows the tree level spectator quark diagram for B meson decay. The factor of three in the hadronic decays of the W accounts for colour charge. As the name suggests, the light quark in the b hadron plays no part in the tree level decay diagram and acts merely as a spectator. Higher order diagrams give corrections to this simple picture. Decays that do not occur through the weak b $\rightarrow$ c decay are commonly known as rare b decays. The simplest rare decay is obtained by replacing the b $\rightarrow$ c transition with the Cabibbo suppressed decay b $\rightarrow$ u. Other rare decays are those dominated by higher order diagrams, such as the one loop 'penguin' diagrams.

2.6.3 The Semileptonic Branching Fraction of b Hadrons

The semileptonic branching fraction of b hadrons is defined as

$$\mathcal{B}_{SL} = \mathcal{B}(\mathrm{b} \rightarrow \mathrm{X}\ell\overline{\nu_\ell}) = \frac{\Gamma(\mathrm{b} \rightarrow \mathrm{X}\ell\overline{\nu_\ell})}{\sum_{\ell'=\mathrm{e},\mu,\tau} \Gamma(\mathrm{b} \rightarrow \mathrm{X}\ell'\overline{\nu_{\ell'}}) + \Gamma_{had} + \Gamma_{rare}} \tag{2.16}$$

where Γ_{had} and Γ_{rare} are the inclusive rates for hadronic and rare hadronic b decays respectively and ℓ represents either an electron or muon.

In the following sections the status of the experimental measurements and theoretical calculations of the inclusive semileptonic branching fraction of b hadrons is discussed.

2.6.3.1 Experimental Measurements

Measurements of $\mathcal{B}_{SL}$ have been made by various experimental groups and fall into two categories; low energy measurements performed at the $\Upsilon(4S)$ resonance ($\sim 10\,\mathrm{GeV}$) and higher energy measurements at the Z^0 resonance ($\sim 91\,\mathrm{GeV}$). A summary of recent preliminary and published results is given in Table 2.4.

Energy regime	Experiment	Channel[g]	$\mathcal{B}_{SL}$ / %
Z^0	ALEPH [20] †	$\mathcal{B}(b \to X\ell\nu_\ell)$	11.01 ± 0.10 (stat.) ± 0.29 (syst.)
	DELPHI [21] †	$\mathcal{B}(b \to X\ell\nu_\ell)$	10.65 ± 0.11 (stat.) ± 0.43 (syst.)
	L3 [22]	$\mathcal{B}(b \to X\ell\nu_\ell)$	10.68 ± 0.11 (stat.) ± 0.44 (syst.)
	OPAL [23] †	$\mathcal{B}(b \to X\mu\nu_\mu)$	10.86 ± 0.08 (stat.) ± 0.43 (syst.)
	Combined [24] †	$\mathcal{B}(b \to X\ell\nu_\ell)$	10.87 ± 0.24
$\Upsilon(4S)$	ARGUS [25]	$\mathcal{B}(B \to Xe\nu_e)$	9.7 ± 0.5 (stat.) ± 0.4 (syst.)
	CLEO [26]	$\mathcal{B}(B \to Xe\nu_e)$	10.49 ± 0.17 (stat.) ± 0.43 (syst.)
	Combined [3]	$\mathcal{B}(B \to X\ell\nu_\ell)$	10.45 ± 0.21

Table 2.4: *Experimental results for the semileptonic branching fractions of b hadrons. Results that are preliminary only are indicated by a †.*

Almost 100 % of $\Upsilon(4S)$ decays are to either a $B^0_d\overline{B^0_d}$ or B^+B^- pair. The higher mass B^0_s, Λ_b and B_c hadrons are kinematically inaccessible. The most recent measurements of $\mathcal{B}(B \to X\ell\nu_\ell)$[h] use a *tagged lepton technique.* B mesons are tagged using a high momentum lepton and the remaining electrons in the event are then classified using charge and angular correlations with the tag lepton [25, 26]. Previous measurements fit the shape of the lepton momentum spectra to determine the fraction of semileptonic

[h] $\mathcal{B}(B \to X\ell\nu_\ell)$ refers to the semileptonic branching fraction of the inclusive sample of $B^\pm/B^0$ mesons at the $\Upsilon(4S)$, whereas $\mathcal{B}(b \to X\ell\nu_\ell)$ is used for the full b hadron sample produced at LEP.

decays [27, 28]. Theoretical uncertainties in the predictions for these spectra result in sizable modelling dependencies and these dependencies are reduced with these new tagged lepton measurements.

The most recent and precise measurements of $\mathcal{B}(\mathrm{b} \to \mathrm{X}\ell\nu_\ell)$ at the Z^0 resonance employ hemisphere b tagging techniques to select high purity samples of b hadron decays. The opposite hemisphere is then searched for high momentum lepton candidates and the fraction of these samples which result from semileptonic b decays are determined using a variety of techniques. The precision of these measurements is again limited by the modelling uncertainties in the semileptonic decay lepton momentum spectra.

The world average for results at the $\Upsilon(4\mathrm{S})$ is $\mathcal{B}^{\mathrm{B}}_{SL} = (10.45 \pm 0.21)\,\%$ [3] whereas a combination of LEP results obtained at the Z^0 resonance gives $\mathcal{B}^{\mathrm{b}}_{SL} = (10.87 \pm 0.24)\,\%$ [24], where the B and b superscripts denote the differing b hadron sample compositions. Different inclusive semileptonic branching fractions are anticipated at the two energies due to the differing b hadron compositions, in particular, the presence of Λ_b baryons at LEP. The Λ_b baryon has been measured to have a significantly lower lifetime ($\sim 1.2\,\mathrm{ps}$) than B mesons ($\sim 1.6\,\mathrm{ps}$) [3]. Therefore, if the semileptonic widths for Λ_b baryons and B mesons are assumed to be the same, and given that the semileptonic branching fraction is related to the lifetimes, τ, by $\mathcal{B}_{SL} = \Gamma_{\mathrm{sl}}/\Gamma_{\mathrm{total}} = \tau\Gamma_{\mathrm{sl}}$, the semileptonic branching fraction of Λ_b baryons would be

$$\begin{aligned} \mathcal{B}(\Lambda_\mathrm{b} \to \mathrm{X}\ell\nu_\ell) &\simeq \frac{\tau_{\Lambda_\mathrm{b}}}{\tau_\mathrm{B}} \cdot \mathcal{B}(\mathrm{B} \to \mathrm{X}\ell\nu_\ell) \\ &\sim 8\,\%. \end{aligned} \tag{2.17}$$

Various experimental estimates of the Λ_b baryon semileptonic branching fraction have been made which agree with this expectation, giving $\mathcal{B}(\Lambda_\mathrm{b} \to \mathrm{X}\ell\overline{\nu_\ell}) \simeq (7.4 \pm 1.1)\,\%$ [29, 30]. Although the uncertainties are large, this indicates that non–spectator effects responsible for the lifetime difference influence the total decay widths and not the semi–leptonic widths and supports the assumption that the semileptonic widths of b mesons and baryons are the same.

The lower semileptonic decay rate for Λ_{b} baryons means that the average semileptonic branching fraction of b hadrons at LEP is expected to be lower than that obtained at the $\Upsilon(4S)$. This is in disagreement with the experimental results, as shown in Table 2.4, although the errors are too large to make any firm conclusions. Understanding the origin of this potential discrepancy, whether it be theoretical or experimental, has motivated precise measurements at both energies and the analysis presented in this thesis provides an updated measurement using OPAL data.

2.6.3.2 Theoretical Calculations

The width for the parton level process $\mathrm{b} \to \mathrm{c}\ell^-\overline{\nu_\ell}$ can be calculated from electroweak theory, discussed in Section 2.4. Calculation of the width for the decay $\overline{\mathrm{B}} \to \mathrm{D}\ell^-\overline{\nu_\ell}$ is complicated by the non–perturbative QCD effects that bind the b and light quarks in the b hadron and which introduce large theoretical uncertainties.

Heavy Quark Effective Theory (HQET) was developed [31–34] to reduce these uncertainties by exploiting the properties of the heavy–light quark system. Consider a hadron composed of a heavy quark Q and 'light degrees of freedom' consisting of light quarks, light antiquarks and gluons. The Compton wavelength of the heavy quark scales as the inverse of the heavy quark mass, $\lambda_Q \sim 1/m_Q$. The light degrees of freedom, on the other hand, are characterised by momenta of the order of Λ_{QCD}, the typical energy scale of the non–perturbative QCD interactions which bind the hadron, corresponding to wavelengths $\lambda_l \sim 1/\Lambda_{QCD}$. Since $\lambda_l \gg \lambda_Q$ the light degrees of freedom cannot resolve features of the heavy quark system other than its conserved gauge quantum numbers. In particular, they cannot probe the actual value of λ_Q, or equivalently the mass of the heavy quark.

The timescale for the heavy quark weak decay τ_Q, is very short compared to the timescale on which the QCD interactions occur, ie. $\tau_Q \sim 1/m_{\mathrm{W}} \ll 1/\Lambda_{QCD}$ where m_{W} is the W boson mass. In the limit where $m_Q \to \infty$, the weak decay of the heavy quark is therefore decoupled from the QCD interactions that occur in the remaining hadronic system. In reality, finite heavy quark masses introduce correction factors of the order of $(\Lambda_{QCD}/m_Q)^2$. The b hadron weak decay width can therefore be written as;

$$\Gamma(\text{b hadron} \to \mathrm{X}\ell\overline{\nu_\ell}) = \Gamma(\mathrm{b} \to \mathrm{c}\ell\overline{\nu_\ell}) + \mathcal{O}(1/m_b^2) \tag{2.18}$$

with m_b in $\mathrm{GeV/c^2}$. For a more comprehensive introduction to HQET refer to [35].

Another important input to the understanding of the semileptonic branching fraction is the charm multiplicity, n_c, the average number of charm or anticharm quarks in the final state of a b hadron weak decay. This can be expressed as

$$n_c = 1 + \mathcal{B}(\mathrm{b} \to \mathrm{X}_{c\overline{c}}) - \mathcal{B}(\mathrm{b} \to \mathrm{X}_{\text{charmless}}) \tag{2.19}$$

where $\mathrm{X}_{c\overline{c}}$ represents any final state containing both a charm and an anticharm quark. These states result from the weak decay of the b quark to a c quark, where the W boson also decays to a $\overline{\mathrm{c}}\mathrm{s}$ pair. $\mathrm{X}_{\text{charmless}}$ represents final states containing no charm hadrons, such as those resulting from semileptonic $\mathrm{b} \to \mathrm{u}\ell\nu_\ell$ decays. Both n_c and $\mathcal{B}_{SL}$ depend on the same hadronic partial widths (Equation 2.16) and therefore share the same sources of theoretical uncertainty.

In the naïve parton model the spectator effects are neglected, giving $\mathcal{B}_{SL} \simeq 13\,\%$ [36], significantly larger than the experimental results, as shown in Table 2.4. The non–perturbative corrections to Equation 2.18 calculated within the $1/m_Q$ HQET expansion prove to be too small to significantly improve the predictions [37]. The dominant theoretical uncertainty in calculating the semileptonic branching fraction in fact results from the calculation of the hadronic decay rate, Γ_{had}, in Equation 2.16. The exact $\mathcal{O}(\alpha_s)$ corrections to the non–leptonic width have been computed and an analysis of the renormalisation scale and scheme dependence has been performed by both Bagan *et al.* [38] and Neubert *et al.* [39]. The results of these calculations are summarised in Figure 2.6 where the theoretical predictions for n_c and $\mathcal{B}_{SL}$ are compared to the experimental results.

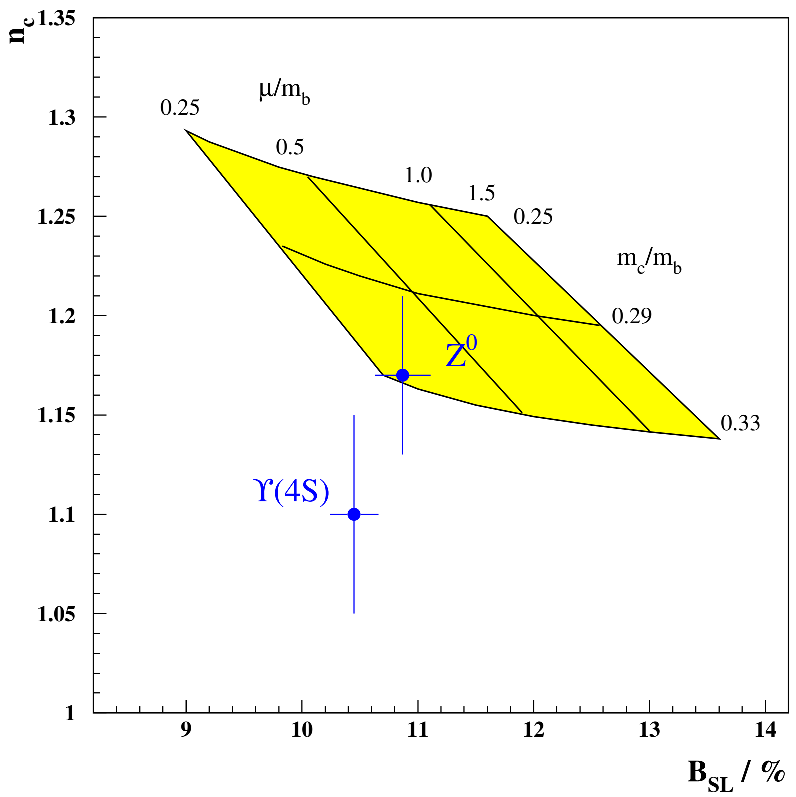

Figure 2.6: *The shaded region shows the theoretical prediction for $\mathcal{B}_{SL}$ and n_c, which are compared to the experimental measurements.*

The QCD corrections increase the partial width $\Gamma(\mathrm{b} \to \mathrm{X}_{c\bar{c}})$ substantially. This has the dual effect of lowering the prediction for $\mathcal{B}_{SL}$ whilst raising n_c. In addition, these corrections introduce substantial theoretical uncertainties. These uncertainties depend on two parameters: the ratio of the charm quark mass to the b quark mass, m_c/m_b, and the QCD renormalisation scale, μ. The dependence on μ reflects the uncertainties due to higher–order QCD corrections to the decay rates.

In summary, given the current level of experimental and theoretical uncertainty, the measurements and predictions for $\mathcal{B}_{SL}$ and n_c are in agreement. Whilst the measurements at the Υ(4S) show a potential discrepancy with theory and Z^0 results, more work is needed to reduce the uncertainties before it could be claimed to present a genuine problem.

2.6.4 Phenomenological Models for Weak b Decays

The momenta of leptons from the decay of heavy hadrons tend to be higher than that from light hadron decays and therefore the lepton momentum distribution provides one of the most efficient methods of identifying leptons from weak b hadron decays.

Unfortunately, accurate predictions of the lepton momentum spectra from weak heavy decays are not possible directly from QCD, and no reliable calculations using HQET have yet been published. Phenomenological models must therefore be employed, and the two main models in current use, the ACCMM [40] model and the ISGW [41] model, are described in the following sections.

2.6.4.1 ACCMM Model

The simplest model for semileptonic B decays is the spectator model in which the decaying b quark is considered as a free particle within the B meson (Figure 2.5). The model of Altarelli *et al.* [40] (ACCMM) considers two important corrections to the spectator model. Firstly, the spectator quark in the B meson is considered as a quasi–free particle with the momentum distribution,

$$f(p) = \frac{4p^2}{\sqrt{\pi p_F^3}} \exp\left(-\frac{p^2}{p_F^2}\right) \tag{2.20}$$

where p_F is the Fermi momentum, a free parameter of the model.

First order perturbative QCD corrections are also included to account for gluon radiation from the quarks. Figure 2.7 shows two such corrections; the left–hand diagram shows real gluon radiation whilst the right–hand diagram represents virtual gluon exchange.

The decay width for the process $\mathrm{B} \to \mathrm{X}_q \ell \nu_\ell$ is given by ;

$$\Gamma(\mathrm{B} \to \mathrm{X}_q \ell \nu_\ell) \simeq \Gamma(\mathrm{b} \to \mathrm{q} \ell \nu_\ell) = |V_{bq}|^2 \left(\frac{G_F^2 m_b^5}{192\pi^3}\right) \eta_{QCD}\ r \tag{2.21}$$

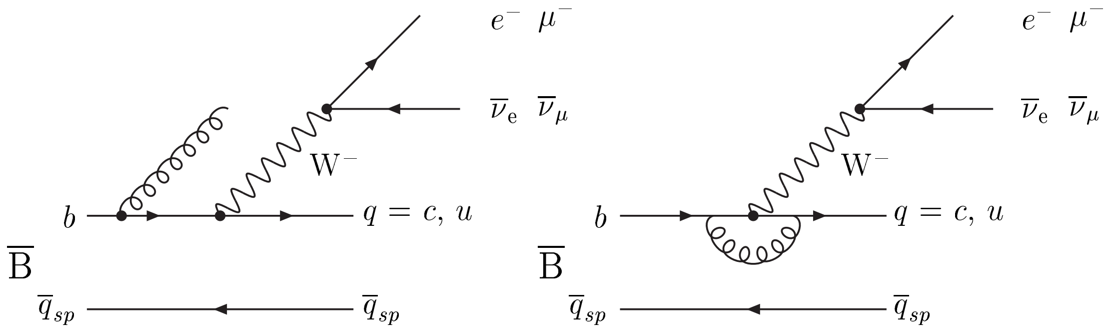

Figure 2.7: *QCD radiative corrections to the spectator level diagram for semileptonic decays.*

where G_F is the Fermi constant, m_b the b quark mass, η_{QCD} a QCD correction factor and r represents the phase space factor for the decay kinematics. In order to satisfy energy–momentum conservation in the B decay, the b quark mass is allowed to vary according to

$$m_b^2 = m_B^2 + m_{sp}^2 - 2m_B\sqrt{p^2 + m_{sp}^2} \tag{2.22}$$

where m_B is the known B meson mass and m_{sp} is the spectator quark mass. The lepton energy spectrum is then given by

$$\frac{\mathrm{d}\Gamma_B}{\mathrm{d}E_\ell}(p_F, m_{sp}, m_q, m_B) = \int_0^{p_{max}} p^2\,\mathrm{d}p\; f(p)\frac{\mathrm{d}\Gamma}{\mathrm{d}E_\ell}(m_b) \tag{2.23}$$

where E_ℓ is the lepton energy, p_{max} is the maximum kinematically allowed value of p and m_q is the mass of the final state quark from the weak decay of the b quark.

The ACCMM model therefore introduces a new parameter, p_F, for the momentum distribution of the spectator quark inside the B meson. In addition, the mass of the spectator, m_{sp}, and the mass of the final quark state, m_q, are also free model parameters. In this way the ACCMM model incorporates bound state effects and reduces the strong dependence on the b quark mass in the decay width of the spectator quark model, Equation 2.21. The values of the model parameters are determined from the data.

The CLEO collaboration have fitted the ACCMM model to their data to determine the model parameters [42]. From these fits the parameters have been measured to be,

$$
\begin{aligned}
p_F &= 298 \pm 59\ (\mathrm{stat.}) \pm 27\ (\mathrm{syst.})\ \mathrm{MeV/c}, \\
m_c &= 1673 \pm 58\ (\mathrm{stat.}) \pm 24\ (\mathrm{syst.})\ \mathrm{MeV/c^2}
\end{aligned}
$$

where the spectator quark mass, m_{sp}, is kept fixed at 150 MeV/c.

The ACCMM model can also be used in a similar manner to model semileptonic D decays. Measurements from DELCO [43] and MARK II [44] for semileptonic D^0 and $D^\pm$ decays have been combined and parameterised using the ACCMM model as a convenient functional form. Taking into account the D boost and experimental resolution, the $c \to \ell$ spectra can be modelled using the parameters $p_F = 467\,\mathrm{MeV/c}$ and $m_s = 1\,\mathrm{MeV/c^2}$, with the $+1$ and -1 sigma variations given by the values $p_F = 353\,\mathrm{MeV/c}$ and $m_s = 1\,\mathrm{MeV/c^2}$, and $p_F = 467\,\mathrm{MeV/c}$ and $m_s = 153\,\mathrm{MeV/c^2}$ respectively.

2.6.4.2 ISGW Model

The model proposed by Isgur *et al.* [41] (ISGW) is an exclusive model which assumes that the semileptonic B decays are saturated by a few final states. After the b quark decays into either a c or u quark, that quark then recombines with the spectator quark to form the final state hadrons. Possible final charm states included are;

- The ground state 1^1S_0, the D meson;
- The first excited state 1^3S_1, the D^* meson;
- The higher states such as 1^3P_2, 1^3P_1, 1^3P_0, 1^1P_1, 2^1S_0 and 2^3S_1. These are collectively referred to as the D^{**} states.

The hadronic current for the exclusive channels is expressed in terms of form factor functions, $F(q^2)$, of the 4–momentum transfer, q^2, between the initial and final state mesons. In semileptonic decays, q^2 is therefore the mass squared of the virtual W boson.

In the ISGW model the authors argue that the heavy mass of the b quark makes it possible to use non–relativistic approximations in modelling the B meson decay. At minimum recoil of the final state meson, corresponding to maximum q^2, the form factors $F(q^2_{max})$ are obtained by solving the Schrödinger Equation with a Coulomb plus linear potential for the ground state B,

$$V(r) = -\frac{4\alpha_s}{3r} + br + c. \tag{2.24}$$

where $\alpha_s = 0.5$, $b = 0.18\,\mathrm{GeV/c^2}$ and $c = -0.84\,\mathrm{GeV}$. The full form factors are then obtained by extrapolating the q^2 dependence using an exponential form,

$$F(q^2) \propto F(q^2_{max}) \exp\left(\frac{q^2 - q^2_{max}}{\kappa q^2_{max}}\right) \tag{2.25}$$

where κ is a parameter introduced to account for relativistic effects. The authors of the ISGW model determined a value $\kappa = 0.7$ from measured pion form factors.

The ISGW model predicts the relative fractions of the three B semileptonic decay channels to be 27 %, 62 % and 11 % for D, $\mathrm{D^*}$ and $\mathrm{D^{**}}$ final states respectively, with the corresponding lepton momentum spectra as shown in Figure 2.8.

Various experimental measurements have been made of the sum of the exclusive D and $\mathrm{D^*}$ fractions of the total semileptonic B decay width. CLEO found $(65 \pm 12)\,\%$ [27] whilst ARGUS measured $(60 \pm 10)\,\%$ [28], both significantly smaller than the fraction (89 %) predicted by the ISGW model. CLEO therefore introduced a modification to the ISGW model where they allowed the $\mathrm{D^{**}}$ fraction to float in their fit to lepton momentum spectra [42]. The fit increased the $\mathrm{D^{**}}$ rate from 11 % to 32 % and was found to better reproduce their data. The ISGW model with 32 % $\mathrm{D^{**}}$ production is commonly referred to as the ISGW** model.

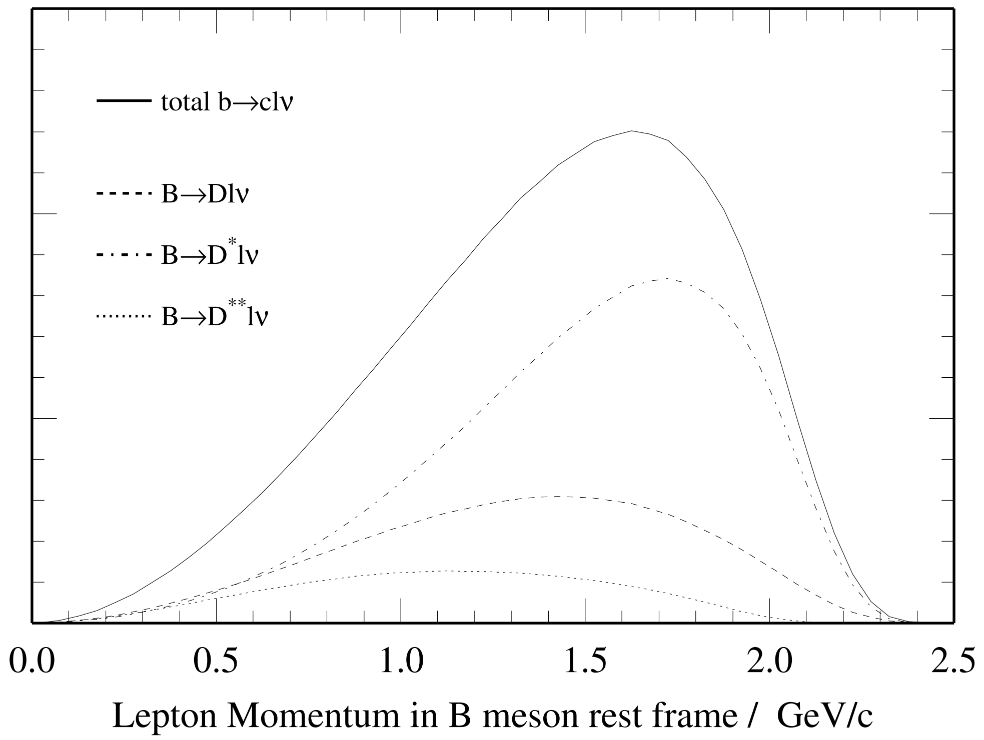

Figure 2.8: *Lepton momentum spectra in the B meson rest frame for $b \to \ell$ decays in the ISGW model, as presented in [45].*

2.6.4.3 Electroweak Radiative Corrections

The effects of electroweak radiative corrections need to be accounted for in the predicted lepton momentum spectra. Whilst these are second order effects, they amount to corrections of the order of 2 to 10 % on the predicted spectra, depending on the lepton energy. In particular, the corrections differ for electrons and muons and therefore must be applied in order to test lepton universality in heavy flavour symmetry.

The effects have been calculated by Atwood and Marciano [46] where three main effects are studied; virtual loops corrections, Coulomb interactions for neutral initial state mesons and low energy bremsstrahlung. Of these effects, only the third was found to alter the shape of the lepton spectra, the other two only change the overall normalisation. The correction to the spectra can be simply expressed as a multiplicative factor C_{ew} given by,

$$C_{ew}(E_\ell) = \left(\frac{E_{max} - E_\ell}{C E_\ell} \right)^r \tag{2.26}$$

where

$$r = \frac{2\alpha}{\pi} \left[\ln \left(\frac{2E_\ell}{m_\ell} \right) - 1 \right] \tag{2.27}$$

and the lepton has mass m_ℓ and energy $E_\ell < E_{max}$.

C is an arbitrary normalisation factor specified in terms of the maximum and average lepton energies,

$$C = \frac{(E_{max} - \overline{E_\ell})}{\overline{E_\ell}}. \tag{2.28}$$

2.6.4.4 Summary of the Model Predictions

Figure 2.9 shows the ACCMM and ISGW model predictions for the semileptonic decays $\mathrm{b} \to \mathrm{c}\ell\overline{\nu_\ell}$ and $\mathrm{b} \to \mathrm{u}\ell\overline{\nu_\ell}$, excluding the radiative corrections, as presented in [45]. The lower mass of the resulting hadronic system in the $\mathrm{b} \to \mathrm{u}$ decays as compared to $\mathrm{b} \to \mathrm{c}$ decays, results in a harder lepton momentum spectrum.

The primary experimental background in identifying leptons from direct decays, $\mathrm{b} \to \ell$, results from leptons from the cascade decays, $\mathrm{b} \to \mathrm{c} \to \ell$, the semileptonic decay of charm hadrons produced from the weak b hadron decay. In order to model these decays, the ACCMM model for $\mathrm{c} \to \ell$ decays are convoluted with measured $\mathrm{B} \to \overline{\mathrm{D}}$ momentum spectrum [47] in order to boost the lepton momentum spectra into the rest frame of the b hadron. The model predictions for $\mathrm{b} \to \mathrm{c} \to \ell$ decays are also shown in Figure 2.9. Leptons from these decays have significantly lower momenta. The corresponding electroweak radiative corrections to the momentum spectra for electrons and muons are also shown in Figure 2.9.

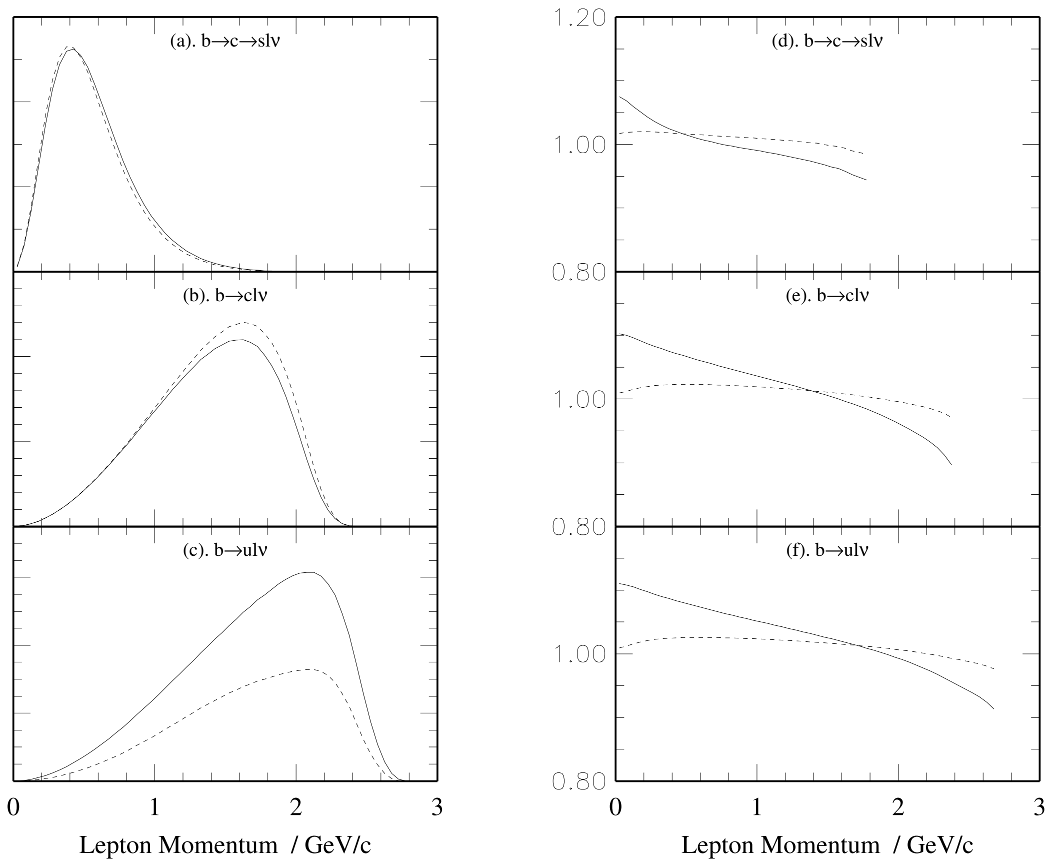

Figure 2.9: *The model predictions for the lepton momentum spectra and the corresponding electroweak radiative corrections, as presented in [45]. On the left, the ACCMM (solid) and ISGW (dashed) spectra are shown. On the right are the electroweak radiative correction factors for electrons (solid) and muons (dashed).*

2.7 Conclusions

This chapter has briefly described the Standard Model of particle physics and has given a summary of the theoretical description of semileptonic decays of b hadrons. The lepton momentum spectra from the phenomenological models for weak decays discussed in the previous sections will be used as the basis for the measurement of the semileptonic branching fraction of b hadrons presented in the following chapters.

Chapter 3

The OPAL Detector

The data used in this analysis were taken using the OPAL detector, one of the four experiments operating at the Large Electron Positron collider (LEP) at CERN. This chapter gives a brief description of the LEP accelerator and an overview of the OPAL experiment.

3.1 The LEP Collider

The LEP collider [48–52] first came into operation in 1989, colliding electrons and positrons at centre of mass energies up to approximately 100 GeV and so directly producing Z^0 bosons. In 1995 LEP finished its precision measurements at the Z^0 resonance and began a series of upgrades enabling higher energies to be reached. In 1997 LEP was able to produce e^+e^- collisions at centre of mass energies exceeding ~ 160 GeV, producing the first observation of W^+W^- pair production. Since that time the energy has been increased further, eventually culminating in collisions with centre of mass energies approaching 200 GeV.

The LEP collider is a large storage ring with a circumference of 26.7 km situated on the French–Swiss border at CERN, just outside Geneva. It lies at a depth of between 50

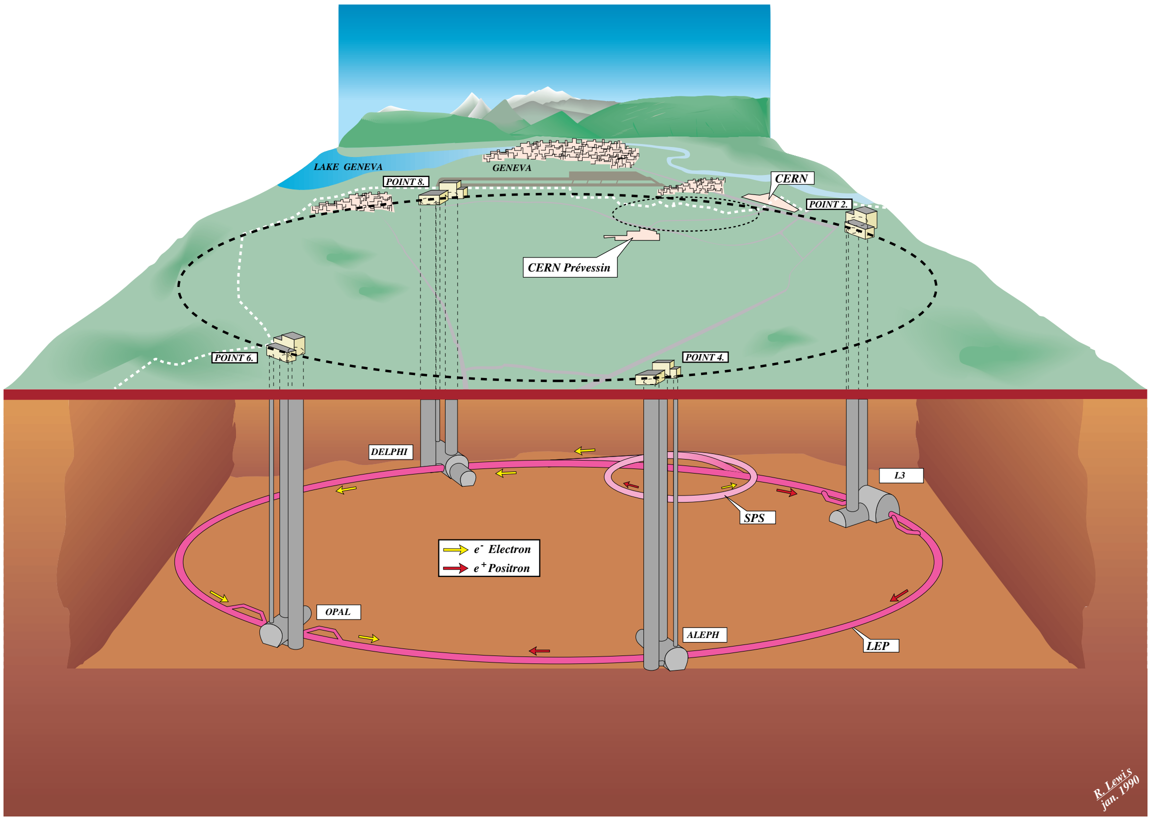

Figure 3.1: *The layout of the LEP collider ring and the four experiments.*

and 130 meters below the surface and inclined by 1.4 % from horizontal due to geological constraints. The ring is not quite circular, with eight curved sections and eight straight sections. The four LEP experiments ALEPH [53], DELPHI [54], L3 [55] and OPAL [56] reside in four of the straight sections, equally spaced around the ring as shown in Figure 3.1. Counter–rotating beams of electrons and positrons are brought into collision at the centres of each of the experiments.

The production of the LEP beam starts in the CERN complex where the LEP injector linac (LIL) [57] produces electrons and accelerates them to 200 MeV. These electrons are directed onto a tungsten target from which emerges both electrons and positrons, which are further accelerated to 600 MeV by a second linac and then stored in the Electron Positron Accumulator ring (EPA). When sufficient electrons and positrons have been produced, they are accelerated to 3.5 GeV by the Proton Synchrotron (PS), then passed on to the Super Proton Synchrotron (SPS) where they are further accelerated to 20 GeV. These beams are finally injected into the LEP ring, and once sufficient intensity has been achieved the beams are then accelerated to the final physics energy. Once the final energy has been reached the beams are brought into focus and allowed to collide at the interaction points. A schematic of the injection system is shown in Figure 3.2.

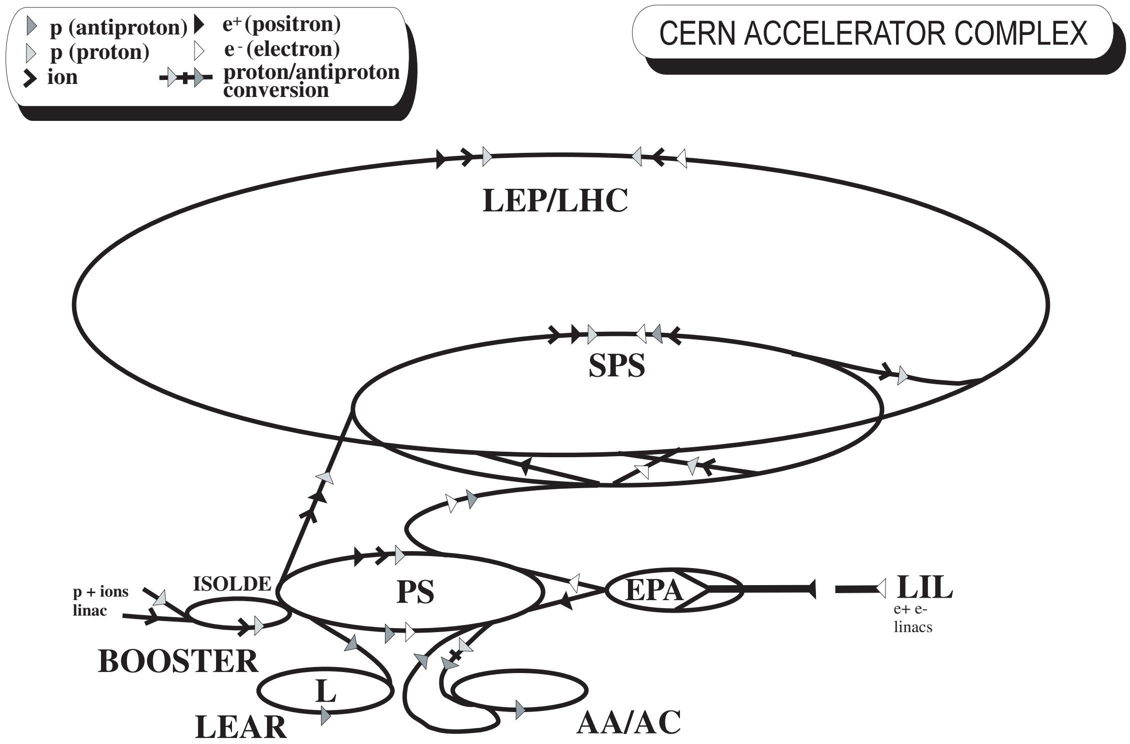

Figure 3.2: *The schematic layout of the CERN injector system for the LEP ring.*

The LEP tunnel houses the beam pipe within which the electrons and positrons circulate. The pipe is kept at a very low pressure, around 10^{-9} Torr, to minimise scattering by interaction with the beam gas. Around the ring are situated the magnets and RF cavities used to control the beam. Dipole magnets, which produce a vertical magnetic field, are used to steer the beam whilst additional quadrupole and sextupole magnets are needed to focus the beam. The RF cavities are used during the acceleration phase to accelerate the beam to the collision energy and also during normal physics running to compensate for the energy lost via synchrotron radiation as the particles orbit the ring.

The particles orbit not as a continuous beam but as a series of bunches equally spaced about the ring. Initially, each beam was split into four bunches, referred to as 4×4 running. During 1993, the number of bunches was increased to eight (8×8) in an attempt to increase the beam luminosity. In order to avoid eight beam crossing points in the 8×8 mode, a Pretzel scheme was adopted which uses electrostatic separators to ensure the beams only cross in the experiments. In 1995 LEP returned to the 4×4 mode and adopted a 'bunch train' scheme where each bunch is further split into four smaller groups, named bunchlets. At each of the four interaction points the beams are tightly focused to maximise the interaction luminosity, achieving a beamspot size of about $150\,\mu$m $\times$ $15\,\mu$m $\times$ 1 cm (horizontal, vertical, longitudinal) at the centre of the experiments.

3.2 The OPAL Detector

The LEP accelerator was designed for precision measurements at the Z^0 resonance, and therefore the four experiments were designed as general purpose detectors capable of studying a wide range of decay channels. The OPAL (Omni Purpose Apparatus for LEP) detector was conceived using proven technologies so as to ensue a well understood and reliable design [56].

OPAL was designed to provide as complete as possible information on the full range of interactions that result from e^+e^- annihilation. These include the precision measurements of the Z^0 decay channels as well as Bhabha scattering and two photon physics, together with searches for new physics beyond the Standard Model. Such considerations, together with the geometrical constraints imposed by the beam pipe resulted in a cylindrical design as shown in Figure 3.3. A cylindrical barrel region surrounds

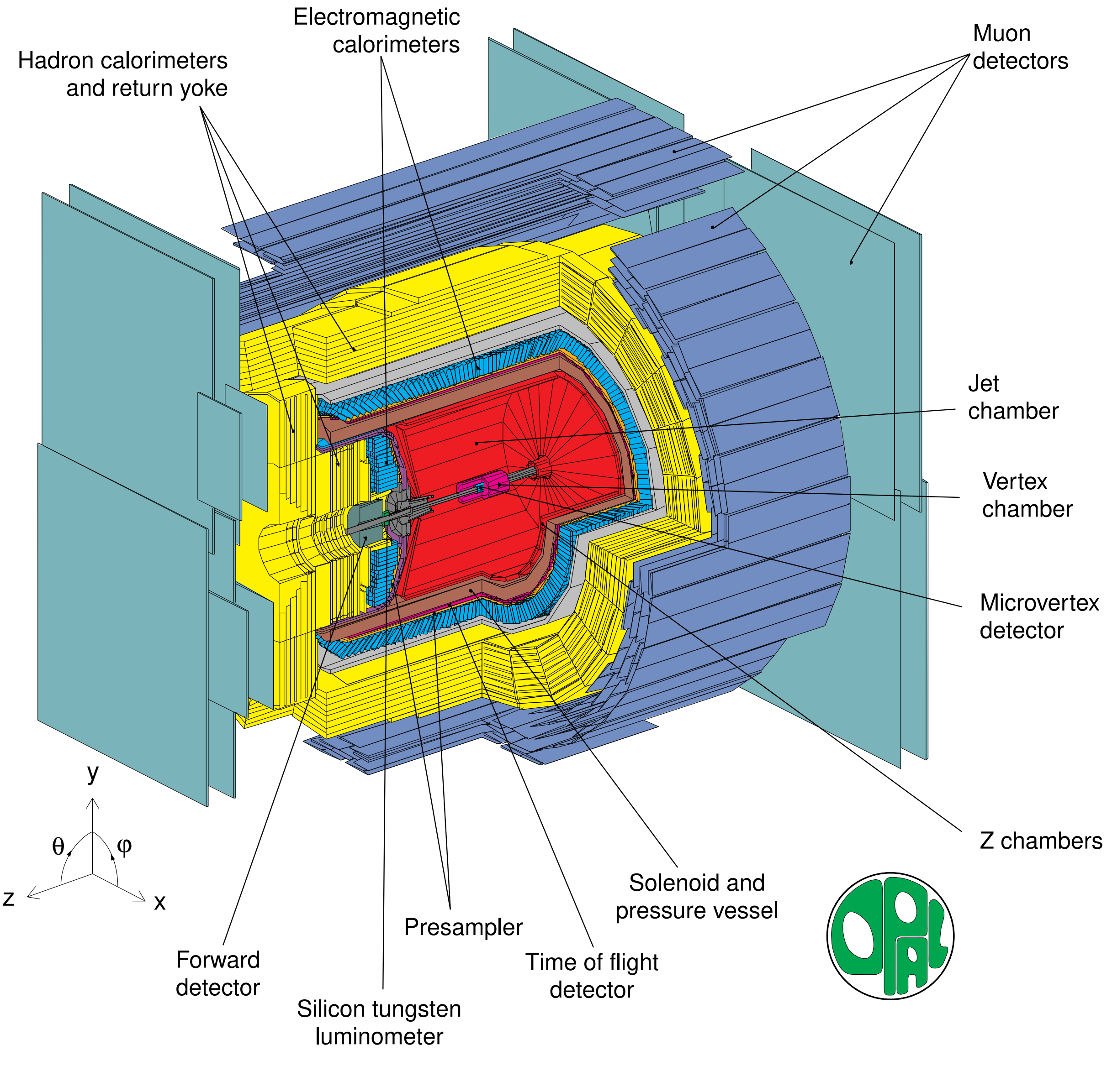

Figure 3.3: *A three–dimensional view of the OPAL detector.*

the beampipe, with the e^+e^- interactions occurring at the centre. Almost complete 4π coverage is obtained by closing the barrel with two endcap detectors.

The OPAL coordinate system is a right-handed Cartesian set $\{\mathrm{x}, \mathrm{y}, \mathrm{z}\}$ with its origin at the centre of OPAL, the nominal interaction point. The z–axis lies along the electron beam direction[a], with the x–axis horizontal and directed towards the centre of LEP. The z–axis is at an inclination of 1.4 % to the horizontal due to the tilt of the LEP ring and therefore the y–axis, which is orthogonal to the other two has a similar inclination from vertical. The cylindrical nature of OPAL devotes itself more conveniently to cylindrical polar coordinates $\{\mathrm{r}, \phi, \mathrm{z}\}$, or spherical polar coordinates $\{\mathrm{r}, \theta, \phi\}$. In cylindrical coordinates ϕ is the angle from the x–axis in the $x - y$ plane and r is the distance from the z–axis in the same plane. In spherical coordinates r is the radial distance from the origin, θ is the angle from the z–axis and ϕ the angle from the x–axis in the $x - y$ plane.

3.2.1 Detector Overview

Through the centre of OPAL runs a narrow beryllium beam pipe. Surrounding this is the silicon microvertex detector providing precise positional measurements close to the interaction point. Next lies the main particle tracking system which comprises various drift chambers; the central vertex chamber, the central jet chamber and the z coordinate chambers. These chambers are contained within a pressure vessel holding the drift chambers at a pressure of 4 bar. The OPAL solenoidal magnet places the inner detectors in a uniform magnetic field of $0.435\,T$ along the z–axis. Together, the drift chambers provide the tracking information needed to reconstruct the $r - \phi$ and z coordinates of charged particles and to determine the particle momenta from the track curvature resulting from the magnetic field. In addition, charge deposition measurements in the jet chamber allow rate of energy deposition ($\mathrm{d}E/\mathrm{d}x$) measurements to be made, providing particle identification.

Surrounding the magnet is the time of flight detector which gives accurate timing

[a] Viewed from above, electrons circulate anti-clockwise around LEP, positrons clockwise.

information, used for triggering purposes and background rejection. Surrounding the time of flight detector is the calorimetry system. Firstly, the electromagnetic calorimeters which use lead–glass blocks to measure the energy carried by electrons, positrons or photons. Prior to this lies the presampler, consisting of thin streamer tubes for the purpose of sampling the energy of electromagnetic showers initiated before reaching the calorimeter. Outside the electromagnetic system is the hadronic calorimeter which consists of limited streamer tubes interleaved with the iron plates of the magnet return yoke and measures the energy of hadronic showers.

The outer layer of OPAL consists of the muon chambers which detect charged particles that have penetrated the absorption material of the calorimeters. Such particles are predominantly muons.

In addition to these detectors, which form the structure shown in Figure 3.3, additional detectors are placed close to the beam pipe on either side of OPAL. These form the forward detectors for particles at very low angles to the beam line and play an important role, for example, in determining the absolute luminosity at OPAL by detecting electrons and positrons arising from small–angle Bhabha scattering.

The following sections will describe the main sub–detector elements of the OPAL detector in more detail.

3.3 Particle Tracking

The tracking of charged particles in OPAL uses the combined information from the various wire chambers and the silicon microvertex detector. Despite the obvious physical differences they all use the same basic processes to detect particles. As a charged particle traverses a medium it will ionise atoms in its path and the resulting electrons and ions can be detected and used to reconstruct the particle track.

OPAL uses two sorts of wire chambers; drift chambers and streamer tubes. The vertex chamber, the large jet chamber and the z chambers are all gaseous drift chambers working from the same principles, differing only in the construction specific to their design. In drift chambers an electric field causes the ionisation to drift towards the anode field wires. Close to the wires, the high local electric field causes an electron avalanche which amplifies the signal which is collected by the anode wires. The chambers consist of many planes of anode wires together with cathode wires interleaved so as to form the desired electric field in the detector volume. The ionisation charge drifts to the nearest anode wire allowing the track to be reconstructed. In the jet chamber, a uniform electric field is created throughout the detector volume, giving a constant drift velocity. This allows measurement of the time taken for the charge from the particle track to drift to the sense wire, which is used to provide tracking information in the plane perpendicular to the sense wires.

In the jet chamber the wires all lie parallel to the z–axis providing tracking primarily in the $r-\phi$ plane[b]. The vertex chamber contains a section configured similarly to the jet chamber, but with the wires more closely packed to give precise measurements close to the interaction point. The vertex chamber also has sets of wires aligned at an angle of 4° to the $r-\phi$ plane to allow z position measurements. Finally, the wires in the z chambers are arranged at 90° to the z–axis and provide precise z coordinate measurements. The barrel muon detectors are also constructed using drift chambers.

Streamer tubes work in a similar manner to drift chambers but the higher field gradients cause the ionisation charge to avalanche as opposed to drift. The endcap muon chambers use streamer tubes.

The silicon microvertex detector operates by collecting the ionisation charge generated as charged particles traverse the silicon wafers. The charge is collected on implanted semiconducting strips providing precise measurements in $r-\phi$ and z.

[b] z measurements in the jet chamber are discussed in Section 3.3.3

3.3.1 The Silicon Microvertex Detector

The silicon microvertex detector provides precise tracking capabilities close to the interaction point, necessary for the accurate reconstruction of the primary interaction vertex and secondary decays.

The detector was first installed in 1991 [58] when it became apparent that the low beam backgrounds permitted a smaller diameter beampipe, thus providing the space necessary for the detector. Figure 3.4 shows the 1991 configuration (μVTX1) with two concentric layers of single-sided silicon detector wafers giving $r - \phi$ readout.

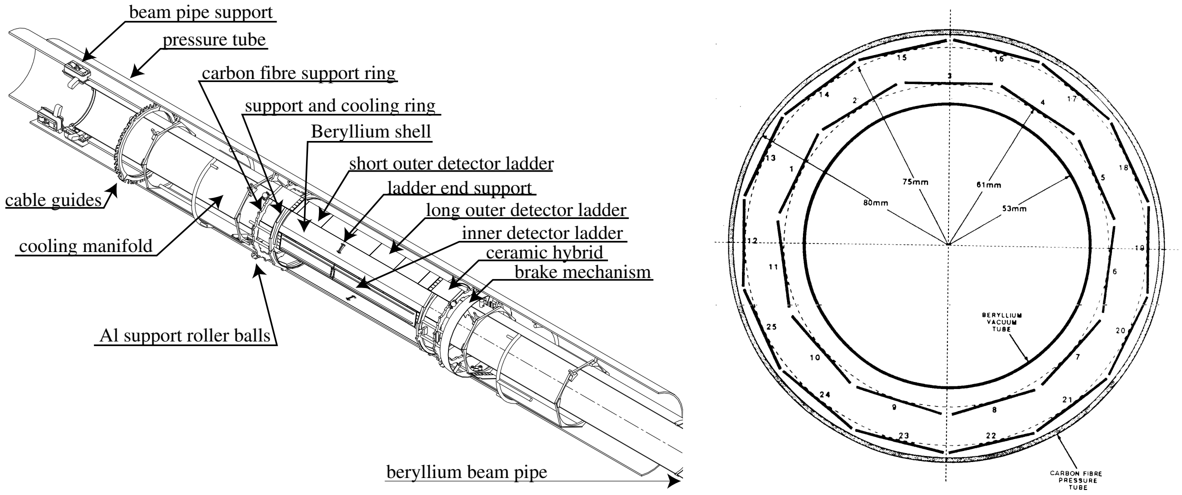

Figure 3.4: *The left–hand side figure shows a cut–away view of the 1991 silicon microvertex detector showing the silicon wafers and readout electronics. On the right, the silicon microvertex detector is viewed along the beam axis. The inner and outer layers of silicon wafers, together with the beryllium beam pipe are shown.*

The original beampipe, which was constructed from a carbon fibre aluminium composite, was replaced with a smaller radius beryllium pipe. Beryllium was chosen because of the small radiation length it presents to incident particles. The microvertex detector was inserted in the region formed between the new and original beampipes. A carbon fibre pressure tube was used to isolate the detector from the 4 bar absolute pressure vessel of the vertex and jet drift chambers and to maintain the low humidity nitrogen atmosphere required at the microvertex detector.

The detector was upgraded (μVTX2) for the 1993 operation [59] by attaching additional wafers to the backs of the $r-\phi$ detectors, with the readout strips oriented perpendicular to those in $r-\phi$ so as to provide z coordinate readout.

The microvertex detector has 11 ladders in the inner barrel and 14 in the outer barrel, at radii of 61 mm and 75 mm respectively, as shown in Figure 3.4. Each ladder consists of 3 silicon wafers 60 mm long and 33 mm wide, daisy-chained together. Each wafer is constructed from 250 μm thick n-type silicon with the strips formed from implanted p-type strips 25 μm apart. For the $r-\phi$ detectors every other strip is instrumented with an aluminium readout strip, giving a readout pitch of 50 μm, whilst for the z wafers, every fourth strip is a readout strip giving a 100 μm readout pitch. The detector extends to $|\cos\theta| < 0.83$ for the inner barrel and $|\cos\theta| < 0.77$ for the outer. The ladders are arranged so as far as possible to avoid lining up the small gaps in the ϕ coverage occurring between adjacent ladders in a barrel. This ensures almost 100 % single hit coverage in ϕ.

A particle traversing the silicon wafer will create electron-hole pairs. The electrons from these pairs drift under the electric field towards the p-type strips where the charge is collected. The charge is collected over a number of strips using capacitive coupling allowing the pulse shape to be reconstructed, which is used to determine the mean hit position. The impact parameter resolution of the detector has been measured to be 10 μm in $r-\phi$ and 15 μm in z using events collected during OPAL running.

The most recent upgrade (μVTX3) [60] was completed for the 1996 data acquisition when the geometrical acceptance of the detector was extended by increasing the two layer polar coordinate acceptance to $|\cos\theta| < 0.89$. The detector geometry was also improved by adding an extra ladder to each layer and giving the ladders a staggered arrangement in $r-\phi$, as shown in Figure 3.5, increasing the ϕ coverage for each barrel to 97 %.

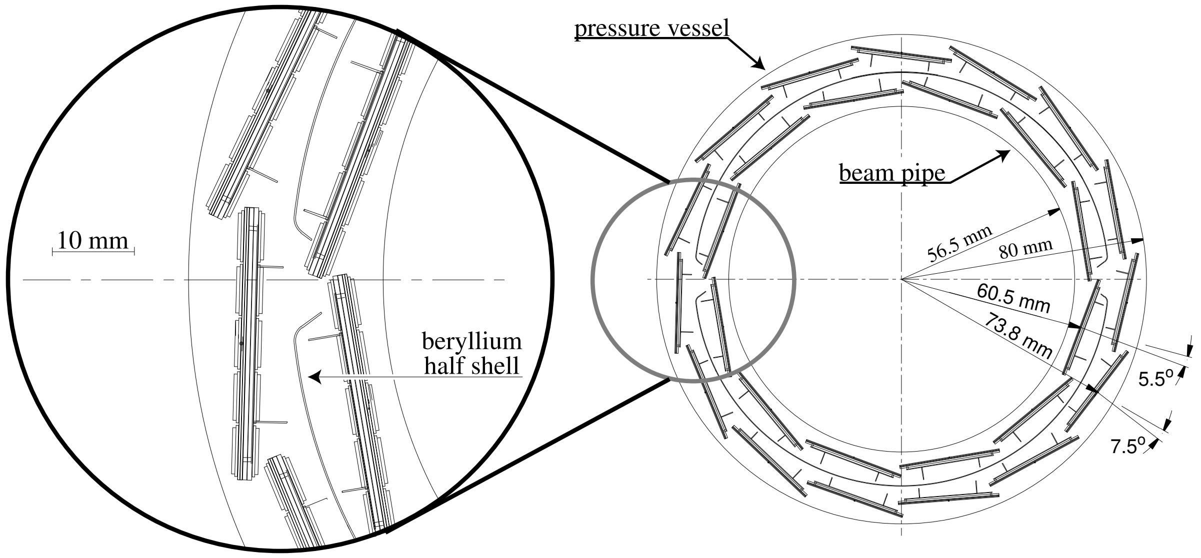

Figure 3.5: *The μVTX3 configuration of the silicon microvertex detector, showing the staggered arrangement of the silicon wafers.*

3.3.2 The Central Vertex Chamber

The vertex drift chamber [61] was initially designed to provide precise tracking in both the $r-\phi$ and $r-z$ planes for the reconstruction of secondary decays. Since the installation of the silicon microvertex detector, the vertex chamber has also aided in the matching of tracks reconstructed in the central jet chamber to silicon microvertex detector hits.

The chamber is 1 m long with an inner radius of 88 mm and an outer radius of 235 mm. It is filled with the same 4 bar mixture of argon (88 %), methane (9.4 %) and iso-butane (2.6 %) as the other central drift chambers. The chamber is split into 36 sectors in ϕ, each of which contains an inner and outer layer termed the axial and stereo layers respectively. The axial layer contains 12 sense anode wires lying parallel to the z–axis, with interlaced cathode wires. Field shaping wires at the cell edges define the desired electric field, as shown in Figure 3.6. The stereo cells are similar to the axial cells, with 6 sense wires inclined by 4° in the $r-z$ plane such that their radial planes coincide with the axial cells at $z = 0$.

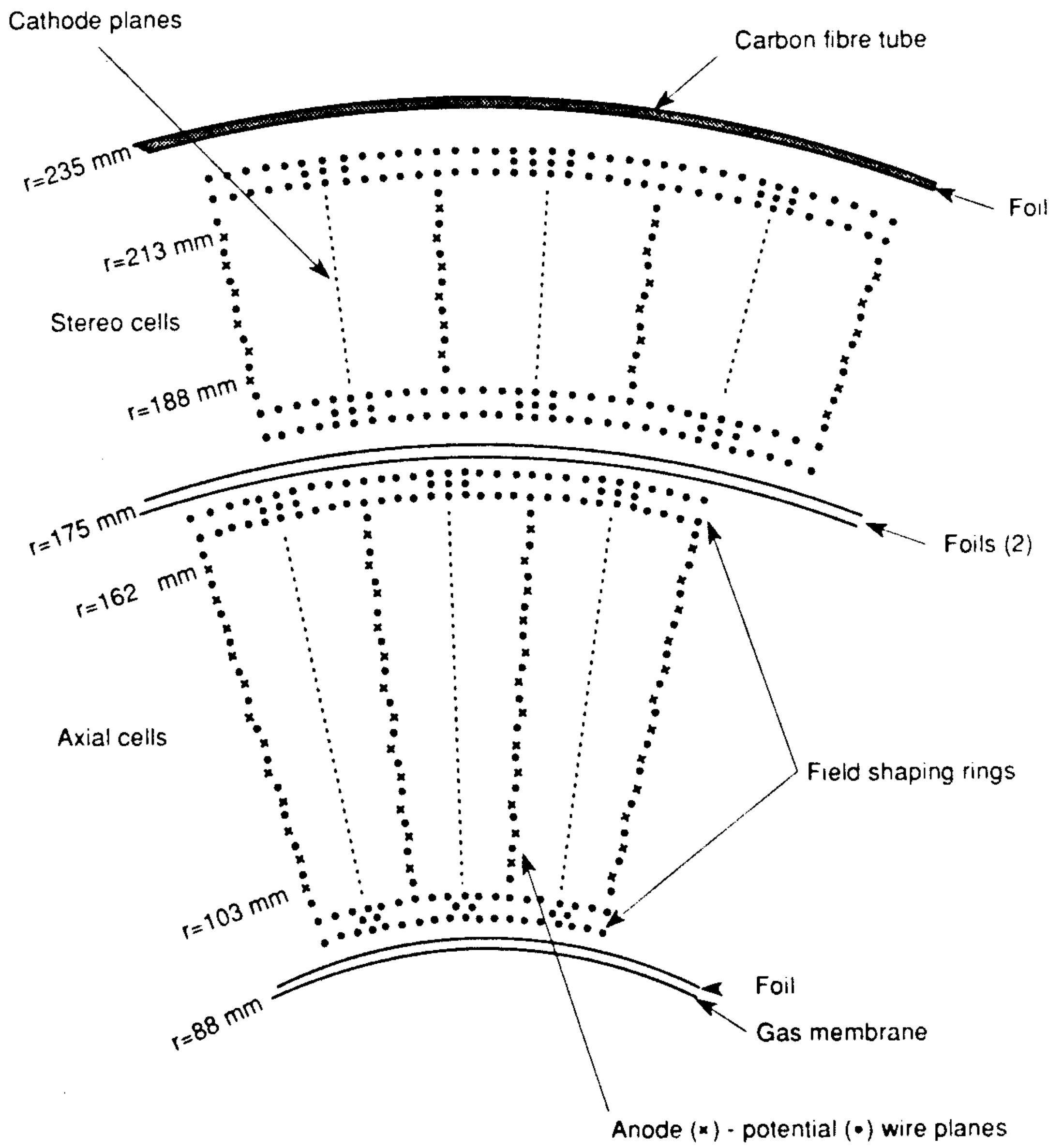

Figure 3.6: *An end–on view of the vertex drift chamber.*

By combining the axial and stereo information offline this arrangement allows for both $r-\phi$ and z coordinate determination with average resolutions of $55\,\mu$m and $700\,\mu$m respectively. The axial chambers cover the region $|\cos\theta| < 0.95$ while the stereo acceptance is $|\cos\theta| < 0.92$. A coarse z measurement is obtained using time difference measurements [62] in the axial wires and this is used in fast track finding for triggering purposes (Section 3.6).

3.3.3 The Central Jet Chamber

At about 4 m long and with inner and outer diameters of 0.5 m and 3.7 m, the central jet chamber [63] provides the primary charged particle tracking capabilities in OPAL. It is designed with excellent space and double track resolution needed to resolve jet-like events, together with specific ionisation loss $\mathrm{d}E/\mathrm{d}x$ measurements providing charged particle identification.

The chamber is divided into 24 sectors each of which contain a radial plane of 159 sense wires, aligned parallel to the z–axis extending from an inner radius of 255 mm to an outer radius of 1835 mm. These wires are equally spaced with a separation of 10 mm and alternate with the field potential wires. In order to resolve any left–right ambiguities, the sense wires are staggered by $\pm 100\,\mu$m with respect to the plane defined by the potential wires. The cathode wires form the boundaries between adjacent sectors. With this arrangement the maximum drift distance varies from 3 cm at the innermost wire to 25 cm at the outermost wire. Within the region $|\cos\theta| < 0.73$ all 159 sense wires are available for tracking, covering 73 % of the full 4π solid angle. Outside this region the track will leave the jet chamber through the endplates resulting in the number of possible tracking hits falling with increasing $|\cos\theta|$. At least 8 wires are available for tracks with $|\cos\theta| < 0.98$, covering 98 % of 4π. A laser system is used to produce track-like ionisation trails in the chamber, which are used to calibrate the detector alignment during running [64].

The jet chamber provides full three dimensional particle tracking. The $r - \phi$ coordinates are determined from the wire positions and drift times. The drift time is obtained through a comparison between the time of arrival of charge on each wire and beam crossing timing information. A coarse measurement of the z coordinate is obtained through charge division, where the ratio of the charge collected at each end of the wire is used to infer the z coordinate. Using these techniques, an $r - \phi$ resolution of $135\,\mu$m at the average drift distance of 70 mm is obtained, whilst the z coordinate is measured to an accuracy of ± 60 mm.

The jet chamber is contained within a magnetic field of $0.435\,T$ providing momentum information through track curvature measurements. From dimuon events, $e^+e^- \to Z^0 \to \mu^+\mu^-$, the momentum resolution has been found to be parameterised by,

$$\frac{\sigma(p_t)}{p_t} = \sqrt{(0.0015\,p_t)^2 + (0.02)^2} \tag{3.1}$$

where the transverse momentum, p_t, is the momentum component in the $r-\phi$ plane, in GeV/c. The chamber also provides $\mathrm{d}E/\mathrm{d}x$ measurements for particle identification. For a minimum ionising particle with at least 130 $\mathrm{d}E/\mathrm{d}x$ measurements a resolution of $\sigma(\mathrm{d}E/\mathrm{d}x)/(\mathrm{d}E/\mathrm{d}x) \sim 3.8\,\%$ is obtained [65]. Particle identification through $\mathrm{d}E/\mathrm{d}x$ measurements is discussed in detail in Chapter 5 in relation to electron identification.

3.3.4 The Z Chambers

The z chambers [66] are installed as a layer of thin drift chambers surrounding the jet chamber barrel. They are designed to provide accurate measurements of the z coordinate of the track endpoints to supplement the relatively imprecise z measurements from charge division in the jet chamber.

There are in total 24 z chambers each 4 m long, 0.5 m wide and 59 mm thick, providing coverage for tracks within $|\cos\theta| < 0.72$ and over 94 % of ϕ. Each chamber consists of 8 cells, each containing 6 sense wires aligned along the ϕ direction at increasing radii, with a stagger of $\pm 250\,\mu$m to resolve any left–right ambiguities. The cells are bidirectional in that the sense wires are located at the centre of each cell with the cathode planes at the edges, such that the ionisation charge can drift towards the sense wires from both directions.

A z resolution between $100\,\mu$m and $350\,\mu$m, depending on the θ angle of the track, is obtained with the z chambers. Using charge division techniques similar to those used in the jet chamber, the ϕ coordinate can be inferred giving an $r-\phi$ resolution of 1.5 cm.

3.3.5 The OPAL Magnet

The central tracking chambers are all contained within a magnetic field provided by the OPAL solenoid. Constructed from a self supporting, water cooled coil of aluminium and glass–epoxy, the magnet is designed to present a minimum of interaction material to incident particles[c]. During operation, a current of about $7000\,A$ provides a uniform axial field of $0.435\,T$ throughout the entire tracking system, stable to within $\pm 0.5\,\%$ over the volume of the central tracking detectors. The return yoke is constructed from soft iron and designed with the aid of compensating coils to keep any stray magnetic fields outside the solenoid to below $0.01\,T$.

3.3.6 The Muon Chambers

The final elements in the OPAL tracking system are the muon chambers. As the outer layer of the OPAL detector they identify muons from their penetrating nature. Particles reaching the chambers have to traverse at least 1.3 m of iron equivalent (corresponding to 7 interaction lengths for pions) and are therefore predominantly muons. The probability of a pion penetrating without interaction is less than 0.1 % and therefore tracks in the central tracking chambers which can be matched to muon chamber hits can be identified as muons.

The muon system is composed of two sets of chambers covering the barrel and endcap regions, arranged so as to provide coverage by at least one layer over 93 % of the solid angle. Isolated muons above 3 GeV/c within this region are identified with practically 100 % efficiency [67], whilst the probability that an isolated pion of 5 GeV/c is misidentified as a muon is less than 1 %.

The barrel muon chambers [68] are composed of 110 large area drift chambers each 1.2 m wide and 90 mm thick divided into 4 modules for easier mounting. On each side of the barrel a module with 44 chambers is mounted. The remaining two modules consist

[c]The solenoid and pressure vessel together present on average only 1.7 radiation lengths.

of 10 chambers in an upper module and 12 in a lower module and which close the gaps providing full coverage in ϕ. The chambers are almost identical, differing only their lengths, which are either 10.4, 8.4 or 6.0 m in order to accommodate the magnet support structure. The region $|\cos\theta| < 0.68$ is covered by four layers, with $|\cos\theta| < 0.72$ covered by at least one layer.

The chambers consist of two cells side by side, each containing an anode wire running the length of the chamber with a maximum drift distance of 297 mm from either side. The chamber walls serve as the cathode, formed from copper clad PC boards with strips to define the electric field. Opposite the anode sense wire the cathode strips form a diamond pattern designed to allow the z coordinate to be measured.

The z coordinate is determined in a three stage process. A fine measurement is obtained using a first set of diamond shaped cathode pads to within 2 mm, modulo the period of the pattern which is 171 mm. A second set of diamond pads with period 1710 mm gives a less precise measurement (± 30 mm) and is used to remove the fine measurement ambiguity. By comparing pulse heights and time differences at each end of the sense wires a coarse z measurement can be obtained to pinpoint the hit in z with a resolution of 2 mm. The resolution in $r - \phi$ is 1.5 mm using drift time information.

The region $0.67 < |\cos\theta| < 0.985$ is covered by the endcap muon chambers which consist of four layers of limited streamer tubes. Each endcap consists of 8 quadrant chambers together with 4 smaller 'patch' chambers which together provide around 150 m^2 of coverage. The quadrants cover most of the acceptance but are limited by other detector elements, such as the beampipe and readout cables. The patch chambers are designed to cover the majority of the remaining regions. Each chamber is composed of 2 layers of streamer tubes aligned perpendicular to each other so as to provide both x and y coordinate measurements. Anode wires run along the length of the chambers at a spacing of 10 mm within plastic U-formed extrusions. Aluminium strips run along the inside of the extrusions and also on the other side of the chamber perpendicular to the sense wire. Thus each coordinate, x and y, for the tracks are measured twice providing an overall positional resolution of 1 mm.

3.4 Calorimetry

The tracking detectors in OPAL provide detailed measurements of the trajectory and momentum of charged particles. The calorimetry systems are designed to provide additional measurements of particle energies, particularly important for neutral particles such as photons which are not detected by the tracking detectors.

The calorimetry system is composed of two main components; the electromagnetic and hadronic calorimeters. The electromagnetic and hadronic calorimeters work in a similar manner, by causing the incident particles to shower into lower energy particles which are absorbed in the calorimeter material and used to measure the energy of the incident particle.

In the case of the electromagnetic calorimeter in OPAL, lead–glass blocks are used as both the absorber and detection medium. The high electric charge of the lead nuclei causes incident photons to convert, forming an e^+e^- pair. Similarly, an incident electron will bremsstrahlung in the presence of the heavy lead nuclei, thus losing energy to radiated photons. These processes will repeat, approximately doubling the number of particles at each stage until the electron energies are too low to allow further bremsstrahlung and they are absorbed into the absorber material. The energy of the incident particle is measured by detecting the Cherenkov radiation emitted in the lead–glass by the energetic electrons in the shower. The lead–glass blocks present sufficient material to incident electrons and photons to completely contain their showers within the blocks so that the number of Cherenkov photons is proportional to the energy of the incident particles.

The hadronic calorimeters work by causing strongly interacting particles to shower via inelastic collisions with nuclei of the absorber material. The process continues until the energies of the shower particles are low enough that they can be absorbed into the absorber material. In OPAL, the absorber material is formed from the magnet return yoke. The iron layers are interleaved with drift chambers which sample the energy of the hadronic shower as it forms, allowing the energy of the incident particle to be measured.

3.4.1 The Electromagnetic Calorimeters

The electromagnetic calorimeter system in OPAL is designed to measure the energy of electrons, positrons and photons in the energy range from tens of MeV up to $\sim 100\,\text{GeV}$. Using lead–glass blocks as a total absorption calorimeter, the system is mounted between the magnet coil and iron return yoke. The system consists of three overlapping units, the barrel calorimeter which surrounds the coil and covers the angular region up to $|\cos\theta| < 0.82$, and two endcap assemblies covering the regions $0.81 < |\cos\theta| < 0.98$.

Due to the presence of the central tracking systems, pressure vessel and magnetic coil, there is about two radiation lengths of material in front of the calorimeters. This means that electromagnetic showers are likely to have been initiated before reaching the calorimeters. For this reason, a thin layer of 'presampler' detectors are placed just in front of the calorimeters, which sample the incoming showers, improving the positional and energy resolution obtained with the entire system.

The barrel electromagnetic calorimeter [56] consists of a cylindrical array of 9440 lead–glass blocks providing 24.5 radiation lengths of absorber material. The blocks are arranged so that their longitudinal axes point towards the interaction point, to minimise cross–over between adjacent blocks. The blocks are slightly rotated from a perfectly pointing geometry however, to prevent tracks escaping undetected through the gaps between adjacent blocks. The blocks have a nominal square cross-section of $10\,\text{cm} \times 10\,\text{cm}$ and a length of 37 cm. In order to achieve the quasi-pointing geometry, sixteen slightly different shapes are used such that the blocks point to a z position between $55.5\,\text{mm} < |z| < 157.9\,\text{mm}$ and away from the beam axis by 30 mm in $r - \phi$.

To detect the Cherenkov light produced by the shower electrons, the end of each block is connected to a phototube via a short light guide. Special phototubes are used that are tolerant to the small residual magnetic fields from the OPAL solenoid. In addition, 2 mm of shielding is provided by a permaloy metal jacket to reduce such fields to a minimum.

The barrel electromagnetic presampler [69, 70] consists of 16 limited streamer tubes each 6623 mm in length arranged to form a barrel layer of radius 2388 mm just in front of the calorimeter. Each chamber contains two layers of anode wires contained within a PVC cell, with readout from 1 cm wide cathode strips on each side of cells providing positional readout in both the $r - \phi$ and z planes.

The endcap calorimeters [71] are constructed from similar lead–glass blocks. Each endcap consists of 1132 square blocks presenting 20.5 radiation lengths, arranged coaxial to the z–axis due to the geometrical constraints imposed by the spatial requirements in the endcaps. They are placed within the full magnetic field and thus cannot use photomultiplier tubes as in the barrel region. Instead, specially designed vacuum phototriodes are used to detect the Cherenkov light. Each endcap calorimeter is instrumented with a presampler [72] consisting of 32 multiwire proportional chambers, arranged into an annulus configuration in front of the detector.

3.4.2 The Hadron Calorimeters

The hadron calorimeters measure the hadronic energy contained within an event by means of total absorption. To achieve this, the calorimeters consist of at least 4 interaction lengths of iron formed from the magnet return yoke, interleaved with detector chambers which sample the shower energy. Typically, showers are initiated within the 2.2 radiation lengths of material present before the hadron calorimeters and thus a significant fraction of their energy does not reach these calorimeters. The electromagnetic calorimeters form the majority of this interaction material and so by using both the electromagnetic and hadronic calorimeter systems in conjunction, it is possible to measure the full hadronic shower energy. The hadron calorimeter comprises three elements, namely the barrel, endcap and poletip regions, which together give 97 % coverage of the full solid angle.

The barrel detector consists of 9 layers of limited streamer tubes [73] interleaved with 8 layers of 100 mm thick iron slabs, spaced by 25 mm and covering radii from 3.39 m to 4.39 m. The barrel detector covers the angular region up to $|\cos\theta| < 0.81$. The endcap calorimeters extend the sensitive region up to $|\cos\theta| < 0.91$, following a similar design as the barrel detector with 8 detector layers interleaved with 7 iron slabs, with 35 mm spacings.

The tubes are instrumented with metallic implants on the chamber walls for readout, with strips on the inner radius walls and pads on the outer. The strips allow single particle tracking, which are predominantly muons, and are therefore useful in providing complimentary information for muon identification. Such information is particularly useful for tracks which lie outside the acceptance of the muon chambers and for low energy tracks which fail to reach the muon chambers. The pads are arranged into geometrical stacks emanating from the interaction point and dividing the solid angle into 976 equal segments. The charge collected on each pad is collected and summed over all pads in a tower, providing energy and positional measurements of hadronic showers.

The pole–tip detectors [74] extend the angular coverage up to $|\cos\theta| < 0.99$ using ten thin multi–wire chambers with nine 80 mm thick iron plates. The pole–tip detectors use a similar strip and pad readout system to that used in the barrel and endcap detectors.

3.4.3 Calorimeter Resolutions

The energy resolution of the OPAL detector is limited by the material lying in front of the calorimeters which cause the showers to be initiated prior to the detector. The presampler detectors compensate partly for the resulting loss in resolution.

From test beam studies, the electromagnetic calorimeter resolution was determined to be $\sigma_E/E = \sqrt{(0.002^2 + 0.063^2/E)}$ in the barrel and $\sigma_E/E = 0.05/\sqrt{E}$ in the endcaps, where E is measured in GeV [56]. The additional material in front of the detectors degrades this resolution by a factor of about two. Using the presampler detectors approximately half of this deterioration can be recovered. The spatial resolution of the energy clusters is $4-6$ mm in $r-\phi$ and about 10 mm in z for the barrel detector and approximately 11 mm for the endcap detectors.

The hadron calorimeter resolution was similarly determined from test beam experiments and was found to be $\sigma_E/E = 1.2/\sqrt{E}$, where E is in GeV [56].

3.5 Other OPAL Elements

3.5.1 Time of Flight Detector

The time of flight detector consists of two components; the barrel and endcap detectors, which together provide precise timing information over almost the full angular coverage of the OPAL detector. The barrel detector consists of 160 thin scintillation counters covering the region $|\cos\theta| < 0.82$ and surrounds the OPAL solenoid. The detector provides low momentum (0.6 to 2.5 GeV/c) charged particle identification, fast triggering information and cosmic ray rejection. The endcap detectors were installed in 1997 and consist of a layer of 120 scintillating tiles between the presampler and electromagnetic calorimeters in each endcap. They provide additional timing information on Minimum Ionising Particles (MIPS) in the endcap regions.

3.5.2 Forward Detectors

The forward detectors [56] are placed close to the beam pipe on either side of the OPAL detector. Their purpose is to detect electrons from low angle Bhabha scattering events which are used to determine the beam luminosity. In addition they allow the tagging of electrons from two photon events ($e^+e^- \to e^+e^-\gamma\gamma$).

The forward detectors are situated at ± 2.4 m from the interaction point and consist of 35 sampling layers of a lead–scintillator sandwich corresponding to 24 radiation lengths. The detector has an energy resolution of $\sigma_E/E \sim 0.17/\sqrt{E}$ for well contained Bhabha events. A silicon tungsten luminosity detector was added in 1993 [75] in the region just in front of the forward detector. The detector consists of two components, one at each side of OPAL, formed from 19 layers of silicon detectors and 18 layers of tungsten and located approximately 2.4 m from the interaction point. A 7 radiation length ring of lead–scintillator layers (gamma catcher) plugs the acceptance gap between the inner edge of the endcap electromagnetic calorimeters and the outer edge of the forward detectors. Finally, the far forward monitor consists of 20 radiation lengths of lead–glass scintillator calorimeters mounted on either side of the beampipe, 7.85 m from the interaction point. The far forward detector is designed to detect electrons which have been deflected by the focusing quadrupoles.

3.5.3 Minimum Ionising Particle (MIP) Plug

Installed for the start of 1997 data taking, the MIP plug consists of 4 layers of 1 cm thick scintillator tiles located at each end of the OPAL detector. The inner two layers are located just behind the gamma catcher and cover the polar angular region $126-220$ mrad. The next layer is located behind these and covers the region $45 - 160$ mrad. These three layers are divided into quadrants in ϕ. The final layer is located between the silicon tungsten luminosity detector and the forward detectors and covers the polar angular region $43 - 130$ mrad. This layer is divided into octants in ϕ. The MIP plug is designed to provide good time resolution and detection efficiency for single minimum ionising particles.

3.6 Trigger and Data Acquisition

Positron and electron bunches collide at the interaction points every $22\,\mu$s in the 4×4 running mode, halving to $11\,\mu$s in the 8×8 mode. In this time interval, the OPAL trigger system [76, 77] must decide whether an interesting physics event has occurred and hence to read out the individual sub–detectors.

Given the large number of channels that require processing when the detector is read out, the rate at which events can be recorded is limited to a few Hertz. This means that the trigger system must be able to select only interesting physics events with a minimum of background.

The system uses a combination of standalone and coincidence signals to identify physics events. The standalone signals use information from tracking chamber multiplicity counts and total energy summations. Coincidence triggers are derived from the tracking chambers, calorimeters, muon chambers and time of flight apparatus by dividing the 4π solid angle into 144 bins; 6 in θ and 24 in ϕ. By counting the hits per bin and correlating back–to–back hits and detector coincidences, a basic image of the event can be reconstructed. The bins overlap so as to reduce inefficiencies at the bin boundaries. The standalone and coincidence triggers are analysed in parallel to provide a fast trigger for physics events, using a programmable set of trigger conditions. If no trigger condition is met the whole detector is reset for the next bunch crossing.

When the trigger conditions are met, the entire detector is read out [78]. Each sub–detector has a local system crate which reads out the sub–detector and in some cases performs some basic data processing. The data are then passed to the event builder which reconstructs the entire event and passes the data to the filter which performs a fast analysis of the data, classifying the event into various categories and removing any remaining background events. The data are then passed on to the offline reconstruction system for final processing and storage. The information is also made available to the OPAL shift crew for data quality checks and detector monitoring purposes.

3.7 OPAL Offline Event Reconstruction

The offline reconstruction program reconstructs the full event from the information stored by the individual sub–detectors. This is performed using the ROPE (Reconstruction of OPAL Events) [79] software package which contains individual modules for each sub–detector to process the sub–detector data using calibration information. More general routines are then used to merge the information from each sub–detector into a complete picture of the event.

The track reconstruction begins in the jet and vertex drift chambers by forming track seeds from triplets of consecutive hits within a sector. Starting from the outer radius where the track densities are lower, these seed tracks are extrapolated inwards so that additional hits can be added and the track refitted. This process continues until the track χ^2 exceeds a given threshold. These segments are then merged to form entire tracks within a sub–detector. The jet chamber tracks are then merged with vertex and z chamber tracks. Finally, silicon microvertex hits are added and the entire track refitted using the full track information.

The completed tracks are characterised using five physics parameters :-

- κ, the track curvature, where $|\kappa| = 1/2\rho$ and ρ is the radius of curvature of the track. κ is signed such that with an axial magnetic field along the positive z–axis, positive values of κ corresponds to a particle with negative charge;
- ϕ_0, the azimuthal angle made by the track tangent in the $r - \phi$ plane at the point of closest approach to the nominal interaction point, the centre of OPAL;
- d_0, the impact parameter in the $r-\phi$ plane to the nominal interaction point. With an axial magnetic field along the z–axis, d_0 is defined as $d_0 = qD$ where q is the track charge in units of e and $D = \rho - \sqrt{x_c^2 + y_c^2}$, where (x_c, y_c) are the coordinates of the centre of the track circle;
- $\tan\lambda = \cot\theta$, where θ is the track polar angle from the positive z–axis;
- z_0, the track z coordinate at the point of closest approach to the interaction point in the $r - \phi$ plane.

The calorimeter information is reconstructed as energy clusters. Starting in the electromagnetic calorimeter, clusters are formed by first looking for a block with an energy deposition above a given threshold value. Surroundings blocks are added if they have an energy deposition above some lower threshold value. This procedure forms large clusters of energetic blocks. These clusters are then split into finer clusters if local maxima are found and the resulting fine cluster energies are corrected for preshowering using presampler information. The cluster positions are found from a weighted average of the block positions and the clusters are then finally associated to reconstructed tracks. A barrel cluster is associated to a track if the track extrapolates from the tracking detectors to within 150 mrad in θ and 80 mrad in ϕ of the cluster position, taking into account multiple scattering in the intermediate material. Similarly endcap clusters are associated if they are within 50 mrad in both θ and ϕ. Hadronic clusters are reconstructed in a similar manner, with the spatial association requirements for the barrel and pole tip detectors 100 mrad in both θ and ϕ. In the endcaps this increases to 200 mrad. The remaining unassociated clusters are then assigned to neutral particles.

Finally, the data are stored in DST (Data Summary Tape) format in terms of the reconstructed tracks and clusters, and are made available for offline analysis. The raw data are also stored so that future improvements, such as better calibrations and improved reconstruction techniques can be incorporated.

Chapter 4

Event Reconstruction and Selection

By the end of data taking in 1995 the OPAL detector had recorded approximately 4.3 million multi–hadronic $Z^0 \rightarrow q\overline{q}$ decays with centre of mass energies around the Z^0 resonance. This chapter describes the raw data sets used in this analysis and the criteria used to select these multi–hadronic decays. Of these hadronic events, roughly 21 % [14] are $Z^0 \rightarrow b\overline{b}$ decays. The techniques used to select a high purity, unbiased sample of $Z^0 \rightarrow b\overline{b}$ decays and the determination of the b purity of the selected sample from the data are described.

4.1 OPAL Data and Monte Carlo

4.1.1 OPAL Data

The raw data set used for this analysis consists of events collected between 1992 and 1995, with centre of mass energies within 3 GeV of the Z^0 peak. The most important trigger requirements used to select multi–hadronic decays are :-

- **Track trigger :** At least two tracks are required with momentum transverse to the z–axis greater than 0.45 GeV/c, originating from the nominal interaction point at the centre of the OPAL detector;

- **Time of flight trigger :** At least three non–adjacent scintillator hits in the time of flight detectors are required;
- **Electromagnetic trigger :** The sum of the raw energy in either the barrel or endcap electromagnetic calorimeters must exceed 6 GeV or 7 GeV respectively.

Various detector status cuts are applied to ensure good quality data. In addition to the requirements imposed by the above triggers, the following detectors are required to have been operational during the data acquisition :-

- The vertex, jet and z tracking chambers for efficient charged particle track reconstruction and the electromagnetic calorimeters for neutral particle detection;
- The silicon microvertex detector, for the precise reconstruction of the primary interaction point and secondary decay vertices, essential for the reconstruction of b hadron decays;
- The muon chambers for muon identification and more stringent requirements on the electromagnetic calorimeters for electron identification.

4.1.2 Monte Carlo Samples

Simulated events, where the true particle species and event kinematics are known, are used to study the performance of the various selection criteria and analysis techniques. These events are termed Monte Carlo events where the name derives from the statistical technique [80] used to generate the events.

The Monte Carlo data used in this thesis were generated using the JETSET7.4 generator [81]. Starting from a quark–antiquark pair produced from the decay of a Z^0 boson or excited photon, JETSET generates a parton shower. The quarks in the shower radiate gluons which in turn form additional quark–antiquark pairs. This process continues until the parton energies are too low for further showering, at which point the hadronisation of the partons into the final state hadrons is simulated. Finally, the decays of short lived hadrons are simulated. This stage is governed by decay tables which outline the possible decay channels and the corresponding branching fractions for each particle species. These tables can be updated when new information becomes available and allows particular decay channels to be studied in detail.

The next stage consists of the simulation of the response of the OPAL detector to these generated events. The program used is based around the GEANT package [82] which allows a detector to be defined in terms of sensitive volumes with specific properties. The OPAL interface to GEANT, named GOPAL [83] (GEANT for OPAL), defines the detector using information from the original technical drawings used to build the OPAL detector. Figure 3.3 shows a cut–away view based on the GOPAL simulation. GEANT simulates the interactions between the particles and the detector, detector noise, inefficiencies and detector resolutions and produces a full simulation of the detector readout in the same format as the real data. This means that the Monte Carlo data is identical in structure to the real data, allowing the same reconstruction code and analysis techniques to be used on both the real and simulated data samples.

4.2 Multi–Hadronic Selection

The data sample used in this analysis consists of multi–hadronic $\mathrm{Z}^0 \rightarrow \mathrm{q\overline{q}}$ events selected from the raw data sets discussed above. Multi–hadronic events are selected using the procedure described in [84]. This selection defines quality requirements to select well defined, 'good', tracks and neutral clusters and uses these to select multi–hadronic events.

A 'good' track satisfies the criteria :-

- $N_{hit} \geq 20$, where N_{hit} refers to the total number of track hits in the vertex, jet and z tracking chambers;

- $|d_0| < 2\,\mathrm{cm}$, where $|d_0|$ is the distance of closest approach between the track and the interaction point, in the $r - \phi$ plane;

- $|z_0| < 40\,\mathrm{cm}$, where z_0 is the z coordinate at the point of closest approach of the track to the interaction point, in the $r - \phi$ plane;

- $|p_t| > 0.05\,\mathrm{GeV/c}$, where p_t is the track momentum transverse to the z–axis;

- $|\cos\theta| < 0.995$, where θ is the azimuthal track angle;

- $\chi^2_{r-\phi} < 999$, where $\chi^2_{r-\phi}$ is the χ^2 from the track fitting procedure in $r - \phi$;

- $\chi^2_z < 999$, where χ^2_z is the χ^2 from the track fitting procedure in $r - z$.

For 'good' electromagnetic clusters, the requirements are :-

- $E_{raw} > 0.1\,\mathrm{GeV}$ ($0.2\,\mathrm{GeV}$) in the barrel (endcaps), where E_{raw} is the uncorrected energy of the cluster;

- $N_{blocks} \geq 2$ if the cluster is in the endcaps, where N_{blocks} is the number of adjacent blocks in the cluster.

In order to be selected as a multi–hadron, the event as a whole must satisfy :-

- $N_{tracks} \geq 5$, where N_{tracks} is the number of good tracks;

- $N_{clusters} \geq 7$, where $N_{clusters}$ is the number of good clusters;

- $\Sigma E_{raw}/2E_{beam} \geq 0.10$, where the summation runs over all good clusters;

- an energy imbalance along the beam direction, $\Sigma(E_{raw}\cos\theta)/\Sigma E_{raw} < 0.65$, where the summations run over all good clusters and θ is the polar angle of the cluster.

The charged track and cluster multiplicity requirements are designed to select multi–hadron events, minimising backgrounds from Z^0 decays to lepton pairs. The energy requirements suppress backgrounds from two–photon events, beam interactions with residual gas in the beam pipe and cosmic rays.

The multi–hadronic selection has been measured to have an efficiency of $\sim 98.4\,\%$ [84] with the majority of the inefficiency arising from reduced detector acceptance towards $|\cos\theta\,| = 1$. The main backgrounds are from $\tau^+\tau^-$ and two–photon events, which have been estimated to form $(0.11 \pm 0.03)\,\%$ and $(0.5 \pm 0.02)\,\%$ of the selected multi–hadronic sample respectively [84].

4.2.1 Additional Quality Requirements for b Hadron Decays

In addition to these criteria, tighter selection cuts are also applied which have been optimised for the selection of b hadron decays. All tracks used in the selection of b decays are also required to pass the following requirements :-

- $N_{jet} \geq 20$, where N_{jet} is the number of hits in the jet chamber;
- $p < 65\,\mathrm{GeV/c}$, where p is the track momentum;
- $p_t > 0.15\,\mathrm{GeV/c}$;
- $|\tan\lambda\,| < 100$;
- $\chi^2_{r-\phi} < 100$;
- $\chi^2_z < 100$;

In addition, electromagnetic clusters are required to satisfy,

- Raw energy of cluster $> 0.05\,\mathrm{GeV}$;
- Corrected energy of barrel clusters $> 0.1\,\mathrm{GeV}$;
- Corrected energy of endcap clusters $> 0.2\,\mathrm{GeV}$.

Tracks and clusters passing these selections are hereafter referred to as 'BT quality'. Events are required to have seven BT quality tracks and seven BT quality clusters. The multi–hadronic pre–selection efficiency of these BT event selection criteria has been measured to be $(98.1 \pm 0.5)\,\%$ [85].

4.3 b Hemisphere Tagging

The analysis presented in this thesis requires a sample of multi–hadronic decays enriched with $\mathrm{Z}^0 \to \mathrm{b\overline{b}}$ decays. Such decays are tagged by reconstructing secondary decay vertices significantly separated from the primary interaction point. The relatively long lifetime ($\sim 1.5\,\mathrm{ps}$), high decay charged multiplicity and high mass ($\sim 5\,\mathrm{GeV/c}$) of b hadrons are used to construct an efficient and discriminating vertex tagging variable.

In order to obtain an unbiased sample of b hadron enriched decays, a hemisphere tagging technique is used. The thrust axis (Section 4.3.2) for the event is computed and then using the plane perpendicular to this axis, passing through the centre of OPAL, the event is divided into two 'thrust' hemispheres. The b–tagging algorithm is then applied to each hemisphere separately. The sample of hemispheres opposite a b–tagged hemisphere forms a sample of b hadron decays free from any biases introduced by the b–tagging algorithm.

4.3.1 Jet Finding

In $\mathrm{Z}^0 \to \mathrm{q\overline{q}(g)}$ decays, the primary quarks and gluons fragment forming hadronic jets with directions that closely follow the momentum in the primary parton state. In the absence of any initial state radiation, the Z^0 is produced at rest and therefore the final state particles must have zero net momentum. Therefore, a primary $\mathrm{q\overline{q}}$ pair results in a pair of jets in an approximately back to back configuration, whilst gluon radiation from the primary partons, $\mathrm{q\overline{q}(g)}$, will result in the formation of additional jets.

The cone jet finding algorithm [86, 87] is used to group the charged tracks and unassociated electromagnetic clusters into jet–like topologies. The algorithm defines a jet as a set of particles that have a total energy greater than a cutoff value ϵ and momentum vectors that lie within a cone of half angle R. In this analysis R = 0.55 radians and $\epsilon = 5.0\,\mathrm{GeV}$, which have been optimised for the reconstruction of b jets [87]. Selected events are required to have two or more reconstructed jets in order to be consistent with $Z^0 \to q\overline{q}(g)$ decays.

The cone algorithm has been found to have superior angular resolution for the jet direction when compared to other possible algorithms [87], providing a better measure of the b hadron direction. In addition, the cone jet finder is well suited to analyses requiring all the particles in a jet to share a common origin, such as the reconstruction of secondary decay vertices. The angular nature of the algorithm makes it better suited to assigning all tracks from secondary decays to the same jet, whilst preventing 'stray' tracks from the opposite hemisphere from being included. This leads to improved secondary vertex reconstruction within individual jets.

4.3.2 Thrust Cuts

The thrust [88] of the event, T, is defined as

$$T = \max_{\hat{\mathbf{n}}} \left(\frac{\sum_i |\mathbf{p}_i \cdot \hat{\mathbf{n}}|}{\sum_i |\mathbf{p}_i|} \right) \tag{4.1}$$

where the summation runs over all BT quality tracks and unassociated clusters in the event. The axis $\hat{\mathbf{n}}$ which maximises the thrust value is called the thrust axis. An event with two well collimated jets will have $T \sim 1$, whilst events with additional jets due to the radiation of energetic gluons will have lower values of T, down to 0.5 for an isotropic distribution of tracks.

The hemisphere b–tagging technique relies on the assumption that the b hadrons occupy opposite thrust hemispheres. Therefore, in order to suppress events containing more than two jets, where the b and $\overline{\mathrm{b}}$ quarks are more likely to have been boosted into the same hemisphere, the thrust is required to be greater than 0.8. In addition, the polar angle of the thrust axis, θ_{th}, must satisfy $|\cos\theta_{\mathrm{th}}| < 0.75$. Such a cut ensures that the majority of the event is contained within the central barrel region where the particle tracking is optimal and silicon microvertex detector information is available.

4.3.3 Primary Vertex Reconstruction

The primary e^+e^- interaction vertex is reconstructed on an event by event basis using the BT quality tracks independently for each thrust hemisphere. Reconstructing a separate primary vertex in each hemisphere avoids potential correlations in the b–tagging performance between the hemispheres resulting from sharing a single primary vertex reconstructed using all BT quality tracks in the event [89].

The primary vertex position is calculated using a three–dimensional χ^2 minimisation technique. The BT quality tracks from a given thrust hemisphere are fitted to a common position, with the LEP beamspot position [90] included as a constraint in the fit. The fit is iterated by repeatedly rejecting the track contributing the largest χ^2 until the remaining tracks are all consistent with a single primary vertex, in that they contribute less than 4 to the overall χ^2. If the fit fails to converge in three dimensions then it is repeated using only $r-\phi$ information. If this also fails the primary vertex position and errors are taken from the LEP beamspot position and width.

4.3.4 Secondary Vertex Reconstruction

The use of the cone jet finding algorithm, discussed in Section 4.3.1, ensures that tracks that originate from secondary decays are largely contained within the same jet. This information is used to aid the finding of secondary decay vertices by limiting the reconstruction to tracks within the same jet.

Secondary vertices are reconstructed using a similar three dimensional χ^2 minimisation technique as used for the primary vertex reconstruction. Additional quality constraints are applied to candidate secondary vertex tracks, namely :-

- $p > 0.5\,\mathrm{GeV}$, where p is the track momentum;
- $b_0 < 0.3\,\mathrm{cm}$, where b_0 is the 'impact parameter', the distance of closest approach of the track to the reconstructed hemisphere primary vertex;
- $\sigma_{b_0} < 0.1\,\mathrm{cm}$, where σ_{b_0} is the error on the track impact parameter.

These requirements tend to favour tracks that originate from b hadron decay vertices rather than the primary vertex due to the hard fragmentation of the b quark. Tracks with the largest χ^2 are iteratively removed from the vertex fit until each track contributes less than 4 to the total χ^2.

The decay length, L, is calculated as the length of the vector joining the primary vertex to the secondary vertex, with the constraint that it lies along the jet axis. L is positively signed if the secondary vertex is displaced from the primary vertex in the direction of the jet momentum and negatively signed otherwise. The error on L, denoted σ_L, is determined from the track error matrices and used to construct the decay length significance variable L/σ_L. This variable forms the basis of the vertex tag discussed in the next section.

4.3.5 b Vertex Flavour Tagging

In order to assess the likelihood that a reconstructed secondary vertex resulted from a b hadron decay, various characteristic variables are used. These variables are discussed briefly below; for more details see [14, 91] :-

- $\boldsymbol{N_{\mathrm{s}}}$, the number of tracks in the secondary vertex. The high mass of b hadrons on average give higher multiplicity decays;
- **The decay length $\boldsymbol{L}$**. The longer lifetime of b quarks compared to the lighter quarks means that on average a b hadron will travel further before decaying;

- **The decay length significance L/σ_L.** The ratio of the decay length, L, to the error on the decay length, σ_L, gives a measure of the significance of a large decay length. b hadron decays tend to have not only long decay lengths but also well defined vertices due to the high vertex multiplicity and therefore have will high impact parameter significances;

- **The reduced decay length significance L_R/σ_{L_R}.** The decay length significance of the secondary vertex, re-fitted with the track with the largest impact parameter significance, b_0/σ_{b_0}, removed gives a measure of the vertex robustness. This is because a vertex caused by one mis-measured track with a large impact parameter will tend to give a low vertex significance with that track removed;

- **The critical track discriminant T_D.** This variable represents the probability that a set of tracks with invariant mass greater than the average charm hadron mass is consistent with having originated from the reconstructed secondary vertex.

The information contained within these variables is combined using an artificial neural network [91]. Artificial neural networks provide an automated method for combining the information in a given set of variables in an optimal manner which not only uses the inherent separation power of each variable, but also the correlations between them. A more detailed discussion of the use of artificial neural networks is given in Chapter 5.

The neural network was trained using a sample of Monte Carlo events such that the neural network output, $\mathrm{NN_{btag}}$, represents the probability that the vertex is due to the decay of a b hadron. The b hemisphere tag is constructed by requiring that the hemisphere contains a reconstructed secondary vertex with a b probability greater than a given threshold value. By varying this threshold value the efficiency and purity of the selection can be varied to suit requirements. Figure 4.1 compares the $\mathrm{NN_{btag}}$ distribution obtained in the data to the Monte Carlo, showing good agreement. A cut on the neural network output of $\mathrm{NN_{btag}} > 0.78$ was applied giving a b purity, defined as the fraction of the tagged hemisphere sample that are in true $\mathrm{Z^0} \to \mathrm{b\bar{b}}$ decays, of $\sim 92\,\%$ with the corresponding selection efficiency being around $31\,\%$.

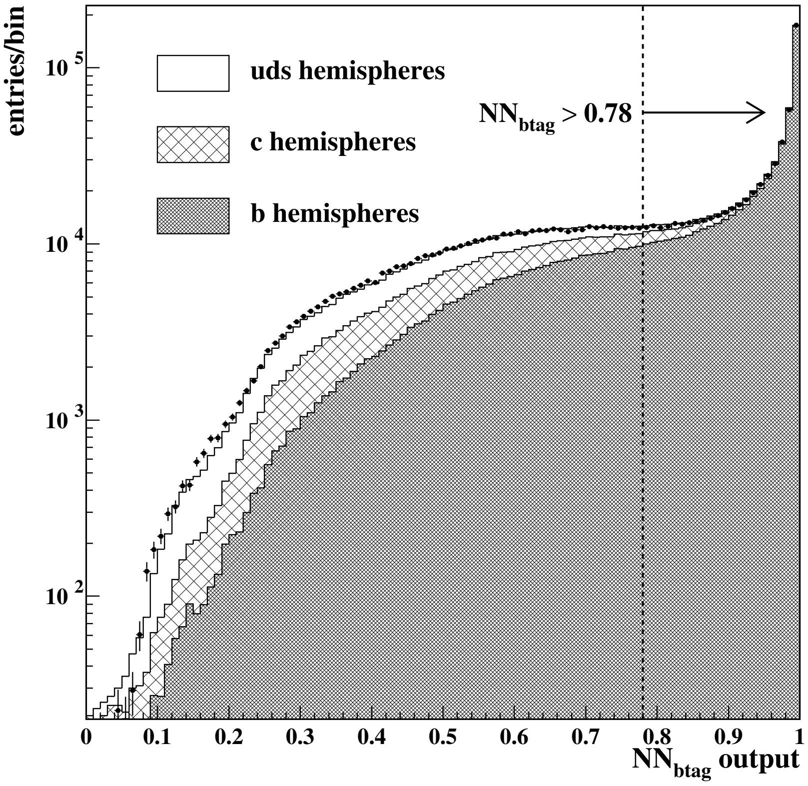

Figure 4.1: *The output distribution for the b–tagging neural network NN_{btag}. The data (points) are compared to the Monte Carlo (solid line). True b vertices are shown by the heavy hatched region, c vertices by the lightly hatched region and uds vertices by the open region. The arrow indicates the cut used to select b decays, $NN_{btag} > 0.78$.*

4.4 Data Samples

Table 4.1 outlines the data samples used in this analysis. A total of 3.35 million multi–hadronic Z^0 decays are selected in the data, of which approximately 2.15 million pass the BT event selection, detector status requirements and thrust cuts. From this sample of events approximately 300 000 b–tagged hemispheres are selected. The detector requirements imposed for electron and muon identification mean that a small fraction of the data b–tagged hemispheres are rejected. The total numbers passing the electron and muon identification criteria are also listed.

Selection	Year	OPAL events	Monte Carlo events		
			5 flavour	$b\overline{b}$	$c\overline{c}$
Multi–hadron	1992	650 428	1 500 000	400 000	400 000
	1993	707 205	1 000 000	275 000	275 000
	1994	1 339 836	4 000 000	3 500 000	1 000 000
	1995	655 807	1 000 000	250 000	250 000
	total	3 353 276	7 500 000	4 425 000	1 925 000
BT + thrust cuts	total	2 150 423	4 606 269	2 788 411	1 230 172
		OPAL hemispheres	Monte Carlo hemispheres		
			5 flavour	$b\overline{b}$	$c\overline{c}$
b–tagged	total	303 366	699 108	1 835 956	48 616
b–tagged + e ID	total	301 303			
b–tagged + μ ID	total	302 577			

Table 4.1: *A summary of the multi–hadronic data and Monte Carlo samples used in this thesis. The top section shows the number of events passing the multi–hadron selection and the refined BT selection combined with the thrust cuts. The total number of hemispheres b–tagged and satisfying the electron and muon identification criteria are also shown.*

A total of 7.5 million multi–hadronic Monte Carlo events are used. These samples contain all five quark flavours (u, d, s, c, and b) kinematically accessible in $Z^0 \to q\overline{q}$ decays. In addition, dedicated samples of 4.425 and 1.925 million primary $b\overline{b}$ and $c\overline{c}$ heavy flavour hadronic decays are also used.

4.5 b Tagged Sample Purity

In order to extract the true number of b hadron decays in the b–tagged sample, the b purity of the sample must be determined. The purity, P_b, defined as the fraction of the b–tagged hemisphere sample that originate from true $Z^0 \to b\overline{b}$ decays, is extracted from the data itself using a double tagging technique in order to minimise systematic uncertainties.

4.5.1 Method

The double tagging technique exploits the independent hemisphere tagging method, using the additional constraint that both hemispheres must necessarily have the same primary flavour. The number of hemispheres passing the b–flavour tagging selection criteria ($N_{\rm t}$) as well as the number of events where both hemispheres are selected ($N_{\rm tt}$) are counted in the data. With the b–tagging efficiencies for the different flavours given by $\eta_{\rm b}$, $\eta_{\rm c}$ and $\eta_{\rm uds}$, the expected numbers can be expressed as ;

$$N_{\rm t} = 2N_{\rm MH}\left(R_{\rm b}\eta_{\rm b} + R_{\rm c}\eta_{\rm c} + R_{\rm uds}\eta_{\rm uds}\right), \tag{4.2}$$

$$N_{\rm tt} = N_{\rm MH}\left(C_{\rm b}R_{\rm b}\eta_{\rm b}^2 + C_{\rm c}R_{\rm c}\eta_{\rm c}^2 + C_{\rm uds}R_{\rm uds}\eta_{\rm uds}^2\right), \tag{4.3}$$

where $N_{\rm MH}$ represents the number of events that passed the multi–hadronic event selection and $R_{\rm uds} \equiv (1 - R_{\rm b} - R_{\rm c})$.

The values of $R_{\rm b}$ and $R_{\rm c}$, the fraction of $\rm Z^0$ events decaying into $\rm b\overline{b}$ and $\rm c\overline{c}$ pairs respectively, are taken from experimental results [3]. The hemisphere correlation coefficients $C_{\rm q}$, where q represents the primary quark flavour, are given by the ratio of the efficiency for tagging both hemispheres in a $\rm q\overline{q}$ event, $\eta_{\rm q\overline{q}}$, over the square of the efficiency for tagging one hemisphere containing that specific flavour, namely, $C_{\rm q} = \eta_{\rm q\overline{q}}/\eta_{\rm q}^2$. Deviations of $C_{\rm q}$ from unity account for the fact that the tagging between the two hemispheres is not completely independent and a small efficiency correlation exist between the hemispheres. The correlation for b events, $C_{\rm b}$, is taken from the Monte Carlo while $C_{\rm c}$ and $C_{\rm uds}$, which have negligible impact on the b purity measurement, are assumed to be unity. The values for $\eta_{\rm c}$ and $\eta_{\rm uds}$ are taken from the Monte Carlo.

The form of Equations 4.2 and 4.3 for $N_{\rm t}$ and $N_{\rm tt}$ makes their physical origin clear; they are simply the sum of the true numbers for each flavour of event occurring in the data, weighted by the corresponding single or double tag efficiency. The equations can however, be trivially re–expressed in terms of the b purity $P_{\rm b}$, using the definition

$$P_{\rm b} = \frac{2N_{\rm MH}R_{\rm b}\eta_{\rm b}}{N_{\rm t}} \tag{4.4}$$

which gives,

$$N_{\mathrm{t}} = \left(\frac{2N_{\mathrm{MH}}}{1-P_{\mathrm{b}}}\right)(R_{\mathrm{c}}\eta_{\mathrm{c}} + R_{\mathrm{uds}}\eta_{\mathrm{uds}}), \tag{4.5}$$

$$N_{\mathrm{tt}} = \frac{N_{\mathrm{MH}}C_{\mathrm{b}}^2}{R_{\mathrm{b}}}\frac{P_{\mathrm{b}}^2}{(1-P_{\mathrm{b}})^2}(R_{\mathrm{c}}\eta_{\mathrm{c}} + R_{\mathrm{uds}}\eta_{\mathrm{uds}})^2 + \left(C_{\mathrm{c}}R_{\mathrm{c}}\eta_{\mathrm{c}}^2 + C_{\mathrm{uds}}R_{\mathrm{uds}}\eta_{\mathrm{uds}}^2\right). \tag{4.6}$$

Whilst the b purity can in principle be determined from the direct solution of either of Equations 4.5 or 4.6, the value of P_{b} is extracted in practise by maximising the log–likelihood of both equations simultaneously in order to obtain the maximum statistical sensitivity. The overall log likelihood can be expressed as the sum of the log likelihoods for N_{t} and N_{tt} (see Appendix A for details) ;

$$\begin{aligned} \ln \mathcal{L}_{total} &= \ln \mathcal{L}_{\mathrm{t}} \quad + \quad \ln \mathcal{L}_{\mathrm{tt}} \\ &= \left(N_{\mathrm{t}}^{\mathrm{DATA}} \ln N_{\mathrm{t}}^{\mathrm{exp}} - N_{\mathrm{t}}^{\mathrm{exp}}\right) \quad + \quad \left(N_{\mathrm{tt}}^{\mathrm{DATA}} \ln N_{\mathrm{tt}}^{\mathrm{exp}} - N_{\mathrm{tt}}^{\mathrm{exp}}\right) \end{aligned} \tag{4.7}$$

where $N_{\mathrm{t}}^{\mathrm{exp}}$ and $N_{\mathrm{tt}}^{\mathrm{exp}}$ are the number of expected single b–tagged hemispheres and double b–tagged events for a given purity, and $N_{\mathrm{t}}^{\mathrm{DATA}}$ and $N_{\mathrm{tt}}^{\mathrm{DATA}}$ are the corresponding numbers selected in the data. Equation 4.7 was maximised using MINUIT [92], which is a software package designed to find the minima of multi–parameter functions and to perform comprehensive error analyses. From a fit to the full data sample, the hemisphere b–tagging purity was measured to be $(91.901 \pm 0.016)\,\%$ where the error is purely statistical.

4.5.2 Systematic Uncertainties

Extensive studies have been presented in a previous OPAL analysis on the systematic differences between data and Monte Carlo for C_{b}, η_{c} and η_{uds} [14]. These same studies were used in this analysis, where similar event selection and b–tagging algorithms are used to assign the systematic uncertainty on P_{b}.

Input parameter	Value	δP_{b} / %
R_{c}	0.177 ± 0.008	± 0.19
R_{b}	0.2169 ± 0.0012	± 0.01
η_{c}	0.0209 ± 0.0002 (MC stat.) $\pm\, 0.0014$ (syst.)	± 0.34
η_{uds}	0.0034 ± 0.0000 (MC stat.) $\pm\, 0.0003$ (syst.)	± 0.22
C_{b}	1.0493 ± 0.0052 (MC stat.) $\pm\, 0.0052$ (syst.)	± 0.01
Total		± 0.45

Table 4.2: *The contributions to the systematic uncertainty on P_b for each input parameter used to measure the b purity in the data after b–tagging. For the input parameters taken from the Monte Carlo, the Monte Carlo statistical and systematic uncertainties are shown separately.*

Table 4.2 shows the individual contributions from each input parameter and the overall systematic error on P_{b}. The dominant modelling uncertainties arise from the Monte Carlo modelling errors on the light flavour efficiencies η_{c} and η_{uds}. In evaluating the systematic errors on these efficiencies the following sources of uncertainty were considered:

Detector resolution : The tracking resolution in the Monte Carlo was varied by applying a multiplicative scaling factor to the difference between the true and reconstructed track parameters for all charged tracks. Independent variations of $\pm 10\,\%$ on the $r-\phi$ and $r-z$ parameters were used to assign the systematic error. Systematic uncertainties due to the charged track reconstruction efficiency and mis–alignment of the silicon microvertex detector are also included, as discussed in detail in [14].

Heavy quark production from gluon splitting : The production of heavy quark pairs via the processes $\mathrm{g} \to \mathrm{b\bar{b}}$ and $\mathrm{g} \to \mathrm{c\bar{c}}$ increases the tagging efficiency in charm and light quark events. The rates of gluon splitting events were adjusted according to experimental results as discussed in [14] and the uncertainties used to evaluate the corresponding systematic errors.

Charm physics : In addition to the sources listed above, the efficiency for tagging charm events, η_{c}, depends on various physical quantities in charm events:

- **Charm quark fragmentation :** The charm tagging efficiency increases with the scaled energy x_E of the weakly decaying charm hadron. The Monte Carlo simulations are tuned to correspond to the experimental measurements [14] for the mean scaled energy $\langle x_E \rangle_{\mathrm{c}}$ using the fragmentation functions of Peterson *et al.*, Collins and Spiller, Kartvelishvili *et al.* and the LUND group (Section 2.6.1). The experimental uncertainties on $\langle x_E \rangle_{\mathrm{c}}$ and the observed variations with the different fragmentation functions are used to assign the associated systematic error on η_{c};

- **Charm hadron production fractions :** Due to the differing lifetimes and decay modes for each charm hadron species, the vertex tagging efficiency in $\mathrm{c\bar{c}}$ events depends on the mixture of weakly decaying charm hadrons. The relative production fractions of $\mathrm{D}^{\pm}$, D^0, $\mathrm{D_s}$ and charm baryons are varied according to the experimentally measured production fractions [14] and used to assign a systematic error on η_{c};

- **Charm hadron lifetimes :** The secondary vertex decay lengths, L, and therefore the tagging efficiencies depend upon the lifetimes of the decaying hadrons. The lifetimes of the weakly decaying charm hadrons were independently varied according to experimental results [3] and used to assign a systematic uncertainty on η_{c};

- **Charged and neutral decay multiplicities :** The charged track multiplicity serves as one of the inputs to the b–tagging neural network and therefore affects the tagging efficiency in $\mathrm{c\bar{c}}$ events. The neutral decay multiplicities also affect the tagging efficiencies since an increased number of neutral particles results in less energy and transverse momentum being available for charged decay products. The average charged and neutral multiplicities in charm decays are varied according to experimental measurements [14] and used to assign a systematic uncertainty on η_{c};

- **K^0 and hyperon production** The branching fractions for $\mathrm{D} \to \mathrm{K}^0, \overline{\mathrm{K}^0}$ and $\Lambda_c^+ \to \Lambda$, and the total production rates for K^0, Λ and other weakly decaying hyperons were varied according to experimental measurements [14]. A systematic error on η_c was assigned according to the observed variations.

$\mathbf{b\overline{b}}$ efficiency correlation uncertainties : The b–tagging efficiency correlation coefficient C_b is determined from the Monte Carlo simulation. These correlations arise from three classes of effects: (1) kinematic correlations due to final state gluon radiation, (2) geometrical correlations due to detector non–uniformities and (3) correlations resulting from the primary vertex determination. A detailed discussion of the Monte Carlo simulation of these effects is given in [14]. Due to the relative sizes of the N_t and N_{tt} samples, where $N_t \gg N_{tt}$, the majority of the statistical power in the likelihood fit for P_b resides in the single tag Equation 4.5. Since Equation 4.5 is independent of the correlation coefficients C_q, the error on C_b therefore results in a negligible uncertainty on the measured b purity.

R_b and R_c : The values for R_b and R_c are taken as the current world averages [3] with the corresponding systematic uncertainty on P_b evaluated by varying the parameters within the experimental errors.

4.5.2.1 Summary of P_b Determination

Using a double tagging technique, the b purity of the b–tagged data sample has been measured from the OPAL data itself. Adding all sources of systematic error in quadrature, the b–tagging purity is measured to be,

$$P_b = (91.90 \pm 0.02 \text{ (stat.)} \pm 0.45 \text{ (syst.)})\,\%$$

corresponding to a b–tagging efficiency of around 30 %.

Chapter 5

Electron and Muon Identification

This chapter describes the techniques used to identify candidate electron and muon tracks in multi–hadronic events, where an improved algorithm for electron identification is developed. The efficiencies for identifying leptons from direct decays, $\mathrm{b} \to \ell$, and cascade decays, $\mathrm{b} \to \mathrm{c} \to \ell$, are taken from the Monte Carlo simulations and a discussion of the systematic uncertainties associated with these efficiencies is presented.

5.1 Electron Identification

In order to efficiently identify electron candidates within multi–hadronic events, it is necessary to combine information from a number of different sources. Making optimal use of all the available information requires a sophisticated algorithm, capable of multi–dimensional discrimination. An artificial neural network is used, since it provides one of the most powerful of such discrimination tools. In the following sections the various physics quantities used in electron identification are discussed.

5.1.1 Preliminary Selections

In addition to the general track selection criteria discussed in Section 4.2.1, candidate electron tracks are first required to pass a preliminary set of selection cuts.

- Candidate tracks are required to have a minimum momentum of 2 GeV/c.
- Candidate tracks are required to have a minimum of 40 jet chamber hits usable for the determination of the specific energy loss (discussed in Section 5.1.3).

These criteria favour electrons from the weak decays of heavy hadrons, such as direct and cascade decays, which tend to form well defined, high momentum tracks.

Candidates passing these criteria are then passed to the main electron identification algorithm, which is described in detail in the following sections.

5.1.2 Input Variable Selection Criteria

The selection of variables to be used as inputs to the electron identification neural network is motivated by two considerations :-

- The performance of the electron identification defined in terms of the efficiency at selecting true electrons compared to the electron purity of the selected sample;
- The systematic uncertainty resulting from determining the electron identification performance from the Monte Carlo simulations.

These considerations may conflict; an optimal performance neural network requires the use of all possible sources of information regardless of how well they are modelled in the Monte Carlo. In the analysis presented in this thesis however, the minimisation of the efficiency systematic errors is important. In order to calculate the true number of $\mathrm{b} \to \mathrm{e}$ and $\mathrm{b} \to \mathrm{c} \to \mathrm{e}$ decays that occurred in the data, the selected samples need to be corrected to account for the selection efficiencies. The size of the data sample is sufficient that for any reasonably efficient set of selection criteria, the resulting statistical errors are small compared to the systematic uncertainties associated with determining these efficiencies from the Monte Carlo. In the following sections, potential inputs are discussed in relation to this specific requirement.

5.1.3 Specific Ionisation

Charged particles traversing a given medium will lose energy by ionisation along their path. The specific ionisation energy loss, $\mathrm{d}E/\mathrm{d}x$, is a function of the velocity of the particle and is essentially independent of the particle mass. The OPAL jet chamber measures both the hit positions and the amount of charge deposited by tracks traversing the chamber, allowing the particle $\mathrm{d}E/\mathrm{d}x$ to be determined. By combining velocity information in the form of $\mathrm{d}E/\mathrm{d}x$ measurements with the particle momentum determined from the track curvature due to the magnetic field, it is possible to estimate the mass of the particle and hence determine its identity [65].

The average specific energy loss of ionising particles can be described by the Bethe–Bloch equation [3, 93] as a function of the particle velocity β,

$$\frac{\mathrm{d}E}{\mathrm{d}x} = -4\pi N_A r_e^2 m_e c^2 z_e^2 Z \frac{1}{A\beta^2}\left(\frac{1}{2}\ln\frac{2m_e c^2\beta^2\gamma^2 T_{max}}{I^2} - \beta^2 - \frac{\delta}{2}\right), \tag{5.1}$$

where T_{max} is the maximum kinetic energy which can be imparted to a free electron in a single collision and z_e is the charge of the incident particle. Z and A are respectively, the atomic number and atomic mass of the medium. N_A is the Avogadro number, r_e is the classical electron radius and m_e is the electron mass. I is the mean ionising potential whilst δ is a density function which takes into account polarisation in the gas.

Figure 5.1 shows $\mathrm{d}E/\mathrm{d}x$ measurements obtained with the OPAL jet chamber [65]. The solid lines show the predicted curves for a given particle species and the points are the measured data.

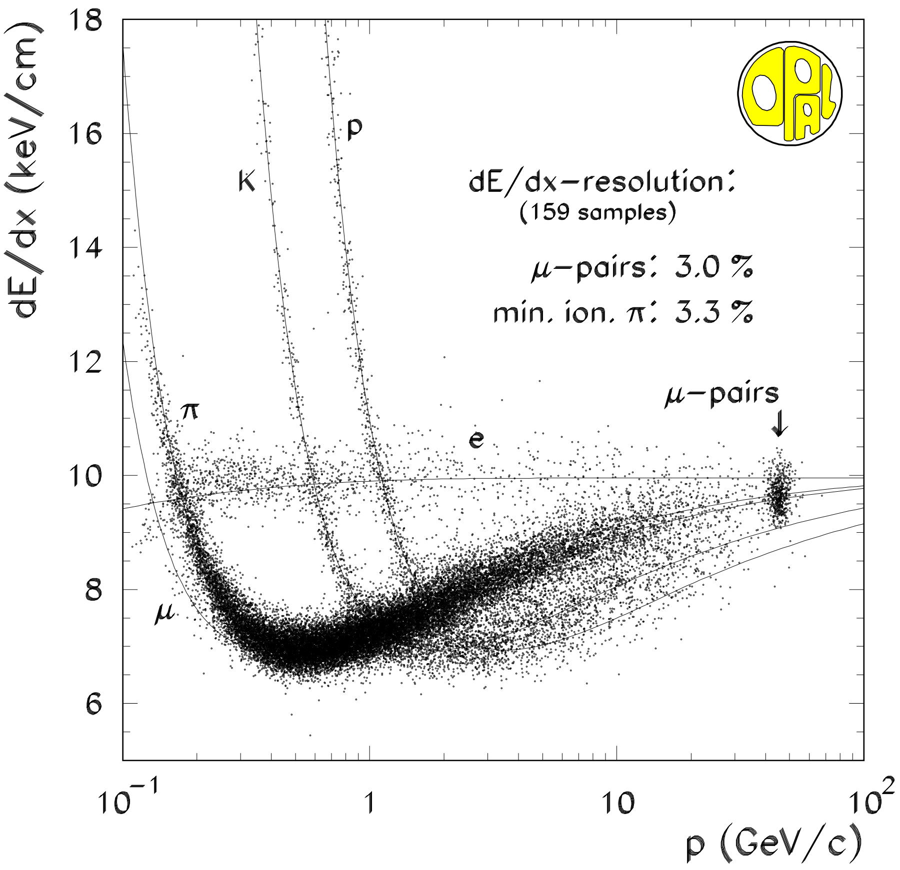

Figure 5.1: *The dE/dx distributions [65]. The points show the data points for multi–hadronic tracks and muon pairs. The Bethe–Bloch predictions for different particle species are shown by the lines.*

The curves show three distinctive regions :-

- **The non–relativistic region**, at low velocities, where the dE/dx curves show a characteristic fall with $1/\beta^2$;
- **The relativistic rise region**, at medium velocities, where dE/dx rises logarithmically as $\ln(\beta^2)$;
- **The Fermi Plateau region**, at high velocities where dE/dx saturates.

The dE/dx curves for different particle species cross at various points, making the separation of these two species difficult in particular regions of momentum. In addition, at high momenta the curves converge to a common value, such that particle species cannot be distinguished using $\mathrm{d}E/\mathrm{d}x$ information. In terms of optimising particle identification capabilities, the figure of merit which needs to be maximised is not the $\mathrm{d}E/\mathrm{d}x$ resolution but the separation power between different species, defined as;

$$S_{\mathrm{d}E/\mathrm{d}x} = \frac{\mathrm{d}E/\mathrm{d}x_{\mathrm{A}} - \mathrm{d}E/\mathrm{d}x_{\mathrm{B}}}{\sigma(\mathrm{d}E/\mathrm{d}x_{\mathrm{A}}) \oplus \sigma(\mathrm{d}E/\mathrm{d}x_{\mathrm{B}})} \tag{5.2}$$

where $\sigma(\mathrm{d}E/\mathrm{d}x)$ is the measurement error on the specific ionisation $\mathrm{d}E/\mathrm{d}x$, and A and B represent two different particle species. The symbol $\oplus$ indicates the quadratic sum of the errors for species A and B.

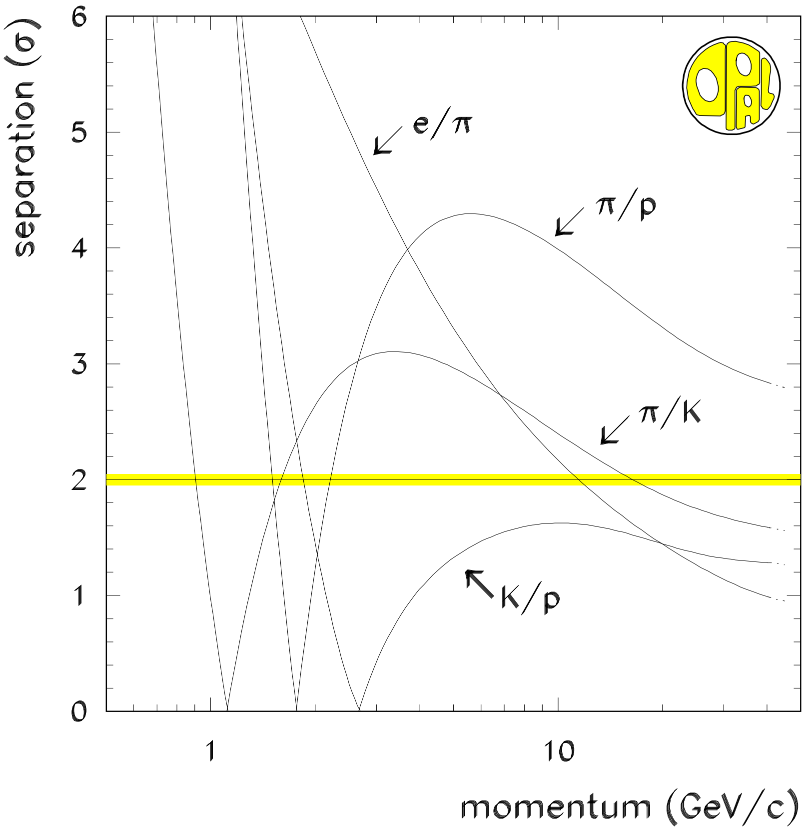

Figure 5.2: *The dE/dx separation power for various particle species in multi–hadronic events, as a function of momentum.*

Figure 5.2 shows the $\mathrm{d}E/\mathrm{d}x$ separation power, $S_{\mathrm{d}E/\mathrm{d}x}$, between given particle species as a function of their momentum. For electron identification through $\mathrm{d}E/\mathrm{d}x$ measurements, pion – electron separation is of prime importance since pions form the main source of background.

The raw value of $\mathrm{d}E/\mathrm{d}x$ measured in the jet chamber is dependent on many of the physical parameters of the chamber. Changes in the gas density due to variations in leakage and leakage compensation for example, will result in gas gain variations of $10-20\,\%$ and therefore similar changes in the raw $\mathrm{d}E/\mathrm{d}x$ values. The jet chamber is calibrated [65, 94] by taking these variations into account in the Bethe–Bloch expectation for $\mathrm{d}E/\mathrm{d}x$. As a consequence, the appropriate parameter used for $\mathrm{d}E/\mathrm{d}x$ particle identification is not the raw value of $\mathrm{d}E/\mathrm{d}x$, but the normalised value defined as,

$$\mathrm{d}E/\mathrm{d}x|_{norm} = \frac{\mathrm{d}E/\mathrm{d}x^{measured} - \mathrm{d}E/\mathrm{d}x^{expected}}{\sigma(\mathrm{d}E/\mathrm{d}x^{expected})} \tag{5.3}$$

where $\mathrm{d}E/\mathrm{d}x^{measured}$ is the raw measured value and $\mathrm{d}E/\mathrm{d}x^{expected}$ the expected value according to the Bethe–Bloch equation, for a particular particle species.

The $\mathrm{d}E/\mathrm{d}x|_{norm}$ is calculated by minimising the χ^2 function

$$\chi^2 = \left(\frac{\mathrm{d}E/\mathrm{d}x^{measured} - \mathrm{d}E/\mathrm{d}x^{expected}}{\sigma(\mathrm{d}E/\mathrm{d}x^{expected})}\right)^2 + \left(\frac{p^{measured} - p^{expected}}{\sigma(p^{expected})}\right)^2 \tag{5.4}$$

where,

$$\sigma(\mathrm{d}E/\mathrm{d}x^{expected}) = \sigma(\mathrm{d}E/\mathrm{d}x^{measured}) \cdot \left(\frac{\mathrm{d}E/\mathrm{d}x^{expected}}{\mathrm{d}E/\mathrm{d}x^{measured}}\right), \tag{5.5}$$

$$\sigma(p^{expected}) = \sigma(p^{measured}) \cdot \left(\frac{p^{expected}}{p^{measured}}\right). \tag{5.6}$$

The χ^2 function is minimised with respect to both $\mathrm{d}E/\mathrm{d}x^{expected}$ and $p^{expected}$ simultaneously according to the Bethe–Bloch equation (5.1) under the hypothesis that the particle is of a particular species. The $\mathrm{d}E/\mathrm{d}x$ values for true particles of the given species will be distributed about the expected values, giving a Gaussian $\mathrm{d}E/\mathrm{d}x|_{norm}$ distribution

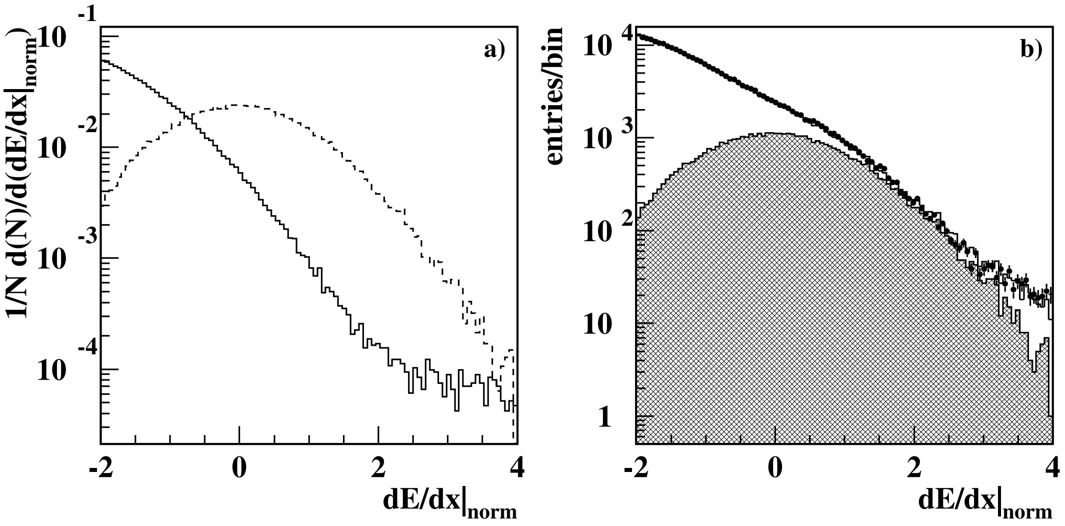

Figure 5.3: *The $dE/dx|_{norm}$ distribution under the electron hypothesis. Figure a) compares the normalised distribution for electrons (dashed) to all other particles (solid) in the Monte Carlo. In Figure b) the data (points) are compared to the Monte Carlo predictions (solid line). The true electron contribution to the Monte Carlo is shown by the hatched region.*

of unit width, centered at zero. Other particles species will cluster away from zero.

Figures 5.3a and 5.3b show the $\mathrm{d}E/\mathrm{d}x|_{norm}$ distributions for tracks in multi–hadronic events, under the electron hypothesis. In Figure 5.3a the distributions normalised to unit area are compared for electrons (dashed line) to all other particles (solid line) in the Monte Carlo. As expected, true electrons form a Gaussian distribution centred at zero, with the remaining background tracks clustering below zero. In Figure 5.3b the inclusive Monte Carlo sample is compared to the data, showing good agreement.

The error on the raw $\mathrm{d}E/\mathrm{d}x$ value, $\sigma(\mathrm{d}E/\mathrm{d}x)$, is derived from the number of $\mathrm{d}E/\mathrm{d}x$ hits, the effective charge seen by the track in the jet chamber, the pathlength of the track within a cell and the error on the track polar angle θ. This variable is less dependent on the physical parameters of the jet chamber and is therefore more stable than the raw $\mathrm{d}E/\mathrm{d}x$ value. The $\sigma(\mathrm{d}E/\mathrm{d}x)$ distribution also holds discriminatory information

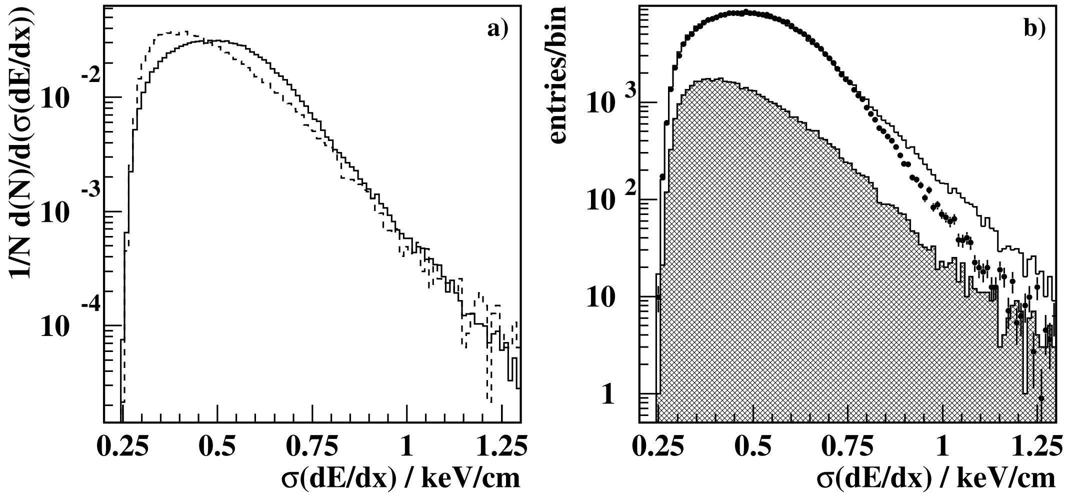

Figure 5.4: *The $\sigma(dE/dx)$ distributions. Figure a) compares the normalised distribution for electrons (dashed) to all other particles (solid) in the Monte Carlo. In Figure b) the data (points) are compared to the Monte Carlo predictions (solid line). The true electron contribution to the Monte Carlo is shown by the hatched region.*

for electron tracks, as shown in Figure 5.4a. Electrons from the decay of short lived heavy hadrons tend to have larger momenta than fragmentation tracks and thus tend to produce better defined tracks, which in turn leads to more hits usable for $\mathrm{d}E/\mathrm{d}x$ measurements and hence a smaller $\mathrm{d}E/\mathrm{d}x$ error. For these reasons $\sigma(\mathrm{d}E/\mathrm{d}x)$ is also a suitable parameter for use in electron identification.

Figure 5.4b compares the data distribution for $\sigma(\mathrm{d}E/\mathrm{d}x)$ to the Monte Carlo. A systematic difference between the data and the Monte Carlo can be seen for tracks with large $\mathrm{d}E/\mathrm{d}x$ errors, where the Monte Carlo over–estimates the number of such tracks. The systematic uncertainties on the Monte Carlo estimate of the performance of the electron selection resulting from this, and all other discrepancies in the electron identification variables described in the proceeding sections, are discussed in Section 5.3.

5.1.4 Electromagnetic Calorimeter Information

Information from the electromagnetic calorimeters can also be used to identify electron candidates. An electron will deposit most of its energy in the electromagnetic calorimeters, unlike hadronic particles which interact less with the lead–glass medium. This can be quantified using the variable E/p, the ratio of the electromagnetic energy associated to a track, to the track momentum measured in the jet chamber. For energies greater than a few GeV the electron mass is negligible in comparison to its energy and so the track momentum (in GeV/c) is approximately equal to its energy (in GeV). Electrons will therefore tend to have E/p values close to one whilst the hadronic backgrounds cluster towards zero. Hadronic showers also tend to be broader than electromagnetic showers and hadronic backgrounds can therefore be further suppressed by using only the energy located close to the extrapolated track position at the electromagnetic calorimeter.

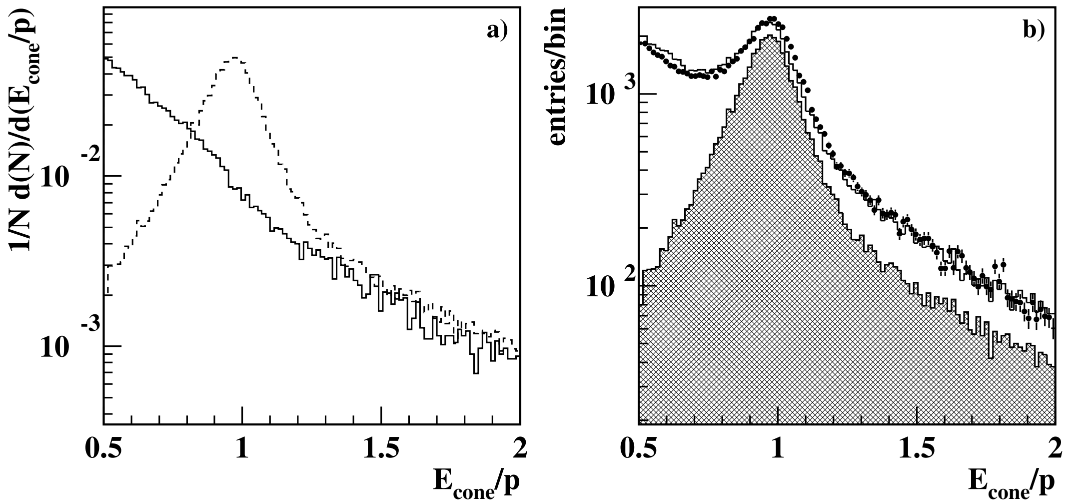

Figure 5.5: *The E_{cone}/p distributions. Figure a) compares the normalised distributions for electrons (dashed) to all other particles (solid) in the Monte Carlo. In Figure b) the data (points) are compared to the Monte Carlo predictions (solid line). The true electron contribution to the Monte Carlo is shown by the hatched region.*

Experimentally, the electromagnetic energy associated to the track is determined by defining a cone around the track direction with a half–angle of 30 mrad. The cone size was optimised in the Monte Carlo simulations so as to fully contain the electron shower whilst rejecting as much of the residual background hadronic energy as possible. The cone is then extrapolated to the electromagnetic calorimeter surface, forming an oval region. Blocks with their centres within this region and with an energy deposition above a given background threshold level are summed to give an estimate of the track energy, E_{cone}. Figure 5.5 shows the E_{cone}/p distributions for tracks in multi–hadronic events. The true electron contribution forms a peak at one whilst the backgrounds cluster towards zero.

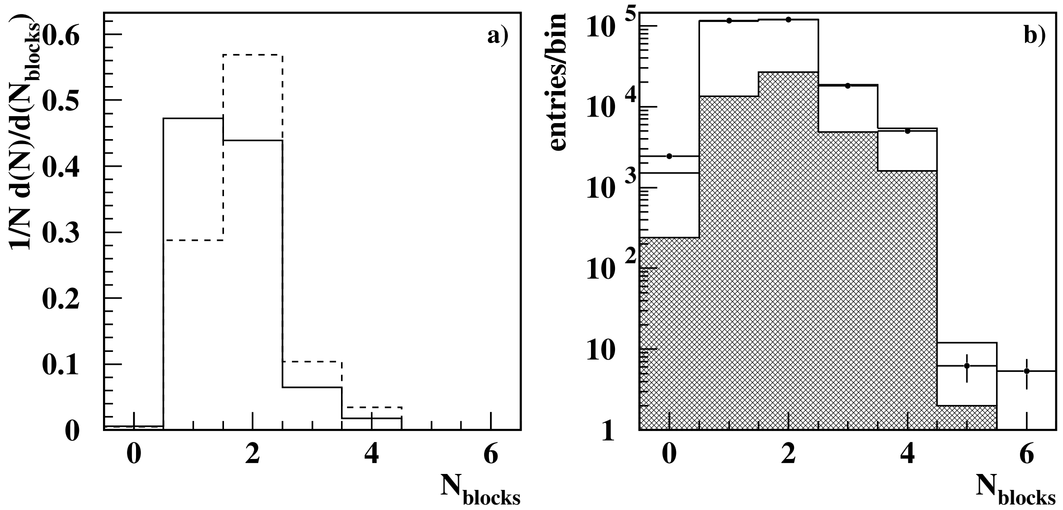

Figure 5.6: *The distributions for N_{blocks}, the number of electromagnetic calorimeter blocks used in the E_{cone} calculation. Figure a) compares the normalised distributions for electrons (dashed) to all other particles (solid) in the Monte Carlo. In Figure b) the data (points) are compared to the Monte Carlo predictions (solid line). The true electron contribution to the Monte Carlo is shown by the hatched region.*

The number of blocks used to calculate E_{cone}/p, termed N_{blocks}, can also be used as a discriminating variable. Figure 5.6a compares the N_{blocks} distribution for electrons to that obtained for all other tracks. Electromagnetic showers are narrow and therefore tend to deposit their energy in only a few blocks. Hadronic showers are less likely to shower in the electromagnetic calorimeters and therefore on average only deposit a small fraction of their total energy. This means that hadronic showers in the electromagnetic calorimeters are less likely to be reconstructed and therefore tend to involve a smaller number of blocks.

5.1.5 Track Momentum

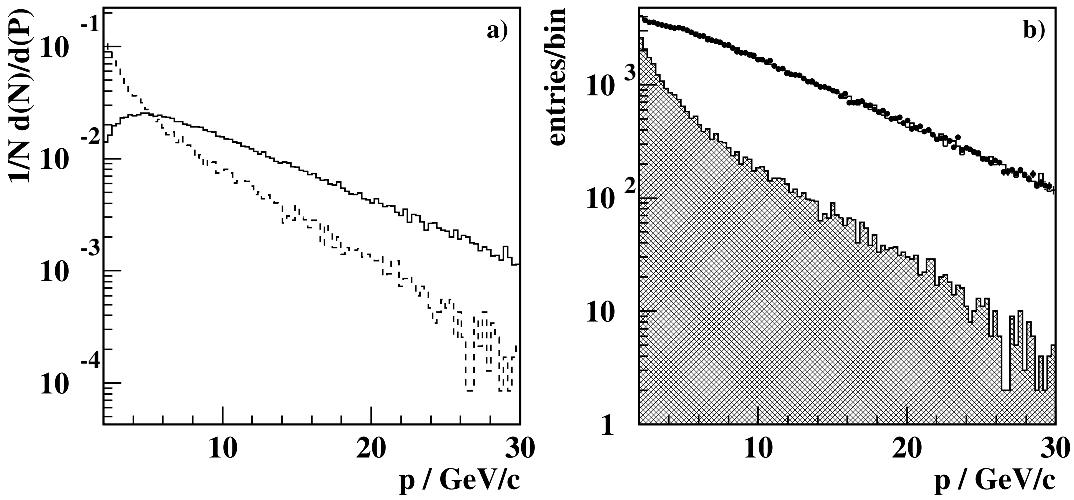

Figure 5.7: *The distributions of the track momentum p. Figure a) compares the distributions for electrons (dashed) to all other particles (solid) in the Monte Carlo. In Figure b) the data (points) are compared to the Monte Carlo predictions (solid line). The true electron contribution to the Monte Carlo is shown by the hatched region.*

The distributions for the track momentum are shown in Figure 5.7. The main benefit from including the momentum in the network inputs results not from its intrinsic discrimination power, but from the correlations it provides with other variables. The discrimination power of the $\mathrm{d}E/\mathrm{d}x|_{norm}$ variable depends strongly on the track momentum, providing the best separation for lower momentum tracks (Figure 5.2). Both the track momentum and electromagnetic calorimeter resolutions improve with increasing momentum and therefore the discrimination power of the E_{cone}/p variable improves with increasing momentum. Including the track momentum as an additional input variable allows the neural network to define the best combination of these variables at all momenta and thus improves the overall network performance.

5.1.6 Track Azimuthal Angle

The track azimuthal angle θ holds information on the region of the detector through which the track traversed. The precision of the track $\mathrm{d}E/\mathrm{d}x$ value depends on the number of central tracking chamber hits used in its determination. For tracks within $|\cos\theta| < 0.73$ all 159 sense wires are available. For increasing $|\cos\theta|$ this number decreases and therefore so does the precision on $\mathrm{d}E/\mathrm{d}x$. The resolution of the track momentum also degrades with decreasing number of tracking hits.

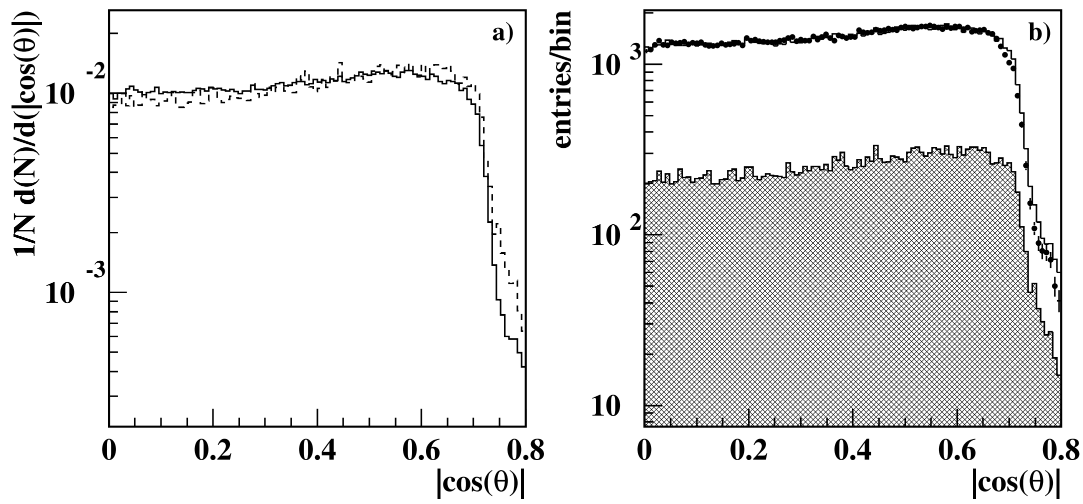

Figure 5.8: *The distributions for* $|\cos\theta|$. *Figure a) compares the distributions for electrons (dashed) to all other particles (solid) in the Monte Carlo. In Figure b) the data (points) are compared to the Monte Carlo predictions (solid line). The true electron contribution to the Monte Carlo is shown by the hatched region.*

The amount of material the track has to traverse prior to the calorimeters also varies with θ. The increased probability of shower initiation in this additional material leads to a degradation of the energy resolution of the calorimeters. These effects can be taken into account by including $|\cos\theta|$ as an additional input variable, the distributions for which are shown in Figure 5.8. Using the modulus of $\cos\theta$ prevents any forward–backward asymmetries in the detector configuration affecting the electron identification.

5.1.7 Track–Cluster Matching Variables

During the event reconstruction charged tracks are associated with electromagnetic clusters, as described in Section 3.7. The quality of these associations can be characterised using the angular matching variables :-

- $\Delta\theta = \theta_{track} - \theta_{cluster}$, the difference in θ between the extrapolated track position at the electromagnetic calorimeter and its associated cluster;
- $\Delta\phi = |\phi_{track} - \phi_{cluster}|$, the absolute difference in ϕ between the extrapolated track position at the electromagnetic calorimeter and its associated cluster.

The distributions for these variables are shown Figure 5.9. Electrons correctly associated with their electromagnetic clusters tend to give better matches than that obtained with hadronic showers or accidental associations and therefore these variables can also be used in identifying electrons.

5.1.8 Artificial Neural Networks

When analysing experimental data a standard procedure is to place various selection cuts on kinematic variables in order to single out desired features. Defining the optimum cuts for a large set of correlated variables can be problematic. Artificial neural networks provide a mechanism for defining such a selection procedure which, with the correct

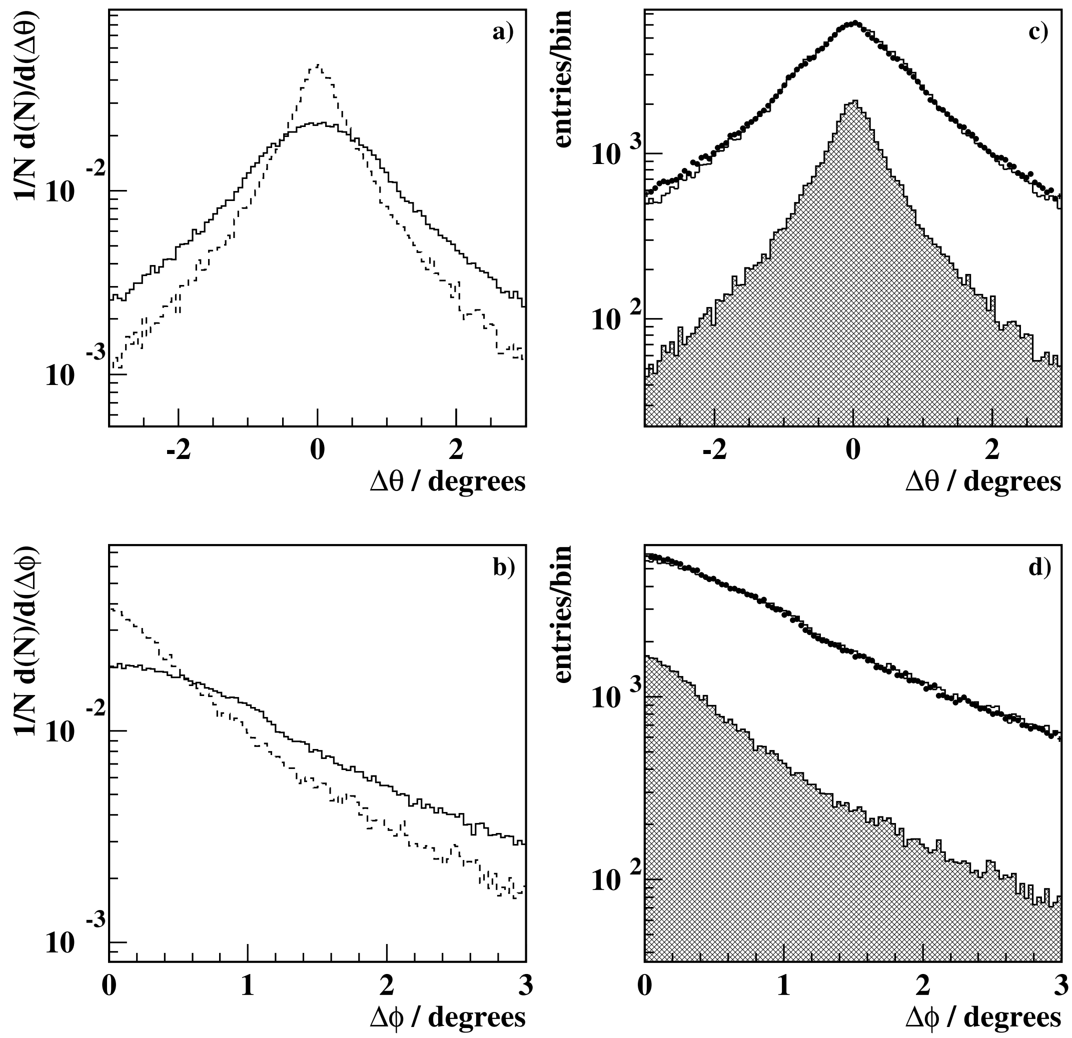

Figure 5.9: *The track–cluster matching variables $\Delta\theta$ and $\Delta\phi$. Figures a) and b) compare the normalised distributions for electrons (dashed) to all other particles (solid) in the Monte Carlo. In figures c) and d) the data (points) are compared to the Monte Carlo predictions (solid line). The true electron contribution to the Monte Carlo is shown by the hatched region.*

training, is able to extract the maximum possible information from a given set of input variables.

In the following sections a basic introduction to the theory of neural networks is presented, together with a description of the training procedure used for the electron identification network. Finally, a discussion of the reliability of the Monte Carlo simulation in terms of the efficiency and purity of the electron selection is given.

5.1.8.1 An Introduction to the Theory of Neural Networks

Artificial Neural Networks (ANN) are computation models inspired by the structure of biological neural systems. The networks discussed below are based on those produced using the JETNET [95] package and are specific to pattern recognition applications. A more detailed introduction to the theory and applications of artificial neural networks can be found in [96, 97].

The basic computational entities of the network are the nodes, which can take real values within a given interval $\{-1, 1\}$ (or $\{0, 1\}$). Information is passed between the nodes via weighted inter–connections. It is the structure of these connections which defines how the neural network operates. In feed–forward networks the connections are unidirectional; the information passes from a set of input nodes through the network to a set of output nodes. This architecture is used in pattern recognition applications where the output nodes represent the desired features of a set of input variables.

Figure 5.10 shows the generic structure of a feed–forward neural network. The basic features are:

The Input layer : The input nodes, x_k, take the values of the input variables. The set of input variables for a particular track are collectively referred to as the input pattern for that track;

The Output Layer : The output nodes, y_i, represent the various features of the input patterns which the network has been trained to distinguish;

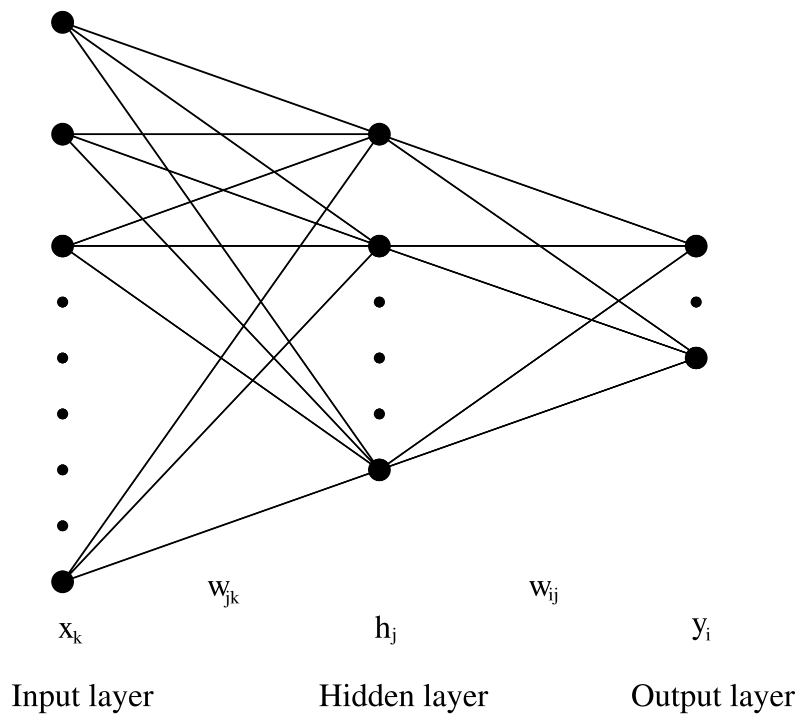

Figure 5.10: *Architecture of a feed–forward artificial neural network.*

The hidden layer : The hidden nodes, h_j, pass information between the input and output layers. It is this layer which gives the network its complex behaviour and non–linear responses, and hence its analytical power. In most cases only one hidden layer is needed, although for particularly complex problems more hidden layers can be used. Networks with more than one hidden layer are generally harder to optimise and are thus only used when absolutely necessary;

The weights : The connections between the nodes in the various layers are controlled by the weights w_{jk} and w_{ij}. These are adjusted during the training process so as to produce the desired mapping from the input patterns to the output features.

The term feed–forward refers to the flow of information in the network; from the input layer through the various hidden layers to the output layer. For such networks, the output nodes can be expressed as an analytical function of the input nodes. For the architecture shown in Figure 5.10 we have;

$$y_i = g\left(\sum_j w_{ij}\; g\left(\sum_k w_{jk}x_k + \theta_j\right) + \theta_i\right) \tag{5.7}$$

where θ_j and θ_i represent threshold values for the nodes to 'activate' and are commonly set to zero.

The *activation functions*, $g(x)$, control the response of the nodes and typically take the form of a sigmoid function. For example,

$$g(x) = \frac{1}{2}\left(1 + \tanh\left(\frac{x}{T}\right)\right) \tag{5.8}$$

where T is the *temperature* of the network and controls the gain of the function $g(x)$. Figure 5.11 shows the activation function for different temperatures.

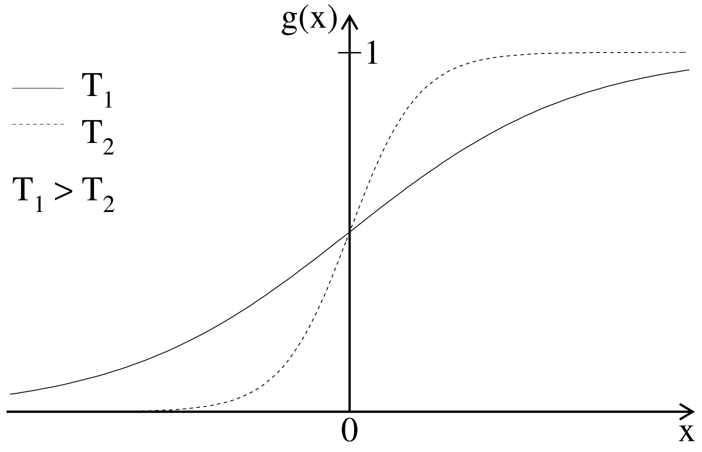

Figure 5.11: *The sigmoid activation function for two different network temperatures.*

For high values of T, the sigmoid function approaches a straight line and the resulting network has a linear response. Such networks are often used in function fitting applications. For pattern recognition, a non–linear response is beneficial and lower temperatures are therefore used. The choice of temperature is relatively arbitrary since the network adjusts accordingly during the training procedure, and in this thesis the most commonly used choice of $T = 1$ was employed.

5.1.8.2 Neural Network Training

Network training refers to the process of adjusting the connection weights so as to map the input patterns to the target output features.

The weights w_{ij} and w_{jk} are determined by minimising an estimator of the fit error between the obtained (o_i) and target (t_i) network outputs for a set of *training data*, with respect to these weights. The most commonly used estimator is the mean square error, defined as

$$E = \frac{1}{2N_{pat}} \sum_{p=1}^{N_{pat}} \sum_{i=1}^{N_{out}} \left(o_i^{(p)} - t_i^{(p)} \right)^2 \tag{5.9}$$

where N_{pat} is the total number of training patterns and N_{out} the number of network output nodes.

Once the weights have been fitted to the training data in this way, the network should be able to recognise data it has not been exposed to; this ability is called the *generalisation* performance of the network. In order to prevent over–learning, where the networks fits to particular fluctuations in the training data set that are not general characteristics of the data, the number of training patterns must be much greater the number of free parameters, the network weights.

The optimisation of such a large number of variables, using a correspondingly sizeable training sample, requires the use of specialised optimisation techniques. The most widely used technique is *back propagation*, where Equation 5.9 is minimised using a gradient descent method. In this method, the weights are updated on a pattern by pattern basis according to the learning rule,

$$\boldsymbol{\omega}^{(p+1)} = \boldsymbol{\omega}^{(p)} + \Delta\boldsymbol{\omega}^{(p)} \tag{5.10}$$

where $\boldsymbol{\omega}$ indicates the vector of all network weights. The change in weight $\boldsymbol{\omega}^{(p)}$, denoted

$\Delta\boldsymbol{\omega}^{(p)}$, is determined from the gradient of the network error for the current input pattern p, denoted $E^{(p)}$,

$$\Delta\boldsymbol{\omega}^{(p)} = -\eta\frac{\partial E^{(p)}}{\partial \boldsymbol{\omega}} \tag{5.11}$$

where η is the learning parameter which controls the rate at which the network converges.

A second term is often added to $\Delta\boldsymbol{\omega}^{(p)}$ to stabilise the learning by retaining some information from the previous iteration, giving,

$$\Delta\boldsymbol{\omega}^{(p)} = -\eta\frac{\partial E^{(p)}}{\partial \boldsymbol{\omega}} + \alpha\Delta\boldsymbol{\omega}^{(p-1)} \tag{5.12}$$

where $0 < \alpha < 1$. Finally, in order to prevent local as opposed to global minima from being found, an additional noise term, σ, is often introduced

$$\Delta\boldsymbol{\omega}^{(p)} = \Delta\boldsymbol{\omega}^{(p)} + \sigma. \tag{5.13}$$

In the *Langevin* scheme a normalised Gaussian noise term is used and the magnitude of the noise is systematically decreased during the training procedure. This technique effectively prevents the network converging prematurely before it has sufficiently explored the parameter space, leading to a higher probability of finding the global minimum.

The data set used in the network training is typically divided into two distinct subsets, termed the *training* and *test* data sets. The training set is used explicitly in the network optimisation whilst the test set is used to assess the performance of the network during the training.

After each iteration through the training data set the average network error (Equation 5.9) is computed for the test data set. Once this error has converged to its minimum value, the network has found the optimal weights and the training is stopped. In order to determine the final network performance it is desirable to use a third data set, the *evaluation* data set, which is independent of both the training and test data sets. Such a set has not been used either explicitly or indirectly in the training and therefore provides a truly statistically independent determination of the final network performance.

5.1.9 Electron Identification Neural Network

The neural network training techniques described above were applied to electron identification using the JETNET [95] package. Eight variables where selected as inputs to a neural network trained to identify electrons :

- The normalised specific ionisation, $\mathrm{d}E/\mathrm{d}x|_{norm}$;
- The error on the specific ionisation, $\sigma(\mathrm{d}E/\mathrm{d}x)$;
- The track E_{cone}/p;
- The number of calorimeter blocks used in the E_{cone} summation, N_{blocks};
- The track momentum, p;
- The track $|\cos\theta|$;
- The track–cluster matching variable, $\Delta\theta$;
- The track–cluster matching variable, $\Delta\phi$.

The parameter ranges for these inputs differ substantially and such differences adversely affect the network training since each input requires very different weights. This can lead to optimisation instabilities and longer training times. Such effects can be prevented by normalising the input variables to a standard range, using an isomorphic functional mapping that preserves the features of the input variables. The actual form of the mapping is arbitrary since the training will adjust to the normalised distributions. The mapping between the raw, x_{raw}, and normalised, x_{norm}, distributions was chosen as,

$$x_{norm} = \frac{1}{\left(1 + e^{\frac{x_{raw} - \langle x_{raw}\rangle}{\sigma_{raw}}}\right)} \tag{5.14}$$

with $\langle x_{raw}\rangle$ the mean and σ^2_{raw} the variance of the input distributions. This mapping produces distributions normalised to between zero and one.

From the Monte Carlo simulation a sample of tracks was selected from events passing the BT multi–hadronic event selection criteria (Section 4.2.1). In addition, the following loose pre–selection criteria were applied to the tracks :-

- $-2 < \mathrm{d}E/\mathrm{d}x|_{norm} < 4$. This rejects the majority of the hadronic tracks whilst retaining practically all true electrons;

- number of $\mathrm{d}E/\mathrm{d}x$ hits > 20. This rejects tracks with the poorest $\mathrm{d}E/\mathrm{d}x$ modelling.

These pre–selection criteria allow the network to focus the training on the rejection of hadronic tracks which most closely resemble true electrons.

A sample of 90 000 tracks was selected using these criteria. This sample was divided equally to form two independent training and test samples, with a 50:50 composition of electrons and background sources. In this way the resulting neural network output can be interpreted as the probability that the track is a true electron.

Neural networks were trained using the input variables. The matching variables $\Delta\theta$ and $\Delta\phi$ were found to improve the network performance only for tracks in the endcaps and therefore these variables are used only in these regions. One hidden layer with 13 nodes was found to be sufficient to fully map the input parameter space onto one output node representing the electron probability. Figure 5.12 shows the output distributions for the resulting network, $\mathrm{NN_e}$. By placing a cut on the network output, a high purity sample of electrons can be selected. In this analysis candidate electron tracks are required to satisfy $\mathrm{NN_e} > 0.9$ giving a network efficiency[a] around 79 % with a purity of approximately 94 %. The systematic uncertainties associated with the Monte Carlo modelling of the $\mathrm{NN_e}$ distribution are discussed in Section 5.3.

[a] Excluding the effects of the track pre–selection criteria.

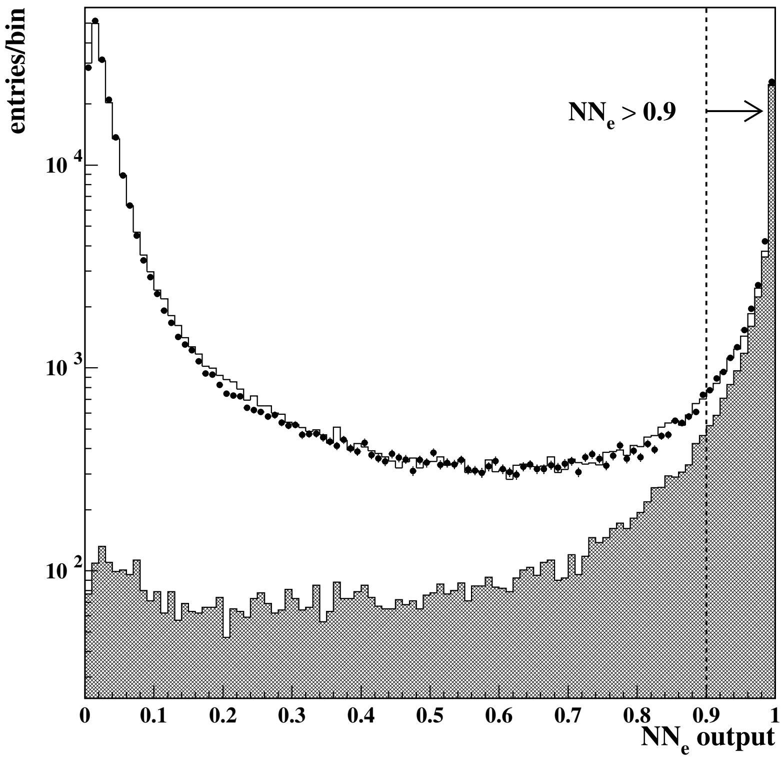

Figure 5.12: *The output distribution for the electron identification neural network NN_e. The data (points) are compared to the Monte Carlo predictions (solid line). The true electron contribution is shown by the hatched region. The selected tracks with $NN_e > 0.9$ are also indicated.*

5.2 Photon Conversion Rejection

Electrons from photon conversions, $\gamma \to e^+e^-$, form an important background to prompt[b] electrons in the neural network tagged sample. Such conversion electrons are rejected using an additional neural network, NN_{cv}, trained to identify them using their distinctive topological and kinematic characteristics. Each identified electron candidate is considered in turn with all other charged tracks in the event and the probability that they form a photon conversion pair is determined using the NN_{cv} network.

[b]Prompt leptons are leptons from either direct, $b \to \ell$ or cascade, $b \to c \to \ell$, decays.

Nine characterising input variables are used in $\mathrm{NN_{cv}}$:-

- The distance between the two tracks at tangency;
- The radius of the first measured tracking chamber hit with respect to the centre of the OPAL detector, for both tracks;
- The radius of the reconstructed vertex of the candidate photon conversion;
- The invariant mass of the pair, assuming both tracks to be electrons;
- The impact parameter of the reconstructed photon with respect to the primary vertex of the event;
- The electron identification network output, $\mathrm{NN_e}$, of the partner track;
- The product of the momentum and charge, for both tracks.

Figure 5.13 shows the distribution for $\mathrm{NN_{cv}}$. By requiring that tracks satisfy the selection $\mathrm{NN_{cv}} < 0.8$, the photon conversion background is substantially reduced, whilst retaining $\sim 98\,\%$ of the $\mathrm{NN_e}$ selected sample of prompt electrons.

5.3 Electron Identification Systematics

The efficiency for selecting electrons and the corresponding purity of the selected samples are determined from the Monte Carlo. In order to assess the systematic uncertainties associated with these measurements, a detailed study of the electron identification and photon conversion rejection neural networks was performed [98]. Two independent methods were used to study the differences between data and Monte Carlo. These are described in the following sections.

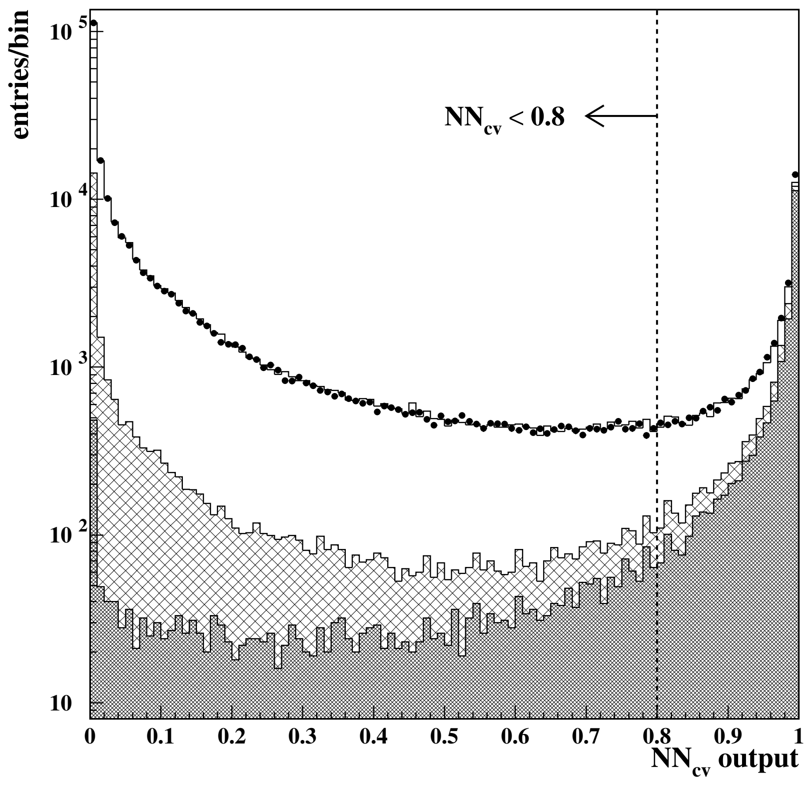

Figure 5.13: *The output distribution for the photon conversion neural network, NN_{cv}. The data (points) are compared to the Monte Carlo predictions (solid line). The true photon conversion contribution is indicated by the darkly hatched region whilst the lightly hatched region shows all other true electrons. The open region shows all non–electron candidates. The selected tracks with $NN_{cv} < 0.8$ are also indicated.*

5.3.1 Test Sample Studies

Various techniques can be used to select samples of tracks enhanced in particular particle species. Pure electron samples can be used to study differences in the selection efficiencies between data and Monte Carlo. Pion samples, the predominant background in the electron selection, are used to study the Monte Carlo modelling of the purity of the electron selection.

The following samples were selected in both the data and Monte Carlo :-

Electron Samples

By placing the tight requirement $\mathrm{NN_{cv}} > 0.999$ on the photon conversion neural network output, a sample $\sim 98\,\%$ pure in photon conversion electrons can be selected in multi–hadronic events. Electrons from Bhabha scattering, $\mathrm{e^+e^-} \rightarrow \mathrm{e^+e^-}$, are selected by requiring that the event contains only two well measured tracks with momenta between 40 GeV/c and 50 GeV/c and which are associated to high energy electromagnetic clusters. Such a sample of tracks is practically 100 % pure in Bhabha electrons.

Pion Background Samples

Pions are identified from two sources. Firstly, $\mathrm{K^0_s} \rightarrow \pi^+\pi^-$ decays were reconstructed using tracks with $\mathrm{d}E/\mathrm{d}x$ values consistent with a pion hypothesis and a reconstructed invariant mass consistent with the $\mathrm{K^0_s}$ mass. Selected tracks gave a sample 97 % pure in pions. Secondly, τ decays to 3 charged tracks were selected according to [99]. These tracks yield a sample 98 % pure in pions.

The Monte Carlo modelling of the electron selection was studied in the electron and pion test samples using the variable δf where,

$$\delta f = \frac{f_{\mathrm{DATA}} - f_{\mathrm{MC}}}{f_{\mathrm{DATA}}} \tag{5.15}$$

and f is the fraction of tracks which pass a given cut on the electron identification output, $\mathrm{NN_e} > \mathrm{NN_e^{cut}}$, in either the data or Monte Carlo. By varying the value of $\mathrm{NN_e^{cut}}$, the modelling of the network can be studied as a function of the network output. For the electron test samples, δf represents the fractional difference between the data and Monte Carlo simulation in the efficiency of the electron selection. For the pion samples, δf represents the fractional difference in the fake rate, the efficiency for mistakenly identifying fake electrons.

Figure 5.14 shows examples of the δf distributions obtained by comparing the 1995 data to 1995 Monte Carlo samples. Similar studies were also performed for the 1992, 1993 and 1994 data sets and similar sized discrepancies where observed, although the

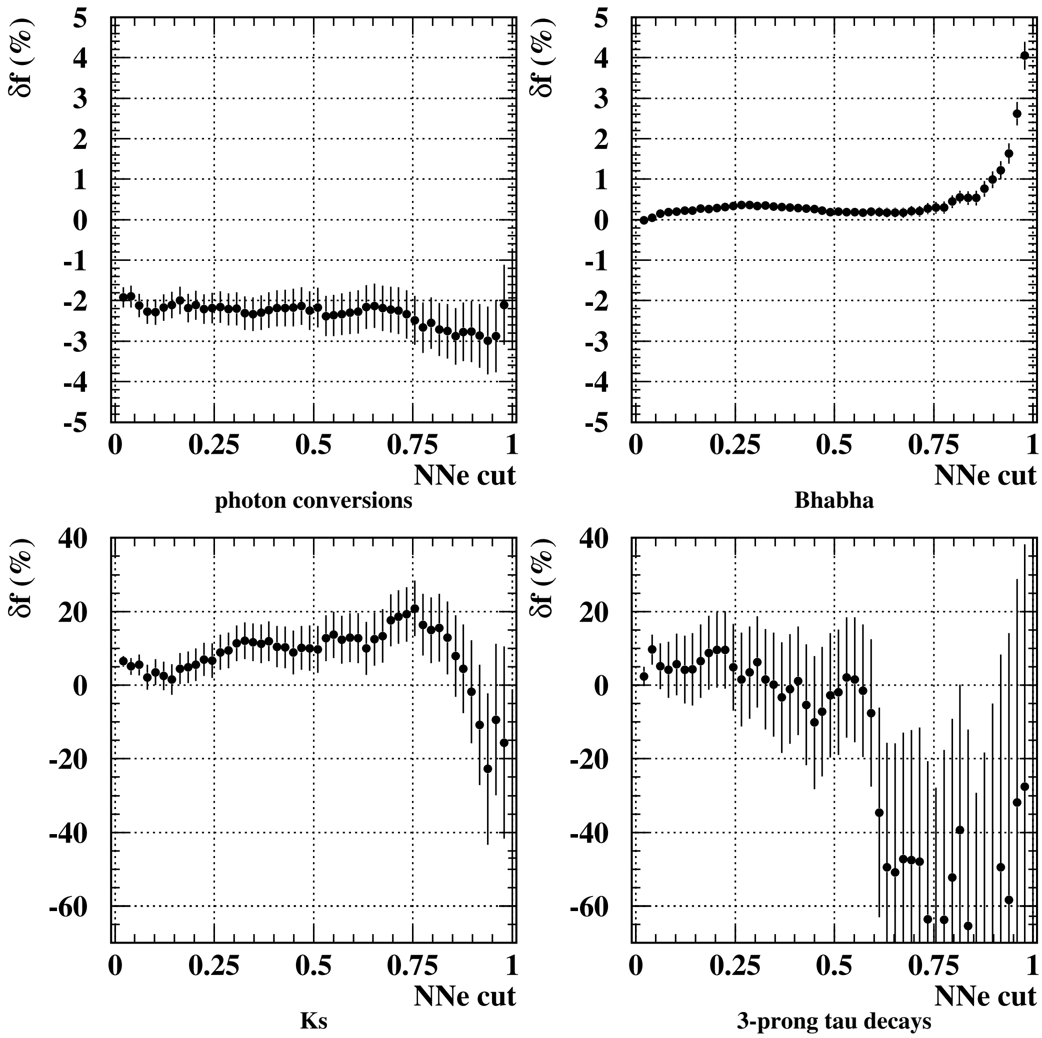

Figure 5.14: *The values of δf obtained with the four test samples, as a function of the NN_e cut position. The upper two plots correspond to the fractional error on the efficiency, whilst the lower two plots show the fractional error on the fake rate.*

differences are not fully correlated between the different years. These studies show that for the pure electron samples the electron identification efficiency is correctly modelled in the Monte Carlo to a relative accuracy of $\sim 4\,\%$ [98]. Using the background samples, the fake rates were found to be correct to within a relative accuracy of $\sim 60\,\%$, although these tests were limited by the low statistics of the test samples.

5.3.2 Input Parameter Modelling

The systematic uncertainties in the modelling of the $\mathrm{NN_e}$ output necessarily stem from discrepancies between data and Monte Carlo in the input distributions. The modelling of each variable was studied in turn, and the impact that any discrepancies between data and Monte Carlo had on the neural network performance was assessed. Finally, a conservative estimate of the overall network systematic uncertainties can be obtained by adding in quadrature the individual errors associated with each input variable.

The modelling of $\mathrm{d}E/\mathrm{d}x|_{norm}$

The quality of the $\mathrm{d}E/\mathrm{d}x|_{norm}$ modelling in the Monte Carlo has been extensively studied [94] showing that the mean of the inclusive $\mathrm{d}E/\mathrm{d}x|_{norm}$ distribution is correct to ± 0.03 and the width to $\pm 2\,\%$. Accordingly, the $\mathrm{d}E/\mathrm{d}x|_{norm}$ was shifted and smeared in the Monte Carlo and the efficiency and purity were recalculated. The variations in the $\mathrm{d}E/\mathrm{d}x|_{norm}$ mean resulted in relative errors of $1.0\,\%$ on the efficiency and $6.0\,\%$ on the fake rate. Variations in the width resulted in relative efficiency and fake rate errors of $0.3\,\%$ and $6.0\,\%$ respectively.

In addition, studies of the $\mathrm{d}E/\mathrm{d}x|_{norm}$ distribution for identified photon conversions [98] show an additional modelling discrepancy for $\mathrm{d}E/\mathrm{d}x|_{norm} < 0$, corresponding to an additional $21\,\%$ error on the electron $\mathrm{d}E/\mathrm{d}x|_{norm}$ width. This results in a relative error of $1.9\,\%$ on the efficiency.

Adding these errors in quadrature, a conservative estimate of the overall error due to $\mathrm{d}E/\mathrm{d}x|_{norm}$ mis–modelling is obtained. A relative efficiency error of $1.9 \oplus 1.0 \oplus 0.3 = 2.2\,\%$ and a relative fake rate error of $6.0 \oplus 6.0 = 8.5\,\%$ are obtained.

The modelling of $\sigma(\mathrm{d}E/\mathrm{d}x)$

The $\sigma(\mathrm{d}E/\mathrm{d}x)$ distribution has been studied [94] and the mean found to be correctly modelled to ± 0.016, resulting in relative errors of $2.4\,\%$ and $15\,\%$ on the efficiency and fake rates respectively.

Differences in the shape of the $\sigma(\mathrm{d}E/\mathrm{d}x)$ distribution are assessed by smearing the width of the distribution by a conservative $\pm 10\,\%$ which encompasses the observed variations between data and Monte Carlo [94]. This leads to relative errors of $1.7\,\%$ and $7\,\%$ on the efficiency and fake rates respectively.

The modelling of E_{cone}/p

For electrons, the E_{cone}/p distribution is approximately a Gaussian distribution centred at one. The Monte Carlo modelling has been studied using Bhabha electrons, identified photon conversions and an electron enhanced sample using the selection $\mathrm{d}E/\mathrm{d}x|_{norm} > 0$ [98]. The mean of the E_{cone}/p has been found to be modelled correctly to within $\pm 2\,\%$ resulting in a relative error on the electron identification efficiency of $0.8\,\%$. The width of the E_{cone}/p distribution is correctly modelled to $\pm 4\,\%$, giving a relative efficiency error of $1.0\,\%$. From studies of the pion background samples, a relative error of $10\,\%$ is assigned to the fake electron rate.

The modelling of N_{blocks}

The predominant mis–modelling of the N_{blocks} variable occurs for tracks with no associated energy E_{cone} and hence with $N_{blocks} = 0$ [98]. The fraction of such tracks is found to differ by $0.9\,\%$ between data and Monte Carlo. These tracks are very unlikely to be identified using the neural network selection and therefore this discrepancy directly relates to a relative efficiency error of $0.9\,\%$. The error on the fake rate due to the modelling of N_{blocks} is negligible.

The modelling of $\Delta\theta$ and $\Delta\phi$

The track–cluster matching variables $\Delta\theta$ and $\Delta\phi$ are well modelled in the Monte Carlo and since they are only used for endcap tracks, they contribute a negligible systematic uncertainty to the modelling of $\mathrm{NN_e}$.

The modelling of the momentum and $|\cos\theta|$ distributions

The neural network modelling is less sensitive to discrepancies in the momentum and $|\cos\theta|$ distributions, since these variables are less discriminating than other input variables. No significant modelling discrepancies were found [98] and therefore no systematic error was assigned for either the momentum or $|\cos\theta|$ variables.

Adding in quadrature the errors on the electron identification efficiency and fake rate as considered above, gives the overall relative systematic errors on the efficiency to be 4 % and the fake rate to be 21 %.

5.3.3 Summary of Electron Identification Systematic Studies

From the studies described in Section 5.3.1 using the test samples, the Monte Carlo modelling of the efficiency is found to be correct to a relative uncertainty of 4 % and the fake rate to a relative 60 % although the fake rate tests are statistically limited. From studying each input in turn, as discussed in Section 5.3.2, the efficiency is again found to be modelled to 4 %, with the fake rate modelled to 21 %. In conclusion, the Monte Carlo efficiencies are found to be correct to a relative accuracy of 4 %, and the fake rate to a relative accuracy of 21 %.

5.3.4 Systematic Studies of Photon Conversion Rejection

Similar systematic studies to those used for the $\mathrm{NN_e}$ selection have been conducted on the effects of the photon conversion rejection on the efficiencies for selecting prompt electrons [98]. These studies show that the photon conversion rejection contributes a small additional relative uncertainty of 0.8 % on the prompt lepton identification efficiencies determined from the Monte Carlo. The additional uncertainty on the fake electron rate was found to be negligible in comparison to that resulting from $\mathrm{NN_e}$.

5.4 Muon Identification

5.4.1 Selection Criteria

Muon candidates are identified using reconstructed track segments in the muon chambers. Each reconstructed charged track is extrapolated from the central detector to the muon chambers using its track parameters. The extrapolated position is compared with the positions of track segments reconstructed in the external muon chambers. In addition to the BT track selection criteria (Section 4.2.1), the muon selection requirements are [100] :-

- Muon candidates are required to have momenta greater than 2 GeV/c;
- $\chi_{\rm pos} < 3$, where $\chi_{\rm pos}$ is the positional matching parameter, defined as

$$\chi^2_{\rm pos} = \left(\frac{\Delta\phi}{\sigma(\Delta\phi)}\right)^2 + \left(\frac{\Delta\theta}{\sigma(\Delta\theta)}\right)^2 \tag{5.16}$$

  where $\Delta\phi$ and $\Delta\theta$ are respectively the differences in ϕ and θ between the extrapolated central detector track position at the muon chambers and the nearest muon segment. The errors, $\sigma(\Delta\phi)$ and $\sigma(\Delta\theta)$, are calculated from the expected multiple scattering effects and the track and muon segment reconstruction errors;
- A 'best–match' requirement. Each muon segment can in principle be matched to more than one charged track. If several tracks are matched to the same muon segment then the ambiguity is resolved by taking only the charged track with the smallest spatial separation from the muon track segment. Figure 5.15 compares the $\chi_{\rm pos}$ distribution for 'best–match' candidates obtained in the data, to the corresponding distribution for the Monte Carlo.

5.4.2 Muon Identification Systematics

The Monte Carlo modelling of the efficiency and purity of the muon selection has been studied in detail elsewhere [101]. To compare the muon selection efficiency in data and Monte Carlo, a sample of muon pairs from two–photon production, $e^+e^- \to e^+e^-\mu^+\mu^-$, was selected. These muons are found in the momentum range 2 to 6 GeV/c, corresponding to $\sim 57\,\%$ of the muon candidates selected in multi–hadronic events. The Monte Carlo was found to underestimate the efficiency in the data by 1.3 %, giving a multi-

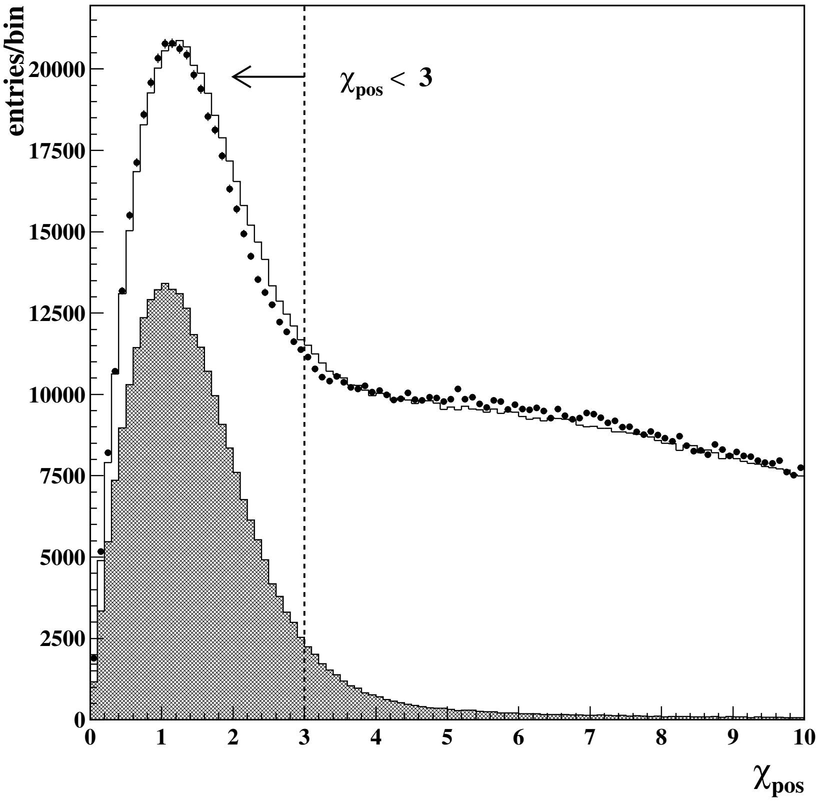

Figure 5.15: *The χ_{pos} distribution for best–match muon candidates. The data (points) are compared to the Monte Carlo predictions (solid line). The true muon contribution is shown by the hatched region. The selected tracks with χ_{pos} < 3 are also indicated.*

plicative correction factor of 1.013 to the measured efficiencies. The relative difference in efficiency is about 0.9 % in the barrel region rising to 5 % in the endcaps.

Using a pure sample of muons from $Z^0 \to \mu^+\mu^-$ decays, the data and Monte Carlo can be compared for muons with momentum greater than $\sim$ 30 GeV/c. A difference of 1.1 % in muon finding efficiency is observed for these muons, although only $\sim$ 0.2 % of the multi–hadronic muon sample have momenta above 30 GeV/c. Based on the distributions of the muons in the various detector regions (87 % in the barrel and 13 % in the endcaps), a relative systematic uncertainty of 1.9 % is assigned to the muon finding efficiency.

To study the fake rate in the muon selection, three different samples were used: identified pions in $K_s^0 \to \pi^+\pi^-$ decays, three prong τ decays, and a kaon enriched sample based on $\mathrm{d}E/\mathrm{d}x$ requirements [101]. From a comparison of the fake muon rates in data and Monte Carlo for these samples, it was determined that a correction factor of 1.11 ± 0.12 must be applied to the Monte Carlo events in order to reproduce the fake rates observed in the data.

5.5 Summary of Lepton Identification

In this chapter the techniques used to identify leptons in multi–hadronic events have been described. Using these selections, the efficiencies to identify leptons from $\mathrm{b} \to \ell$ and $\mathrm{b} \to \mathrm{c} \to \ell$ decays are determined from the Monte Carlo simulations. The ACCMM model was used to simulate the momentum spectra for lepton from $\mathrm{b} \to \ell$ and $\mathrm{b} \to \mathrm{c} \to \ell$ decays, as described in Section 2.6.4.1 [102]. The measured efficiencies are

$$
\begin{aligned}
\epsilon_{\mathrm{b}\to e} &= (56.62 \pm 2.31 \text{ (syst.)})\,\% \\
\epsilon_{\mathrm{b}\to \mu} &= (67.94 \pm 1.29 \text{ (syst.)})\,\% \\
\epsilon_{\mathrm{b}\to\mathrm{c}\to e} &= (33.06 \pm 1.35 \text{ (syst.)})\,\% \\
\epsilon_{\mathrm{b}\to\mathrm{c}\to \mu} &= (42.77 \pm 0.81 \text{ (syst.)})\,\%
\end{aligned}
$$

where the errors result from the systematic uncertainties discussed in the previous sections. These efficiencies include the effects of the lepton pre–selection criteria.

Figure 5.16a shows the identification efficiencies for leptons from $\mathrm{b} \to \ell$ and $\mathrm{b} \to \mathrm{c} \to \ell$ decays, as a function of the lepton momentum in the b hadron rest frame, p_{rest}, including the effect of the pre–selection criteria. Leptons with low rest frame momenta require a higher boost from the b hadron momentum in order to be pre–selected and therefore a reduction in the selection efficiencies is expected at low rest frame momenta, due to the $p > 2\,\mathrm{GeV/c}$ pre–selection requirement.

Figures 5.16b and 5.16c compare the lepton p_{rest} distributions for all $\mathrm{b} \to \ell$ and $\mathrm{b} \to \mathrm{c} \to \ell$ decays to those selected by the electron and muon identification criteria. For $\mathrm{b} \to \ell$ decays the selection biases are very small and consequently the candidate leptons form a representative sample of all leptons from $\mathrm{b} \to \ell$ decays. For cascade decays, the selection criteria inefficiencies at very low rest frame momenta are more important since the average lepton momenta from $\mathrm{b} \to \mathrm{c} \to \ell$ decays is lower than that from $\mathrm{b} \to \ell$ decays. However, given the small fraction of the total $\mathrm{b} \to \mathrm{c} \to \ell$ sample with low momenta the selection biases are not important.

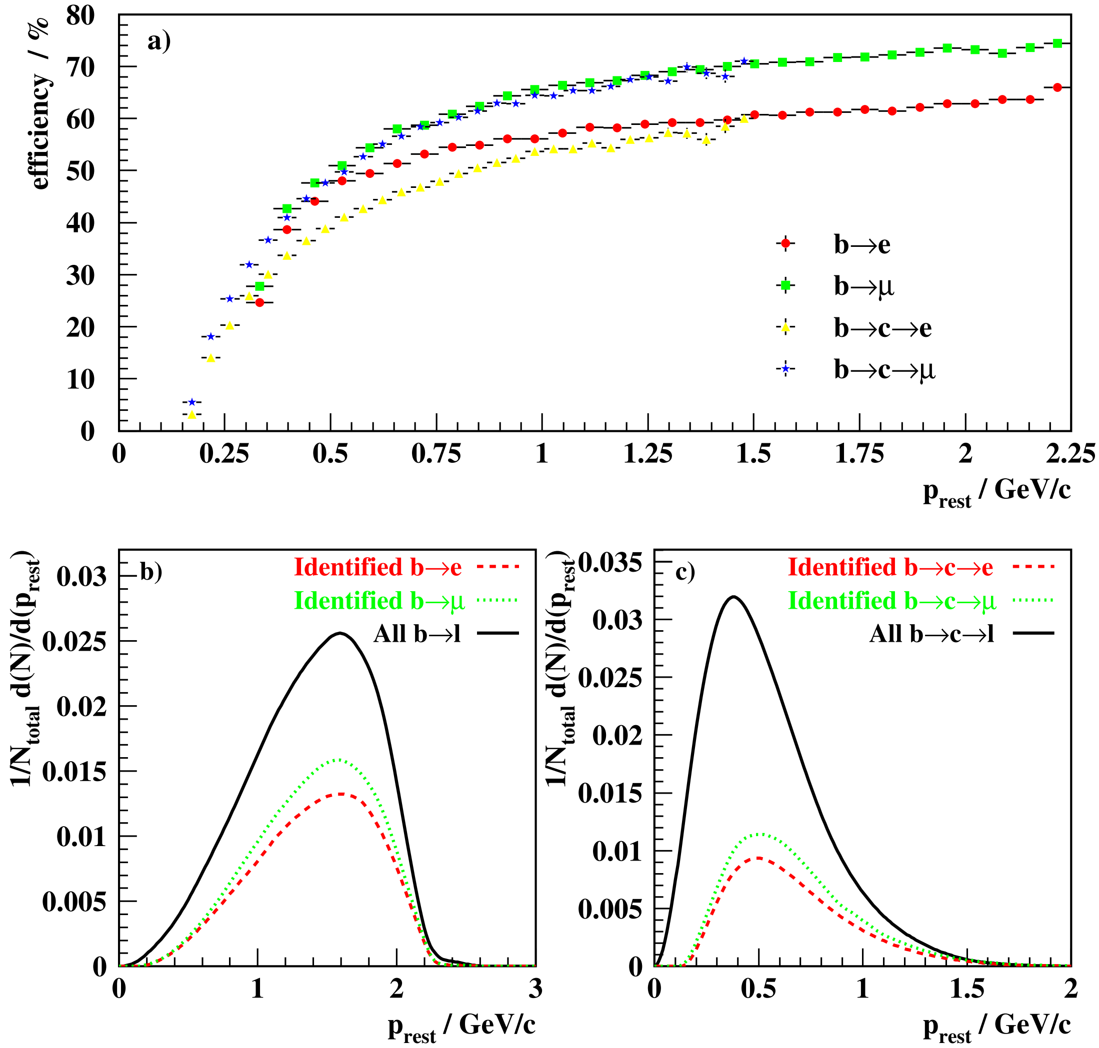

Figure 5.16: *Figure a) shows the lepton identification efficiencies for $b \to \ell$ and $b \to c \to \ell$ decays, as a function of the lepton momentum in the b hadron rest frame, including the effects of the lepton pre–selection criteria. Figures b) and c) compare the p_{rest} distributions for all $b \to \ell$ and $b \to c \to \ell$ decays (solid black), to those obtained with leptons selected by the electron (dashed red) and muon (dotted green) identification criteria.*

Chapter 6

Identifying Semileptonic b Decays

In order to calculate the semileptonic branching fractions $\mathcal{B}(\mathrm{b} \to \mathrm{X}\ell\nu_\ell)$ and $\mathcal{B}(\mathrm{b} \to \mathrm{c} \to \mathrm{X}\ell\nu_\ell)$, it is first necessary to determine the fraction of the selected lepton samples that originate from $\mathrm{b} \to \ell$ and $\mathrm{b} \to \mathrm{c} \to \ell$ decays. This chapter outlines the techniques used in the identification of these sources of leptons and the methods used to determine their contribution to the overall lepton samples selected in the data.

6.1 Analysis Method

Chapter 4 describes the use of a lifetime based b–tagging method to select a sample of b enriched hemispheres in the data. A search for lepton candidates is performed in the hemispheres opposite a b–tagged hemisphere in events containing one or two such hemispheres, using the techniques outlined in Chapter 5. Due to the different b hadron lifetimes and decay modes, the b–tagging efficiencies vary slightly amongst the different species, which can lead to a small bias in the relative fractions of b hadrons in the b–tagged hemispheres. Such biases are avoided by using the hemisphere opposite to the b–tagged hemisphere. In addition, this method avoids potential correlations between the b–flavour tagging and lepton selections which might arise if the b–tagging and lepton selections were applied in the same hemisphere.

In order to determine semileptonic branching fractions, the fraction of the selected lepton samples that originate from direct, $\mathrm{b} \rightarrow \ell$, and cascade, $\mathrm{b} \rightarrow \mathrm{c} \rightarrow \ell$, semileptonic decays must first be determined. This can be achieved by fitting the Monte Carlo momentum distributions to the data using the various phenomenological models for the lepton momentum spectra in semileptonic decays, as discussed in Section 2.6.4. The dominant systematic errors in this method are the theoretical uncertainties resulting from the differences between the various models. In order to reduce these modelling dependencies a new method is presented in this thesis where the momentum information is combined with other discriminating variables through artificial neural networks trained to distinguish leptons from semileptonic b decays. These neural networks and the fitting procedure are described in detail in the following sections.

6.2 Lepton Classification

6.2.1 Composition of Lepton Samples

The composition of lepton samples selected in the Monte Carlo from hemispheres opposite a b–tagged hemisphere is shown in Table 6.1. The main contributions to the samples come from direct, $\mathrm{b} \rightarrow \ell$, and cascade, $\mathrm{b} \rightarrow \mathrm{c} \rightarrow \ell$, decays. The remaining sources are collectively referred to as background in the following sections.

Fake muons form the largest source of background in the muon sample. These fake muons are due mainly to light mesons passing through the hadronic calorimeter without showering. Fake electrons are less common and consist mainly of mis–identified pions. These fake leptons tend to have lower momentum or transverse momentum (with respect to the jet axis) than leptons from either $\mathrm{b} \rightarrow \ell$ or $\mathrm{b} \rightarrow \mathrm{c} \rightarrow \ell$ decays.

The decays $\mathrm{b} \rightarrow \bar{\mathrm{c}} \rightarrow \ell$, where the $\bar{\mathrm{c}}$ originates from the virtual W boson decay (see Figure 2.5), form an important background to $\mathrm{b} \rightarrow \mathrm{c} \rightarrow \ell$ decays. Leptons from either of these two types of decay tend to be produced with less transverse momentum than

Contributions to selected lepton samples	Electrons	Muons
$b \to \ell$	54.7 %	43.0 %
$b \to c \to \ell$	27.1 %	23.0 %
fake leptons	3.3 %	18.5 %
non–prompt leptons	5.3 %	7.3 %
$b \to \bar{c} \to \ell$	3.5 %	3.1 %
$b \to \tau \to \ell$	2.5 %	1.8 %
$b \to J/\Psi \to \ell^+\ell^-$	0.9 %	0.7 %
primary $c\bar{c}$ events	2.4 %	2.2 %
primary uds events	0.2 %	0.2 %
$g \to c\bar{c}$	0.2 %	0.1 %
$g \to b\bar{b}$	< 0.001 %	< 0.001 %

Table 6.1: *Composition of the selected Monte Carlo samples of lepton candidates opposite a b–tagged hemisphere.*

leptons from direct $b \to \ell$ decays. In addition, in $b \to \bar{c} \to \ell$ decays the b quark also decays predominantly to a c quark, giving two charm quarks in the final hadronic state. Due to the presence of two heavy quarks in the final state, the momentum available for leptons from $b \to \bar{c} \to \ell$ decays is lower on average than that available in $b \to c \to \ell$ decays. Another small contribution arises from semileptonic b decays to τ leptons which then decay leptonically, $b \to \tau \to \ell$.

True leptons in primary $b\bar{b}$ events which do not originate from the semileptonic decay of a b or c quark, for example electrons from photon conversions, are grouped together as non–prompt leptons. A smaller contribution to the backgrounds are leptons from charm and light flavour (uds) events. Due to the high b purity of the selected data sample, these sources are greatly suppressed. The selected lepton samples also contain small contributions from $b \to J/\psi \to \ell^+\ell^-$ decays, which are discussed further in Section 7.3.1.7. Leptons originating from the decay of heavy quarks produced from gluon splitting, $g \to b\bar{b}$ or $g \to c\bar{c}$, are suppressed due to the requirement that the thrust of the event is greater than 0.8 (Section 4.3.2).

6.2.2 Identifying Leptons from Semileptonic b Decays

Instead of attempting to reject the various backgrounds, the fractions of leptons from $\mathrm{b} \to \ell$ and $\mathrm{b} \to \mathrm{c} \to \ell$ decays in the selected samples are determined by comparing the distributions of several kinematic variables in the data to those obtained in the Monte Carlo. Artificial neural networks are used to extract the maximum amount of information from the kinematic variables. A first neural network, $\mathrm{NN_{b\ell}}$, is trained to discriminate leptons from $\mathrm{b} \to \ell$ decays while another, $\mathrm{NN_{bc\ell}}$, is trained to identify $\mathrm{b} \to \mathrm{c} \to \ell$ decays.

6.2.2.1 The $\mathrm{NN_{b\ell}}$ and $\mathrm{NN_{bc\ell}}$ Input Variables

Various kinematic variables are used as input variables to the neural networks $\mathrm{NN_{b\ell}}$ and $\mathrm{NN_{bc\ell}}$ which were trained using the JETNET [95] neural network package[a], separately for electrons and muons. Training samples were used consisting of 70 000 electron and 90 000 muon candidates identified in the Monte Carlo in the hemispheres opposite to b–tagged hemispheres.

In total eight kinematic variables are used as inputs to the networks :-

- **lepton momentum $\boldsymbol{p}$:** the lepton candidate total momentum;
- **lepton $\boldsymbol{p_t}$:** the transverse momentum calculated with respect to the nearest jet axis, excluding the lepton candidate itself;
- **lepton jet energy :** the energy of the jet containing the lepton candidate;
- **sub–jet energy :** the energy of the sub–jet (defined below) containing the lepton candidate;
- **$\boldsymbol{p_t}$ sum :** the scalar sum of transverse momenta of charged tracks in the lepton jet;
- **impact parameter significance :** the impact parameter of the candidate lepton track with respect to the primary vertex, divided by the error on this distance;

[a]See Section 5.1.8 for a more detailed introduction to artificial neural networks.

- **lepton Q_{jet} :** the lepton candidate charge multiplied by the jet charge (defined below) of the jet containing the lepton, including the lepton candidate track;

- **opposite Q_{jet} :** the lepton candidate charge multiplied by the jet charge of the most energetic jet in the hemisphere opposite the lepton candidate.

In $\mathrm{b} \to \ell$ decays, the lepton momentum spectrum reflects the hard fragmentation of the primary b hadron and is thus particularly efficient at separating these leptons from other sources. Similarly, the high mass of the b hadron induces a high lepton momentum in the rest frame of the weakly decaying b hadron, which, once boosted along the b jet direction, gives a harder p_t spectrum for $\mathrm{b} \to \ell$ than $\mathrm{b} \to \mathrm{c} \to \ell$ or background decays.

The total energy of the lepton jet has sensitivity to leptons from direct and cascade decays since b jets are expected to have lower visible energy in semileptonic decays due to the emission of an energetic neutrino.

The smaller mass of charm hadrons relative to b hadrons forces the non–leptonic decay products from a charm semileptonic decay to follow the lepton direction more closely than in b decays. The neutrino in a charm decay also carries less energy on average than the neutrino in a primary $\mathrm{b} \to \ell$ decay. These differences mean that the energy deposited by neutral and charged particles in the vicinity of the lepton candidate, the lepton sub–jet energy, will be on average lower in $\mathrm{b} \to \ell$ decays than in $\mathrm{b} \to \mathrm{c} \to \ell$ and light flavour decays. The lepton jet is therefore divided into two sub–jets, where the initial sub–jet seeds are the lepton track and the other tracks in the jet, as described in [103]. Each track and unassociated electromagnetic cluster is then reassigned iteratively until each one is closer in angle to its assigned sub–jet axis than to the other. No track or cluster is added to the sub–jet containing the lepton candidate beyond an invariant mass upper limit of $2.5\,\mathrm{GeV/c^2}$. The 'sub–jet energy' used for the neural network input refers to the sub–jet including the lepton candidate.

The scalar sum of p_t of all charged tracks in a jet characterises the width and multiplicity of the jet, both of which are known to differ slightly for b jets compared to lighter quarks [104]. The summation runs over all BT quality tracks (Section 4.2.1).

The lepton impact parameter significance is the distance of closest approach of the track to the primary vertex divided by the uncertainty on this distance. Larger impact parameter significances are expected for leptons from secondary decays, such as $\mathrm{b} \to \ell$ and $\mathrm{b} \to \mathrm{c} \to \ell$ decays, than for tracks from the primary vertex, such as fragmentation tracks.

The final two variables consist of the reconstructed lepton charge multiplied by the jet charge, for the jet associated with the lepton and for the most energetic jet in the opposite hemisphere. The jet charge is the weighted sum of all track charges in the jet,

$$Q_{jet} = \frac{\sum_i Q_i \cdot {p_i}^{0.5}}{\sum_i {p_i}^{0.5}} \tag{6.1}$$

where Q_i is the track charge, p_i is the track momentum and the summation runs over all BT quality (Section 4.2.1) charged tracks in the jet, including the lepton candidate itself. The momentum factor increases the sensitivity of the jet charge to higher momentum tracks from secondary decays in relation to lower momentum fragmentation tracks. The exponent of 0.5 has been found to optimise the jet charge sensitivity in b hadron decays [105].

Leptons from $\mathrm{b} \to \ell$ decays have the same charge as the weakly decaying b quark and therefore the 'lepton Q_{jet}' variable shows a positive correlation between the lepton charge and associated jet charge. Leptons from $\mathrm{b} \to \mathrm{c} \to \ell$ decays have opposite charge to the decaying b quark and hence show a negative correlation with the lepton jet charge, whilst leptons from $\mathrm{b} \to \bar{\mathrm{c}} \to \ell$ decays have a positive correlation with the lepton jet charge. In the absence of $\mathrm{B}^0 - \overline{\mathrm{B}^0}$ mixing, the correlations between the lepton charge in one hemisphere and the jet charge in the opposite hemisphere, embodied in the 'opposite Q_{jet}' variable, are opposite to those of the jet associated with the lepton. In decays where one of the b quarks fragments into a B^0 ($\overline{\mathrm{B}^0}$) meson which then proceeds to mix into a $\overline{\mathrm{B}^0}$ (B^0) meson before decaying weakly, the charge correlations for the opposite Q_{jet} variable are reversed.

The eight input variables used by the neural networks are shown for electrons in Figures 6.1 and 6.2 and for muons in Figures 6.3 and 6.4. Three categories of Monte Carlo decays are shown: direct $\mathrm{b} \to \ell$ decays, cascade $\mathrm{b} \to \mathrm{c} \to \ell$ decays, and all other sources grouped together as background. Good agreement can be seen between the data and Monte Carlo simulations. Combining the information from these variables using artificial neural networks allows not only the intrinsic separation power of each variable to be used, but also takes into account correlations between them.

6.2.2.2 The $\mathbf{NN_{b\ell}}$ and $\mathbf{NN_{bc\ell}}$ Output Distributions

The shapes of the neural network output variables $\mathrm{NN_{b\ell}}$ and $\mathrm{NN_{bc\ell}}$ are shown in Figures 6.5 and 6.6 respectively, for electron candidates and in Figures 6.7 and 6.8 for muon candidates.

The $\mathrm{NN_{b\ell}}$ and $\mathrm{NN_{bc\ell}}$ distributions for the electron and muon networks are very similar, reflecting the fact that the same information is contained within the input distributions. However, the background classes are different between electrons and muons and consequently, differing levels of separation are obtained. It is for this reason that it was necessary to train the networks separately for electron and muon candidates.

The discrimination power of a given distribution can be quantified using the *figure of merit*. The figure of merit, F, measures the difference in the distributions obtained for two different classes of event. If F equals zero the distributions are identical and this variable holds no discrimination power between the two classes, whilst if F is one, the distributions have no overlap at all and complete separation is possible. Analytically, F is defined by the inverse correlation function,

$$F = \alpha_1 \alpha_2 \int_{-\infty}^{+\infty} \frac{(f_1(x) - f_2(x))^2}{\alpha_1 f_1(x) + \alpha_2 f_2(x)} \mathrm{d}x \tag{6.2}$$

where class 1 contributes a fraction α_1 of the total sample with normalised distribution $f_1(x)$, whilst class 2 contributes fraction $\alpha_2 = 1 - \alpha_1$ with normalised distribution $f_2(x)$ [106].

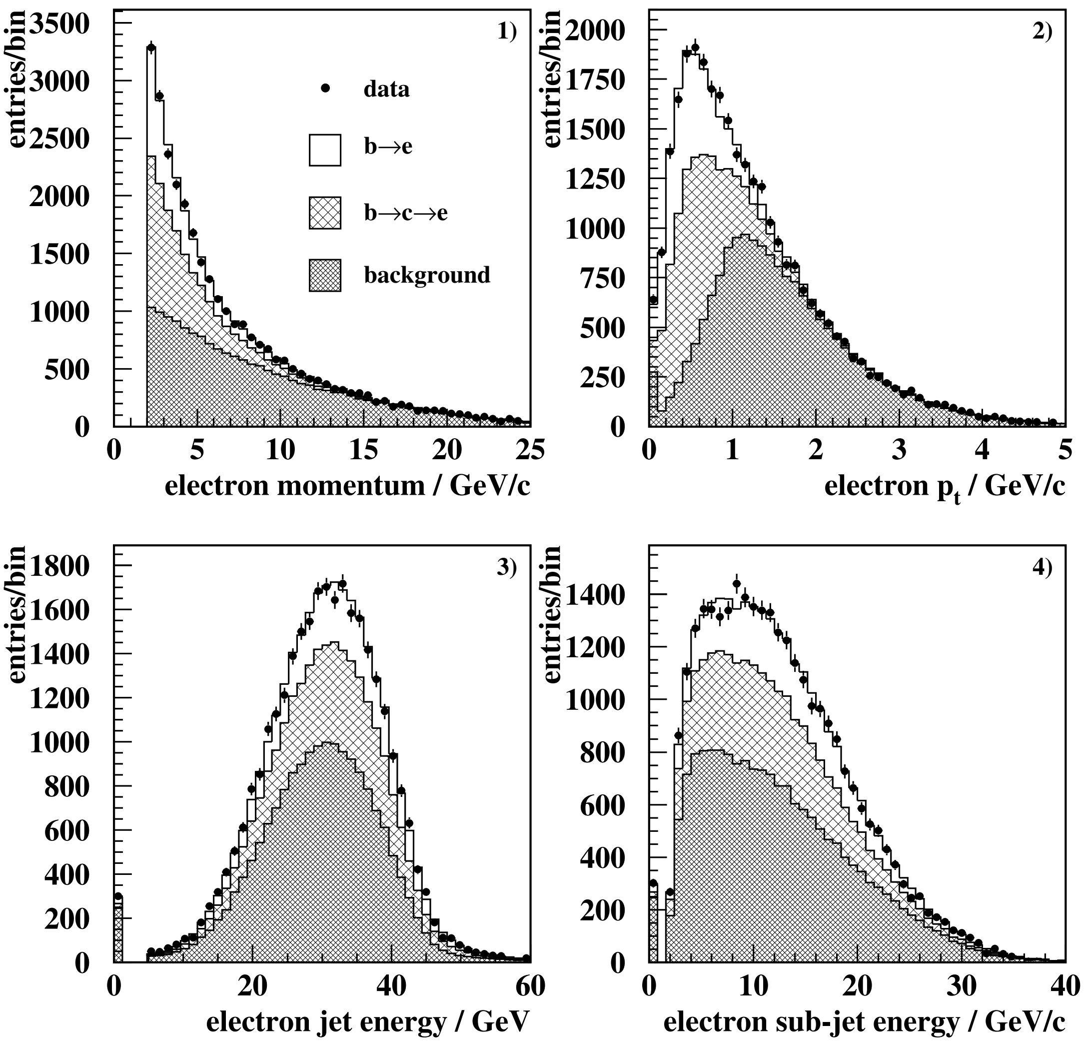

Figure 6.1: *Input variables 1–4 for the electron candidate neural networks $NN_{b\ell}$ and $NN_{bc\ell}$.*

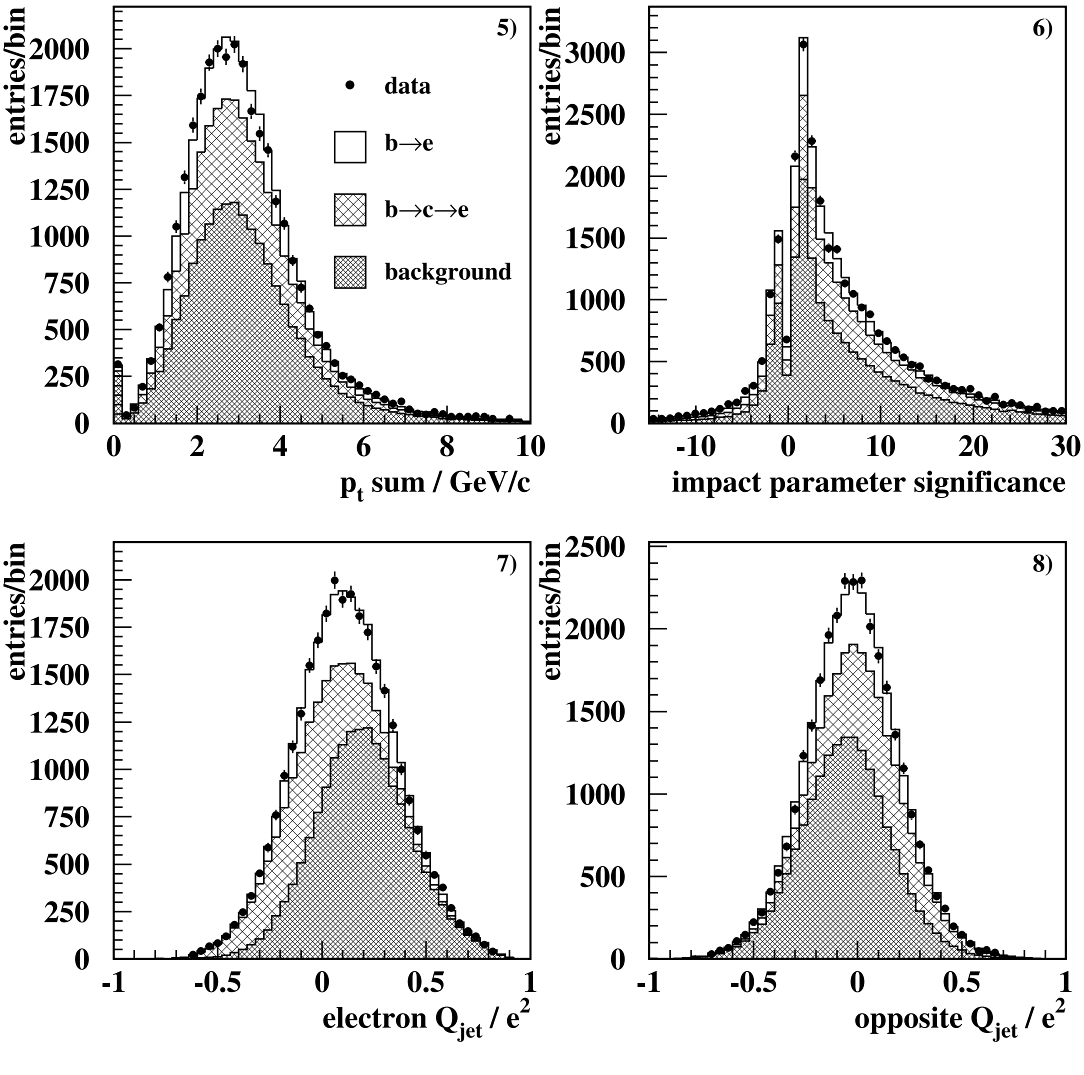

Figure 6.2: *Input variables 5–8 for the electron candidate neural networks $NN_{b\ell}$ and $NN_{bc\ell}$.*

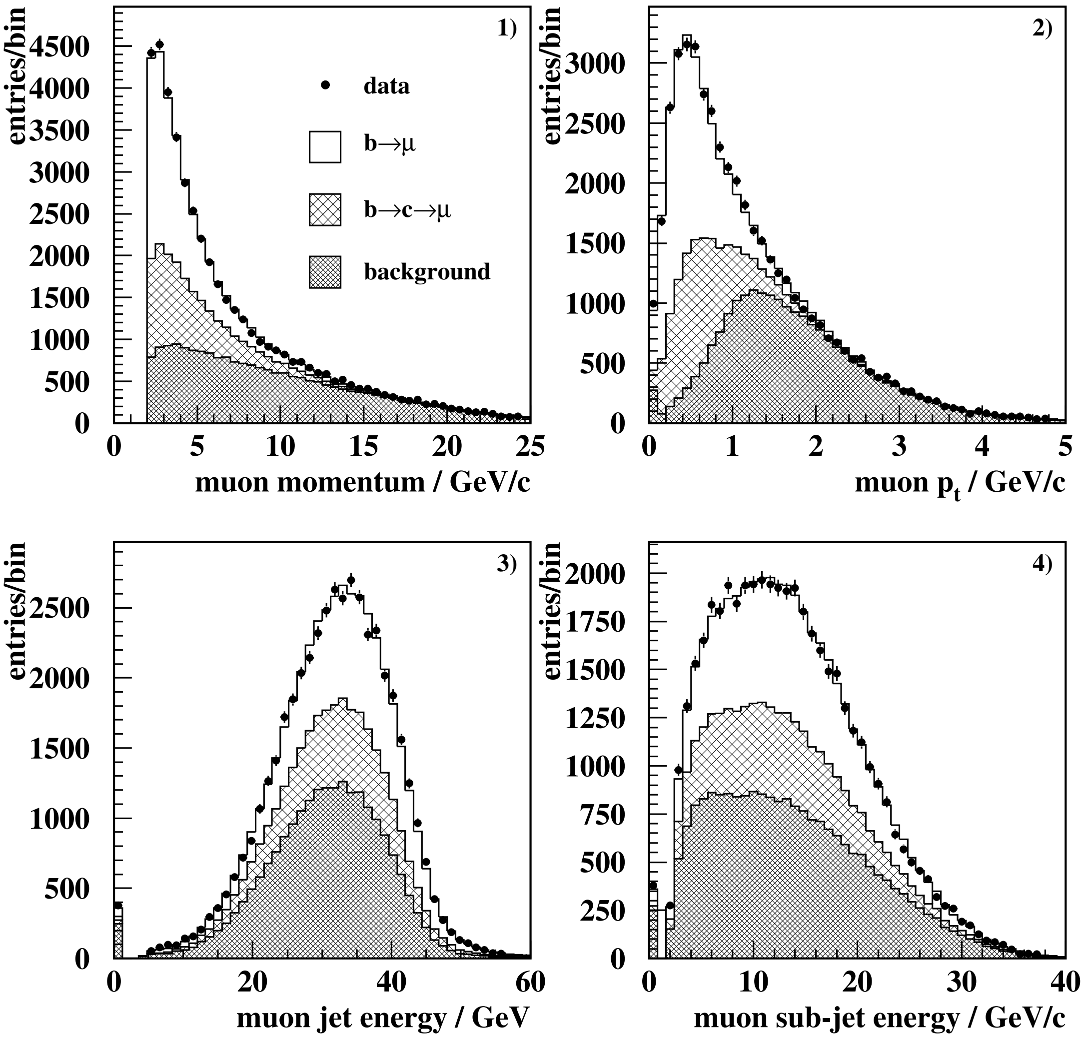

Figure 6.3: *Input variables 1–4 for the muon candidate neural networks $NN_{b\ell}$ and $NN_{bc\ell}$.*

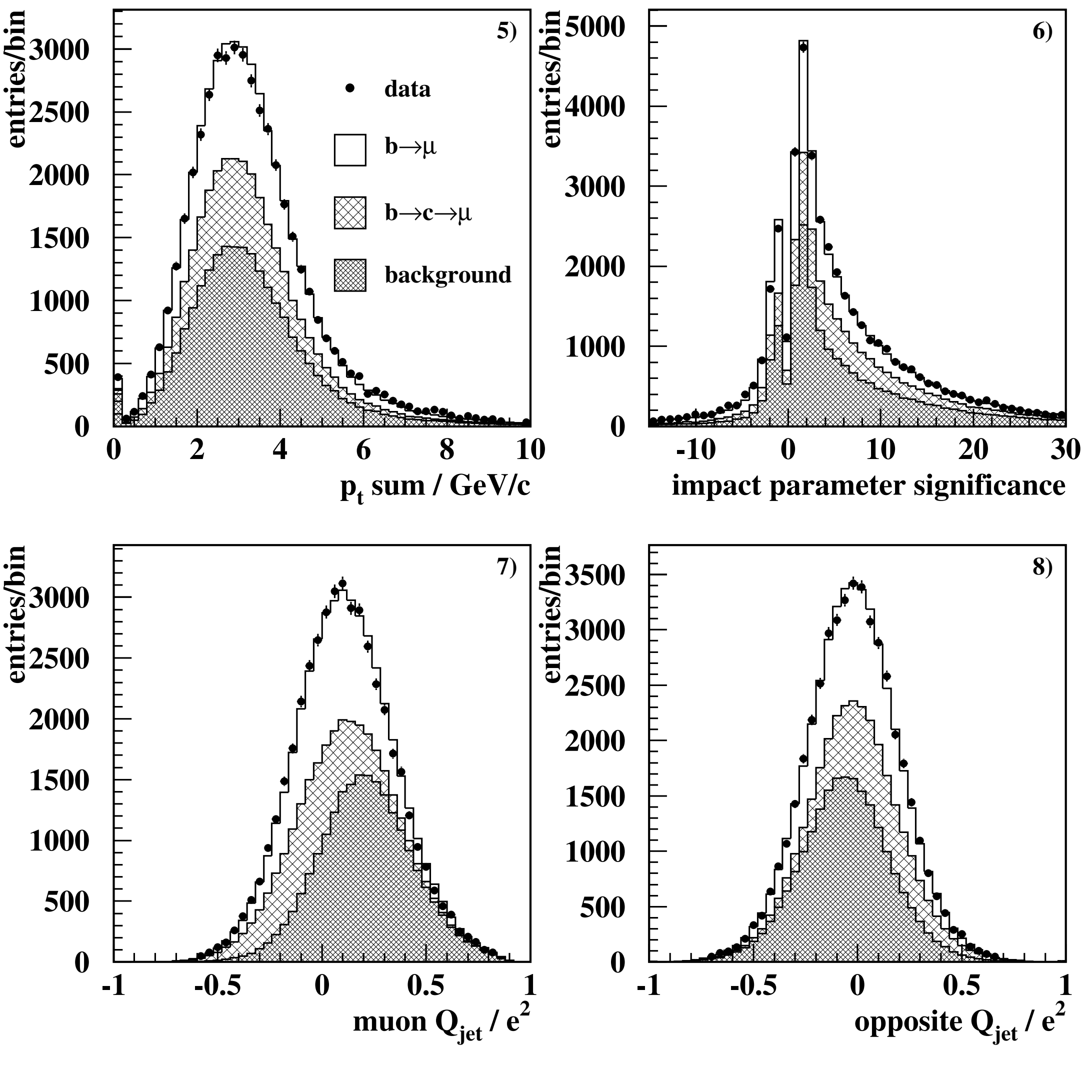

Figure 6.4: *Input variables 5–8 for the muon candidate neural networks $NN_{b\ell}$ and $NN_{bc\ell}$.*

Table 6.2 shows the figures of merit for the discrimination of $\mathrm{b} \to \ell$ and $\mathrm{b} \to \mathrm{c} \to \ell$ decays for each of the input distributions, and for the $\mathrm{NN_{b\ell}}$ and $\mathrm{NN_{bc\ell}}$ network outputs, as calculated from the Monte Carlo. In each case the $\mathrm{b} \to \ell$ or $\mathrm{b} \to \mathrm{c} \to \ell$ distributions are compared to the inclusive distribution for all remaining lepton candidates.

Variable	$\mathrm{b} \to \mathrm{e}$	$\mathrm{b} \to \mathrm{c} \to \mathrm{e}$	$\mathrm{b} \to \mu$	$\mathrm{b} \to \mathrm{c} \to \mu$
momentum p	0.165	0.084	0.246	0.038
transverse momentum p_t	0.378	0.195	0.444	0.091
lepton jet energy	0.009	0.006	0.011	0.004
sub–jet energy	0.017	0.006	0.020	0.002
p_t sum	0.003	0.002	0.002	0.002
impact parameter	0.012	0.009	0.011	0.009
lepton Q_{jet}	0.161	0.178	0.154	0.102
opposite Q_{jet}	0.049	0.049	0.033	0.035
$\mathrm{NN_{b\ell}}$	0.519	–	0.569	–
$\mathrm{NN_{bc\ell}}$	–	0.363	–	0.214

Table 6.2: *Figures of merit for the discrimination of $b \to \ell$ and $b \to c \to \ell$ decays for each of the input variables to the $NN_{b\ell}$ and $NN_{bc\ell}$ neural networks, compared to the corresponding values for the neural networks themselves.*

The p_t distributions offer the best discrimination power for $\mathrm{b} \to \ell$ decays, as expected since these variables are the most sensitive to the lepton momentum spectrum in the rest frame of the weakly decaying b hadron. The lepton total momentum is less discriminating due to the Lorentz boost the lepton receives from the b hadron. For the separation of $\mathrm{b} \to \mathrm{c} \to \ell$ decays, the p_t distributions are not as efficient as for $\mathrm{b} \to \ell$ decays since the lower momentum spectra have a higher cross–over with the background distributions. For these decays, the Q_{jet} variables provide roughly equivalent discriminating power. The remaining input variables are less discriminating singly, but due to correlations between the input variables their contributions to the neural networks are not negligible.

The dominant differences between the electron and muon samples reside in the composition of the background and the relative contribution of the background to the overall lepton samples. Therefore, for $\mathrm{b} \to \ell$ decays which are comparatively easy to discriminate from the background, the performances of $\mathrm{NN_{b\ell}}$ networks are very similar. For $\mathrm{b} \to \mathrm{c} \to \ell$ decays which are harder to separate from the background, the differences in the background samples have a more pronounced effect on the performance of the $\mathrm{NN_{bc\ell}}$ networks. The higher background fraction in the muon samples results in muons from $\mathrm{b} \to \mathrm{c} \to \mu$ decays being harder to distinguish than electrons from $\mathrm{b} \to \mathrm{c} \to \mathrm{e}$ decays.

6.3 Determining the Lepton Sample Compositions

The fractions of the lepton samples selected in the data that originate from $\mathrm{b} \to \ell$ and $\mathrm{b} \to \mathrm{c} \to \ell$ decays are determined by fitting the $\mathrm{NN_{b\ell}}$ and $\mathrm{NN_{bc\ell}}$ distributions obtained in the Monte Carlo to the data.

Five free parameters are used in the fitting procedure :-

- $\boldsymbol{f(\mathrm{b} \to \mathrm{e})}$: the fraction of candidate electrons from $\mathrm{b} \to \mathrm{e}$ decays;
- $\boldsymbol{f(\mathrm{b} \to \mathrm{c} \to \mathrm{e})}$: the fraction of candidate electrons from $\mathrm{b} \to \mathrm{c} \to \mathrm{e}$ decays;
- $\boldsymbol{f(\mathrm{b} \to \mu)}$: the fraction of candidate muons from $\mathrm{b} \to \mu$ decays;
- $\boldsymbol{f(\mathrm{b} \to \mathrm{c} \to \mu)}$: the fraction of candidate muons from $\mathrm{b} \to \mathrm{c} \to \mu$ decays.

  The fraction of remaining backgrounds are fixed as $1 - f(\mathrm{b} \to \ell) - f(\mathrm{b} \to \mathrm{c} \to \ell)$, independently for the electron and muon samples. These six fractions are used to form the inclusive Monte Carlo distributions, normalised to the respective number of leptons observed in the data.

- $\boldsymbol{\epsilon_{\mathrm{b}}}$, the Peterson b fragmentation model parameter (Section 2.6.1).

  The p and p_t momentum spectra for prompt and cascade leptons are strongly dependent on the momentum of the weakly decaying parent b hadron. In turn, the momentum spectrum of the b hadron depends on the details of the fragmentation of the primary b quark into the b hadron. The model of Peterson *et al.* is used

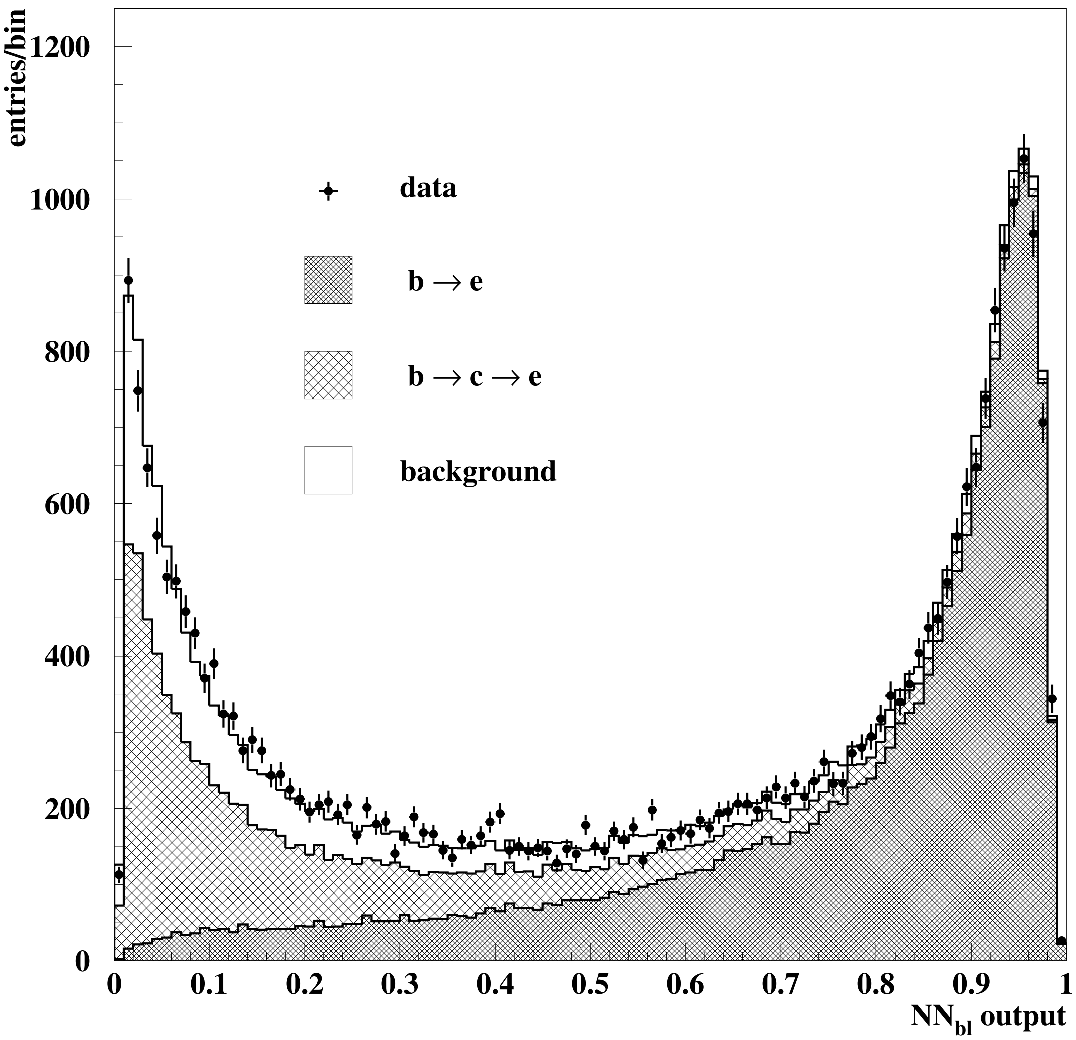

Figure 6.5: *The $NN_{b\ell}$ neural network output distribution for the identification of electrons from $b \to e$ decays.*

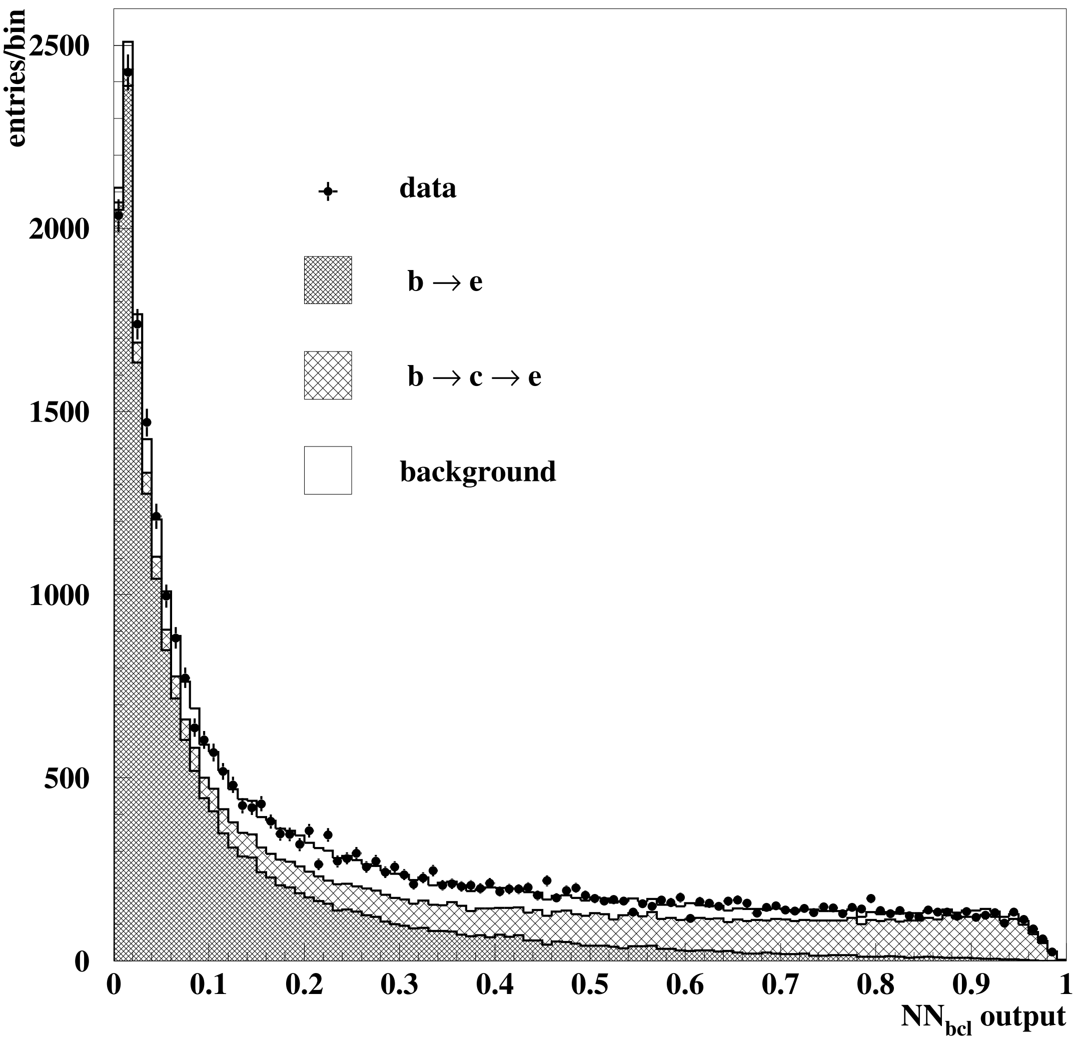

Figure 6.6: *The $NN_{bc\ell}$ neural network output distribution for the identification of electrons from $b \to c \to e$ decays.*

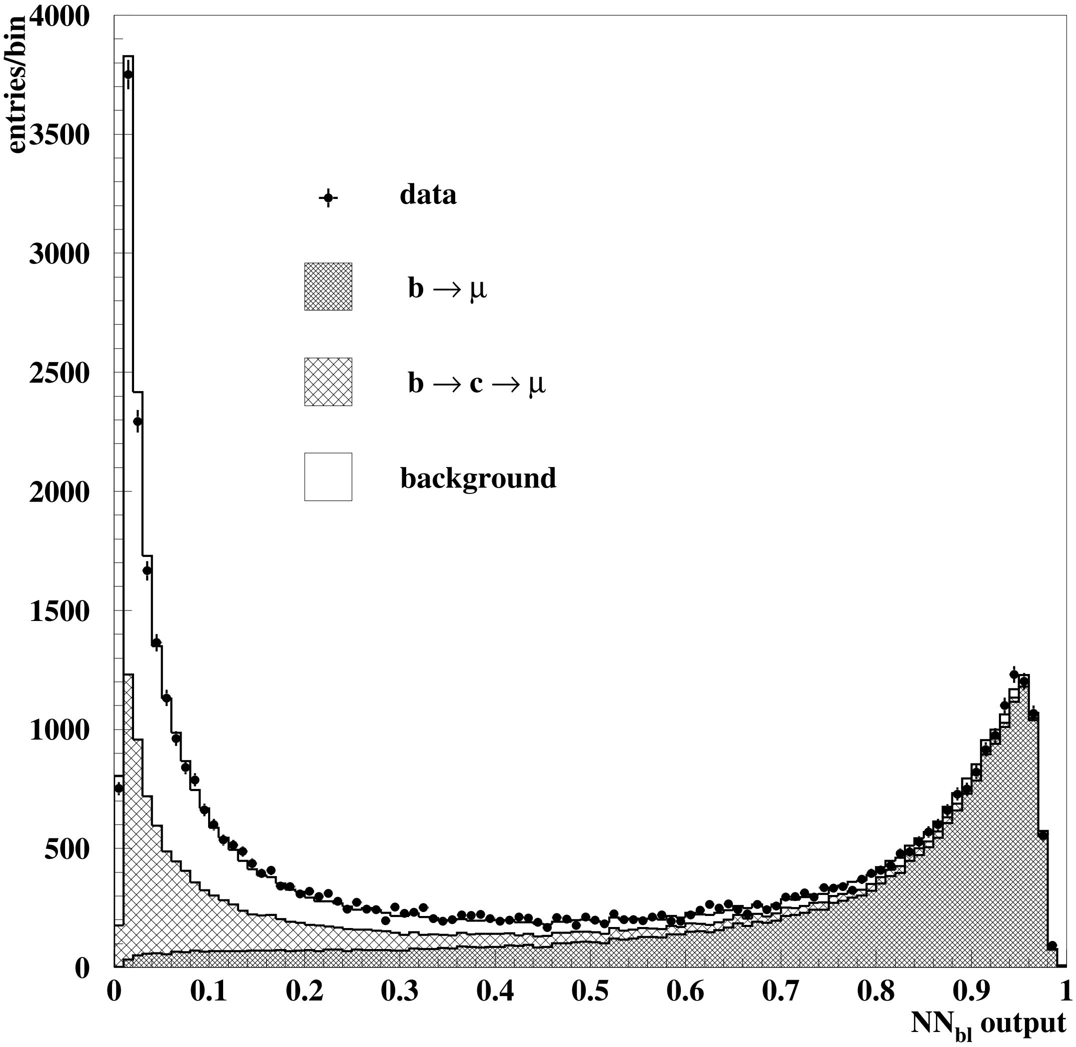

Figure 6.7: *The $NN_{b\ell}$ neural network output distribution for the identification of muons from $b \to \mu$ decays.*

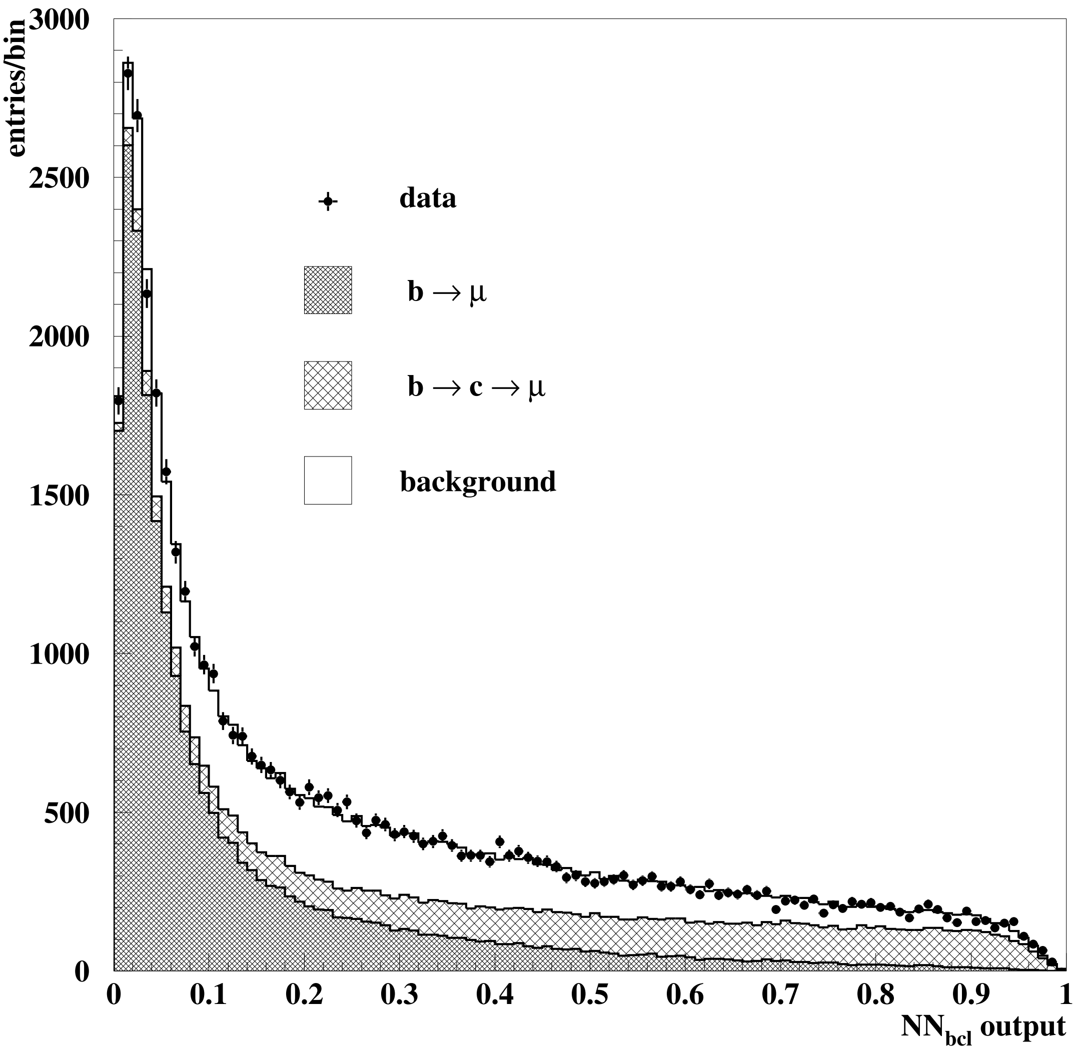

Figure 6.8: *The $NN_{bc\ell}$ neural network output distribution for the identification of muons from $b \to c \to \mu$ decays.*

in the Monte Carlo to describe the distribution of the b fragmentation variable z, the fraction of the b quark momentum carried by the b hadron produced during fragmentation. Allowing the Peterson model parameter, ϵ_{b}, to be a free parameter in the fit reduces the systematic uncertainties associated with the choice of b fragmentation model and model parameter. This is achieved using a reweighting method in which the Monte Carlo events are weighted to give a z distribution corresponding to the desired value of ϵ_{b}. A common value of ϵ_{b} is used for the electron and muon distributions. This introduces a small correlation between the two lepton samples which are otherwise independent. For this reason the electron and muon samples are fitted simultaneously.

In order to obtain the maximum statistical separation power, two dimensional distributions are formed from the outputs of the $\mathrm{NN}_{\mathrm{b}\ell}$ and $\mathrm{NN}_{\mathrm{bc}\ell}$ networks, with 20 bins in $\mathrm{NN}_{\mathrm{b}\ell}$ and 20 in $\mathrm{NN}_{\mathrm{bc}\ell}$ (20×20). This method allows the correlations between the distributions to be taken into account in addition to their intrinsic discrimination power. The method of maximum likelihood was used to fit the Monte Carlo distributions to the data. The log likelihood expressions for the electron and muon distributions were calculated using the methods described in Appendix A and take into account the limited statistics in the Monte Carlo samples. The combined likelihood for the electron and muon samples were maximised for the five fit parameters using the MINUIT [92] package.

The two dimensional distributions for each of the three Monte Carlo contributions are shown in Figures 6.10a-c and 6.11a-c, for electron and muon candidates respectively. These figures show that the distributions are sparsely populated in the regions towards $\mathrm{NN}_{\mathrm{b}\ell} = \mathrm{NN}_{\mathrm{bc}\ell} = 1$, since the neural networks rarely classify a lepton as both a $\mathrm{b} \to \ell$ and $\mathrm{b} \to \mathrm{c} \to \ell$ candidate. In order to prevent the limited Monte Carlo and data statistics in these regions from adversely affecting the fit procedure, an isomorphic transformation is applied to effectively spread the $\mathrm{b} \to \ell$ peak into the sparse region. This distributes the information over the fit region more evenly, without any loss of information or introduction of artificial biases into the distributions.

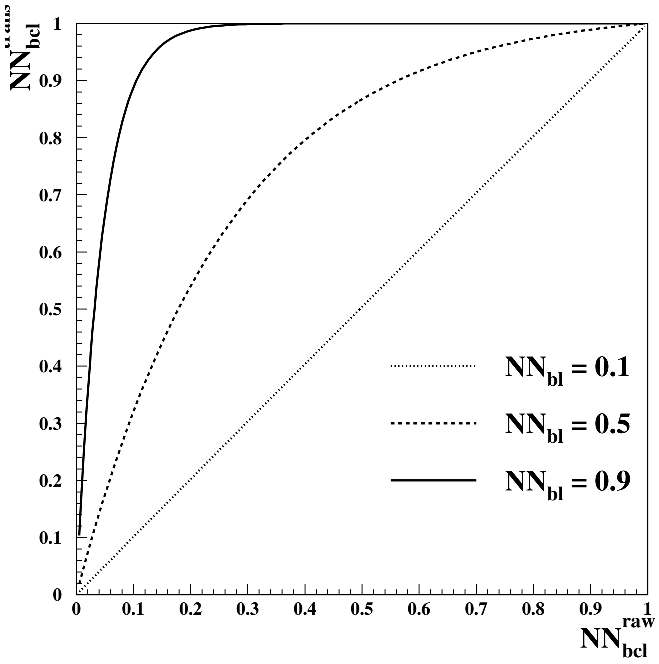

Figure 6.9: *The transformation function for the $NN_{bc\ell}$ network output, for 3 different values of $NN_{b\ell}$.*

Figure 6.9 shows the transformation function between the raw and transformed $\mathrm{NN}_{\mathrm{bc}\ell}$ values. A simple functional form is used,

$$\mathrm{NN}_{\mathrm{bc}\ell}^{\mathrm{trans}} = \frac{1 - e^{-\alpha \cdot \mathrm{NN}_{\mathrm{bc}\ell}^{\mathrm{raw}}}}{1 - e^{-\alpha}} \tag{6.3}$$

where the strength of the transformation, α, is itself a function of the $\mathrm{NN}_{\mathrm{b}\ell}$ output variable,

$$\alpha = \kappa \cdot (\mathrm{NN}_{\mathrm{b}\ell})^{a} \tag{6.4}$$

where κ and a are fixed parameters. This form was found to provide evenly distributed transformed functions with a minimum of arbitrary parameters. The fitted results were found to be insensitive to the particular form of the transformation used, as discussed in Section 6.4. The values $\kappa = 30$ and $a = 3$ where chosen for the main analysis since they produced the most uniformly transformed distributions. The transformed distributions for the full electron and muon samples are shown in Figures 6.10d and 6.11d.

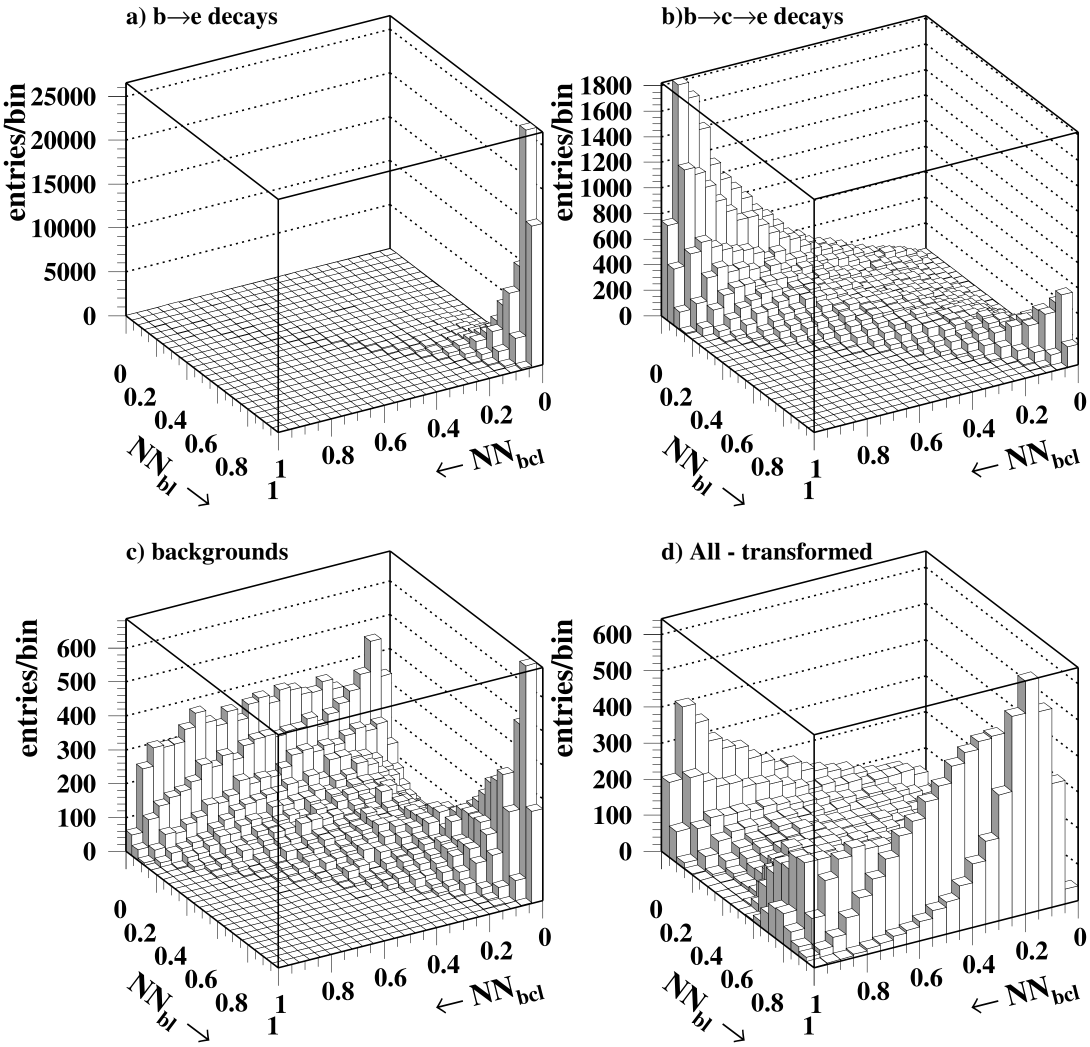

Figure 6.10: *The two–dimensional distributions formed from the $NN_{b\ell}$ and $NN_{bc\ell}$ neural networks for electron candidates. The three Monte Carlo contributions for a) $b \to e$, b) $b \to c \to e$ and c) backgrounds are shown separately. Figure d) shows the overall distribution with the transformed $NN_{bc\ell}$ network output.*

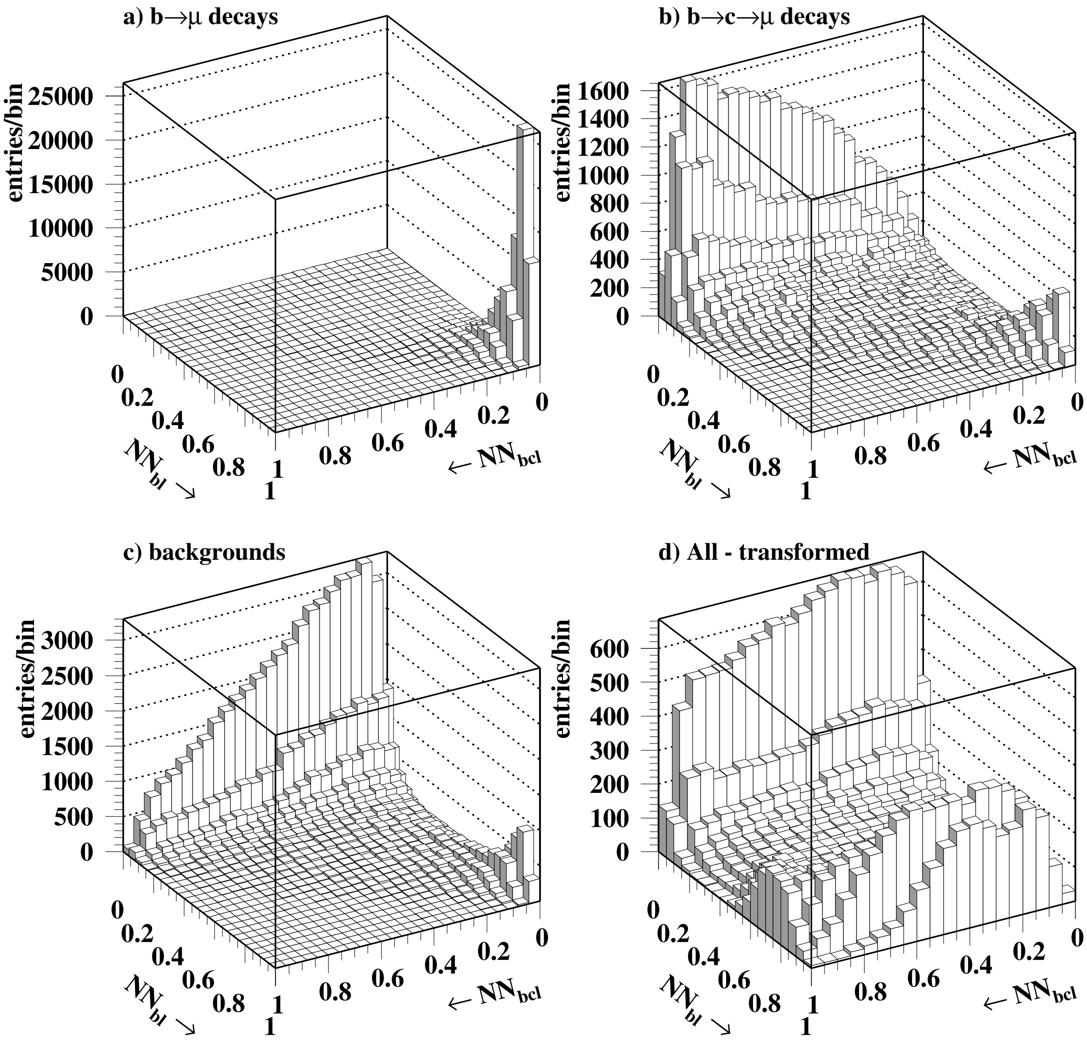

Figure 6.11: *The two–dimensional distributions formed from the $NN_{b\ell}$ and $NN_{bc\ell}$ neural networks for muon candidates. The three Monte Carlo contributions for a) $b \to \mu$, b) $b \to c \to \mu$ and c) backgrounds are shown separately. Figure d) shows the overall distribution with the transformed $NN_{bc\ell}$ network output.*

6.3.1 Monte Carlo Lepton Samples

The Monte Carlo samples of leptons used in the fitting procedure were selected using the same lepton identification criteria as in the data and are also required to be opposite a b–tagged hemisphere. The selected samples are detailed in Table 6.3 where the contributions to the $b \to \ell$, $b \to c \to \ell$ and background samples for each year are outlined. The background classes are also further subdivided into those originating from primary $b\overline{b}$, $c\overline{c}$ and light flavour (uds) events.

Year	$b \to \ell$	$b \to c \to \ell$	Backgrounds		
			$b\overline{b}$	$c\overline{c}$	uds
Electrons					
1992	14 372	7 223	3 426	854	69
1993	11 907	5 989	3 016	545	19
1994	109 005	54 546	27 859	2 272	107
1995	12 472	6 318	3 269	581	25
Total	147 756	74 076	37 570	4 252	220
Muons					
1992	17 306	9 317	11 617	1 623	187
1993	14 075	7 716	9 574	1 011	44
1994	127 563	68 758	87 188	4 059	280
1995	14 515	7 905	9 855	1 024	82
Total	173 459	93 696	118 234	7 717	593

Table 6.3: *Summary of the lepton samples identified in the Monte Carlo in hemispheres opposite a b–tagged hemisphere.*

The use of additional primary $b\overline{b}$ and $c\overline{c}$ Monte Carlo samples to increase the statistical precision in the fit means that the raw composition of the selected samples does not correspond to the natural mixture of the five flavours (u, d, s, c and b) in the data. In order to account for this when fitting to the data, the raw samples are reweighted such that the weighted samples correspond to a true five flavour composition. The Monte Carlo samples are also reweighted so that the relative fractions of events from each year of Monte Carlo agree with those collected in the data.

6.4 Monte Carlo Tests of Fitting Procedure

To test the fitting procedure, the Monte Carlo sample is divided into two equal sub–samples. The first sub–sample is used as a substitute for the real data in the fit procedure whilst the second is retained as the Monte Carlo reference sample. The fitted parameters for the first sample can then be compared to the true information from the Monte Carlo to establish the reliability of the fit. In order to increase the statistical precision of the tests, the b–tagging requirement was removed for the $\mathrm{b} \to \ell$ and $\mathrm{b} \to \mathrm{c} \to \ell$ lepton samples. For these samples, the shapes of the $\mathrm{NN_{b\ell}}$ and $\mathrm{NN_{bc\ell}}$ distributions show only a weak dependence on whether the hemisphere b–tagging requirement was applied. Therefore, removing the requirement for these decays provides a more stringent test of the fit procedure whilst retaining the features of the b–tagged fit.

The fitted fractions of $\mathrm{b} \to \ell$ and $\mathrm{b} \to \mathrm{c} \to \ell$ decays, and the Peterson b fragmentation parameter ϵ_b agree with the true values as shown in Table 6.4. The relative fractions of $\mathrm{b} \to \ell$ and $\mathrm{b} \to \mathrm{c} \to \ell$ decays in these test samples are larger than those listed in Table 6.1 due to the removal of the b–tagging requirement for these sources of leptons.

Fitted Parameter	Electrons		Muons	
	true / %	fitted / %	true / %	fitted / %
$f(\mathrm{b} \to \ell)$	61.06	60.97 ± 0.12	54.63	54.72 ± 0.10
$f(\mathrm{b} \to \mathrm{c} \to \ell)$	30.74	30.86 ± 0.16	29.46	29.47 ± 0.15
background	8.20	8.17 ± 0.20	15.91	15.82 ± 0.19
b fragmentation	true		fitted	
parameter ϵ_b	0.00380		0.00382 ± 0.00008	

Table 6.4: *The true composition and the measured fractions from the fitting procedure for the Monte Carlo sub–samples are shown for electrons and muons separately. The generated and fitted values for the Peterson b fragmentation parameter ϵ_b are also shown.*

To test the stability of the fit procedure with respect to the number of bins used for the distributions, the Monte Carlo test was repeated with the binning ranging from

5×5 up to 40×40 bins in the $\mathrm{NN}_{\mathrm{b}\ell}$ versus $\mathrm{NN}_{\mathrm{bc}\ell}$ distributions. Figure 6.12 shows the fractional difference (in %) between the fitted and true values for each of the five free fit parameters, defined as,

$$\Delta P = \frac{P_{fitted} - P_{true}}{P_{true}}, \tag{6.5}$$

where P is the fitted parameter. There are no biases in the fitted parameters with respect to variations in the binning. The test was also repeated for varying values of the transformation parameters κ and a (Equation 6.4). Figure 6.13 shows the stability of the fitted parameters with respect to changes in these parameters which correspond to substantial variations in the shape of the transformed distributions. Again, no biases were observed in the results. These tests demonstrate that the fit procedure is insensitive to the particular form of the transformation used and the choice of the size of bins, and is therefore reliable.

To check further for biases in the fit procedure the same Monte Carlo sample was used for both the data and Monte Carlo reference samples used in the fit. The statistical variations between the two samples were removed in this test and the fitted results should reproduce the true values exactly with any biases showing up clearly as deviations. No evidence for biases was found.

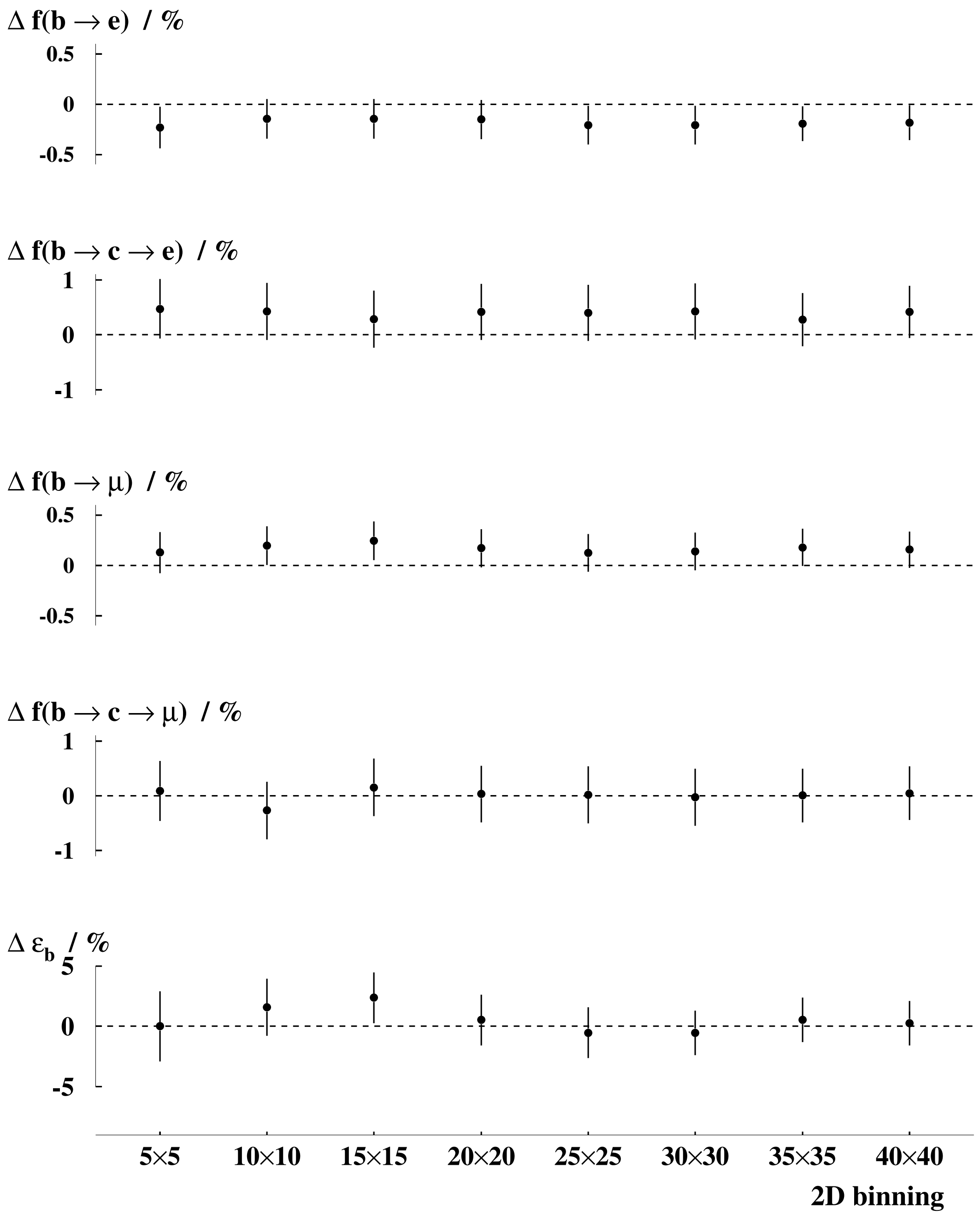

Figure 6.12: *The fractional difference in percent (Equation 6.5) between the fitted and true values for each of the free fit parameters as a function of the binning size.*

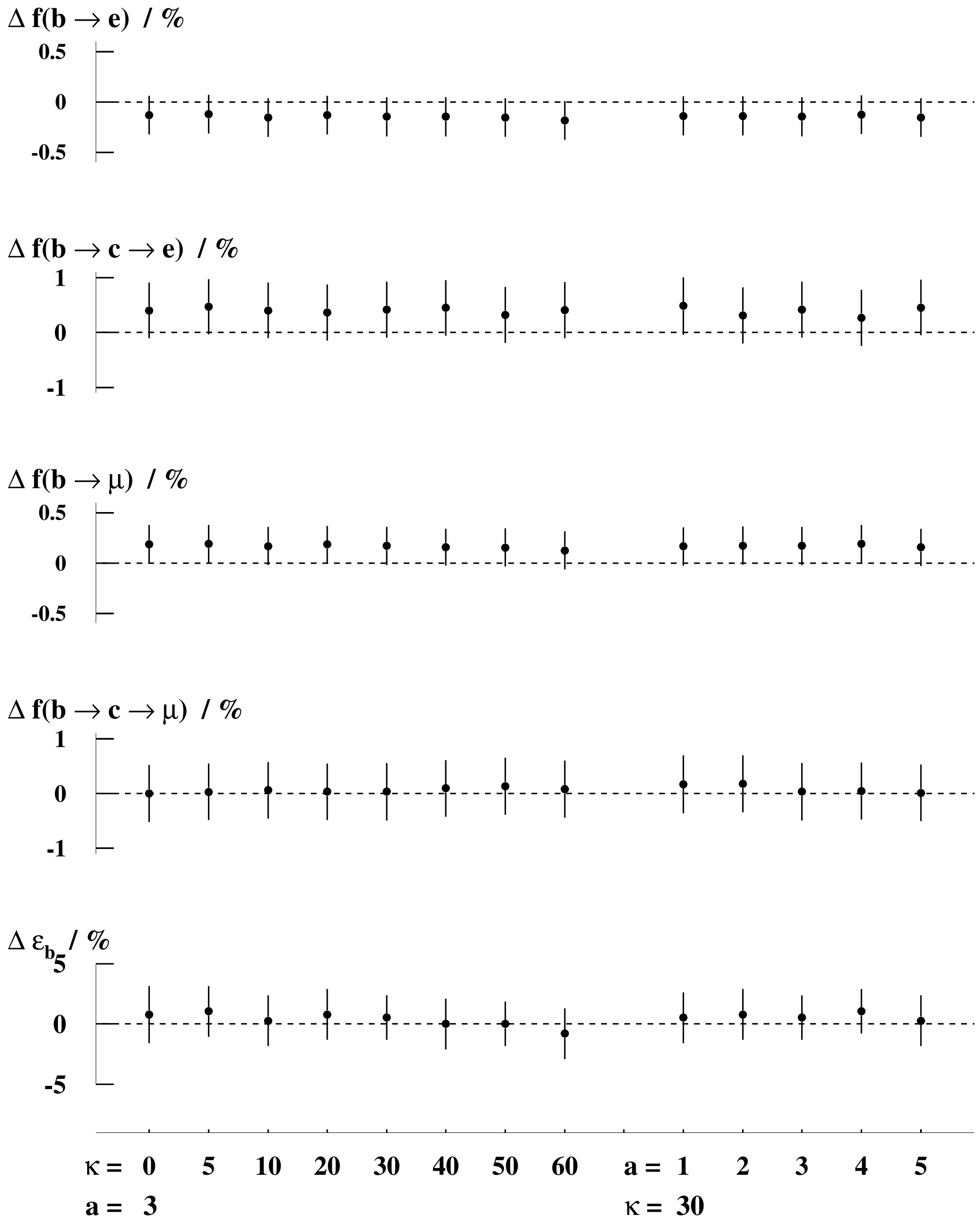

Figure 6.13: *The fractional difference in percent (Equation 6.5) between the fitted and true values for each of the free fit parameters as a function of the parameters used for the $NN_{bc\ell}$ transformation (Equations 6.3 and 6.4). The leftmost set of points are for varying κ with a constant $a = 3$, whilst the rightmost are obtained by varying a with κ fixed to 30.*

Chapter 7

Results

In the previous chapter the Monte Carlo fit techniques used to determine the composition of the selected lepton candidate samples were described. In this chapter, the results of the fit to the data are discussed and the resulting semileptonic branching fractions are calculated. Various corrections which are applied to the Monte Carlo in order to better model the data are described, together with the associated systematic uncertainties. The theoretical uncertainties associated with the choice of b fragmentation and semileptonic b decay models are also determined. Finally, the agreement between data and the various semileptonic decay and fragmentation models is discussed.

7.1 Calculation of the Branching Fractions

The semileptonic branching fractions are given by

$$\begin{aligned}\mathcal{B}(\mathrm{b} \to \mathrm{X}\ell\nu_\ell) &= \frac{N_{\mathrm{b}\to\ell}}{N_\mathrm{b}} \\ &= \frac{N_\ell \cdot f(\mathrm{b}\to\ell)}{\epsilon_{\mathrm{b}\to\ell}} \cdot \frac{1}{N_{\mathrm{b-tags}} \cdot P_\mathrm{b}} \qquad (7.1)\end{aligned}$$

where $N_{\mathrm{b}\to\ell}$ is the number of hemispheres containing a semileptonic b decay and N_b is the total number of true b hemispheres.

The fraction of $\mathrm{b} \to \ell$ decays determined by the fit, $f(\mathrm{b} \to \ell)$, multiplied by the number of lepton candidates, N_ℓ, yields the number of $\mathrm{b} \to \ell$ decays in the selected lepton sample. The total number of b events that decayed semileptonically, $N_{\mathrm{b}\to\ell}$, is then obtained by correcting this number to account for the lepton detection efficiency, $\epsilon_{\mathrm{b}\to\ell}$. The total number of weak b decays in the b–tagged sample, N_b, is obtained from the total number of b–tagged hemispheres, $N_{\mathrm{b-tags}}$, scaled by the sample b purity, P_b, as extracted from the data. The semileptonic branching fractions are determined separately for the electron and muon channels. With $\epsilon_{\mathrm{b}\to\mathrm{c}\to\ell}$ and $f(\mathrm{b} \to \mathrm{c} \to \ell)$ replacing the corresponding expressions for $\mathrm{b} \to \ell$ decays, a similar equation for $\mathcal{B}(\mathrm{b} \to \mathrm{c} \to \mathrm{X}\ell\nu_\ell)$ is obtained.

In the following sections, the results of the fit to the data are presented and the corresponding semileptonic branching fractions are calculated.

7.2 Results

The selected lepton samples used in this thesis are outlined in Table 7.1. A total of 29 516 candidate electrons were selected in the data from a sample of 301 303 b–tagged hemispheres where the detector status criteria for electron identification were satisfied[a]. Similarly, 44 832 candidate muons were selected from 302 577 b–tagged hemispheres which also satisfied the muon identification detector status requirements.

The Monte Carlo fit to the full data sample yields the following semileptonic decay fractions and Peterson b fragmentation parameter,

$$
\begin{aligned}
f(\mathrm{b} \to \mathrm{e}) &= 0.5726 \pm 0.0042, \\
f(\mathrm{b} \to \mathrm{c} \to \mathrm{e}) &= 0.2596 \pm 0.0055, \\
f(\mathrm{b} \to \mu) &= 0.4620 \pm 0.0034, \\
f(\mathrm{b} \to \mathrm{c} \to \mu) &= 0.2166 \pm 0.0051, \\
\epsilon_b &= 0.00573 \pm 0.00040,
\end{aligned}
$$

[a]The detector status criteria for lepton identification are discussed in Section 4.1.1.

where the errors are the data statistical uncertainties. The full statistical correlation matrix for the fitted parameters is shown in Table 7.2.

The measurement of the b purity from the data, described in Chapter 4, and the efficiencies for identifying leptons from semileptonic decays, determined in Chapter 5 give

$$\begin{aligned} P_{\mathrm{b}} &= 91.90\,\%, \\ \epsilon_{\mathrm{b}\to e} &= 56.62\,\%, \\ \epsilon_{\mathrm{b}\to\mu} &= 67.94\,\%, \\ \epsilon_{\mathrm{b}\to\mathrm{c}\to e} &= 33.06\,\%, \\ \epsilon_{\mathrm{b}\to\mathrm{c}\to\mu} &= 42.77\,\%. \end{aligned}$$

Using these results the semileptonic branching fractions are determined using Equation 7.1 as

$$\begin{aligned} \mathcal{B}(\mathrm{b}\to \mathrm{X}e\nu_e) &= (10.78 \pm 0.08\ (\mathrm{stat.}))\,\%, \\ \mathcal{B}(\mathrm{b}\to \mathrm{X}\mu\nu_\mu) &= (10.96 \pm 0.08\ (\mathrm{stat.}))\,\%, \\ \mathcal{B}(\mathrm{b}\to \mathrm{c}\to \mathrm{X}e\nu_e) &= (8.37 \pm 0.17\ (\mathrm{stat.}))\,\%, \\ \mathcal{B}(\mathrm{b}\to \mathrm{c}\to \mathrm{X}\mu\nu_\mu) &= (8.17 \pm 0.19\ (\mathrm{stat.}))\,\%. \end{aligned}$$

where the errors are statistical only.

From the fitted Peterson b fragmentation parameter, the corresponding value for $\langle x_E \rangle_{\mathrm{b}}$, the mean fraction of the beam energy carried by the weakly decaying b hadron, can be determined from the Monte Carlo, giving

$$\langle x_E \rangle_{\mathrm{b}} = 0.709 \pm 0.003\ (\mathrm{stat.}). \tag{7.2}$$

In the following sections the systematic and modelling uncertainties on the semileptonic branching fractions and $\langle x_E \rangle_{\mathrm{b}}$ are discussed.

Year	Electrons		Muons	
	Candidates	b–tagged hemispheres	Candidates	b–tagged hemispheres
1992	4 999	56 617	8 160	56 734
1993	6 413	64 838	9 793	65 237
1994	12 777	126 342	19 049	127 309
1995	5 327	53 506	7 830	53 297
Total	29 516	301 303	44 832	302 577

Table 7.1: *The lepton candidate samples selected in the data in the hemispheres opposite a b–tagged hemisphere. The number of b–tagged hemispheres in events passing the electron and muon identification detector status criteria are also shown.*

	$f(\mathrm{b} \to \mathrm{e})$	$f(\mathrm{b} \to \mathrm{c} \to \mathrm{e})$	$f(\mathrm{b} \to \mu)$	$f(\mathrm{b} \to \mathrm{c} \to \mu)$	ϵ_b
$f(\mathrm{b} \to \mathrm{e})$	1.000				
$f(\mathrm{b} \to \mathrm{c} \to \mathrm{e})$	−0.348	1.000			
$f(\mathrm{b} \to \mu)$	0.125	−0.021	1.000		
$f(\mathrm{b} \to \mathrm{c} \to \mu)$	0.015	−0.003	−0.262	1.000	
ϵ_b	0.323	−0.054	0.388	0.047	1.000

Table 7.2: *The statistical correlation matrix for the fitted parameters.*

7.3 Systematic and Modelling Uncertainties

The Monte Carlo does not provide a perfect model of the data and various corrections are applied in order to produce a better simulation. The Monte Carlo was generated with various physical quantities set according to the experimental results available at that time. In many cases these quantities have since been updated and the Monte Carlo must be corrected accordingly. In addition, discrepancies between the data and Monte Carlo simulation are studied to assess the resulting systematic uncertainties on the results. The treatment of the theoretical uncertainties resulting from the modelling of the b fragmentation and semileptonic decay lepton momentum spectra are also described. The following sections discuss these corrections in detail, with the resulting uncertainties shown in Table 7.3.

7.3.1 Systematic Effects

7.3.1.1 Lepton Finding Efficiencies

The systematic uncertainties relating to the prompt lepton selection efficiencies are discussed in detail in Chapter 5. A relative error of 4 % was assigned to the electron identification selection with an additional relative uncertainty of 0.8 % arising from the rejection of electrons from photon conversions. The muon identification selection was assigned a 1.9 % relative error.

7.3.1.2 Finite Monte Carlo Statistics

The fit is performed taking into account finite Monte Carlo statistics in the log likelihood definition (see Appendix A). The errors returned by the fitting procedure therefore contain components due to the size of both the data and Monte Carlo samples added in quadrature. The data and Monte Carlo statistical uncertainties are separated by repeating the fit using a likelihood expression that assumes infinite Monte Carlo statis-

Parameter	$\mathcal{B}(\mathrm{b\to e})$	$\mathcal{B}(\mathrm{b\to c\to e})$	$\mathcal{B}(\mathrm{b}\to\mu)$	$\mathcal{B}(\mathrm{b\to c}\to\mu)$	$\langle x_E\rangle_\mathrm{b}$
systematic sources					
lepton efficiency	∓0.440	∓0.341	∓0.208	∓0.155	
MC statistics	±0.019	±0.042	±0.022	±0.049	±0.0010
b hadron species	∓0.013	±0.022	∓0.012	±0.030	∓0.0006
$\mathcal{B}(\mathrm{b\to X_u}\ell\nu_\ell)$	±0.004		±0.009	±0.022	∓0.0020
$\mathrm{B^0-\overline{B^0}}$ mixing	±0.002	±0.016	∓0.002	±0.007	±0.0002
lepton fake rate	±0.006	∓0.048	±0.037	∓0.106	∓0.0003
fake lepton spectrum		∓0.003	∓0.002	∓0.042	
$\mathcal{B}(\mathrm{b}\to\tau\to\ell)$	∓0.026	∓0.013	∓0.021	∓0.019	±0.0003
$\mathcal{B}(\mathrm{b}\to\bar{\mathrm{c}}\to\ell)$	∓0.004	∓0.081	∓0.023	∓0.064	±0.0003
$\mathcal{B}(\mathrm{b\to J/\Psi}\to\ell^+\ell^-)$	∓0.004		∓0.002		±0.0001
Λ_b polarisation	±0.004	±0.006	±0.005	±0.026	$^{-0.0013}_{+0.0020}$
detector resolution	±0.074	±0.113	±0.055	±0.086	±0.0004
P_b : R_c	±0.022	±0.017	±0.022	±0.017	
R_b	∓0.001	∓0.001	∓0.001	∓0.001	
$\langle x_E\rangle_\mathrm{c}$	±0.004	±0.003	±0.004	±0.003	
$\mathrm{g\to b\overline{b}}$	±0.016	±0.013	±0.016	±0.013	
$\mathrm{g\to c\overline{c}}$	±0.010	±0.008	±0.010	±0.008	
$\mathcal{B}(\mathrm{D\to K^0_s})$	±0.011	±0.008	±0.011	±0.008	
$\mathrm{D^0}$ lifetime	±0.002	±0.002	±0.002	±0.002	
$\mathrm{D^+}$ lifetime	±0.003	±0.002	±0.003	±0.002	
$\mathrm{D_s}$ lifetime	±0.001	±0.001	±0.001	±0.001	
D charged mult.	±0.011	±0.008	±0.011	±0.008	
D neutral mult.	∓0.024	∓0.018	∓0.024	∓0.018	
$f(\mathrm{c\to D^\pm,\ D^0})$	±0.017	±0.014	±0.017	±0.014	
$f(\mathrm{c\to D_s})$	±0.002	±0.001	±0.002	±0.001	
$f(\mathrm{c}\to\Lambda_\mathrm{c})$	∓0.007	∓0.005	∓0.007	∓0.005	
experimental systematic	±0.450	±0.377	±0.227	±0.234	$^{+0.0031}_{-0.0027}$
model–dependent sources					
$\mathrm{b}\to\ell$	$^{-0.078}_{+0.207}$	$^{+0.126}_{-0.211}$	$^{-0.101}_{+0.221}$	$^{+0.206}_{-0.320}$	$^{-0.0051}_{+0.0081}$
$\mathrm{b\to c}\to\ell$	$^{-0.072}_{+0.057}$	$^{+0.149}_{-0.059}$	$^{-0.064}_{+0.058}$	$^{+0.168}_{-0.048}$	$^{+0.0009}_{-0.0008}$
fragmentation	$^{+0.047}_{-0.028}$	$^{+0.225}_{-0.144}$	$^{+0.096}_{-0.070}$	$^{+0.236}_{-0.180}$	$^{-0.0118}_{+0.0102}$
total models	$^{+0.220}_{-0.110}$	$^{+0.298}_{-0.262}$	$^{+0.248}_{-0.139}$	$^{+0.355}_{-0.370}$	$^{+0.0131}_{-0.0129}$

Table 7.3: *Summary of all experimental systematic and model–dependent uncertainties on $\mathcal{B}(b\to X\ell\nu_\ell)$ and $\mathcal{B}(b\to c\to X\ell\nu_\ell)$ (shown separately for electrons and muons), and $\langle x_E\rangle_b$. All errors are absolute errors given in percent (except for $\langle x_E\rangle_b$). The sign on each contribution indicates the correlation between this systematic uncertainty and the final results.*

tics. This yields the data statistical errors only and allows the Monte Carlo statistical contribution to be determined. The Monte Carlo statistical errors quoted in Table 7.3 include this contribution to the Monte Carlo statistical error added in quadrature with the Monte Carlo errors resulting from the b–purity measurement, as listed in Table 4.2.

7.3.1.3 b Hadron Species

The shape of the $\mathrm{NN}_{\mathrm{b}\ell}$ and $\mathrm{NN}_{\mathrm{bc}\ell}$ distributions for leptons from $\mathrm{b} \to \ell$ or $\mathrm{b} \to \mathrm{c} \to \ell$ decays differ slightly according to the species of the weakly decaying b hadron. The largest difference is observed for leptons from Λ_{b} baryon decays when compared to all other b hadrons. A correction must be made to account for differences in the relative abundance of the different species of b hadrons in data and Monte Carlo. Experimental measurements [3] give the production fraction of $\mathrm{B}^{\pm}$ and B^0 combined to be $(79.4\ ^{+2.5}_{-3.1})\,\%$, $\mathrm{B}^0_{\mathrm{s}} = (10.5\ ^{+1.8}_{-1.7})\,\%$ and $\Lambda_{\mathrm{b}} = (10.1\ ^{+3.9}_{-3.1})\,\%$.

An additional correction must be made to account for the observed difference in the semileptonic branching fraction for inclusive Λ_{b}, $(7.4 \pm 1.1)\,\%$ [29, 30], and the $\mathrm{B}^{\pm}/\mathrm{B}^0$ mixture as measured at the $\Upsilon(4\mathrm{S})$ resonance, $(10.45 \pm 0.21)\,\%$ [3]. Since no such measurement exists for $\mathrm{B}^0_{\mathrm{s}}$ mesons, it is assumed that $\mathrm{B}^0_{\mathrm{s}}$ has the same semileptonic branching fraction as $\mathrm{B}^{\pm}$ and B^0 mesons.

The Monte Carlo sample is reweighted so that it corresponds to the experimentally measured mixture of b hadrons. The Λ_{b} fraction in the Monte Carlo is varied by one standard deviation using the combined errors from the measurements of the Λ_{b} fraction and the semileptonic branching fractions for each b hadron species. This obtains the corresponding contributions to the systematic uncertainties on the results.

7.3.1.4 Weak $\mathrm{b} \to \mathrm{u}$ Transitions

Leptons from $\mathrm{b} \to \mathrm{u}\ell\nu_\ell$ decays form a small percentage of the total $\mathrm{b} \to \ell$ samples since the $\mathrm{b} \to \mathrm{u}$ transition is Cabibbo suppressed relative to $\mathrm{b} \to \mathrm{c}$ decays (Section 2.4). However, due to the small mass of the resulting hadronic system produced in $\mathrm{b} \to \mathrm{u}$ decays, such leptons tend to have higher momenta on average than those from $\mathrm{b} \to \mathrm{c}$ decays and thus produce significantly different $\mathrm{NN}_{\mathrm{b}\ell}$ and $\mathrm{NN}_{\mathrm{bc}\ell}$ distributions.

Combining two recent measurements [107, 108] an experimental measurement for semileptonic $\mathrm{b} \to \mathrm{u}$ decays is obtained giving $\mathcal{B}(\mathrm{b} \to \mathrm{X_u}\ell\nu_\ell) = (0.184 \pm 0.079)\,\%$. The branching fraction in the Monte Carlo is corrected accordingly and the errors used to assign the systematic uncertainties.

7.3.1.5 $\mathbf{B^0 - \overline{B^0}}$ Mixing

The use of jet charge information in the $\mathrm{NN}_{\mathrm{b}\ell}$ and $\mathrm{NN}_{\mathrm{bc}\ell}$ neural networks introduces a weak dependence on the level of $\mathrm{B^0} - \overline{\mathrm{B^0}}$ mixing (Section 6.2.2).

The rate of $\mathrm{B^0} - \overline{\mathrm{B^0}}$ mixing is described by the mixing parameter χ, which is the time integrated probability that a $\mathrm{B^0}$ ($\overline{\mathrm{B^0}}$) meson produced during fragmentation mixes and then decays weakly as a $\overline{\mathrm{B^0}}$ ($\mathrm{B^0}$). For inclusive semileptonic decays the mixing parameter is defined as

$$\chi = \frac{\Gamma\left(\overline{\mathrm{B^0}} \to \mathrm{B^0} \to \ell^+ X\right)}{\Gamma\left(\mathrm{B^0}/\overline{\mathrm{B^0}} \to \ell^\pm X\right)} = \frac{\Gamma\left(\mathrm{B^0} \to \overline{\mathrm{B^0}} \to \ell^- X\right)}{\Gamma\left(\mathrm{B^0}/\overline{\mathrm{B^0}} \to \ell^\pm X\right)}. \tag{7.3}$$

The rate of $\mathrm{B^0}$ mixing in the Monte Carlo is adjusted to correspond to experimental results. The $\mathrm{B^0_d} - \overline{\mathrm{B^0_d}}$ mixing parameter is set to $\chi_\mathrm{d} = 0.172 \pm 0.010$ [3] whilst maximal $\mathrm{B^0_s} - \overline{\mathrm{B^0_s}}$ mixing is used according to the current experimental limit of $\chi_\mathrm{s} > 0.4975$ at the 95 % confidence level [3].

7.3.1.6 Composition of Background Sample

The fitting procedure compares the data to three categories of leptons: $\mathrm{b} \to \ell$ decays, $\mathrm{b} \to \mathrm{c} \to \ell$ decays and background. The fit itself determines the lepton sample compositions in terms of these three categories, such that their relative abundance in the Monte Carlo sample has no influence on the fitted results. However, the composition of the background samples could differ between data and Monte Carlo. Differences in the $\mathrm{NN}_{\mathrm{b}\ell}$ and $\mathrm{NN}_{\mathrm{bc}\ell}$ distributions for the various sources in the background result in a small systematic uncertainty on the fitted results. The shapes of the distributions are similar for non–prompt and fake leptons in $\mathrm{b\overline{b}}$ events but exhibit significant differences to those arising from lighter flavours. The composition of the Monte Carlo sample is discussed in Section 6.2.1. Given that the b purity found in the data is very close to that seen in the Monte Carlo, $(91.90 \pm 0.45)\,\%$ and $(91.25 \pm 0.03)\,\%$ respectively, reweighting the small contributions from light flavour events to account for this difference has a negligible effect on the results.

The Monte Carlo modelling of the fake lepton rates in the electron and muon selections is discussed in Sections 5.3 and 5.4.2. A correction factor of 1.11 ± 0.12 must be applied to the fraction of fake muons in the Monte Carlo to better reproduce the data. For electrons, no correction is required but a relative error of $\pm 21\,\%$ is assigned to the fake rate. The Monte Carlo is reweighted according to these corrections and the errors used to assign a systematic uncertainty due to fake leptons.

A shifted momentum spectrum between data and Monte Carlo for fake leptons would change the shape of the $\mathrm{NN}_{\mathrm{b}\ell}$ and $\mathrm{NN}_{\mathrm{bc}\ell}$ distributions. The total and transverse momentum distributions obtained in the data are compared to the Monte Carlo in Figures 6.1 and 6.3, showing good agreement. Nevertheless, small variations in these distributions are allowed by adjusting the momentum spectrum for fake and non–prompt leptons by $\pm 25\,\mathrm{MeV/c}$, roughly $\pm 0.5\,\%$ of the mean lepton momentum. The $\mathrm{NN}_{\mathrm{b}\ell}$ and $\mathrm{NN}_{\mathrm{bc}\ell}$ neural network input variables and outputs are recalculated with these modified momenta and the fit is repeated. The resulting differences in the fitted results are used to assign the systematic uncertainty.

The background sample also has to be adjusted to reflect the $\mathrm{b} \to \tau \to \ell$ content of the data. In such cases where the tau lepton decays to a high momentum electron or muon, the lepton closely resembles those arising from semileptonic $\mathrm{b} \to \ell$ and $\mathrm{b} \to \mathrm{c} \to \ell$ decays. The Monte Carlo events are reweighted according to the branching fractions $\mathcal{B}(\mathrm{b} \to \tau \to \mathrm{e}) = (0.463 \pm 0.071)\,\%$ and $\mathcal{B}(\mathrm{b} \to \tau \to \mu) = (0.452 \pm 0.069)\,\%$ [3] and the errors used to determine the corresponding systematic uncertainties.

The $b \to \bar{c} \to \ell$ fraction in the background is also varied to assess its effect on the fitted results. The selected events are reweighted to set this branching fraction to $(1.62\ ^{+0.44}_{-0.36})\,\%$ according to an experimental estimate detailed in [109].

7.3.1.7 Contributions from $b \to J/\Psi \to \ell^+\ell^-$ Decays

Leptons from $b \to J/\Psi \to \ell^+\ell^-$ decays have similar kinematic characteristics to direct $b \to \ell$ leptons and therefore produce similar output distributions for the $NN_{b\ell}$ and $NN_{bc\ell}$ neural networks. For this reason, leptons from $b \to J/\Psi \to \ell^+\ell^-$ decays are included with the $b \to \ell$ sample in the fitting procedure and a small correction is applied to the fitted $f(b \to \ell)$ fractions to account for their contribution.

The experimental value given in [3] for $\mathcal{B}(b \to J/\Psi + X)$ is $(1.16 \pm 0.10)\,\%$. Combined with a recent BES measurement for $\mathcal{B}(J/\Psi \to \ell^+\ell^-) = (5.87 \pm 0.10)\,\%$ [110], this gives $\mathcal{B}(b \to J/\Psi \to \ell^+\ell^-) = (0.0681 \pm 0.0060)\,\%$. The numbers of selected leptons from $b \to J/\Psi \to \ell^+\ell^-$ events reconstructed in the Monte Carlo are adjusted accordingly and the fitted $f(b \to \ell)$ fractions corrected to subtract the $b \to J/\Psi \to \ell^+\ell^-$ contributions.

7.3.1.8 Λ_b Polarisation

The shape of the lepton momentum spectra from the semileptonic decays of Λ_b baryons depend upon the degree of polarisation of the Λ_b. Leptons from Λ_b decays are reweighted to simulate a momentum spectrum corresponding to $-56\,\%$ polarisation according to [111]. The systematic uncertainties are calculated using the polarisation range $-13\,\%$ to $-87\,\%$, the $95\,\%$ confidence level limits [111].

7.3.1.9 Detector Resolution

The tracking resolution and reconstruction efficiencies could be slightly different between data and Monte Carlo. The reconstructed track parameters are smeared by a conservative $\pm 10\,\%$ in the Monte Carlo and the lepton detection efficiencies and the fit fractions are recalculated. The b purity is also re–evaluated using the input parameters from the smeared Monte Carlo. The differences in the final values for $\mathcal{B}(\mathrm{b} \to \mathrm{X}\ell\nu_\ell)$, $\mathcal{B}(\mathrm{b} \to \mathrm{c} \to \mathrm{X}\ell\nu_\ell)$ and the b fragmentation parameter are used to estimate this source of systematic uncertainty.

7.3.1.10 b Tagging Purity

The systematic uncertainty on the b–tagging b purity obtained from the data is discussed in Section 4.5. This effect constitutes a $0.49\,\%$ relative error on the final values for $\mathcal{B}(\mathrm{b} \to \mathrm{X}\ell\nu_\ell)$ and $\mathcal{B}(\mathrm{b} \to \mathrm{c} \to \mathrm{X}\ell\nu_\ell)$. The errors shown in Table 4.2 have been split into more categories in Table 7.3 to show the separate contributions from R_c, R_b, $\langle x_E \rangle_\mathrm{c}$ (the mean fraction of the beam energy carried by weakly decaying charmed hadrons), gluon splitting to $\mathrm{b\overline{b}}$ and $\mathrm{c\overline{c}}$ pairs, the branching fraction of charmed mesons into $\mathrm{K^0_s}$, charmed lifetimes, decay multiplicities of charmed mesons and charm production fractions. The errors resulting from the uncertainty in the b purity due to detector resolution and finite Monte Carlo statistics are combined with the other contributions from these sources of error.

7.3.2 Modelling Dependencies

7.3.2.1 Semileptonic b Decay Models

Existing published and preliminary $\mathcal{B}(\mathrm{b} \to \mathrm{X}\ell\nu_\ell)$ measurements [20–23] depend heavily on the modelling of the semileptonic decay. The exact shape of the lepton momentum spectrum is not known and little theoretical progress has been made in recent years. The use of the neural networks $\mathrm{NN}_{\mathrm{b}\ell}$ and $\mathrm{NN}_{\mathrm{bc}\ell}$ to distinguish $\mathrm{b} \to \ell$ and $\mathrm{b} \to \mathrm{c} \to \ell$ decays from the background reduces the dependence of the branching fractions on the shape of the lepton momentum spectrum by making use of additional information. Nevertheless, the simulation of the weak b hadron decays and the prediction of the lepton momentum spectrum is still a large source of theoretical uncertainty.

Different decay models are used to estimate the effects of the modelling on the fitted parameters and lepton identification efficiencies (Section 2.6.4). The Monte Carlo events are reweighted to reproduce the various predictions for lepton momentum spectra in the b hadron rest frame. The ACCMM model [40] is used for $\mathrm{b} \to \ell$ decays with the ISGW and ISGW** [41] models providing the $+1\sigma$ and -1σ deviations respectively, as prescribed in [102]. For the cascade decays, $\mathrm{b} \to \mathrm{c} \to \ell$, the ACCMM model predictions for the $\mathrm{c} \to \ell$ lepton momentum spectra are combined with CLEO measurements of the $\mathrm{b} \to \mathrm{D}$ momentum spectrum for the central results, as described in [102], with the $\pm 1\sigma$ errors derived from the experimental uncertainties on these momentum spectra. Although the models were derived for B^0 and $\mathrm{B}^{\pm}$ mesons only, all b hadrons are reweighted. This has a very small effect on the central results but provides a more conservative estimate of the modelling uncertainties than when only the B^0 and $\mathrm{B}^{\pm}$ decays are reweighted. The agreement between the data and these and other semileptonic decay models is further investigated in Section 7.7.

Since the b–tagging requirement highly suppresses contributions from primary $\mathrm{c\bar{c}}$ events, the error arising from the modelling of the lepton momentum spectra from semileptonic decays in charm events, $\mathrm{c} \to \ell$, is negligible. These decays are simply reweighted to the central ACCMM model as described in [102].

The minimum momentum cut of 2 GeV/c imposed on the selected leptons means that the measured lepton identification efficiencies correspond to a restricted momentum range. The effect of the extrapolation below the minimum momentum is taken into account when evaluating the lepton selection efficiencies corresponding to the different models.

7.3.2.2 b Fragmentation Models

Several models have been proposed to describe the heavy quark fragmentation process and these are discussed in Section 2.6.1. The function of Peterson *et al.* [15] was used to simulate fragmentation in $\mathrm{b\overline{b}}$ and $\mathrm{c\overline{c}}$ events in the Monte Carlo. For b hadrons, the Peterson parameter is determined from the fit by reweighting the Monte Carlo events. For charm events, the parameter is varied to describe a $\langle x_E \rangle_\mathrm{c}$ for charm hadrons of 0.484 ± 0.008 [102]. As prescribed in [102], the models of Collins and Spiller [16] and Kartvelishvili *et al.* [17] are used to estimate the systematic uncertainties arising from the shape of the b quark fragmentation function, quoted as the $+1\sigma$ and -1σ errors respectively. These models also have one free parameter. The Monte Carlo is reweighted to simulate each function and the corresponding free parameter determined from the fit.

The effects of the differing fragmentation functions and fitted parameters on the lepton efficiencies are also included in the fragmentation modelling errors quoted in Table 7.3. The systematic uncertainties associated with the b fragmentation models are determined from the observed variations in the derived values of branching fractions and $\langle x_E \rangle_\mathrm{b}$ obtained with the various fragmentation functions. The agreement between the data and these models is further discussed in Section 7.7.

7.4 Results

The input distributions for the $\mathrm{NN_{b\ell}}$ and $\mathrm{NN_{bc\ell}}$ neural networks and the resulting network output distributions presented in Chapter 6, show the Monte Carlo distributions adjusted according to the fitted parameters and systematic corrections discussed in the previous sections. Good agreement between the data and Monte Carlo is observed; the χ^2/bin for the fitted $\mathrm{NN_{b\ell}}$ distributions is 1.25 and 1.00 for electrons and muons respectively, whilst for the $\mathrm{NN_{bc\ell}}$ distributions the χ^2/bin is 1.15 and 0.88, respectively.

	Electrons	Muons
P_{b}	0.9190 ± 0.0002 (stat.) ± 0.0045 (syst.)	
$N_{\mathrm{b-tags}}$	301303	302577
N_ℓ	29516	44832
$\epsilon_{\mathrm{b}\to\ell}$	0.5662 ± 0.0231 (syst.)	0.6794 ± 0.0129 (syst.)
$f(\mathrm{b}\to\ell)$	$0.5726 \pm 0.0042 \pm 0.0041$ (syst.)	$0.4620 \pm 0.0034 \pm 0.0031$ (syst.)
$\mathcal{B}(\mathrm{b}\to \mathrm{X}\ell\nu_\ell)$	$(10.780 \pm 0.079 \pm 0.450\ ^{+0.220}_{-0.109})$ %	$(10.964 \pm 0.081 \pm 0.227\ ^{+0.248}_{-0.139})$ %
$\epsilon_{\mathrm{b}\to\mathrm{c}\to\ell}$	0.3306 ± 0.0135 (syst.)	0.4277 ± 0.0081 (syst.)
$f(\mathrm{b}\to\mathrm{c}\to\ell)$	$0.2596 \pm 0.0055 \pm 0.0047$ (syst.)	$0.2166 \pm 0.0051 \pm 0.0045$ (syst.)
$\mathcal{B}(\mathrm{b}\to\mathrm{c}\to \mathrm{X}\ell\nu_\ell)$	$(8.370 \pm 0.177 \pm 0.377\ ^{+0.298}_{-0.262})$ %	$(8.167 \pm 0.192 \pm 0.234\ ^{+0.355}_{-0.370})$ %

Table 7.4: *Results for the combined data sample including all systematic uncertainties for electrons and muons. The uncertainties due to semileptonic decay and fragmentation modelling are shown in the last error on the branching fractions.*

	$\mathcal{B}(\mathrm{b}\to \mathrm{X}e\nu_e)$	$\mathcal{B}(\mathrm{b}\to\mathrm{c}\to \mathrm{X}e\nu_e)$	$\mathcal{B}(\mathrm{b}\to \mathrm{X}\mu\nu_\mu)$	$\mathcal{B}(\mathrm{b}\to\mathrm{c}\to \mathrm{X}\mu\nu_\mu)$
$\mathcal{B}(\mathrm{b}\to \mathrm{X}e\nu_e)$	1.00			
$\mathcal{B}(\mathrm{b}\to\mathrm{c}\to \mathrm{X}e\nu_e)$	0.40	1.00		
$\mathcal{B}(\mathrm{b}\to \mathrm{X}\mu\nu_\mu)$	0.34	−0.22	1.00	
$\mathcal{B}(\mathrm{b}\to\mathrm{c}\to \mathrm{X}\mu\nu_\mu)$	−0.26	0.53	−0.22	1.00

Table 7.5: *The full correlation matrix from the averaging procedure for the $\mathcal{B}(b \to Xe\nu_e)$, $\mathcal{B}(b \to X\mu\nu_\mu)$, $\mathcal{B}(b \to c \to Xe\nu_e)$ and $\mathcal{B}(b \to c \to X\mu\nu_\mu)$ branching fractions.*

All the relevant quantities needed to calculate the semileptonic branching fractions $\mathcal{B}(\mathrm{b} \to \mathrm{X}\ell\nu_\ell)$ and $\mathcal{B}(\mathrm{b} \to \mathrm{c} \to \mathrm{X}\ell\nu_\ell)$ are summarised in Table 7.4. The values

$$\begin{aligned}
\mathcal{B}(\mathrm{b} \to \mathrm{X}e\nu_e) &= (10.78 \pm 0.08\ (\mathrm{stat.}) \pm 0.45\ (\mathrm{syst.}) \ {}^{+\,0.22}_{-\,0.11}\ (\mathrm{model}))\,\%, \\
\mathcal{B}(\mathrm{b} \to \mathrm{X}\mu\nu_\mu) &= (10.96 \pm 0.08\ (\mathrm{stat.}) \pm 0.23\ (\mathrm{syst.}) \ {}^{+\,0.25}_{-\,0.14}\ (\mathrm{model}))\,\%, \\
\mathcal{B}(\mathrm{b} \to \mathrm{c} \to \mathrm{X}e\nu_e) &= (8.37 \pm 0.18\ (\mathrm{stat.}) \pm 0.38\ (\mathrm{syst.}) \ {}^{+\,0.30}_{-\,0.26}\ (\mathrm{model}))\,\%, \\
\mathcal{B}(\mathrm{b} \to \mathrm{c} \to \mathrm{X}\mu\nu_\mu) &= (8.17 \pm 0.19\ (\mathrm{stat.}) \pm 0.23\ (\mathrm{syst.}) \ {}^{+\,0.36}_{-\,0.37}\ (\mathrm{model}))\,\%
\end{aligned}$$

are obtained for electrons and muons independently, showing good consistency with lepton universality. These four branching fractions are combined to obtain

$$\begin{aligned}
\mathcal{B}(\mathrm{b} \to \mathrm{X}\ell\nu_\ell) &= (10.83 \pm 0.10\ (\mathrm{stat.}) \pm 0.20\ (\mathrm{syst.}) \ {}^{+\,0.20}_{-\,0.13}\ (\mathrm{model}))\,\%, \\
\mathcal{B}(\mathrm{b} \to \mathrm{c} \to \mathrm{X}\ell\nu_\ell) &= (8.40 \pm 0.16\ (\mathrm{stat.}) \pm 0.21\ (\mathrm{syst.}) \ {}^{+\,0.33}_{-\,0.29}\ (\mathrm{model}))\,\%
\end{aligned}$$

where ℓ represents either an electron or a muon.

The results were combined taking into account the full correlation matrix which combines the statistical correlations resulting from the fit procedure, as shown in Table 7.2, with the systematic correlations resulting from the correlated systematic and modelling errors shown in Table 7.3. The same averaging mechanism was used as that for the combined LEP heavy flavour results which are described in detail in [102] and obtained from [112]. The overall correlation matrix for the individual results is given in Table 7.5.

The combined value derived for $\mathcal{B}(\mathrm{b} \to \mathrm{c} \to \mathrm{X}\ell\nu_\ell)$ is outside the range given by $\mathcal{B}(\mathrm{b} \to \mathrm{c} \to \mathrm{X}e\nu_e)$ and $\mathcal{B}(\mathrm{b} \to \mathrm{c} \to \mathrm{X}\mu\nu_\mu)$ due to large off–diagonal terms in the covariance matrix and strong correlations with the $\mathcal{B}(\mathrm{b} \to \mathrm{X}\ell\nu_\ell)$ measurements. The combined statistical error on $\mathcal{B}(\mathrm{b} \to \mathrm{X}\ell\nu_\ell)$ is larger than the individual errors on $\mathcal{B}(\mathrm{b} \to \mathrm{X}e\nu_e)$ and $\mathcal{B}(\mathrm{b} \to \mathrm{X}\mu\nu_\mu)$ since the statistical errors from $\mathcal{B}(\mathrm{b} \to \mathrm{c} \to \mathrm{X}e\nu_e)$ and $\mathcal{B}(\mathrm{b} \to \mathrm{c} \to \mathrm{X}\mu\nu_\mu)$ also contribute.

Figure 7.1 shows the central results and one sigma error contours for the $\mathcal{B}(\mathrm{b} \to \mathrm{X}\ell\nu_\ell)$ and $\mathcal{B}(\mathrm{b} \to \mathrm{c} \to \mathrm{X}\ell\nu_\ell)$ results, comparing the individual lepton channels to the combined

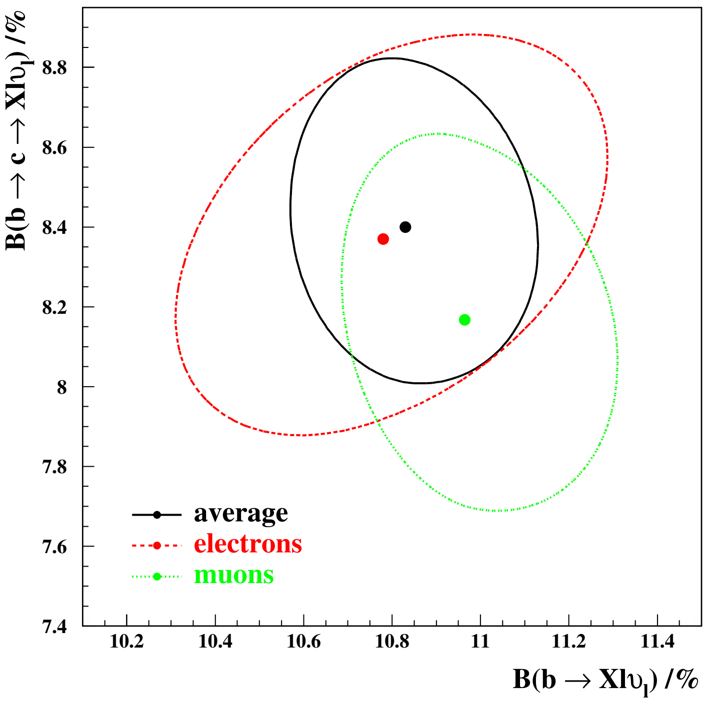

Figure 7.1: *The central results and one sigma error contours for the $\mathcal{B}(b \to X\ell\nu_\ell)$ and $\mathcal{B}(b \to c \to X\ell\nu_\ell)$ results. The results for electrons (dashed red) and muons (dotted green) are compared to the correlated average (solid black).*

results. This figure does not show the correlations between the individual lepton channels.

From the fitted b fragmentation model parameters, the average value of the fraction of the beam energy carried by the weakly decaying b hadron is obtained, giving

$$\langle x_E \rangle_{\rm b} = 0.709 \pm 0.003\ (\text{stat.}) \pm 0.003\ (\text{syst.}) \pm 0.013\ (\text{model})$$

where the modelling error is dominated by the choice of b fragmentation model.

7.5 Agreement between Data and Monte Carlo

In order to verify that the systematic and modelling uncertainties discussed in Section 7.3 give realistic errors on the final results, it is necessary to establish that these variations encompass any discrepancies between data and Monte Carlo relevant to the $\mathrm{NN}_{\mathrm{b}\ell}$ and $\mathrm{NN}_{\mathrm{bc}\ell}$ neural networks.

Figures 7.2 and 7.3 show for each network input variable the ratio of the data to the Monte Carlo, for the selected electron and muon candidates respectively. The shaded regions show the upper and lower bounds on the Monte Carlo variations due to the systematic and modelling uncertainties, evaluated by adding linearly the $\pm 1\sigma$ variations for each source of uncertainty. This gives a conservative estimate of the overall Monte Carlo variations since the correlations between the individual corrections are not taken into account. Overall, good agreement between the data and Monte Carlo is observed with the residual differences encompassed by the systematic and modelling variations.

The corresponding ratios for the $\mathrm{NN}_{\mathrm{b}\ell}$ and $\mathrm{NN}_{\mathrm{bc}\ell}$ distributions are presented in Figure 7.4, showing that the systematic and modelling variations which encompass the differences between data and Monte Carlo for the input parameters also cover the discrepancies in the neural network outputs. Systematic trends are present in the $\mathrm{NN}_{\mathrm{b}\ell}$ distributions where the data is systematically lower than the Monte Carlo in the regions towards $\mathrm{NN}_{\mathrm{b}\ell} = 1$, and correspondingly higher for $\mathrm{NN}_{\mathrm{b}\ell} \lesssim 0.8$ due to the Monte Carlo normalisation to the data. These differences are discussed further in Section 7.7 where the agreement between the data and Monte Carlo for the various theoretical models used to describe semileptonic b decays and b fragmentation is studied.

Additional checks were also performed to assess directly the effect that any discrepancies between data and Monte Carlo in the description of the neural network input variables had on the performance of the $\mathrm{NN}_{\mathrm{b}\ell}$ and $\mathrm{NN}_{\mathrm{bc}\ell}$ neural networks. For each input variable in turn, the differences between the means of the distributions in the data and Monte Carlo were assessed. The fit procedure was then repeated twice, with this variable in the Monte Carlo shifted by $\pm$ twice the observed difference. The resulting variations in the fitted parameters were found to be consistent with those discussed in Section 7.3 and small when compared to the combined systematic and modelling uncertainties.

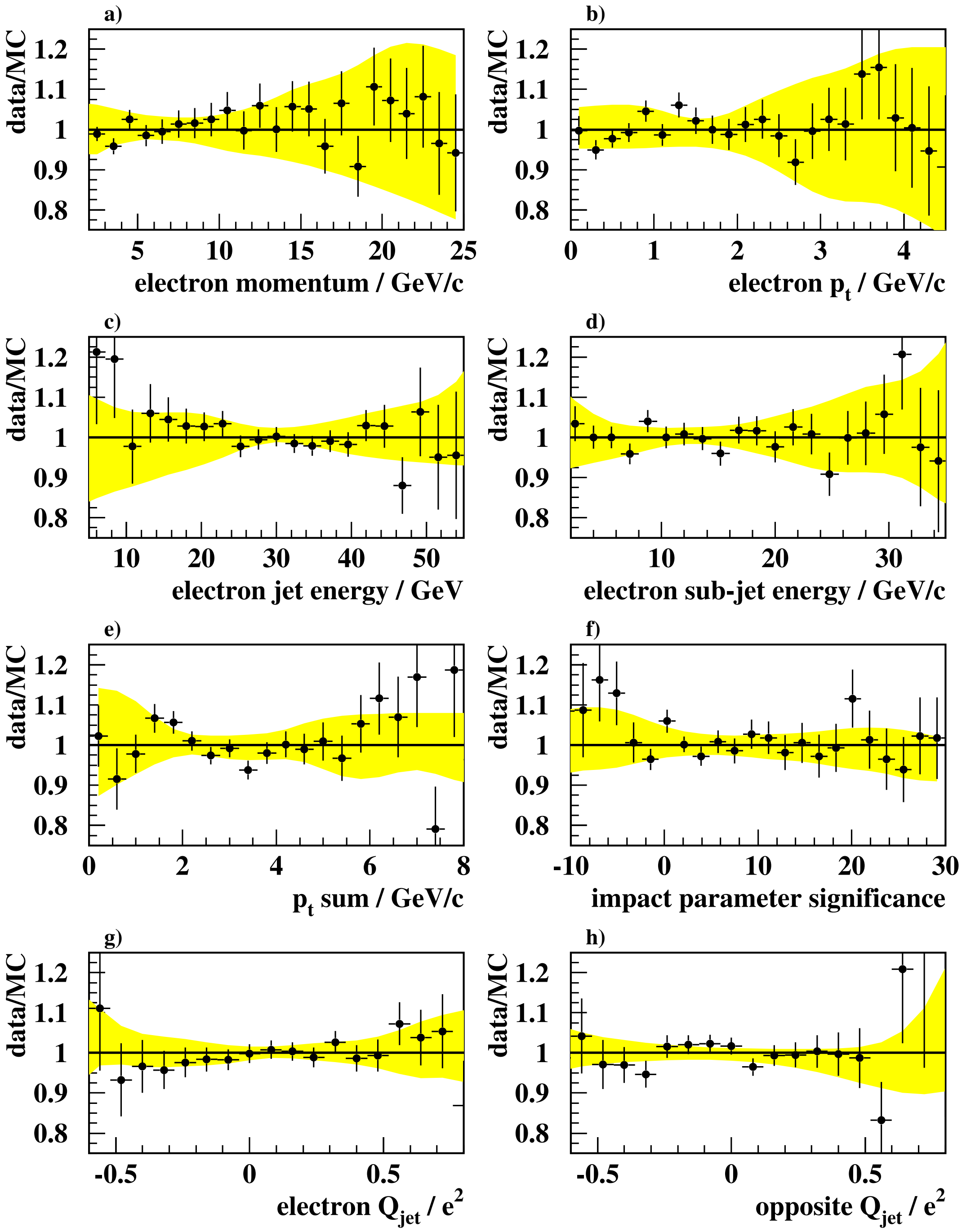

Figure 7.2: *The ratio of the data to Monte Carlo for each input variable for the electron $NN_{b\ell}$ and $NN_{bc\ell}$ neural networks. The shaded regions show the Monte Carlo variations due to the systematic and modelling uncertainties.*

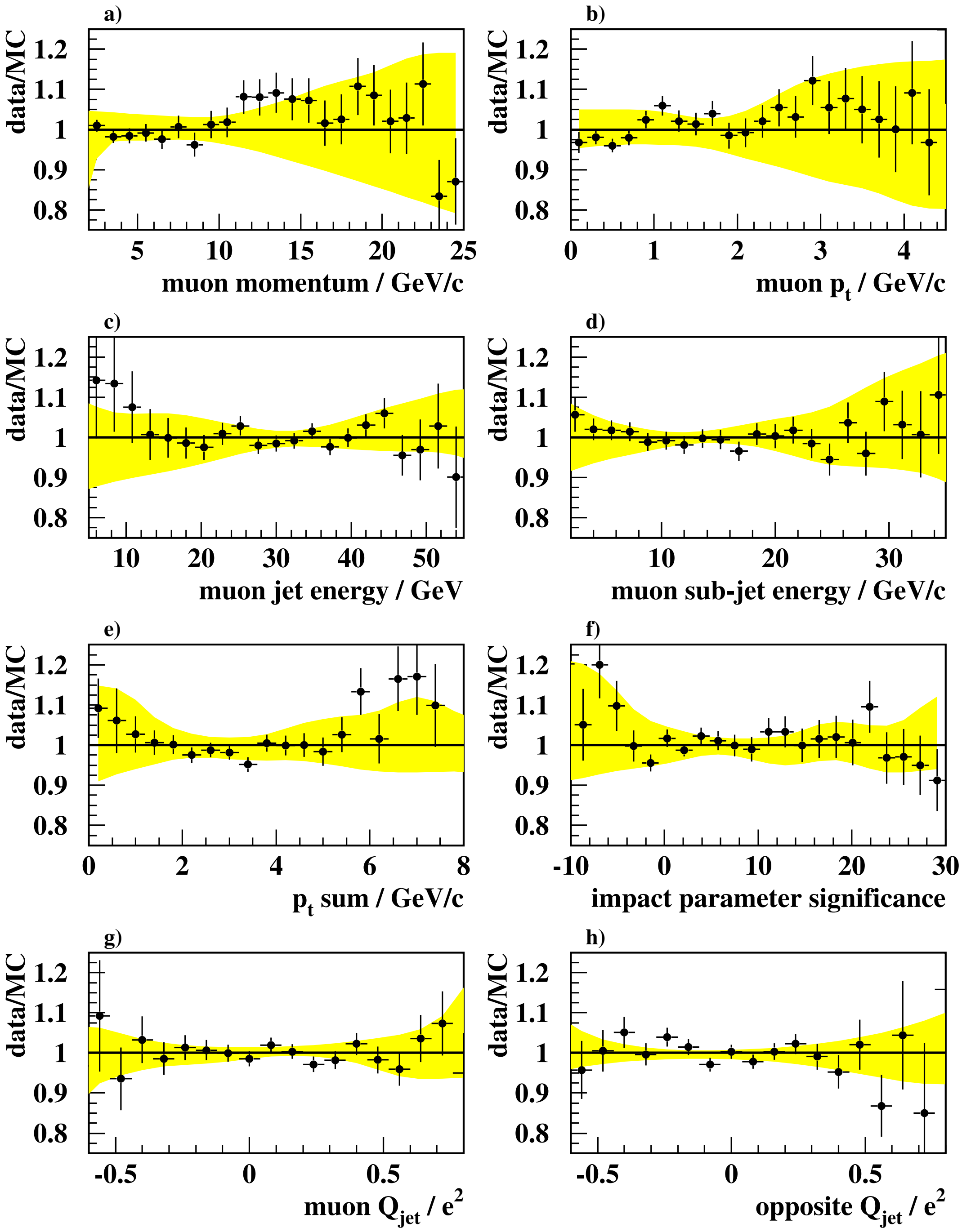

Figure 7.3: *The ratio of the data to Monte Carlo for each input variable for the muon $NN_{b\ell}$ and $NN_{bc\ell}$ neural networks. The shaded regions show the Monte Carlo variations due to the systematic and modelling uncertainties.*

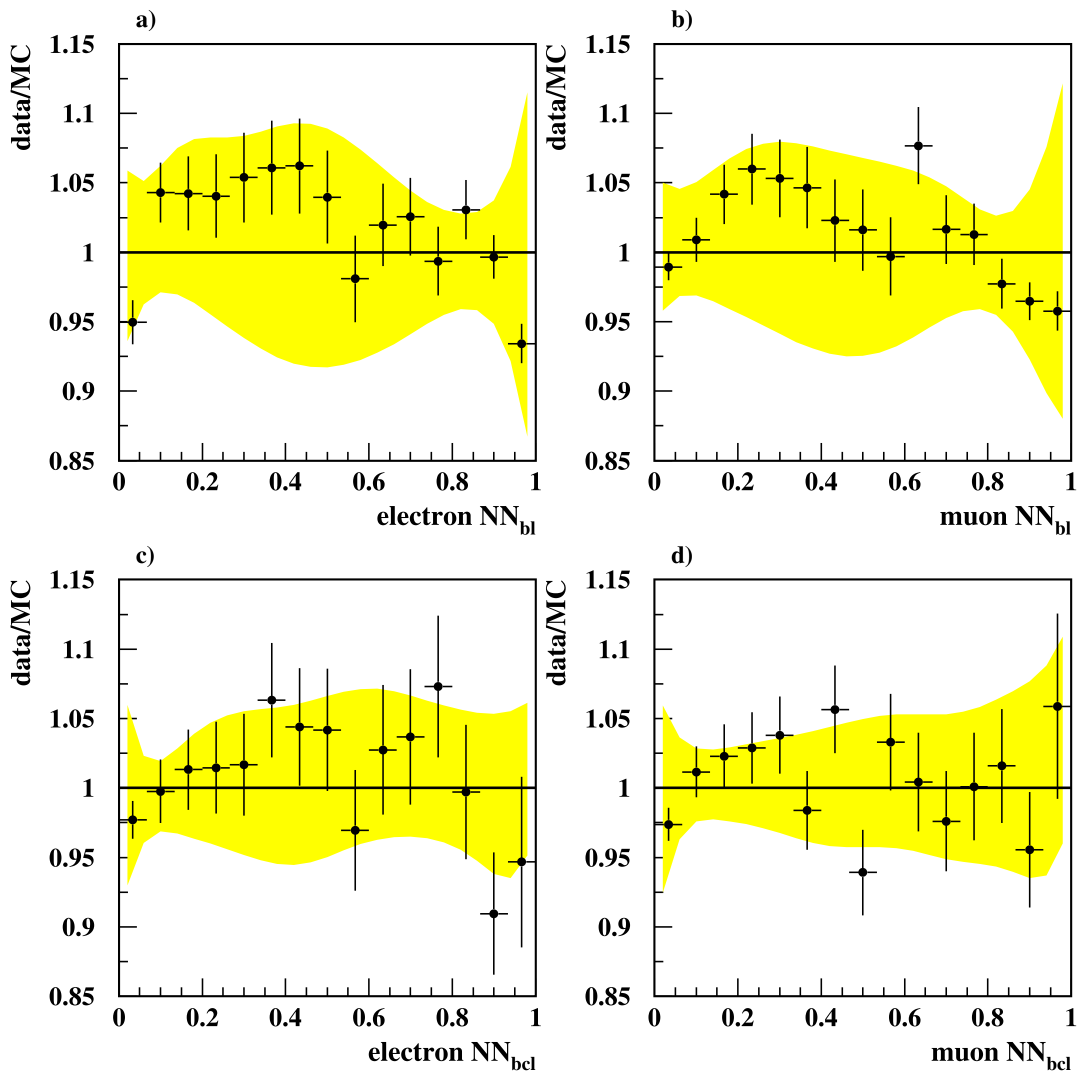

Figure 7.4: *The ratio of the data to the Monte Carlo for the $NN_{b\ell}$ and $NN_{bc\ell}$ neural network distributions. The shaded regions show the Monte Carlo variations due to the systematic and modelling uncertainties.*

7.6 Consistency Checks

Various tests are performed on the data to check the stability of the results by varying the lepton selection criteria.

- The minimum lepton momentum cut is increased from the nominal 2.0 GeV/c to 5.0 GeV/c in steps of 0.5 GeV/c and the branching fractions $\mathcal{B}(\mathrm{b} \to \mathrm{X}\ell\nu_\ell)$ and $\mathcal{B}(\mathrm{b} \to \mathrm{c} \to \mathrm{X}\ell\nu_\ell)$ are recalculated at each point.

- The fit is performed over a restricted range of the $\mathrm{NN}_{\mathrm{b}\ell}$ distribution, $\mathrm{NN}_{\mathrm{b}\ell} > \mathrm{NN}_{\mathrm{b}\ell}^{\mathrm{cut}}$, with the cut value ranging from 0.0 to 0.6 in steps of 0.1. For each cut value $\mathcal{B}(\mathrm{b} \to \mathrm{X}\ell\nu_\ell)$ is recalculated.

- The fit is performed over a restricted range of the $\mathrm{NN}_{\mathrm{bc}\ell}$ distribution, $\mathrm{NN}_{\mathrm{bc}\ell} > \mathrm{NN}_{\mathrm{bc}\ell}^{\mathrm{cut}}$, with the cut value ranging from 0.0 to 0.4 in steps of 0.1. For each cut value $\mathcal{B}(\mathrm{b} \to \mathrm{c} \to \mathrm{X}\ell\nu_\ell)$ is recalculated.

The results are given in Figure 7.5 where the errors are statistical only.

Increasing either the minimum momentum or $\mathrm{NN}_{\mathrm{b}\ell}$ cut values primarily removes the background contributions and $\mathrm{b} \to \mathrm{c} \to \ell$ decays, increasing the $\mathrm{b} \to \ell$ purity of the lepton samples. No significant momentum biases are seen in the $\mathcal{B}(\mathrm{b} \to \mathrm{X}\ell\nu_\ell)$ results as shown in Figure 7.5a. Figure 7.5b shows the results obtained for the $\mathcal{B}(\mathrm{b} \to \mathrm{X}\ell\nu_\ell)$ branching fractions with an increasing cut value on the $\mathrm{NN}_{\mathrm{b}\ell}$ network output. Again, no significant variations are observed.

The model–dependent errors are not shown in Figure 7.5 but they increase substantially as the cut values are raised since the efficiencies for selecting the prompt leptons decrease and the corresponding modelling uncertainties on the efficiency extrapolations below the cut values become large. In particular, the minimum momentum and $\mathrm{NN}_{\mathrm{b}\ell}$ cuts reject a substantial fraction of the $\mathrm{b} \to \mathrm{c} \to \ell$ lepton samples (see Figures 6.1, 6.3, 6.5 and 6.7) such that it is meaningless is evaluate $\mathcal{B}(\mathrm{b} \to \mathrm{c} \to \mathrm{X}\ell\nu_\ell)$ for these tests.

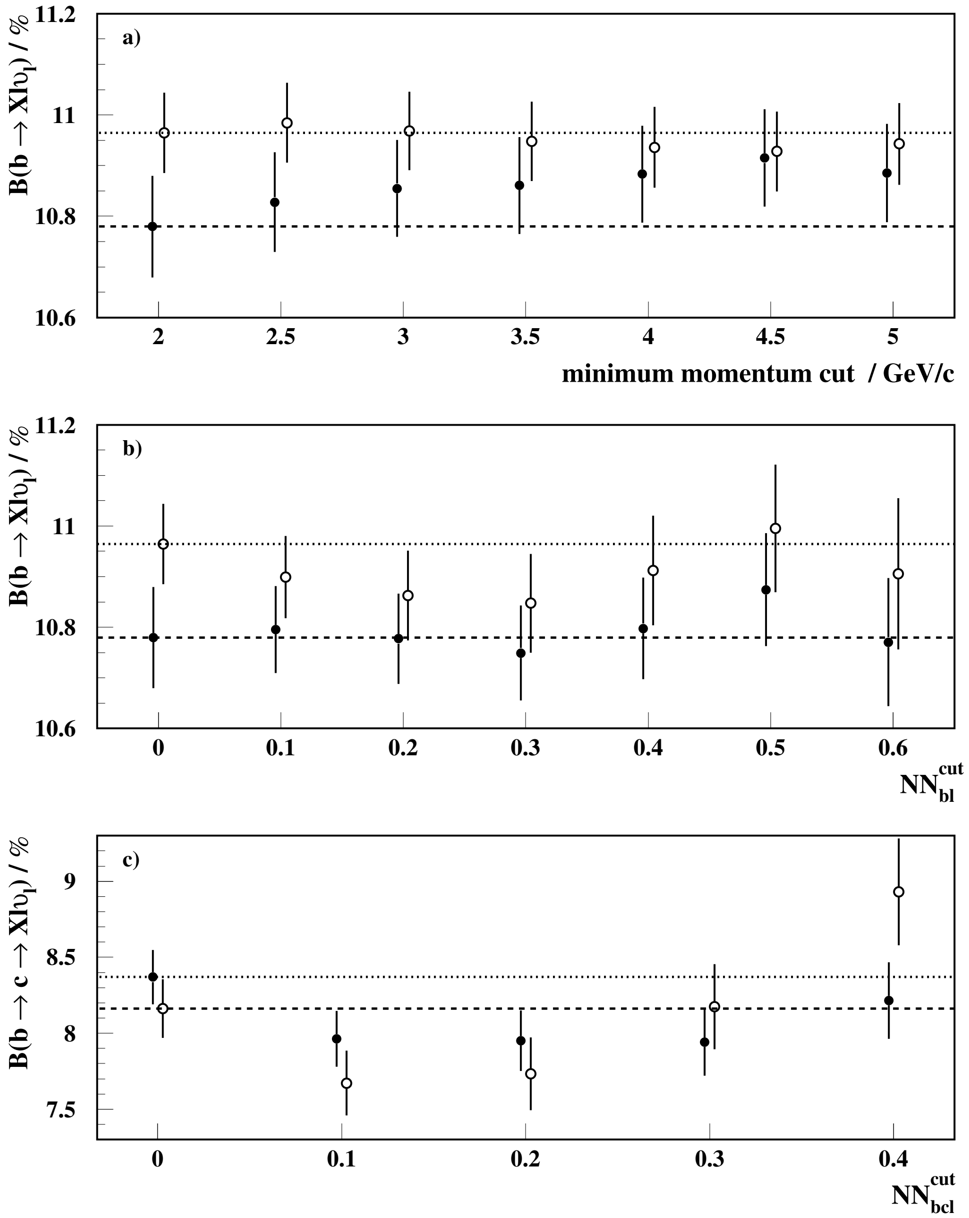

Figure 7.5: *Consistency checks on the central values derived for $\mathcal{B}(b \to X\ell\nu_\ell)$ and $\mathcal{B}(b \to c \to X\ell\nu_\ell)$ for electrons (solid circles) and muons (open circles). The dark and light dashed lines show the central results for electrons and muons respectively. Figure a) shows the variation of the $\mathcal{B}(b \to X\ell\nu_\ell)$ branching fractions with the minimum momentum cut. Figure b) shows the stability of $\mathcal{B}(b \to X\ell\nu_\ell)$ with an an increasing cut on the $NN_{b\ell}$ network output, whilst Figure c) shows the equivalent test for $\mathcal{B}(b \to c \to X\ell\nu_\ell)$ with an increasing $NN_{bc\ell}$ cut. The errors are statistical only.*

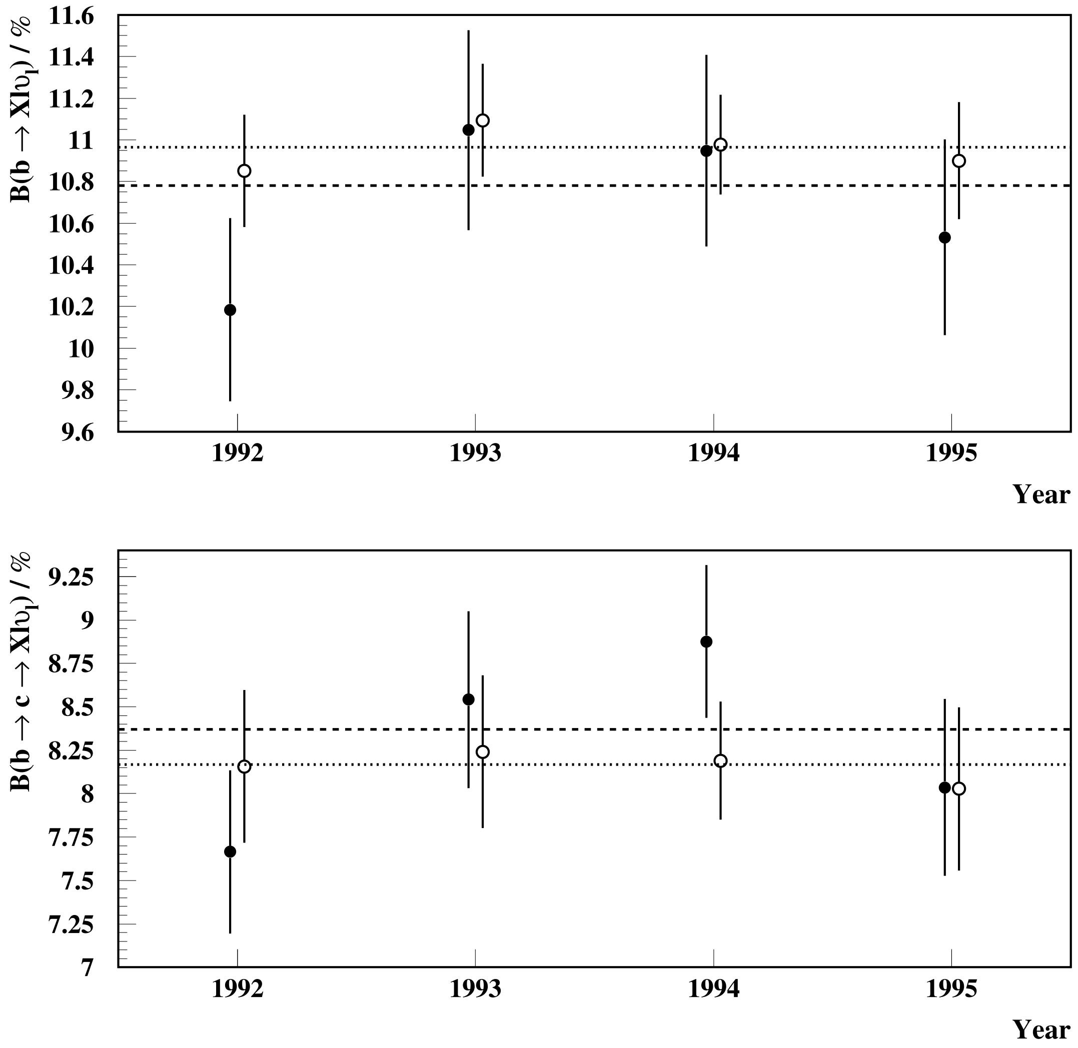

Figure 7.6: *The measured $\mathcal{B}(b \to X\ell\nu_\ell)$ and $\mathcal{B}(b \to c \to X\ell\nu_\ell)$ branching fractions using the data from each year separately to form statistically independent samples, for electrons (solid circles) and muons (open circles). The dark and light dashed lines show the combined results for electrons and muons respectively. Errors are the statistical and uncorrelated systematic contributions only.*

Figure 7.5c shows the results obtained for $\mathcal{B}(\mathrm{b} \to \mathrm{c} \to \mathrm{X}\ell\nu_\ell)$ with a cut applied to the $\mathrm{NN}_{\mathrm{bc}\ell}$ output, increasing the $\mathrm{b} \to \mathrm{c} \to \ell$ purity of the lepton samples. A small bias is observed, but is not significant given the increasing systematic and modelling uncertainties.

Finally, the data are divided into four statistically independent sub–samples corresponding to the year in which the data were collected. A fit is performed to each year of data using the same combined Monte Carlo sample as used for the full analysis. The b–tagging purities and lepton identification efficiencies are recalculated for each data sub–set separately. The results for $\mathcal{B}(\mathrm{b} \to \mathrm{X}\ell\nu_\ell)$ and $\mathcal{B}(\mathrm{b} \to \mathrm{c} \to \mathrm{X}\ell\nu_\ell)$ for both tests are shown in Figure 7.6 where the errors correspond to the statistical uncertainties and uncorrelated systematic errors. All results are consistent with the central results within errors.

7.7 Semileptonic Decay and Fragmentation Models

The main results presented in Section 7.4 use the prescriptions discussed previously to model b fragmentation (Section 7.3.2.2) and the lepton momentum spectra from semileptonic decays (Section 7.3.2.1) and to evaluate the associated modelling uncertainties. These prescriptions [102] are followed by all four LEP experiments in order to establish a common set of systematic and modelling uncertainties, which facilitates the combination of individual measurements for the LEP average results.

In this section, a study of the agreement between the data and various phenomenological models is presented. Various models for the lepton momentum spectra from $\mathrm{b} \to \ell$ decays are investigated, which affect both the lepton total and transverse momentum spectra. For each $\mathrm{b} \to \ell$ decay model, three different fragmentation functions are also studied, those of Peterson *et al.* [15], Collins and Spiller [16] and Kartvelishvili *et al.* [17]. These functions primarily affect the lepton total momentum spectrum, leaving the transverse momentum distribution unaltered.

Six semileptonic $b \to \ell$ decay models are investigated :-

- **ACCMM model** [40] (Section 2.6.4.1) :

  The model parameters were tuned to the CLEO data [42]. Their values are fixed as given in [102]: the Fermi momentum of the spectator quark, $p_F = 298\,\mathrm{MeV/c}$, the mass of the charm quark, $m_c = 1673\,\mathrm{MeV/c^2}$, and the mass of the spectator quark, $m_{sp} = 150\,\mathrm{MeV/c^2}$.

- **ISGW model** [41] (Section 2.6.4.2) :

  This model has no free parameters and the D^{**} contributions are predicted to account for 11 % of all b decays.

- **ISGW** model** [102] (Section 2.6.4.2) :

  This is the ISGW model modified such as to allow the total contributions from D^{**}, $f_{D^{**}}$, to account for 32 % of all b decays, as determined from CLEO data [42].

- **ISGW2 model** [113] :

  A revised version of the ISGW model incorporating constraints from heavy quark symmetry, hyperfine distortions of wave functions and form factors with more realistic high–recoil behaviour. This model predicts that the sum of all D^{**} contributions accounts for 9.3 % of the total b decay width.

- **ISGW2** model** :

  This is the ISGW2 model modified to allow the sum of all D^{**} contributions to be an additional free parameter of the fit.

- **ACCMM* model** :

  This is the ACCMM model with free parameters. The Fermi momentum parameter p_F and the mass of the charm quark m_c are treated as additional free parameters in the fit. The spectator quark mass was fixed at $m_{sp} = 150\,\mathrm{MeV/c^2}$.

For each of these semileptonic $\mathrm{b} \to \ell$ decay models the analysis is repeated, using each of the three different b fragmentation models. The resulting semileptonic branching fractions $\mathcal{B}(\mathrm{b} \to \mathrm{X}\ell\nu_\ell)$ and $\mathcal{B}(\mathrm{b} \to \mathrm{c} \to \mathrm{X}\ell\nu_\ell)$, and $\langle x_E \rangle_\mathrm{b}$ are re–calculated. The same models are used to simulate $\mathrm{b} \to \mathrm{c} \to \ell$ decays and to assess the associated modelling uncertainties, as described in Section 7.3.2.1.

Figures 7.7 and 7.8 show the fitted distributions for the $\mathrm{NN}_{\mathrm{b}\ell}$ network outputs for each of these models compared to the data, for electrons and muons respectively. The figures focus on the $\mathrm{b} \to \ell$ peak regions of the $\mathrm{NN}_{\mathrm{b}\ell}$ distributions corresponding to $\mathrm{NN}_{\mathrm{b}\ell} > 0.8$, which are most sensitive to the variations from the different models. The fit is performed over the full range of the neural network output (from zero to one) as in the main analysis. From these fits to the data, the $\mathrm{NN}_{\mathrm{b}\ell} > 0.8$ region is determined to be approximately 93 % pure in $\mathrm{b} \to \ell$ decays.

The results for the branching fractions $\mathcal{B}(\mathrm{b} \to \mathrm{X}\ell\nu_\ell)$ and $\mathcal{B}(\mathrm{b} \to \mathrm{c} \to \mathrm{X}\ell\nu_\ell)$ obtained using each combination of b fragmentation and $\mathrm{b} \to \ell$ decay models are summarised in Table 7.6, together with the statistical, systematic and modelling uncertainties. All errors are calculated according to the procedures outlined in the preceding sections, apart from the modelling error which accounts for $\mathrm{b} \to \mathrm{c} \to \ell$ decay modelling. The values obtained for the decay model parameters as well as for the free parameter in the b fragmentation functions are also given in Table 7.6. The results for $\langle x_E \rangle_\mathrm{b}$ corresponding to the various fitted b fragmentation functions are also given. The χ^2/bin is calculated using the $\mathrm{NN}_{\mathrm{b}\ell} > 0.8$ portion of the distributions as shown in Figures 7.7 and 7.8, and incorporate the statistical, systematic and modelling uncertainties from both the electron and muon samples. These are given only as an indicator of the agreement between the Monte Carlo and the data.

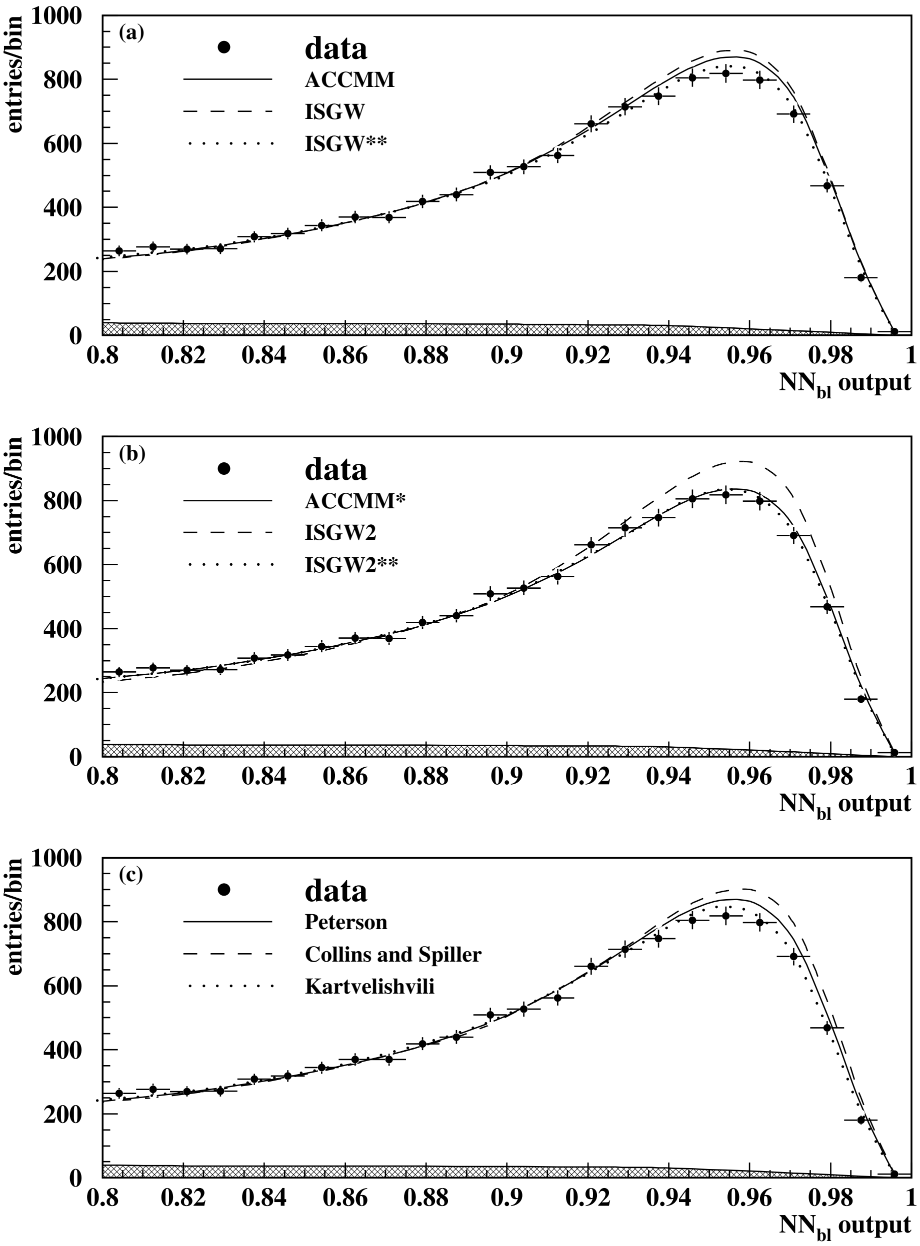

Figure 7.7: *The fitted distributions for the $NN_{b\ell}$ neural network output for electrons with a) the ACCMM, ISGW and ISGW** models; b) the ISGW2, ISGW2** and ACCMM* models; c) the ACCMM model with the Peterson, Collins and Spiller and Kartvelishvili b fragmentation functions. The Peterson function is used to describe the b fragmentation in a) and b). The shaded areas show the contributions from sources other than $b \to e$ in the data, as extracted from the fit.*

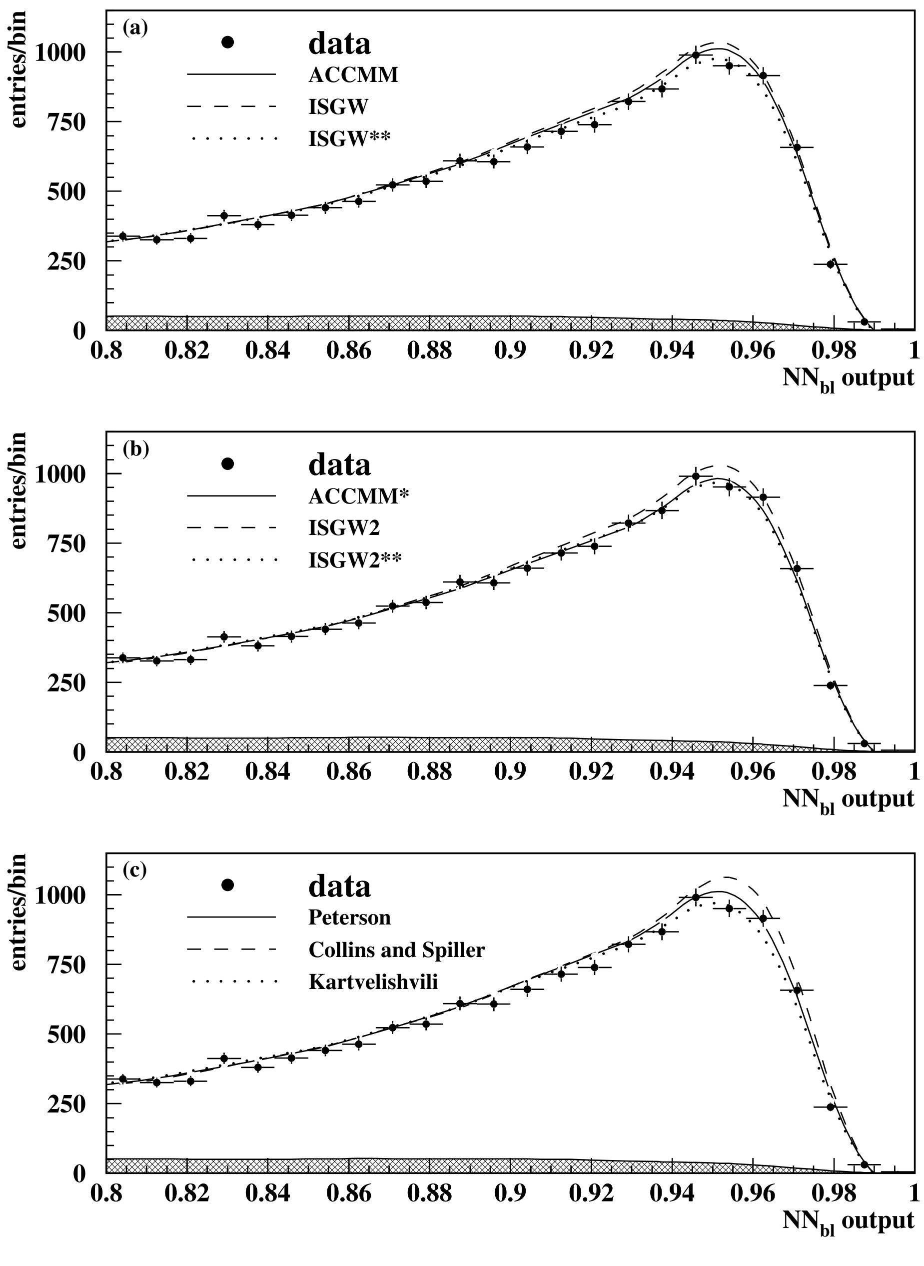

Figure 7.8: *The fitted distributions for the $NN_{b\ell}$ neural network output for muons with a) the ACCMM, ISGW and ISGW** models; b) the ISGW2, ISGW2** and ACCMM* models; c) the ACCMM model with the Peterson, Collins and Spiller and Kartvelishvili b fragmentation functions. The Peterson function is used to describe the b fragmentation in a) and b). The shaded areas show the contributions from sources other than $b \to \mu$ in the data, as extracted from the fit.*

$b \to \ell$ model	$b \to \ell$ model parameters	Fragmentation parameter	$\langle x_E \rangle_b$	$\mathcal{B}(b \to Xe\nu_e)$ / %	$\mathcal{B}(b \to X\mu\nu_\mu)$ / %	$\mathcal{B}(b \to c \to Xe\nu_e)$ / %	$\mathcal{B}(b \to c \to X\mu\nu_\mu)$ / %	χ^2/bin
Peterson *et al.*								
ACCMM	fixed	0.00573 ± 0.00062	0.709 ± 0.004	$10.78 \pm 0.08 \pm 0.45\ ^{-0.07}_{+0.06}$	$10.96 \pm 0.08 \pm 0.23\ ^{-0.06}_{+0.06}$	$8.37 \pm 0.18 \pm 0.38\ ^{+0.15}_{-0.06}$	$8.17 \pm 0.19 \pm 0.23\ ^{+0.17}_{-0.05}$	64/48
ISGW	fixed	0.00655 ± 0.00070	0.705 ± 0.004	$10.70 \pm 0.08 \pm 0.45\ ^{-0.07}_{+0.06}$	$10.86 \pm 0.08 \pm 0.23\ ^{-0.07}_{+0.06}$	$8.50 \pm 0.18 \pm 0.38\ ^{+0.16}_{-0.06}$	$8.37 \pm 0.19 \pm 0.24\ ^{+0.16}_{-0.04}$	98/48
ISGW**	fixed	0.00456 ± 0.00051	0.718 ± 0.004	$10.99 \pm 0.08 \pm 0.46\ ^{-0.07}_{+0.06}$	$11.19 \pm 0.08 \pm 0.23\ ^{-0.06}_{+0.06}$	$8.16 \pm 0.18 \pm 0.37\ ^{+0.14}_{-0.06}$	$7.85 \pm 0.20 \pm 0.23\ ^{+0.19}_{-0.07}$	37/48
ISGW2	fixed	0.00787 ± 0.00083	0.698 ± 0.004	$10.69 \pm 0.08 \pm 0.45\ ^{-0.07}_{+0.06}$	$10.86 \pm 0.08 \pm 0.23\ ^{-0.07}_{+0.06}$	$8.62 \pm 0.18 \pm 0.38\ ^{+0.16}_{-0.06}$	$8.55 \pm 0.19 \pm 0.24\ ^{+0.15}_{-0.03}$	131/48
ISGW2**	$f_{D^{**}} = 45 \pm 5\,\%$	0.00446 ± 0.00055	0.719 ± 0.004	$10.95 \pm 0.08 \pm 0.45\ ^{-0.09}_{+0.07}$	$11.15 \pm 0.08 \pm 0.23\ ^{-0.08}_{+0.07}$	$8.17 \pm 0.18 \pm 0.37\ ^{+0.19}_{-0.07}$	$7.85 \pm 0.20 \pm 0.23\ ^{+0.40}_{-0.08}$	35/48
ACCMM*	$p_F = 837^{+204}_{-217}$ MeV/c $m_c = 1287^{+142}_{-135}$ MeV/c	0.00465 ± 0.00054	0.717 ± 0.004	$10.95 \pm 0.09 \pm 0.46\ ^{-0.11}_{+0.08}$	$11.15 \pm 0.09 \pm 0.23\ ^{-0.10}_{+0.08}$	$8.16 \pm 0.18 \pm 0.37\ ^{+0.23}_{-0.08}$	$7.84 \pm 0.20 \pm 0.23\ ^{+0.51}_{-0.09}$	38/48
Collins and Spiller								
ACCMM	fixed	0.00342 ± 0.00062	0.698 ± 0.004	$10.83 \pm 0.08 \pm 0.45\ ^{-0.07}_{+0.06}$	$11.06 \pm 0.08 \pm 0.23\ ^{-0.07}_{+0.06}$	$8.60 \pm 0.18 \pm 0.38\ ^{+0.15}_{-0.06}$	$8.40 \pm 0.19 \pm 0.24\ ^{+0.18}_{-0.06}$	148/48
ISGW	fixed	0.00421 ± 0.00074	0.693 ± 0.004	$10.74 \pm 0.08 \pm 0.45\ ^{-0.07}_{+0.06}$	$10.95 \pm 0.08 \pm 0.23\ ^{-0.07}_{+0.06}$	$8.72 \pm 0.18 \pm 0.38\ ^{+0.16}_{-0.06}$	$8.61 \pm 0.19 \pm 0.24\ ^{+0.17}_{-0.05}$	202/48
ISGW**	fixed	0.00241 ± 0.00044	0.705 ± 0.004	$11.05 \pm 0.08 \pm 0.46\ ^{-0.07}_{+0.06}$	$11.30 \pm 0.08 \pm 0.23\ ^{-0.07}_{+0.06}$	$8.39 \pm 0.18 \pm 0.38\ ^{+0.14}_{-0.06}$	$8.09 \pm 0.20 \pm 0.23\ ^{+0.20}_{-0.08}$	84/48
ISGW2	fixed	0.00556 ± 0.00096	0.687 ± 0.004	$10.72 \pm 0.08 \pm 0.45\ ^{-0.07}_{+0.06}$	$10.94 \pm 0.08 \pm 0.23\ ^{-0.07}_{+0.06}$	$8.83 \pm 0.18 \pm 0.39\ ^{+0.16}_{-0.06}$	$8.79 \pm 0.19 \pm 0.24\ ^{+0.16}_{-0.04}$	253/48
ISGW2**	$f_{D^{**}} = 43 \pm 5\,\%$	0.00251 ± 0.00044	0.704 ± 0.004	$11.00 \pm 0.08 \pm 0.45\ ^{-0.09}_{+0.07}$	$11.24 \pm 0.08 \pm 0.23\ ^{-0.08}_{+0.07}$	$8.43 \pm 0.18 \pm 0.38\ ^{+0.19}_{-0.07}$	$8.14 \pm 0.20 \pm 0.23\ ^{+0.41}_{-0.06}$	80/48
ACCMM*	$p_F = 679^{+180}_{-192}$ MeV/c $m_c = 1287^{+146}_{-138}$ MeV/c	0.00252 ± 0.00043	0.704 ± 0.004	$10.94 \pm 0.09 \pm 0.45\ ^{-0.11}_{+0.08}$	$11.19 \pm 0.09 \pm 0.23\ ^{-0.10}_{+0.08}$	$8.43 \pm 0.18 \pm 0.38\ ^{+0.23}_{-0.08}$	$8.14 \pm 0.20 \pm 0.23\ ^{+0.49}_{-0.09}$	88/48
Kartvelishvili *et al.*								
ACCMM	fixed	10.04 ± 0.57	0.720 ± 0.005	$10.75 \pm 0.08 \pm 0.45\ ^{-0.07}_{+0.06}$	$10.89 \pm 0.08 \pm 0.23\ ^{-0.07}_{+0.06}$	$8.23 \pm 0.18 \pm 0.37\ ^{+0.15}_{-0.06}$	$7.99 \pm 0.19 \pm 0.23\ ^{+0.16}_{-0.04}$	41/48
ISGW	fixed	9.40 ± 0.54	0.714 ± 0.005	$10.69 \pm 0.08 \pm 0.45\ ^{-0.07}_{+0.06}$	$10.80 \pm 0.08 \pm 0.23\ ^{-0.07}_{+0.06}$	$8.36 \pm 0.18 \pm 0.37\ ^{+0.16}_{-0.06}$	$8.20 \pm 0.19 \pm 0.24\ ^{+0.15}_{-0.03}$	56/48
ISGW**	fixed	11.23 ± 0.63	0.729 ± 0.005	$10.94 \pm 0.08 \pm 0.45\ ^{-0.07}_{+0.06}$	$11.10 \pm 0.08 \pm 0.23\ ^{-0.06}_{+0.06}$	$8.01 \pm 0.18 \pm 0.37\ ^{+0.14}_{-0.06}$	$7.66 \pm 0.20 \pm 0.22\ ^{+0.18}_{-0.06}$	48/48
ISGW2	fixed	8.58 ± 0.49	0.706 ± 0.005	$10.69 \pm 0.08 \pm 0.45\ ^{-0.07}_{+0.06}$	$10.81 \pm 0.08 \pm 0.23\ ^{-0.07}_{+0.06}$	$8.48 \pm 0.18 \pm 0.38\ ^{+0.16}_{-0.06}$	$8.39 \pm 0.19 \pm 0.24\ ^{+0.14}_{-0.02}$	73/48
ISGW2**	$f_{D^{**}} = 46 \pm 5\,\%$	11.44 ± 0.67	0.731 ± 0.005	$10.91 \pm 0.08 \pm 0.45\ ^{-0.08}_{+0.07}$	$11.07 \pm 0.08 \pm 0.23\ ^{-0.07}_{+0.06}$	$8.01 \pm 0.18 \pm 0.37\ ^{+0.19}_{-0.07}$	$7.65 \pm 0.20 \pm 0.22\ ^{+0.39}_{-0.09}$	53/48
ACCMM*	$p_F = 1063^{+409}_{-368}$ MeV/c $m_c = 1153^{+184}_{-199}$ MeV/c	10.96 ± 0.64	0.727 ± 0.005	$10.95 \pm 0.09 \pm 0.46\ ^{-0.11}_{+0.11}$	$11.11 \pm 0.10 \pm 0.23\ ^{-0.10}_{+0.11}$	$8.00 \pm 0.18 \pm 0.37\ ^{+0.23}_{-0.10}$	$7.64 \pm 0.20 \pm 0.22\ ^{+0.52}_{-0.20}$	39/48

Table 7.6: *Branching fractions $\mathcal{B}(b \to X\ell\nu_\ell)$ and $\mathcal{B}(b \to c \to X\ell\nu_\ell)$ (given in %) derived by comparing the data to various semileptonic decay models for $b \to \ell$ decays. The quoted errors on the branching fractions correspond to the statistical, systematic and $b \to c \to \ell$ modelling errors, respectively. The fitted $b \to \ell$ decay model parameters are also given when appropriate. The fitted b fragmentation function parameters, and the corresponding values for $\langle x_E \rangle_b$ are presented. The combined statistical, systematic and $b \to c \to \ell$ modelling errors are given for all fitted model parameters. The χ^2/bin is calculated using the portion of the $NN_{b\ell}$ output shown in Figures 7.7 and 7.8, using all uncertainties from both the electron and muon samples; these are given as an indicator of the quality of the fit. All models and their parameters are described in the text*

7.7.1 Discussion of Results

Although the statistical precision of the tests is insufficient to allow any firm statements to be made concerning the various models, certain trends in the results can be summarised :-

• For the ACCMM* model, the best fit to the data is obtained with the b fragmentation model of Peterson *et al.*, giving

$$\begin{aligned} p_F &= (837 \pm 143\ \text{(stat.)} \pm 132\ \text{(syst.)}\ {}^{+234}_{-186}\ \text{(model)}) \\ m_c &= (1287 \pm 100\ \text{(stat.)} \pm 87\ \text{(syst.)}\ {}^{+112}_{-136}\ \text{(model)})\,\mathrm{MeV/c^2} \end{aligned}$$

where the mass of the spectator quark is kept fixed at $150\,\mathrm{MeV/c^2}$. The correlation coefficient between these model parameters is high at -0.970.

The systematic errors are calculated using the same scheme as described in Section 7.3. The modelling errors correspond to the b fragmentation and $\mathrm{b} \to \mathrm{c} \to \ell$ decay models added in quadrature and are dominated by the uncertainties resulting from the choice of b fragmentation model. These values are consistent with recent theoretical calculations of p_F using the relativistic quark model, which give predictions around 500 to $600\,\mathrm{MeV/c}$ [114, 115], and the world average charm mass of 1100 to $1400\,\mathrm{MeV/c^2}$ taken from [3].

• The ISGW** and ISGW2** models also give good agreement with the data. However, these models are less theoretically sound since they are modifications to the original models to allow the overall fraction of D** contributions to be a free fit parameter.

In the ISGW model the fraction of D** in the final state, $f_{\mathrm{D^{**}}}$, is predicted to be 11 %. In the modified ISGW** model this is increased to 32 % in order to better reproduce the CLEO data [42]. For the ISGW2** model, the best agreement with the OPAL data is found with the Peterson b fragmentation model when the D** contribution amounts to,

$$f_{\mathrm{D^{**}}} = (45 \pm 3\ \text{(stat.)} \pm 3\ \text{(syst.)} \pm 4\ \text{(model)})\,\%$$

of the total width, instead of the 9.3 % derived in the original ISGW2 model. Again, the modelling error contains uncertainties from both the b fragmentation and $\mathrm{b} \to \mathrm{c} \to \ell$ decay models. The ISGW2 model gives worse agreement with the data than the ISGW model.

• Allowing the ISGW2** and ACCMM* model parameters to be free fit parameters produces very similar Monte Carlo distributions for the $\mathrm{NN}_{\mathrm{b}\ell}$ neural networks. Accordingly, the resulting $\mathcal{B}(\mathrm{b} \to \mathrm{X} e \nu_e)$ and $\mathcal{B}(\mathrm{b} \to \mathrm{X} \mu \nu_\mu)$ branching fractions are very similar for these models, and slightly higher than the central results obtained using the ACCMM model. In addition, the branching fractions are more stable with respect to variations in the b fragmentation model.

• The fragmentation function of Collins and Spiller is generally disfavoured by the data, for all semileptonic decay models investigated. The fragmentation functions of Peterson *et al.* or Kartvelishvili *et al.* provide equally good fits to the data.

Chapter 8

Conclusions

8.1 Summary of Results

In this thesis, measurements of the inclusive semileptonic branching fractions of b hadrons, $\mathcal{B}(\mathrm{b} \to \mathrm{X}\ell\nu_\ell)$ and $\mathcal{B}(\mathrm{b} \to \mathrm{c} \to \mathrm{X}\ell\nu_\ell)$, and the average fraction of the beam energy carried by the weakly decaying b hadron, $\langle x_E \rangle_\mathrm{b}$, have been presented.

The final results for the semileptonic branching fractions are

$$\begin{aligned} \mathcal{B}(\mathrm{b} \to \mathrm{X}\ell\nu_\ell) &= (10.83 \pm 0.10\ (\mathrm{stat.}) \pm 0.20\ (\mathrm{syst.})\ {}^{+\,0.20}_{-\,0.13}\ (\mathrm{model}))\,\%, \\ \mathcal{B}(\mathrm{b} \to \mathrm{c} \to \mathrm{X}\ell\nu_\ell) &= (8.40 \pm 0.16\ (\mathrm{stat.}) \pm 0.21\ (\mathrm{syst.})\ {}^{+\,0.33}_{-\,0.29}\ (\mathrm{model}))\,\%. \end{aligned}$$

This $\mathcal{B}(\mathrm{b} \to \mathrm{X}\ell\nu_\ell)$ measurement is the most precise to date at the Z^0 resonance, while the $\mathcal{B}(\mathrm{b} \to \mathrm{c} \to \mathrm{X}\ell\nu_\ell)$ result is more precise than the current world average value of $(7.8 \pm 0.6)\,\%$ [3].

The $\mathcal{B}(\mathrm{b} \to \mathrm{X}\ell\nu_\ell)$ measurement presented here is consistent with the current world average of all measurements taken at the Z^0 resonance, $\mathcal{B}^\mathrm{b}_{SL} = (10.99 \pm 0.23)\,\%$ [3], based on a global fit to several electroweak parameters and including specific measurements of $\mathcal{B}(\mathrm{b} \to \mathrm{X}\ell\nu_\ell)$ [22, 116–121]. It is also in good agreement with a preliminary average of the most recent and precise published and preliminary LEP results obtained at the Z^0 resonance, $\mathcal{B}^{\mathrm{b}}_{SL} = (10.87 \pm 0.24)\,\%$ [24].

On the other hand, this measurement for $\mathcal{B}(\mathrm{b} \to \mathrm{X}\ell\nu_\ell)$ is still larger than the measurement at the $\Upsilon(4\mathrm{S})$ of $\mathcal{B}^{\mathrm{B}}_{SL} = (10.45 \pm 0.21)\,\%$ [3], the semileptonic branching fraction for B^0 and $\mathrm{B}^\pm$ mesons, when it is expected to be lower due to the presence of Λ_{b} baryons at the Z^0 resonance, as discussed in Section 2.6.3.1. Correcting for this expected difference, the discrepancy between this result and the $\Upsilon(4\mathrm{S})$ measurement is about 1.8 standard deviations.

The measurement of $\mathcal{B}(\mathrm{b} \to \mathrm{X}\ell\nu_\ell)$ is also consistent with the theoretical calculations discussed in Section 2.6.3.2, which are shown in Figure 2.6 where the average results for $\mathcal{B}_{SL}$ and the related quantity n_c, the average number of charm hadrons produced per b decay, are compared to the theoretical predictions [38, 39].

The average value of the fraction of the beam energy carried by the weakly decaying b hadron is also obtained from this analysis, giving

$$\langle x_E \rangle_{\mathrm{b}} = 0.709 \pm 0.003\ (\mathrm{stat.}) \pm 0.003\ (\mathrm{syst.}) \pm 0.013\ (\mathrm{model}).$$

which is in good agreement with published results [2, 3].

All the measurements presented here are statistically independent of and consistent with similar results derived in a previous OPAL analysis [116], where the quantities

$$\begin{aligned} \mathcal{B}(\mathrm{b} \to \mathrm{X}\ell\nu_\ell) &= (10.5 \pm 0.6\ (\mathrm{stat.}) \pm 0.5\ (\mathrm{syst.}))\,\% \\ \mathcal{B}(\mathrm{b} \to \mathrm{c} \to \mathrm{X}\ell\nu_\ell) &= (7.7 \pm 0.4\ (\mathrm{stat.}) \pm 0.7\ (\mathrm{syst.}))\,\% \\ \langle x_E \rangle_{\mathrm{b}} &= 0.697 \pm 0.006\ (\mathrm{stat.}) \pm 0.011\ (\mathrm{syst.}) \end{aligned}$$

were extracted from a global fit for these and two other parameters; R_{b}, the fraction of Z^0 events decaying into $\mathrm{b}\overline{\mathrm{b}}$ and the mean $\mathrm{B}^0 - \overline{\mathrm{B}^0}$ mixing parameter χ. However, the uncertainties related to assessing the systematic correlations between these old results and those presented in this thesis means that no overall gain in precision is obtained by combining them. Therefore the results presented in this thesis supersede the results previously published in [116].

In Section 7.7 the results obtained using various phenomenological models for the lepton momentum spectra in semileptonic b decays are described. For the results discussed above, the free parameters of these models are fixed to the values prescribed in [102], as determined by CLEO [42]. Allowing these model parameters to be additional free parameters in the fit to the OPAL data yields significantly different values. Correspondingly, the values for the semileptonic branching fractions, $\mathcal{B}(\mathrm{b} \to \mathrm{X}\ell\nu_\ell)$, derived from these fits are slightly higher than the main results discussed above. However, the statistical precision of these tests is insufficient to allow any firm conclusions concerning the various models to be made.

8.2 Outlook

The semileptonic branching fractions presented in this thesis represent an analysis of the OPAL data taken at the Z^0 resonance and the precision of the results are limited by the experimental systematic and theoretical modelling uncertainties. The use of phenomenological models to describe the lepton momentum spectra introduces large uncertainties and therefore more precise predictions are required for future advances. Heavy–quark effective theory (HQET) provides a mechanism for understanding semileptonic decays from first principles and theoretical efforts are currently underway to produce the lepton momentum spectra from HQET and thus to provide more rigorously motivated predictions for future analyses.

The LEP experiments finished collecting Z^0 data in 1995 and therefore the currently emerging measurements represent the final results from the LEP collaborations. Whilst substantial theoretical advances may provoke future revisions to these results, new experimental results from CERN are therefore only expected with the advent of the LHC experiments. Elsewhere however, the CLEO detector is currently being upgraded [122] to match the increased luminosity at the CESR collider, and will provide new results at the $\Upsilon(4S)$ resonance. Two new e^+e^- colliders are also due to start running in 1999, the PEP-II and KEK-B facilities, designed to run at the $\Upsilon(4S)$, with their respective experiments BaBar [123] and BELLE [124]. At existing colliders, the HERA-B [125] experiment and the upgraded Tevatron experiments CDF [126] and D0 [127] will come into operation before the year 2001. Thus, a wealth of new data expected over the next few years will provide improvements on the current results.

Eventually, the high statistics at the LHC pp collider, expected to be operational around 2005, will supersede these experiments. Supplying the two general purpose experiments, ATLAS [128] and CMS [129], and the dedicated b physics experiment LHC-b [130], the accelerator is expected to deliver in excess of 10^{11} b hadrons per year, providing precision tests of the Standard Model in the b physics sector.

Appendix A

The Likelihood Function

Consider a set of data values $\{x_1, x_2, x_3, \ldots, x_N\}$ drawn from a given probability density $P(x; \eta)$, which is also dependent on a parameter η. The probability that the data are consistent with a particular value of η, denoted η', is given by the product of the individual probabilities for each data point. This product is called the *likelihood* $\mathcal{L}(x_1, x_2, x_3, \ldots, x_N; \eta = \eta')$ where,

$$\begin{aligned} \mathcal{L}(x_1, x_2, x_3, \ldots, x_N; \eta = \eta') &= P(x_1; \eta') \cdot P(x_2; \eta') \cdot P(x_3; \eta') \cdots P(x_N; \eta') \\ &= \prod_i P(x_i; \eta'). \end{aligned} \tag{A.1}$$

Conversely, the likelihood equation can be maximised with respect to η to give an estimator of the value of η'. It is often convenient in such cases to take the natural log of the likelihood function giving,

$$\begin{aligned} \ln(\mathcal{L}) &= \ln\left[\prod_i P(x_i; \eta')\right] \\ &= \sum_i \ln\left[P(x_i; \eta')\right] \end{aligned} \tag{A.2}$$

Consider a typical experimental situation in which a data distribution is compared to a Monte Carlo simulation. The probability of obtaining r events in a given bin of the distribution, if the mean expected value from the Monte Carlo is λ, is given by the *Poisson* probability distribution,

$$P(r;\lambda) = \frac{e^{-\lambda}\lambda^r}{r!} \tag{A.3}$$

which expressed as a log–likelihood gives,

$$\begin{aligned} \ln(\mathcal{L}) &= \ln\left[P(r;\lambda)\right] \\ &= \ln\left(\frac{e^{-\lambda}\lambda^r}{r!}\right) \\ &= \ln\left(e^{-\lambda}\right) + \ln\left(\lambda^r\right) - \ln\left(r!\right). \end{aligned} \tag{A.4}$$

Ignoring the constant term $\ln(r!)$ this gives

$$\ln(\mathcal{L}) = r\ln\lambda - \lambda. \tag{A.5}$$

Equation A.5 can be trivially extended to give the log–likelihood function that the entire data distribution is consistent with the Monte Carlo prediction. If the data is split into N_{bins} bins with d_i events in bin i, where the predicted population is f_i, the likelihood function is given by,

$$\ln(\mathcal{L}) = \sum_{i=1}^{N_{bins}} \left(d_i \ln f_i - f_i\right) \tag{A.6}$$

This expression correctly accounts for data bins with a low number of entries and is commonly referred to as a *binned log–likelihood.*

Equation A.6 is appropriate if the Monte Carlo sample is sufficiently large that any statistical fluctuations in the predicted distributions are negligible in comparison to those in the data. In order to take limited Monte Carlo statistics into account, Poisson variations in the f_i values must be incorporated into the likelihood expression.

The Monte Carlo distribution, f_i, is formed from the number of Monte Carlo events from source j in bin i, a_{ji}, and the strength of that contribution P_j, namely,

$$f_i = N_D \sum_{j=1}^{N_{source}} \frac{P_j a_{ji}}{N_j} \tag{A.7}$$

where N_{source} is the total number of sources in the Monte Carlo, N_D is the total number of events in the data sample and N_j the total number of events in the Monte Carlo sample for source j,

$$N_D = \sum_{i=1}^{N_{bins}} d_i, \qquad N_j = \sum_{i=1}^{N_{bins}} a_{ji}. \tag{A.8}$$

Finite Monte Carlo Statistics can then be taken in account by replacing the number of events a_{ji} in Equation A.7 by some (unknown) expected number of events A_{ji},

$$f_i = N_D \sum_{j=1}^{N_{source}} \frac{P_j A_{ji}}{N_j}. \tag{A.9}$$

From each A_{ji}, the corresponding a_{ji} are then generated from a Poisson distribution, since $A_{ji} \ll N_j$. The total likelihood which is now to be maximised is the combined probability of the observed $\{d_i\}$ and the observed $\{a_{ji}\}$,

$$\ln \mathcal{L} = \sum_{i=1}^{N_{bins}} (d_i \ln f_i - f_i) + \sum_{i=1}^{N_{bins}} \sum_{j=1}^{N_{source}} (a_{ji} \ln A_{ji} - A_{ji}). \tag{A.10}$$

The estimates for the contribution of each source to the total Monte Carlo distributions, p_j, and the A_{ji} parameters are obtained by maximising the log–likelihood. Although this method correctly incorporates the effects of finite Monte Carlo statistics it introduces additional unknowns, the A_{ji} parameters, which also need to be determined.

The theoretical details for incorporating Monte Carlo statistics have now been outlined. The mathematical and computational algorithms for minimising Equation A.10 have been implemented within the HBOOK [131] package by Barlow *et al.* as described in [132] and further details can be found in these references.

Bibliography

[1] D. Griffiths, *Introduction to Elementary particles*, John Wiley and Sons, 1987.

[2] M. G. Green, S. L. Lloyd, P. N. Ratoff and D. R. Ward, *Electron – Positron Physics at the Z*, Institute of Physics Publishing, 1998.

[3] Particle Data Group, C. Caso *et al.*, Review of particle physics[a], *Eur. Phys. J.* **C3**, 1 (1998).

[4] H. Fritzsch, M. Gell-Mann and H. Leutwyler, Advantages of the color octet gluon picture, *Phys. Lett.* **47B**, 365 (1973).

[5] S. L. Glashow, Partial symmetries of weak interactions, *Nucl. Phys.* **22**, 579 (1961).

[6] S. Weinberg, A model of leptons, *Phys. Rev. Lett.* **19**, 1264 (1967).

[7] A. Salam, Weak and electromagnetic interactions, Originally printed in "Svartholm: Elementary Particle Theory, Proceedings of the Nobel Symposium held in 1968 at Lerum, Sweden", Stockholm 1968, 367-377.

[8] N. Cabibbo, Unitary symmetry and leptonic decays, *Phys. Rev. Lett.* **10**, 531 (1963).

[9] M. Kobayashi and T. Maskawa, CP violation in the renormalizable theory of weak interaction, *Prog. Theor. Phys.* **49**, 652 (1973).

[a] http://durpdg.dur.ac.uk/lbl/

[10] L. Wolfenstein, Parametrization of the Kobayashi–Maskawa matrix, *Phys. Rev. Lett.* **51**, 1945 (1983).

[11] C. Jarlskog, Commutator of the quark mass matrices in the standard electroweak model and a measure of maximal CP violation, *Phys. Rev. Lett.* **55**, 1039 (1985).

[12] C. Jarlskog, A basis independent formulation of the connection between quark mass matrices, CP violation and experiment, *Z. Phys.* **C29**, 491 (1985).

[13] P. W. Higgs, Spontaneous symmetry breakdown without massless bosons, *Phys. Rev.* **145**, 1156 (1966).

[14] OPAL Collaboration, G. Abbiendi *et al.*, A measurement of R_b using a double tagging method, *Eur. Phys. J.* **C8**, 217 (1999).

[15] C. Peterson, D. Schlatter, I. Schmitt and. P.M. Zerwas, Scaling violations in inclusive e^+e^- annihilation spectra, *Phys. Rev.* **D27**, 105 (1983).

[16] P. D. B. Collins and T. P. Spiller, The fragmentation of heavy quarks, *J. Phys.* **G11**, 1289 (1985).

[17] V. G. Kartvelishvili, A. K. Likhoded and V. A. Petrov, On the fragmentation functions of heavy quarks into hadrons, *Phys. Lett.* **B78**, 615 (1978).

[18] B. Andersson, G. Gustafson and B. Soderberg, A general model for jet fragmentation, *Z. Phys.* **C20**, 317 (1983).

[19] OPAL Collaboration, G. Alexander *et al.*, A study of b quark fragmentation into B^0 and B^+ mesons at LEP, *Phys. Lett.* **B364**, 93 (1995).

[20] ALEPH Collaboration, D. Buskulic *et al.*, Measurement of the semileptonic b branching ratios from inclusive leptons in Z decays, (1995), Contributed Paper to EPS-HEP-95 Brussels, EPS-0404.

[21] DELPHI Collaboration, Measurement of the semileptonic b branching ratios and $\bar{\chi}_b$ from inclusive leptons in Z^0 decays, (1997), Contributed Paper to EPS-HEP-97 Jerusalem, EPS-415.

[22] L3 Collaboration, M. Acciarri *et al.*, Measurement of the branching ratios $\mathrm{b} \to e\nu\mathrm{X}$, $\mu\nu\mathrm{X}$, $\tau\nu\mathrm{X}$ and $\nu\mathrm{X}$, *Z. Phys.* **C71**, 379 (1996).

[23] OPAL Collaboration, Measurement of the semileptonic branching fraction of inclusive b–hadrons, OPAL Physics Note PN334, contributed paper to ICHEP 98 Vancouver ICHEP'98 #370 .

[24] LEP Collaboration, D. Abbaneo *et al.*, A combination of preliminary electroweak measurements and constraints on the Standard Model, (1999), CERN-EP-99-015.

[25] ARGUS Collaboration, H. Albrecht *et al.*, A model independent determination of the inclusive semileptonic decay fraction of B mesons, *Phys. Lett.* **B318**, 397 (1993).

[26] CLEO Collaboration, B. Barish *et al.*, Measurements of the B semileptonic branching fraction with lepton tags, *Phys. Rev. Lett.* **76**, 1570 (1996).

[27] CLEO Collaboration, R. Fulton *et al.*, Exclusive and inclusive semileptonic decays of B mesons to D mesons, *Phys. Rev.* **D43**, 651 (1991).

[28] ARGUS Collaboration, H. Albrecht *et al.*, Exclusive semileptonic decays of B mesons to D mesons, (1992), DESY-92-029.

[29] OPAL Collaboration, K. Ackerstaff *et al.*, Measurement of the semileptonic branching fraction of inclusive b baryon decays to Λ, *Z. Phys.* **C74**, 423 (1997).

[30] ALEPH Collaboration, R. Barate *et al.*, A measurement of the semileptonic branching ratio $\mathcal{B}(\text{b-baryon} \to \mathrm{p}l\bar{\nu}\mathrm{X})$ and a study of inclusive $\pi^{\pm}$, $\mathrm{K}^{\pm}$, $(\mathrm{p}, \bar{\mathrm{p}})$ production in Z^0 decays, *Eur. Phys. J.* **C5**, 205 (1998).

[31] M. A. Shifman and M. B. Voloshin, On annihilation of mesons built from heavy and light quark and $\mathrm{B}^0 - \overline{\mathrm{B}^0}$ oscillations, *Sov. J. Nucl. Phys.* **45**, 292 (1987).

[32] M. A. Shifman and M. B. Voloshin, On production of D and D^* mesons in B meson decays, *Sov. J. Nucl. Phys.* **47**, 511 (1988).

[33] N. Isgur and M. B. Wise, Weak decays of heavy mesons in the static quark approximation, *Phys. Lett.* **B232**, 113 (1989).

[34] N. Isgur and M. B. Wise, Weak transition form–factors between heavy mesons, *Phys. Lett.* **B237**, 527 (1990).

[35] A. F. Falk, The heavy quark expansion of QCD, (1996), hep-ph/9610363.

[36] G. Altarelli and S. Petrarca, Inclusive beauty decays and the spectator model, *Phys. Lett.* **B261**, 303 (1991).

[37] I. Bigi, B. Blok, M. A. Shifman and A. Vainshtein, The baffling semileptonic branching ratio of B mesons, *Phys. Lett.* **B323**, 408 (1994).

[38] E. Bagan, P. Ball, V. M. Braun and P. Gosdzinsky, Theoretical update of the semileptonic branching ratio of B mesons, *Phys. Lett.* **B342**, 362 (1995).

[39] M. Neubert and C. T. Sachrajda, Spectator effects in inclusive decays of beauty hadrons, *Nucl. Phys.* **B483**, 339–370 (1997).

[40] G. Altarelli, N. Cabibbo, G. Corbò, L. Maiani and G. Martinelli, Leptonic decay of heavy flavours: A theoretical update, *Nucl. Phys.* **B208**, 365 (1982).

[41] N. Isgur, D. Scora, B. Grinstein and M. Wise, Semileptonic B and D decays in the quark model, *Phys. Rev.* **D39**, 799 (1989).

[42] CLEO Collaboration, S. Henderson *et al.*, Measurements of semileptonic branching fractions of B mesons at the Upsilon(4S) resonance, *Phys. Rev.* **D45**, 2212 (1992).

[43] W. Bacino *et al.*, The semileptonic decays of the D meson, *Phys. Rev. Lett.* **43**, 1073 (1979).

[44] R. M. Baltrusaitis *et al.*, A direct measurement of charmed D^+ and D^0 semileptonic branching ratios, *Phys. Rev. Lett.* **54**, 1976 (1985).

[45] R. Wang, *Measurements on the Inclusive Semileptonic Branching Fraction of B mesons at the Upsilon(4S) Resonance*, PhD thesis, University of Minnesota, December 1994, UMI-95-17404.

[46] D. Atwood and W. J. Marciano, Radiative corrections and semileptonic B decays, *Phys. Rev.* **D41**, 1736 (1990).

[47] CLEO Collaboration, D. Bortoletto *et al.*, Inclusive and exclusive decays of B mesons to final states including charm and charmonium mesons, *Phys. Rev.* **D45**, 21 (1992).

[48] I. Wilson and H. Henke, The LEP main ring accelerating structure, Technical report, CERN, Nov. 1989, CERN 89-09.

[49] LEP design report: Vol. 1. the LEP injector chain, CERN-LEP/TH/83-29.

[50] LEP design report: Vol. 2. the LEP main ring, CERN-LEP/84-01.

[51] LEP design report: Vol. 3. LEP 2, CERN-AC/96-01.

[52] S. Myers, *The LEP Collider, from design to approval and commissioning*, CERN, 1991, Presented at CERN Accelerator School: The LEP Collider from Design to Approval and Commissioning, Geneva, Switzerland, Nov 26, 1990, CAS: CERN accelerator school, 6th John Adams Memorial lecture.

[53] ALEPH Collaboration, D. Decamp *et al.*, ALEPH: A detector for electron – positron annihilations at LEP, *Nucl. Instrum. Meth.* **A294**, 121 (1990).

[54] DELPHI Collaboration, P. Aarnio *et al.*, The DELPHI detector at LEP, *Nucl. Instrum. Meth.* **A303**, 233 (1991).

[55] L3 Collaboration, B. Adeva *et al.*, The construction of the L3 experiment, *Nucl. Instrum. Meth.* **A289**, 35 (1990).

[56] OPAL Collaboration *et al.*, The OPAL detector at LEP, *Nucl. Inst. and Meth.* **A305**, 275 (1991).

[57] R. Belbeoch *et al.*, Study on the linac injector project for LEP (LIL), Technical report, CERN, 1982, LAL/RT/82-01.

[58] P. P. Allport *et al.*, The OPAL silicon microvertex detector, *Nucl. Instrum. Meth.* **A324**, 34 (1993).

[59] P. P. Allport *et al.*, The OPAL silicon strip microvertex detector with two coordinate readout, *Nucl. Instrum. Meth.* **A346**, 476 (1994).

[60] S. Anderson *et al.*, The extended OPAL silicon strip microvertex detector, *Nucl. Instrum. Meth.* **A403**, 326 (1998).

[61] J. R. Carter *et al.*, The OPAL vertex drift chamber, *Nucl. Instrum. Meth.* **A286**, 99 (1990).

[62] R. Shally, R. J. Hemingway and A. C. McPherson, Track fitting in the OPAL vertex detector with stereo wires, *Nucl. Instrum. Meth.* **A260**, 132 (1987).

[63] H. M. Fischer *et al.*, The OPAL jet chamber, *Nucl. Instrum. Meth.* **A283**, 492 (1989).

[64] O. Biebel *et al.*, The laser system for calibration and monitoring of the OPAL jet chamber, *Nucl. Instrum. Meth.* **A320**, 183 (1992).

[65] M. Hauschild *et al.*, Particle identification with the OPAL jet chamber, *Nucl. Instrum. Meth.* **A314**, 74 (1992).

[66] H. Mes *et al.*, Design and tests of the z coordinate drift chamber system for the OPAL central detector at LEP, *Nucl. Instrum. Meth.* **A265**, 445 (1988).

[67] OPAL Collaboration, R. Akers *et al.*, Improved measurements of the neutral current from hadron and lepton production at LEP, *Z. Phys.* **C61**, 19 (1994).

[68] R. Akers *et al.*, The OPAL muon barrel detector, *Nucl. Inst. and Meth.* **A357**, 253 (1995).

[69] Ji-Gang An *et al.*, Influence of gas mixture and primary ionization on the performance of limited streamer mode tubes, *Nucl. Instrum. Meth.* **A267**, 386 (1988).

[70] Ji-Gang An *et al.*, A study of the selfquenched streamer mode using a nitrogen laser, *Nucl. Instrum. Meth.* **A267**, 396 (1988).

[71] M. Akrawy *et al.*, Development studies for the OPAL endcap electromagnetic calorimeter using vacuum photo triode instrumented lead glass, *Nucl. Inst. and Meth.* **A290**, 76 (1990).

[72] C. Beard *et al.*, Thin, high gain wire chambers for electromagnetic presampling in OPAL, *Nucl. Instr. Meth.* **A286**, 117 (1990).

[73] G. Artusi *et al.*, Limited streamer tubes for the OPAL hadron calorimeter, *Nucl. Inst. and Meth.* **A279**, 523 (1989).

[74] G. Mikenberg, Thin gap gas chambers for hadronic calorimetry, *Nucl. Instrum. Meth.* **A265**, 223 (1988).

[75] B. E. Anderson *et al.*, The OPAL silicon – tungsten calorimeter frontend electronics, *IEEE Trans. Nucl. Sci.* **41**, 845 (1994).

[76] M. Arignon *et al.*, The pretrigger system of the OPAL experiment at LEP, *Nucl. Instrum. Meth.* **A333**, 330 (1993).

[77] M. Arignon *et al.*, The trigger system of the OPAL experiment at LEP, *Nucl. Instrum. Meth.* **A313**, 103 (1992).

[78] J. Baines *et al.*, The data acquisition system of the OPAL detector at LEP, *Nucl. Inst. and Meth.* **A325**, 271 (1993).

[79] C. Hawkes *et al.*, *ROPE410 Users' Guide*, February 1996, OPAL Offline Note 16 / OFFL-0487 (unpublished).

[80] R. Y. Rubinstein, *Simulation and the Monte Carlo Method*, John Wiley and Sons inc., 1986.

[81] T. Sjöstrand, High-energy physics event generation with PYTHIA 5.7 and JETSET 7.4, *Comput. Phys. Commun.* **82**, 74 (1994).

[82] CERN Application Software Group, *GEANT – Detector Description and Simulation Tool*, CERN, May 1995, CERN Program Library Long Writeup W5013.

[83] J. Allison *et al.*, The detector simulation program for the OPAL experiment at LEP, *Nucl. Inst. and Meth.* **A317**, 47 (1992).

[84] OPAL collaboration, G. Alexander *et al.*, Measurement of the Z^0 line shape parameters and the electroweak couplings of charged leptons, *Z. Phys.* **C52**, 175 (1991).

[85] OPAL Collaboration, P. D. Acton *et al.*, Measurement of $\Gamma(Z^0 \to b\bar{b})/\Gamma(Z^0 \to \mathrm{hadrons})$ using leptons, *Z. Phys.* **C58**, 523 (1993).

[86] OPAL Collaboration, R. Akers *et al.*, QCD studies using a cone based jet finding algorithm for e^+e^- collisions at LEP, *Z. Phys.* **C63**, 197 (1994).

[87] L. del Pozo, Jet finding with a cone algorithm, OPAL Technical Note TN170 (unpublished), June 1993.

[88] E. Farhi, A QCD test for jets, *Phys. Rev. Lett.* **39**, 1587 (1977).

[89] R. Batley, Are two primary vertices better than one ?, OPAL Technical Note TN478 (unpublished), April 1997.

[90] R. Hawkings and S. de Jong, The beam spot location in 1994 data, OPAL Technical Note TN321 (unpublished), September 1995.

[91] R. Hawkings, High performance b–tagging using 3D vertexing and neural networks, OPAL Technical Note TN515 (unpublished), September 1997.

[92] F. James and M. Roos, 'MINUIT' A system for function minimization and analysis of the parameter errors and correlations, *Comput. Phys. Commun.* **10**, 343 (1975).

[93] H. A. Bethe, *andbuch der Physik 24/1*, page 491, J. Springer Verlag Berlin, 1933.

[94] R. Pérez-Ochoa, Improved dE/dx calibration at LEP1, OPAL Technical Note TN562 (unpublished), August 1998.

[95] C. Peterson, T. Rögnvaldsson, and L. Lonnblad, JETNET 3.0: A versatile artificial neural network package, *Comput. Phys. Commun.* **81**, 185 (1994).

[96] Ben J. A. Kröse and Patrick van der Smagt, *An introduction to neural networks*[b], The University of Amsterdam, fifth edition, 1993.

[97] C. Peterson and T. Rögnvaldsson, An introduction to artificial neural networks, Lecture notes, 1991 CERN school of computing, LU TP 91-23.

[98] O. Cooke and C. Jones, Neural network electron and photon conversion identification, OPAL Technical Note TN556 (unpublished), July 1998.

[99] OPAL Collaboration, K. Ackerstaff *et al.*, Measurement of the strong coupling constant α_s and the vector and axial vector spectral functions in hadronic τ decays, *Eur. Phys. J.* **C7**, 571 (1999).

[100] Muon Identification Working Group, Identification of muons in hadronic Z^0 decays, OPAL Technical Note TN107 (unpublished), July 1992.

[101] D. Charlton and P. Gagnon, Muon identification efficiency and background for PASS7 LEP1 data, OPAL Technical Note TN572 (unpublished), October 1998.

[102] The LEP Collaboration, ALEPH, DELPHI, L3 and OPAL, Combining heavy flavor electroweak measurements at LEP, *Nucl. Instrum. Methods* **A378**, 101 (1996).

[103] OPAL Collaboration, R. Akers *et al.*, A study of b meson oscillations using dilepton events, *Z. Phys.* **C66**, 555 (1995).

[104] OPAL Collaboration, R. Akers *et al.*, Studies of charged particle multiplicity in b quark events, *Z. Phys.* **C61**, 209 (1994).

[b] http://www.robotic.dlr.de/Smagt/books/neuro-intro.ps.gz

[105] OPAL Collaboration, K. Ackerstaff *et al.*, Measurements of the b quark forward – backward asymmetry around the Z^0 peak using jet charge and vertex charge, *Z. Phys.* **C75**, 385 (1997).

[106] G. Bahan and R. Barlow, Identification of b jets using neural networks, *Comput. Phys. Commun.* **74**, 199 (1993).

[107] ALEPH Collaboration, R. Barate *et al.*, Determination of $|V_{ub}|$ from the measurement of the inclusive charmless semileptonic branching ratio of b hadrons, *Eur. Phys. J.* **C6**, 555 (1999).

[108] L3 Collaboration, M. Acciarri *et al.*, Measurement of the inclusive charmless semileptonic branching fraction of beauty hadrons and a determination of $|V_{ub}|$ at LEP, *Phys. Lett.* **B436**, 174 (1998).

[109] Input parameters for the LEP electroweak heavy flavour results for summer 1998 conferences, LEPHF98-01[c] (unpublished) used for the Combination of Preliminary Electroweak Measurements and Constraints on the Standard Model, ALEPH, DELPHI, L3 and OPAL collaborations, the LEP Electroweak Working Group, and the SLD Heavy Flavour and Electroweak Groups, **CERN-EP/99-015**, October 1998.

[110] BES Collaboration, J. Z. Bai *et al.*, Determination of J/Ψ leptonic branching fraction via $\Psi(2S) \to \pi^+\pi^-\ J/\Psi$, *Phys. Rev.* **D58**, 092006 (1998).

[111] OPAL Collaboration, G. Abbiendi *et al.*, Measurement of the average polarisation of b baryons in hadronic Z^0 decays, *Phys. Lett.* **B444**, 539 (1998).

[112] P. Wells, Private communication.

[113] D. Scora and N. Isgur, Semileptonic meson decays in the quark model: An update, *Phys. Rev.* **D52**, 2783 (1995).

[c] http://www.cern.ch/LEPEWWG/heavy/

[114] D. S. Hwang, C. S. Kim and W. Namgung, Average kinetic energy of heavy quark in semileptonic B decay, *Phys. Rev.* **D54**, 5620 (1996).

[115] W. F. Palmer, E. A. Paschos and P. H. Soldan, Momentum distribution in the decay $B \to J/\Psi + X$, *Phys. Rev.* **D56**, 5794 (1997).

[116] OPAL Collaboration, R. Akers *et al.*, Measurement of the $B^0 - \overline{B^0}$ mixing, $\Gamma(Z^0 \to b\overline{b})/\Gamma(Z^0 \to \text{hadrons})$ and semileptonic branching ratios for b flavored hadrons in hadronic Z^0 decays, *Z. Phys.* **C60**, 199 (1993).

[117] ALEPH Collaboration, D. Buskulic *et al.*, Measurement of the b forward – backward asymmetry and mixing using high p_T leptons, *Phys. Lett.* **B384**, 414 (1996).

[118] ALEPH Collaboration, D. Buskulic *et al.*, Heavy flavor production and decay with prompt leptons in the ALEPH detector, *Z. Phys.* **C62**, 179 (1994).

[119] DELPHI Collaboration, P. Abreu *et al.*, Measurement of $\Gamma(b\overline{b})/\Gamma(\text{had})$ using impact parameter measurements and lepton identification, *Z. Phys.* **C66**, 323 (1995).

[120] L3 Collaboration, M. Acciarri *et al.*, Measurement of the $B^0 - \overline{B^0}$ mixing parameter and the $Z^0 \to b\overline{b}$ forward – backward asymmetry, *Phys. Lett.* **B335**, 542 (1994).

[121] L3 Collaboration, O. Adriani *et al.*, Measurement of the $e^+e^- \to b\overline{b}$ and $e^+e^- \to c\overline{c}$ forward backward asymmetries at the Z^0 resonance, *Phys. Lett.* **B292**, 454 (1992).

[122] S. Stone, CLEO-III: A detector to measure rare B decays and CP violation, *Nucl. Instrum. Meth.* **A368**, 68–73 (1995).

[123] D. Boutigny *et al.*, BaBar technical design report, SLAC-R-0457.

[124] K. Rybicki, BELLE: Detector for studying the CP violation at the KEK B factory, In *Stara Lesna 1998, Hadron structure '98* 268-279.

[125] B. Schwingenheuer, Status of the HERA-B experiment, In *Batavia 1998, Heavy quarks at fixed target* 45-54.

[126] P. Azzi, The CDF silicon detector upgrade, *Nucl. Instrum. Meth.* **A419**, 532 (1998).

[127] S. Abachi *et al.*, The D0 upgrade, *Nucl. Instrum. Meth.* **A408**, 103 (1998).

[128] P. Sherwood, B physics with the ATLAS detector, *Nucl. Phys. Proc. Suppl.* **75B**, 315 (1999).

[129] R. Kinnunen, CMS detector and its potential for B physics, *Nucl. Phys. Proc. Suppl.* **75B**, 327 (1999).

[130] D. Websdale, LHC-B: A dedicated b physics detector for the LHC, *Nucl. Phys. Proc. Suppl.* **50**, 333–342 (1996).

[131] R. Brun, *HBOOK : A histogramming package*, 1994, CERN Program Library Long writeup Y205[d].

[132] R. Barlow and C. Beeston, Fitting using finite Monte Carlo samples, *Comput. Phys. Commun.* **77**, 219 (1993).

[d]http://consult.cern.ch/writeups/hbook/